ΒΛΟΓΙΑΝΝΙΤΗΣ ΣΩΤΗΡΙΟΣ

ΣΧΟΛΗ ΜΗΧΑΝΟΛΟΓΩΝ ΜΗΧΑΝΙΚΩΝ

«Σχεδιασμός και υπολογιστική αξιολόγηση των μηχανικών ιδιοτήτων προσθετικά κατασκευασμένων δίσκων από SS316L με εσωτερική πλεγματική δομή χρησιμοποιώντας τη μέθοδο των πεπερασμένων στοιχείων»

Τομέας: Μηχανολογικών Κατασκευών και Αυτόματου Ελέγχου

Επιβλέπων: Σπιτάς Βασίλειος, Καθηγητής ΕΜΠ

Αθήνα, 2024

VLOGIANNITIS SOTIRIOS

"Design and computational evaluation of the mechanical behavior of additively-manufactured SS316L disks with internal lattice structure using the finite element method"

SCHOOL OF MECHANICAL ENGINEERING

Section: Mechanical Design and Control Systems

Supervisor: Spitas Vasileios, NTUA Professor

Athens, 2024

1. Aknowledgements

I extend my sincere gratitude to the individuals and organizations who have played instrumental roles in the completion of this research project. Their support, guidance and contributions have been invaluable throughout the journey.

I would like to express my deepest appreciation to my research supervisor, Dr. Spitas Vasileios and Dr. Rogkas Nikolaos, for their unwavering support, insightful guidance, and expert knowledge. Their mentorship has been instrumental in shaping the direction and focus of this research.

Special thanks are due to my colleagues and peers who provided valuable insights, engaging discussions, and a collaborative environment that enriched the research process. The exchange of ideas and perspectives has been crucial in developing a well-rounded and comprehensive study.

I am grateful for the support and resources provided by ANiMA Technical Commercial SA. The access to cutting-edge facilities and the conducive research environment have significantly contributed to the successful execution of this project.

I acknowledge the financial support from Andronikidis Konstantinos, which has enabled the realization of this research initiative. Their commitment to advancing scientific knowledge is commendable, and I am thankful for the opportunities they have provided.

Lastly, I extend my heartfelt thanks to my family and friends for their unwavering encouragement, understanding, and patience throughout this endeavor. Their support has been a constant source of motivation.

This project represents the collective effort of many, and I am grateful for the collaborative spirit that has characterized every stage of the research.

<u>Υπεύθυνη δήλωση</u> για λογοκλοπή και για κλοπή πνευματικής ιδιοκτησίας:

Έχω διαβάσει και κατανοήσει τους κανόνες για τη λογοκλοπή και τον τρόπο σωστής αναφοράς των πηγών που περιέχονται στον οδηγό συγγραφής Διπλωματικών Εργασιών. Δηλώνω ότι, από όσα γνωρίζω, το περιεχόμενο της παρούσας Διπλωματικής Εργασίας είναι προϊόν δικής μου εργασίας και υπάρχουν αναφορές σε όλες τις πηγές που χρησιμοποίησα.

Οι απόψεις και τα συμπεράσματα που περιέχονται σε αυτή τη Διπλωματική εργασία είναι του συγγραφέα και δεν πρέπει να ερμηνευθεί ότι αντιπροσωπεύουν τις επίσημες θέσεις της Σχολής Μηχανολόγων Μηχανικών ή του Εθνικού Μετσόβιου Πολυτεχνείου.

Ονοματεπώνυμο

Contents

2. Abstract

In response to the automotive industry's critical demands for enhanced lightweighting, widespread decentralized manufacturing capabilities, and meticulous precision optimization, this project embarks on the innovative redesign of clutch disk architecture extending its scope to a comparative analysis of lattice structure disks. The study delves into the mechanical properties of various disks by incorporating different lattice structures as infill. Different unit cells, including tetrahedral, BCC, and I-type, are meticulously designed using Fusion 360.

This approach facilitates the creation of various disk configurations, specifically tailored for use in dry friction clutches while eliminating the need for a traditional bulk core, capitalizing on the latest breakthroughs in additive manufacturing. This pioneering design strategy seeks to amalgamate the superior features of both dry and wet friction clutches, thus contributing valuable insights to the clutch technology.

A comprehensive Finite Element Analysis is constructed in ANSYS to analyze the response of the disk design to static loads, adopting the theory of uniform wear. Mechanical strength and stiffness in compressive direction are meticulously observed for each design.

Key variables, including total deformation, equivalent elastic strain, equivalent stress, strain energy, and force reaction, are scrutinized. Through this collaborative effort, we aim to deepen our understanding of lattice structures, offering insights that will not only refine clutch disk design but also contribute to broader advancements in automotive engineering.

Body-centered cubic (BCC) lattice models exhibit maximum deformation, while tetrahedral exhibits the least deformation. Notably, the BCC 50% configuration demonstrates a higher average deformation than the BCC 12% counterpart. Furthermore, I-type configurations exhibit lower elastic strain, while tetrahedral patterns display intermediate levels, elucidating the diverse deformation characteristics inherent in different lattice designs and densities. Within the BCC patterns, a direct correlation emerges between density and stress levels, where higher density corresponds to elevated maximum and average stress values, indicating a more pronounced structural response. In contrast, the I-type configurations reveal an inverse relationship, with higher density correlating with lower maximum and average stress levels. This underscores the critical role of geometric considerations in ensuring structural integrity and optimal performance. Additionally, strain energy and force reaction demonstrates a sharper increase in I-type configurations compared to BCC patterns as density rises.

In summary, while each lattice configuration showcases unique deformation patterns, comparing maximum and average deformation values offers valuable insights into their structural behavior, contributing to a deeper understanding of their response to external forces and aiding optimization for diverse engineering applications.

3. Abbreviations

FEA – finite element analysis

SS316L – stainless steel 316L

SLM – selective laser melting

LPBF – laser powder bed fusion

TPMS – triple periodic minimal surface

SC – simple cubic

BCC – body-center cubic

FCC – face-centered cubic

AM – additive manufacturing

3D – three-dimensional

CTE - Coefficient of Thermal Expansion Matrix

4. Introduction

The pursuit of innovative solutions in clutch disk design is a fascinating journey into the core of automotive engineering, focusing on enhancing performance, durability, and efficiency. Collaborative research efforts play a pivotal role in this quest, bringing together diverse expertise from across the industry and academia. The automotive industry's pursuit of optimized powertrain efficiency and reduced environmental impact has driven diverse approaches to clutch disk design. Moreover, as the automotive landscape evolves, the integration of novel materials and design philosophies becomes imperative. Recognizing the importance of exploring various methodologies, the effort aims to comprehensively assess the mechanical and performance attributes of different lattice structures within clutch disks.

Traditional clutch disks are typically made from a combination of high-friction materials and metals, but researchers are now experimenting with composites, ceramics, and even advanced polymers. These materials can offer superior heat resistance, reduced weight, and improved wear characteristics, leading to longer-lasting clutch components and enhanced performance.

In addition to materials, the geometry and structure of clutch disks are undergoing a transformative reevaluation, with particular emphasis on lattice structures. The integration of lattice structures presents an exciting opportunity to enhance clutch performance. In the research, the replacement of conventional spring mechanisms with various lattice structures is being explored, aiming to optimize engagement smoothness and overall functionality. This shift towards lattice structures signifies a novel approach in advancing clutch disk design, pushing the boundaries of conventional methodologies for improved performance and durability.

In this research, Fusion360 is employed for design, providing a robust platform to conceptualize and refine designs, ensuring precision and efficiency in the development process. Utilizing Ansys for FEA enables in-depth analyses, evaluating the structural integrity and performance characteristics of clutch disk designs under various conditions. Additionally, the material of choice, SS316L from the additive manufacturing library, stems from the manufacturing process using Laser-Powder Bed Fusion (L-PBF) technology. SS316L, renowned for its durability and heat resistance, serves as the cornerstone of the innovative approach. Through the strategic integration of tools and materials, the aim is to advance clutch disk design, enhancing performance and efficiency in automotive engineering.

The primary focus of the comparative analysis is to meticulously examine and contrast various lattice structures across different infill densities. The importance of this comparative exploration resonates across multiple dimensions, enriching the broader discourse on lattice structure design in mechanical engineering.

5. Literature Review

5.1 Lattices

Reducing weight while preserving the structural integrity of components presents an ongoing challenge in manufacturing sectors, particularly in the aerospace and automotive industry [1]. This research delves into how the manipulation of lattice geometry dimensions can optimize mechanical properties, making them suitable for aerospace and automotive applications.

The emergence of additive manufacturing has unlocked new possibilities in the creation of functional materials, focusing on structural design rather than chemical composition. Arising from this innovation is a novel category of advanced materials known as lattice structures. These are three-dimensional constructs made up of interconnected struts, shells, plates, or combinations of these elements, arranged in a repetitive pattern [28,42,56].

Explorations in lattice structures have encompassed a range of unit cell sizes, feature dimensions, and overall lattice thicknesses to understand and optimize their potential applications [28]. These structures provide substantial design flexibility, allowing for customizable feature-pore morphology and interconnectivity, which makes them highly adaptable for achieving specific physical properties. Moreover, the extensive design flexibility inherent in these lattice structures opens up further opportunities for customization and optimization, thereby facilitating the achievement of enhanced performance [58]. To date, extensive research has been conducted on the physical properties of lattice structures, revealing their significant potential for various applications. These include use as lightweight materials [44], energy absorbers [20], heat dissipaters [57], heat insulators [5], and electromagnetic absorbers/insulators [66], demonstrating their versatile capabilities *(Figure 5.1)*.

Figure 5.1 Examples of lattice structures applications

The drive for structures that are both lighter and stronger has led to the rapid development and adoption of new, more sophisticated materials. This progress is significantly supported by computational modeling techniques. These tools are crucial not only for structural analysis and synthesis but also for the optimal design of materials, such as through topology optimization. This approach integrates material science with structural engineering to create efficient, innovative solutions for complex engineering challenges [11]. Topology optimization and the creation of internal lattice structures are common techniques employed to reduce weight while preserving the strength of components. Despite being effective optimization strategies, they are not without their limitations. Components optimized through topology methods can sometimes underperform when subjected to unanticipated load conditions. Additionally, the generation of lattices using commercial software often faces constraints in crafting ideal lattice structures with precisely controlled geometric parameters, frequently leading to the production of lattices composed of repetitive unit cells [1].

The hierarchical topology optimization model for multiscale structural design seeks to identify the best material distribution across various interconnected structural scales. This aims to optimize both the structure and its material comprehensively [11].

This research delves into how the manipulation of lattice geometry dimensions can optimize mechanical properties, making them suitable for aerospace and automotive applications.

5.2 Classification of Lattice Structures

Porous materials are extensively utilized in both natural and engineering contexts due to their outstanding specific mechanical responses and the ability to tailor their properties. Nevertheless, the challenge with lightweight cellular solids is their propensity for severe localized deformation, leading to catastrophic failure, which compromises their damage resistance and restricts their application to scenarios of minimal strain [17]. These materials, including random foams and honeycombs, play a critical role in the engineering field, particularly in sectors like aerospace, automotive, and construction, due to their advanced material properties. Random foams are valued for their low elastic modulus and flexibility, but their unpredictable nature requires the implementation of high safety margins during their use *(Figure 5.2).* Honeycomb structures are recognized for their exceptional mechanical characteristics; however, their highly directional properties limit their application to scenarios where hazards are foreseeable *(Figure 5.3).* The advent of Additive Manufacturing (AM) technologies has enabled the creation of a novel category of porous material known as lattice structures. These structures are characterized by their three-dimensional, architecturally designed features, which can include struts, plates, shells, or a combination *(Figure 5.4).* As a result, lattice structures exhibit distinctive physical properties and find application across a wide range of fields [67].

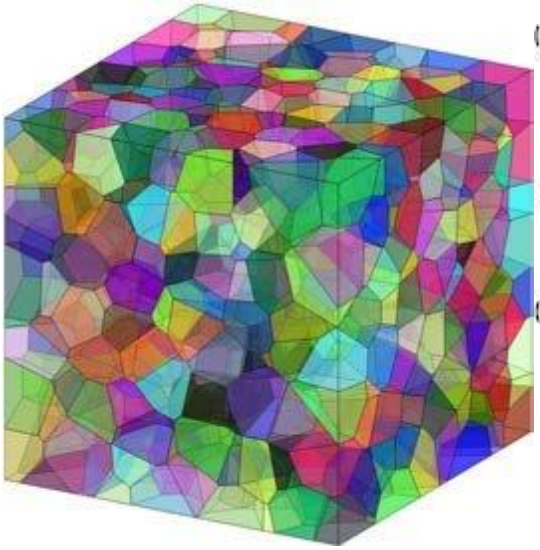

Figure 5.2 3D Voronoi lattice

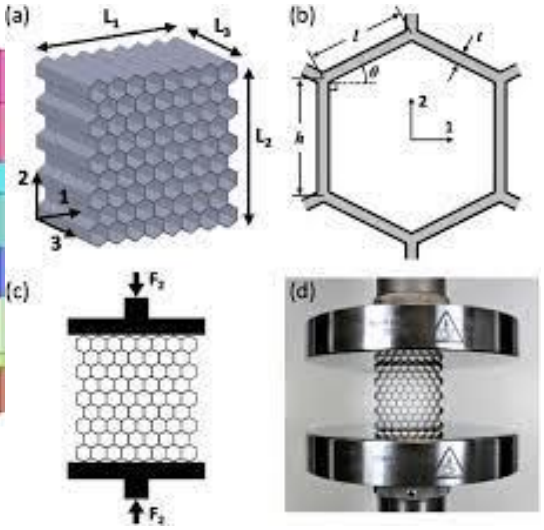

Figure 5.3 Honeycomb structure

Figure 5.4 Different three-dimensional lattice structures

Despite the virtually unlimited possibilities with the design of lattices, there are only two intrinsic factors sufficient in defining a lattice structure. First, the lattice morphology, and second, the relative density. The lattice morphology pertains to the distinctive structures that lattices can adopt. The relative density then refers to the volume fraction of the solid parts of the lattice structure with respect to the volume of its bounding box. In other words, lattices with a higher relative density have thicker struts, shells, or cell walls *(Figure 5.5).* The

unit cell size then falls under as an extrinsic factor, e.g. increased unit cell size only results in a proportional scaling of all features in a lattice *(Figure 5.6 E).* A final characteristic is the cell repetition, which refers to any number of times a unit cell, either the same one or a different one, is repeated across any direction to form a repeating lattice.

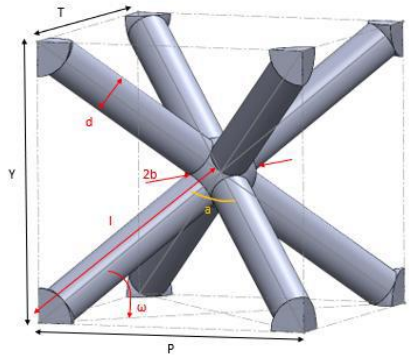

Figure 5.5 Parametric lattice unit cell

Lattice structures are characterized as arrangements of periodic and repeating unit cells, composed of three-dimensional, spatially architected features. Given their non-restrictive definition, lattice structures can encompass a wide array of feature types, offering almost limitless design options. In this context, based on their physical characteristics, we classify lattice structures into three main types: truss, triply periodic minimal surface (TPMS), and plate. Additionally, there is a fourth category that includes hybrid forms combining elements of these primary structures [28] *(Figure 5.5).*

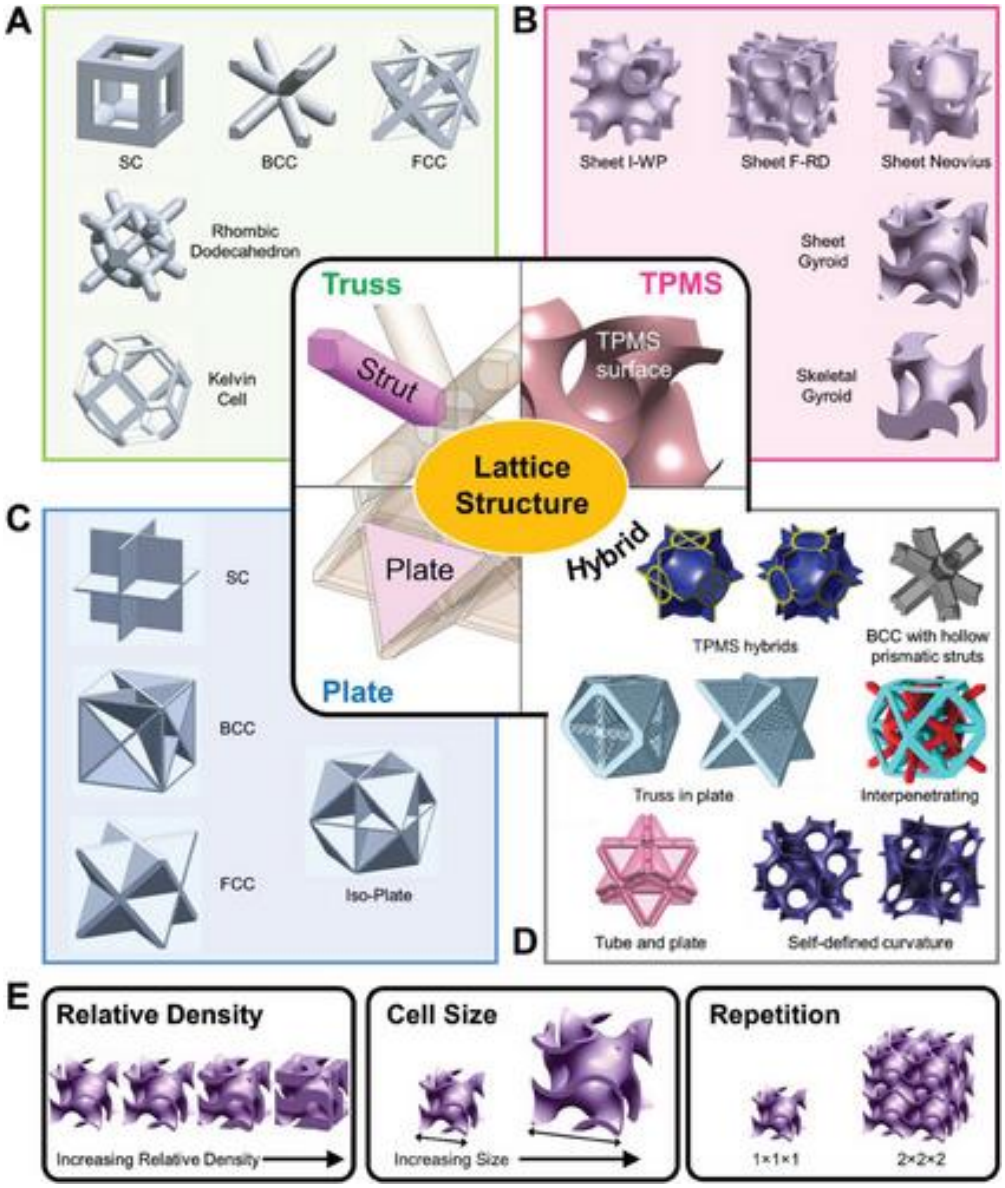

Figure 5.6 Lattice structures classification

5.2.1 Truss Lattices

Truss lattices, akin to their architectural analogues, are composed of interconnected struts converging at nodes (*Figure 5.6 A*). The orientation of struts, their number, and the node count are key elements defining the truss lattice structure. The straightforward nature of truss lattice design motifs permits extensive design freedom, leading to a vast array of design possibilities. Prominent and extensively studied designs often draw inspiration from Bravais lattices, including simple cubic (SC), body-centered cubic (BCC), and face-centered cubic (FCC)

crystal structures [31,14,58]. Truss lattices based on alternative geometries encompass those derived from biological structures [13,62], polyhedrons [9,65], and covalent bonds [9]. Additionally, truss lattices can be developed through topological optimization using finite element software *(Figure 5.7).* While struts in these lattices are typically uniform, designs incorporating tapered or heterogeneously cross-sectioned struts also exist, catering to customized mechanical properties [28] *(Figure 5.8).*

Figure 5.7 Truss lattice with topology optimization

Figure 5.8 Heterogeneously cross-sectioned struts

5.2.2 TPMS Lattices

Triply periodic minimal surface (TPMS) lattices are structures whose geometry is defined by TPMS surfaces *(Figure 5.6 B).* TPM surfaces are three-dimensional mathematical surfaces characterized by non-intersecting segments and zero mean curvature *(Figure 5.10).* These surfaces were first introduced by Hermann Schwarz in 1865 and later expanded upon by Alan Schoen in 1970, who introduced additional TPMS surfaces. Common types of TPMS lattices include the Gyroid, Diamond, Primitive, I-WP, Neovius, and F-RD [19]. Each TPMS surface is described by its unique parametric equation; for example, the gyroid is defined by the equation: $\sin(x)\cos(y) + \sin(y)\cos(z) + \sin(z)\cos(x) = t$, where $t = 0$. The most basic TPMS lattices are derived from thickened mathematical surfaces, also known as sheet TPMS or, alternatively, shell lattices due to their smooth curvature. A different form of TPMS lattice is based on the inverse of the volume occupied by the thickened sheet [2], resulting in skeletal TPMS. Unlike shell lattices, skeletal TPMS structures resemble truss lattices with smooth struts. To achieve enhanced directional strength or isotropy, various modifications of TPMS lattices have been developed. These modifications include altered parameter [16] and variations in wall thickness [62].

Figure 5.10 Different TPMS lattice cubes

5.2.3 Plate Lattices

Plate lattices, a relatively recent innovation, bear similarities to truss lattices in their configuration, comprising strategically arranged plates *(Figure 5.11)*. For example, plate lattices based on Bravais lattices involve positioning plates at the close-pack planes of these crystal structures [44] *(Figure 5.6 C)*. The concept of the first plate lattice was introduced by Berger et al., who also demonstrated that a structure combining SC+FCC plates could achieve the Hashin-Shtrikman upper bounds for isotropic elasticity [6]. However, plate lattices derived from Bravais lattices typically exhibit a closed-cell morphology, which limits their manufacturability using many 3D printing techniques. To overcome this limitation, the concept of “semi-plate” lattices has been introduced, where the plates are designed with strategically placed pores to enable the removal of feedstock material that might get trapped within closed cells [44, 27].

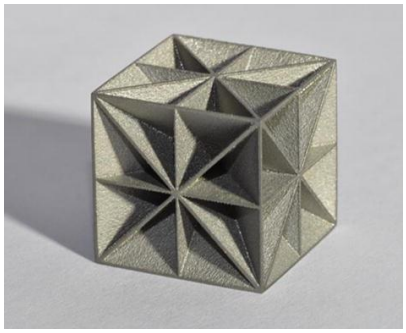

Figure 5.11 Plate lattice metal cube

5.2.4 Hybrid Structures

Struts, shells, and plates are the three most common types of features observed in lattice structures. Nonetheless, various works have reported modifications or hybrid combinations of these features *(Figure 2.6 D)*, in search for novel lattices with unique properties. One popular class is a variant of truss lattices–tube lattices–where the struts are made hollow instead of being solid. Lattices of both cylindrical and prismatic tubes have been reported [63, 43, 62]. Other popular types also include shell lattices defined based on other novel mathematical definitions and criteria, apart from the TPMS criteria [38,8]. In terms of hybridization and combination, combinations of shells and tubes [7], tubes and plates [30], TPMS and plates [10], TPMS and struts [21], struts and plates [43,29,49], interpenetrating lattice [67,68] exist. In addition to occurring at the unit cell level, hybridization also occurs when arranging multiple unit cells. For instance, the repeating lattice consists of unit cells that are different from one another. These include the functionally graded [64], fractal [9], hierarchical [69,16] and heterogeneous [37] types of arrangements.

5.3 Metallic Lattices

Additive manufacturing (AM) fabricated metallic lattice structures have been offering increasingly versatile opportunities in lightweight applications due to the combination of high mechanical properties of metallic materials and tunable properties by lattice structures [24, 33, 67]. It is also highly regarded for its capacity to efficiently fabricate metallic components that closely match final designs, reducing both the time and material waste associated with traditional manufacturing techniques. This innovative approach presents a significant challenge to established repetitive production methods [15,26].

Presently, a significant portion of research in aerospace applications is centered on enhancing energy efficiency, along with reducing fuel consumption and exhaust emissions. However, there remains an urgent need to explore methods to minimize material usage and weight of components, contributing to the conservation of increasingly scarce natural resources [4]. Past studies have delved into the utilization of materials with high specific strength, including magnesium, aluminum, titanium, and high-strength steels [35],[68], [25]. Additionally, research has investigated structural design modifications aligned with actual load conditions, such as the sandwich design that achieves weight reduction through increased stiffness or fewer joining elements [36]. Yet, these approaches often demand the creation of complex geometries, posing significant manufacturing challenges.

In this context, Additive Manufacturing (AM) technologies, notably Selective Laser Melting, have emerged as a means to fabricate intricate 3D lattice structures [47], while also curtailing production time and costs. Parthasarathy observed that AM technologies offer design versatility and enable the creation of closed or open cell structures with locally tailored stiffness and optimized compatibility [4].

The advancement of laser powder bed fusion techniques, such as selective laser melting (SLM), has enabled the production of these intricate micro-architectures using metallic powder as the primary material source [71]. The ability to create metal components directly from digital data using fully automated, single-piece equipment and feedstock materials, without the need for additional hard tooling, holds significant potential. Immediate impacts of such technology include substantial reductions in both cost and lead time, the capability to manufacture small batches or unique components on demand, and the flexibility to prototype and fabricate advanced, high-performance, and more efficient components that are unachievable with traditional manufacturing methods due to limitations in geometry, material, microstructure, and properties *(Figure 5.12).* These advantages are well-recognized, and metal 3D printing is currently utilized for limited production across various sectors by industry, research and development institutions, and governments worldwide [**12**].

Figure 5.12 GE Case study

In 2018, Zhang et al. explored the mechanical behaviors and energy absorption capacities of three TPMS configurations—Primitive, Diamond, and Gyroid—manufactured through selective laser melting (SLM) using 316L stainless steel. They categorized the failure modes and assessed the printing precision via numerical analyses. Their findings underscored that the mechanical properties and deformation patterns are highly dependent on the geometry of the unit cell. Among these, Diamond-type TPMS structures demonstrated the highest stiffness, stress at the onset of plateau, and energy absorption capabilities when compared to body-centered cubic lattices. The correlation between the mechanical responses predicted by explicit finite element models and those observed in experiments was strong. The simulations also indicated that Diamond and Gyroid structures maintain relatively even stress distributions under compression, leading to consistent collapse behaviors and efficient energy absorption [60].

Austenitic stainless steel 316L (SS316L) is extensively utilized in various industries due to its favorable mechanical properties, robust wear resistance, superior corrosion resistance, and affordability. SS316L is particularly amenable to processing via Laser Powder Bed Fusion (LPBF), and a multitude of research studies have been dedicated to exploring its microstructure and mechanical characteristics [39,22,35,41,52]. Unlike traditional processing methods where steel strengthening often leads to reduced ductility, LPBF-produced SS316L can achieve both high strength and ductility. This is attributed to its hierarchical microstructure, which includes grain structure, solidification cellular structures, and dislocations, as detailed in [4,50,52]. This

complex microstructure is the primary determinant of its mechanical properties, which can be finely tuned through variations in the LPBF process parameters.

5.4 Tetrahedral Lattice

The tetrahedral lattice structure *(Figure 5.13)* is renowned for its lightweight and high strength-to-weight ratio [61]. Kooistra et al. have comprehensively analyzed the effective properties of tetrahedral lattice cores. They were developed with the consideration of topology's role in the mechanical behavior of cellular materials. These lattice structures have been suggested as potential cores for sandwich panel structures, where they demonstrate structural competitiveness with other core materials, such as closed-cell honeycomb [23]. The way lattice truss core materials behave mechanically is influenced by the inherent characteristics of the materials they're made of and their density compared to the surrounding material. Therefore, enhancing the mechanical properties of lattices can be achieved by using materials with high specific stiffness [61]. While both lattice truss and honeycomb core sandwich panels offer structural advantages over metal foam core panels, lattice truss cores, being open-cell, offer additional possibilities for multifunctional applications like cross-flow heat exchange, shape morphing, and high-intensity dynamic load protection. They also show promise for impact energy absorption applications, an area where honeycombs, egg box structures, and even stochastic metal foam topologies have garnered significant interest [23].

Zhang's study has shown that composite lattice truss core materials address a previously existing gap in the relationship between strength and density properties of materials. This suggests that they have the potential to serve as excellent candidates for ultra-lightweight cores in sandwich structures [61].

Sugimara et al. observed that the shear response of the material remains linear up to the point of failure, despite an observable shift in slope at the onset of loading. The material undergoes sudden failure when the shear stress reaches a critical threshold. Following the initial drop in stress, the stress–strain curve exhibits no fluctuations, indicating that the majority of struts failed almost simultaneously, exhibiting brittle fracture characteristics. Upon detailed inspection, it was evident that struts under tensile stress fractured with minimal deformation, while those under compressive stress remained undamaged, with no evidence of buckling. A significant portion (70–80%) of the fractures occurred in the tensile struts, though a notable amount of nodal failure was also present in some samples. Nodal failures were more pronounced in cases where there was misalignment of the specimen relative to the shear plane [40].

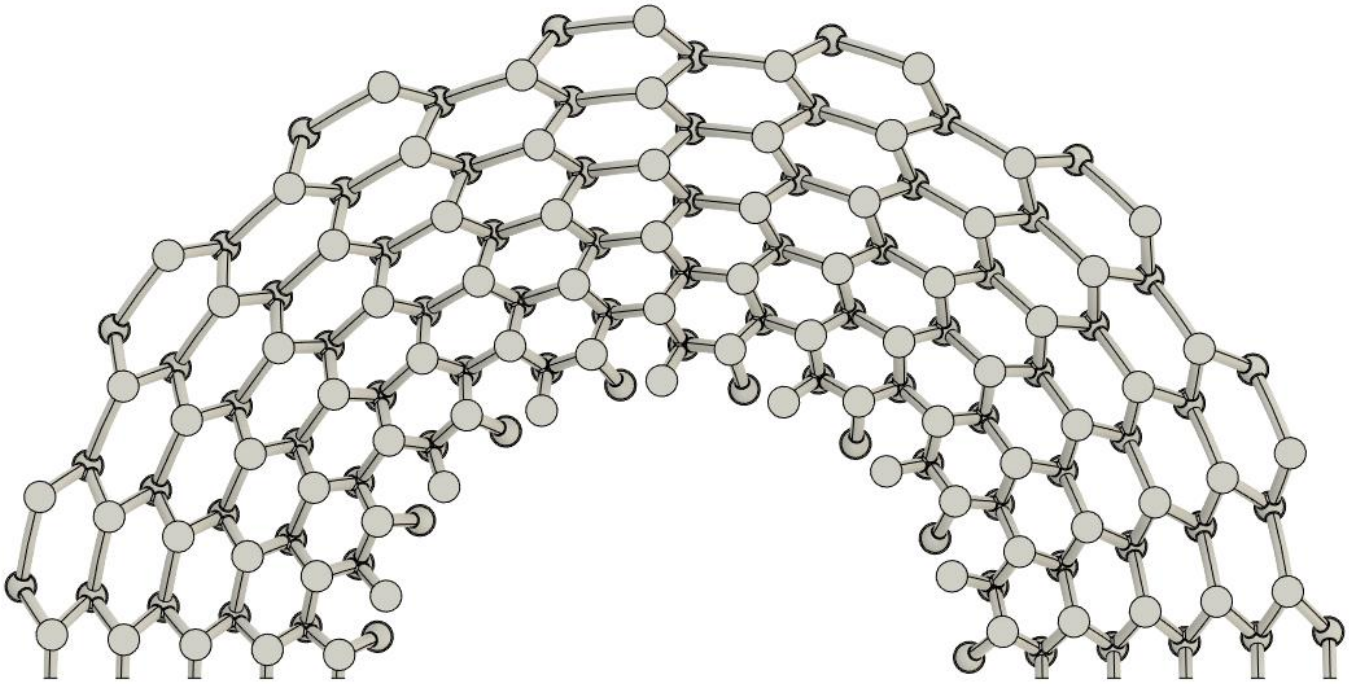

Figure 5.13 Tetrahedral lattice in cylindrical coordinates

5.5 Body Centered Cubic (BCC) Lattice

Tancogne-Dejean and Dirk Mohr (2018) delved into the intricate details of Body-Centered Cubic (BCC) truss lattices, connecting the nearest neighbors in the BCC lattice through beams to form a unit cell. Their work further explained the significance of beam intersections, termed "nodes," and how their volume fraction relative to the solid matter increases with the metamaterial's relative density. BCC lattice's cubic symmetry and inherent strength, makes it ideal for supporting compressive loads [70]. Its structure's compatibility with the disk's core, without producing damaged lattices, is emphasized, illustrating its robustness and adaptability *(Figure 5. 14).*

To accommodate variations in structural demand, both uniform and tapered beam designs were considered. Tapered beams, whose cross-sectional diameter varies quadratically along their length, offer a means to adjust the lattice's flexural stiffness without altering its relative density. This approach was quantitatively supported by modified expressions for relative density that account for the tapering effect, showcasing the meticulous balance between structural design and material efficiency in optimizing BCC lattice structures for advanced engineering applications. The primary assumptions for the model include:

(1) Uniformity among beams, all possessing a circular cross-section that might vary along their length, composed of an isotropic linear elastic material;

(2) The nodes maintain a fixed orientation relative to each other, a premise supported by the BCC structure's periodicity and the symmetry of the undeformed lattice around the BCC unit cell's central node. It's important to note the co-axial arrangement of beams at the nodes, with one beam entering and another exiting each node;

(3) Nodes are treated as immovable entities, with the lattice's flexibility arising solely from the beams' deformation, which span between these fixed nodes;

(4) The node centers move according to a predefined affine local displacement field.

The behavior of BCC lattices under large strain compression through numerical analysis, revealed that their crushing response remains consistent across varying relative densities, characterized by a monotonically ascending engineering stress-strain curve up to the point of densification. This indicates a stable crush response under compression. Both theoretical insights and numerical models affirm that beam cross-section tapering significantly enhances the specific mechanical properties of BCC lattices. Specifically, the modifications lead to substantial improvements in the effective Young's modulus and specific energy absorption, with observed increases of up to 70% and 45%, respectively. This suggests that strategic design alterations in the beam cross-sections can markedly optimize the mechanical performance of BCC lattice structures [43].

Maskery's et. al. (2015) study delves into the impact of cell size and the number of cells on constructing more comprehensive models for understanding the mechanical behavior of lattice structures. By analyzing the modulus and ultimate tensile strength of lattice tensile specimens with various unit cell sizes and consistent relative density, we aim to grasp how these mechanical properties relate to different lattice design parameters. This understanding is pivotal for developing effective design tools, such as finite element methods, to optimize the performance of lattice parts manufactured through additive manufacturing (AM) processes. Their findings revealed significant decreases in modulus and strength as cell size increases, contrary to previous suggestions attributing such reductions to increasing strut porosity. Their relationships can forecast the properties of lattice column structures comprising body-centered cubic (BCC) cells and may be adaptable to other part geometries [70]

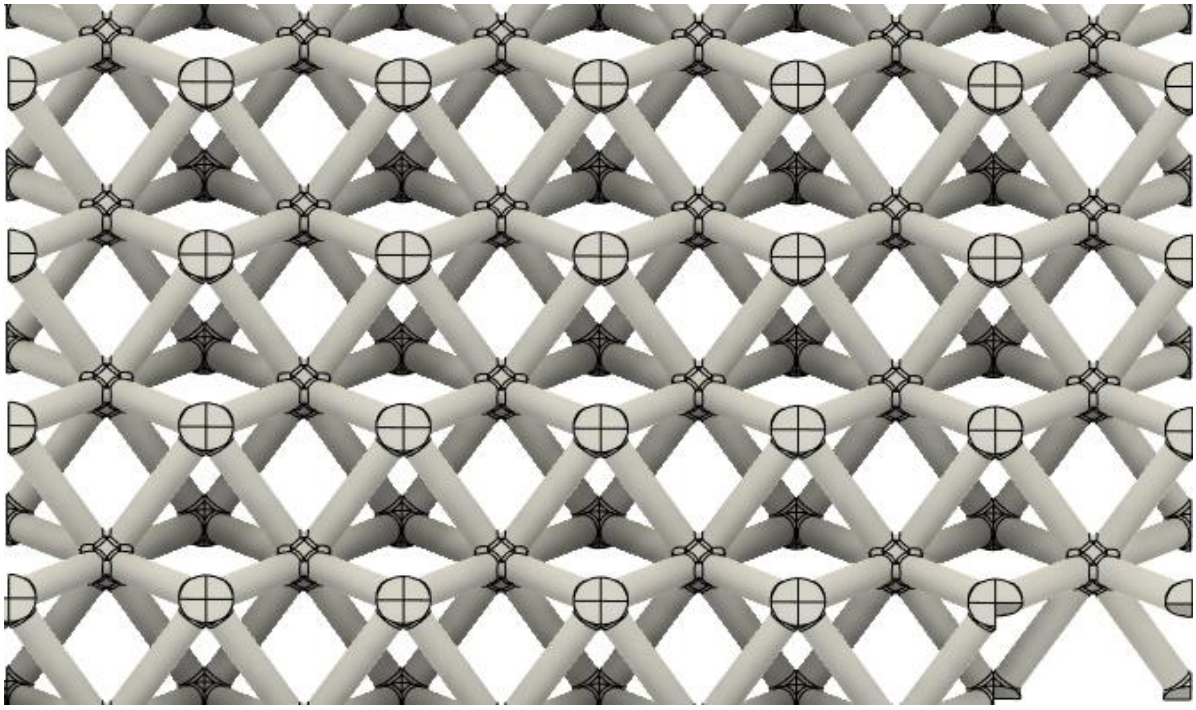

Figure 5.14 Body Centered Cubic (BCC) lattice

5.6 I-type Lattice

The I-type lattice geometry is highlighted for its innovative design, allowing for adjustable parameters to achieve a snug fit within the clutch disk's core. This section elaborates on the design considerations for strut cross-section thickness and inclination angles, catering to various relative densities. The document emphasizes the I-type cell's versatility and its ability to maintain structural integrity without the need for nodes, which simplifies the design and manufacturing process *(Figure 5.15).*

In 2018 Karamoozian introduced a groundbreaking brake disc design featuring periodic lattice truss substructures, with a focus on evaluating its dynamic stability. A comprehensive methodology combining theoretical modeling, experimental modal analysis, and finite element methods (FEM) is utilized to examine the disc's susceptibility to squeal noise. The brake system was theoretically represented as a rotating annular disc under in-plane frictional forces. The study determined the natural frequencies and forced response of the brake disc, with finite element analysis results serving as a validation. Experimental modal analysis was conducted on the lattice brake rotor/pad assembly under free-free boundary conditions to derive modal properties for the FEM [72]. This analysis was further enriched by incorporating models for heat convection during braking and the nonlinear contact forces between the rotor and pads, derived from the SAE J2521 drag

braking noise test simulations. The investigation compared the likelihood of squeal noise between the novel lattice and traditional vanned brake discs, measuring squeal propensity through the standard deviation of statistical brake instability occurrences. Findings indicated that the lattice design significantly reduced squeal propensity within the low frequency range of 4 to 8 kHz.

A novel I-type lattice structure was introduced, characterized by its alignment of truss topologies to effectively bear loads. Distinct from conventional lattice designs, the innovative I-structure incorporates unique node types, where the connections are made between strut members, and brazed nodes are strategically placed between the struts and the face plates.

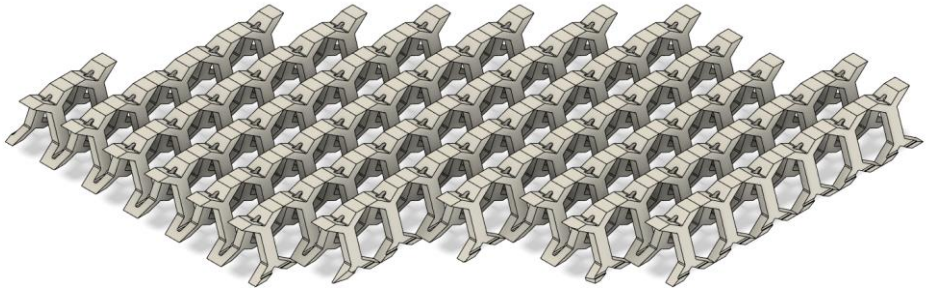

Figure 5.15 I-type lattice structure

6. Methodology

In this study, we employed a methodology that incorporates a variety of lattice unit cells, specifically the tetrahedral, body-centered cubic (BCC), and I-type geometries, as designed in Kechri's 2022 research. These selected geometries fall under the category of truss lattices and were integrated into the design with varying densities yet uniform dimensions. Utilizing Autodesk's Fusion 360, these unit cells were meticulously replicated across a disk's surface, which was designed with a central bore—measuring an inner diameter of 33mm and an outer diameter of 86.5mm.

6.1 Unit cells and lattice generation

For the BCC geometries *(Figure 6.1-4)* and tetrahedral *(Figure 6.11-18)*, two densities were explored: 12% and 50%. In contrast, the I-type geometries were tested at densities of 12% and 30% *(Figure 6.5-10)*. The dimensional specifications for the BCC and I-type unit cells were standardized at 3.875mm in each axis. However, the tetrahedral unit cells featured variable dimensions of 4.789mm along the x-axis, 4.474mm along the y-axis, and 3.875mm along the z-axis. Any unit cell that extended beyond the set boundaries was systematically excluded from the model.

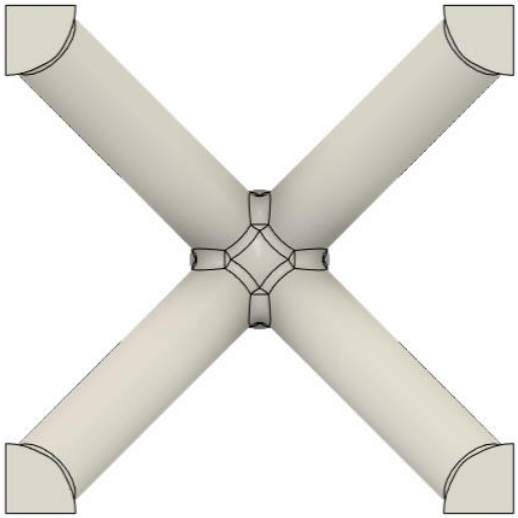

Figure 6.1 BCC 12% unit cell side view

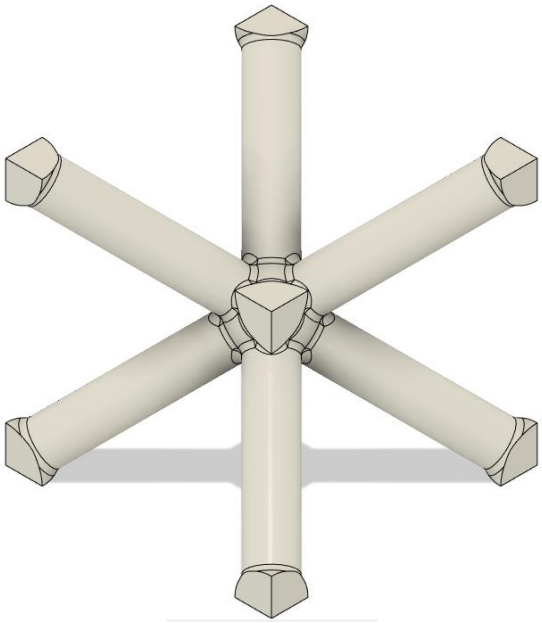

Figure 6.2 BCC 12% unit cell orthogonic view

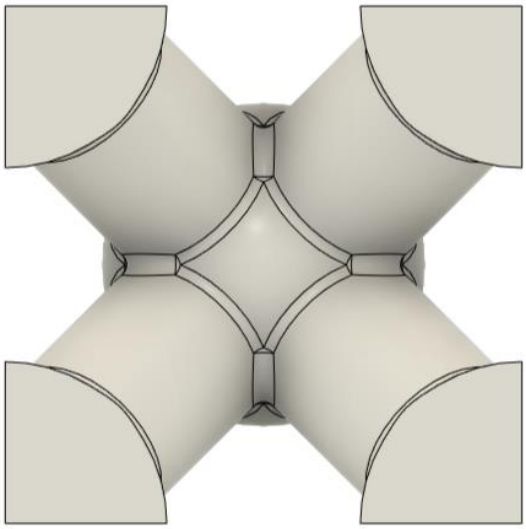

Figure 6.3 BCC 50% unit cell side view

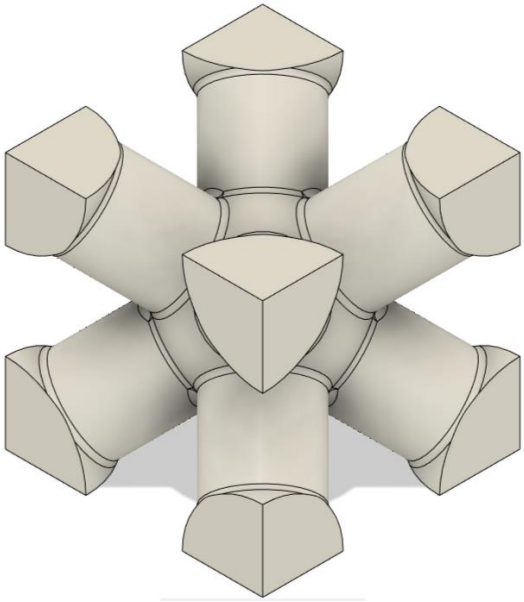

Figure 6.4 BCC 50% unit cell side view

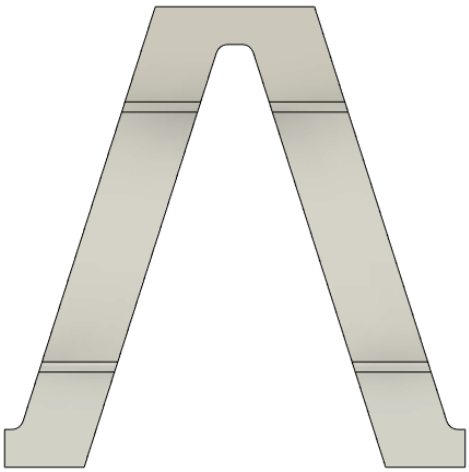

Figure 6.5 I-type 12% unit cell side view

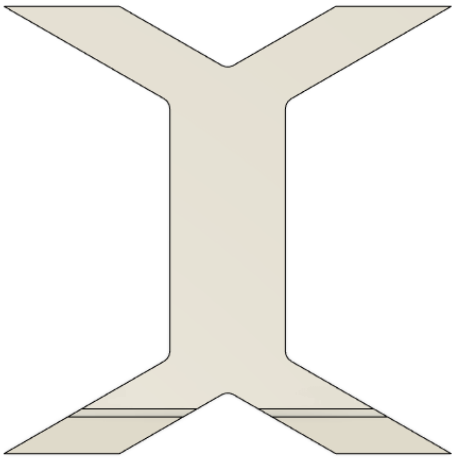

Figure 6.6 I-type 12% unit cell side view

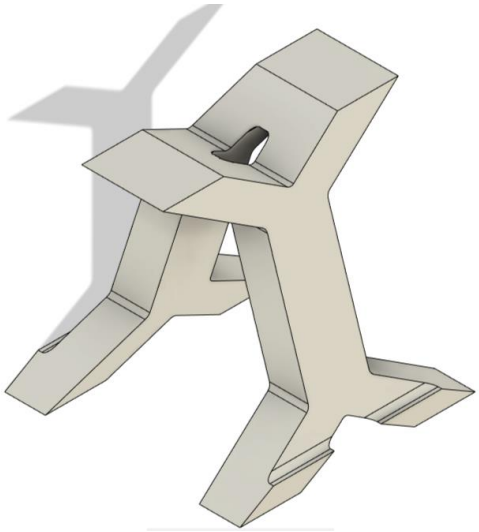

Figure 6.7 I-type 12% unit cell orthogonic view

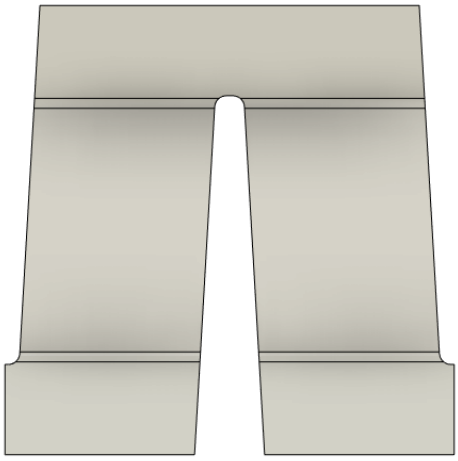

Figure 6.8 I-type 30% unit cell side view

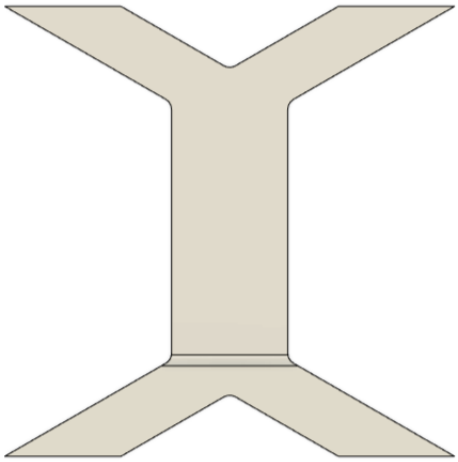

Figure 6.9 I-type 30% unit cell front view

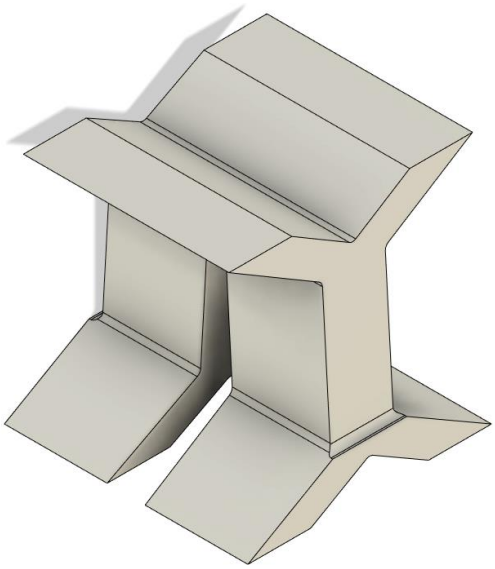

Figure 6.10 I-type 30% unit cell orthogonic view

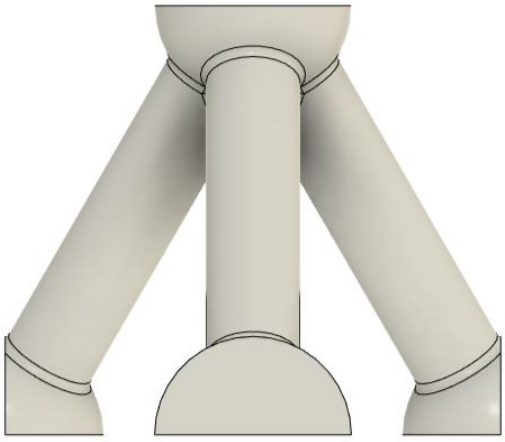

Figure 6.11 Tetrahedral 12% unit cell side view

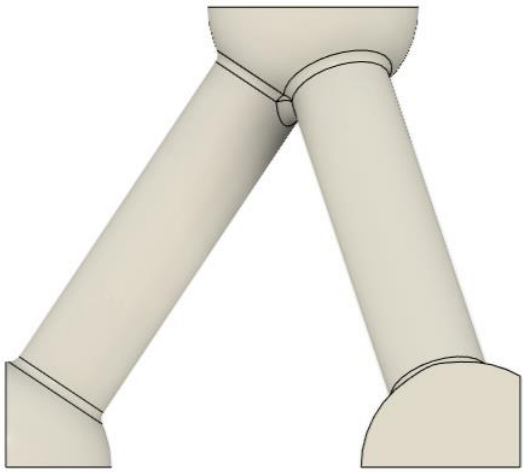

Figure 6.12 Tetrahedral 12% unit cell front view

Figure 6.13 Tetrahedral 12% unit cell top view

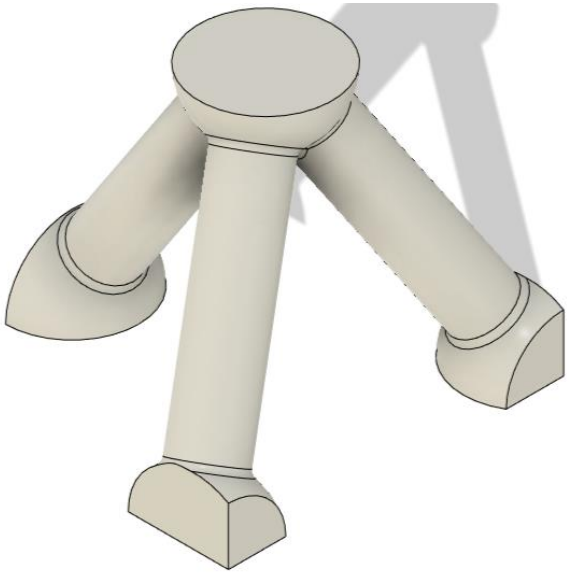

Figure 6.14 Tetrahedral 12% unit cell orthogonic view

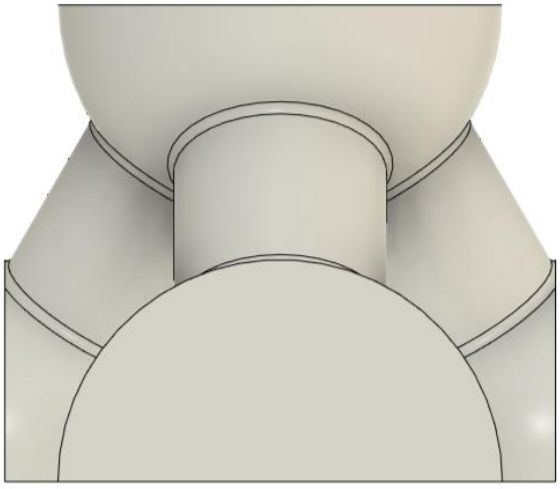

Figure 6.15 Tetrahedral 50% unit cell front view

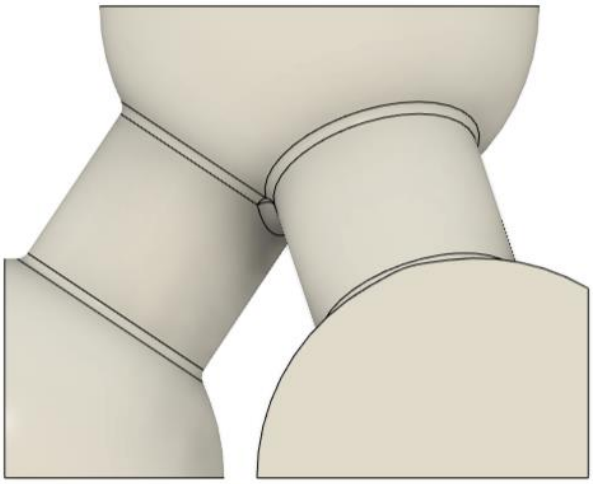

Figure 6.16 Tetrahedral 50% unit cell side view

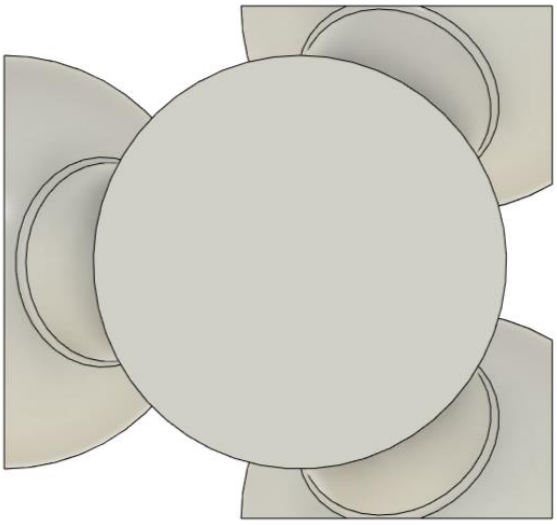

Figure 6.17 Tetrahedral 50% unit cell top view

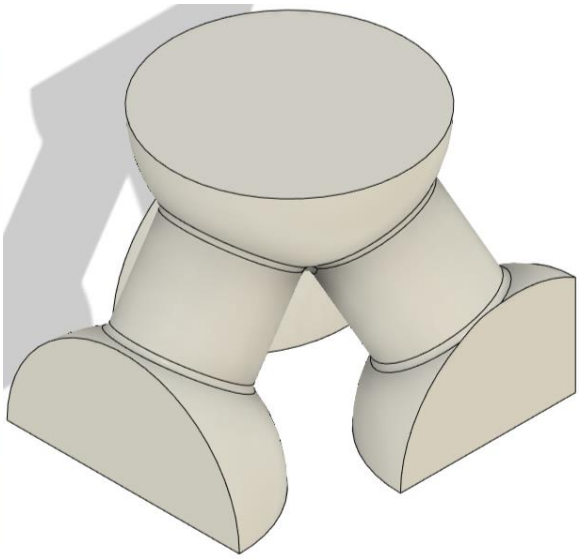

Figure 6.18 Tetrahedral 50% unit cell orthogonic view

This meticulous process culminated in the creation of intricate sandwich-like structures, where the lattice configuration is seamlessly integrated between two cylindrical plates, each featuring a central bore. These plates, effectively encapsulating the lattice structure, have a meticulously maintained thickness of 1mm, offering a robust yet nuanced encapsulation that harmonizes structural integrity with material distribution *(Figure 6.19-22).*

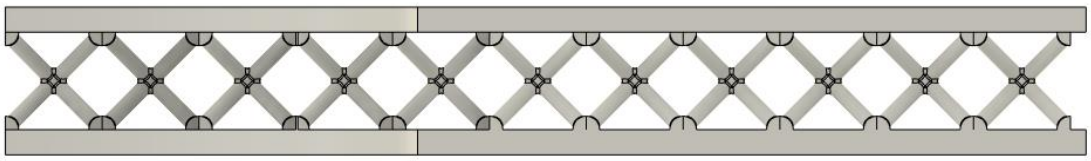

Figure 6.19 BCC 12% Sandwich structure – Front view

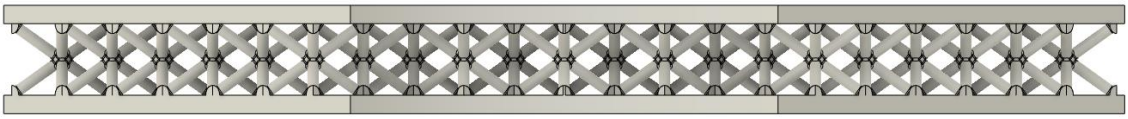

Figure 6.20 BCC 12% Sandwich structure – Front-Right view

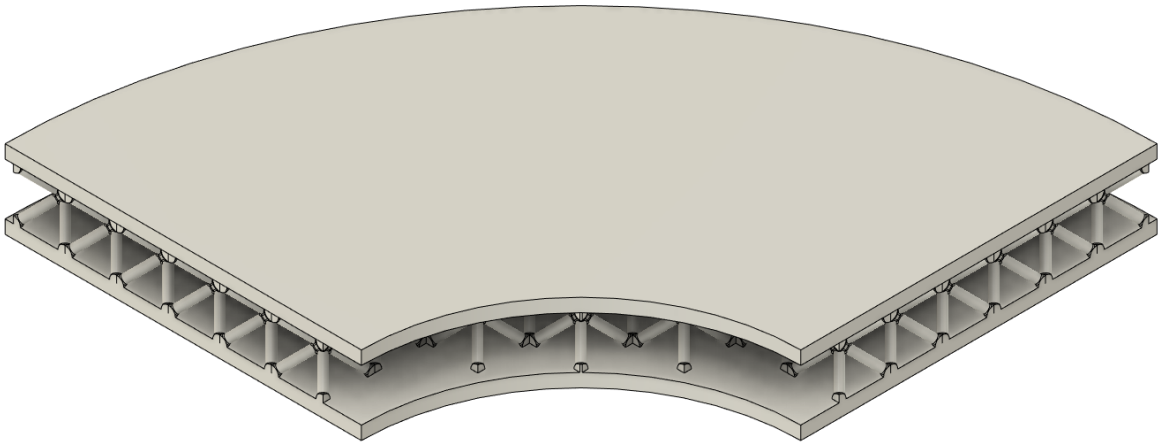

Figure 6.21 BCC 12% Sandwich structure – Orthogonic view

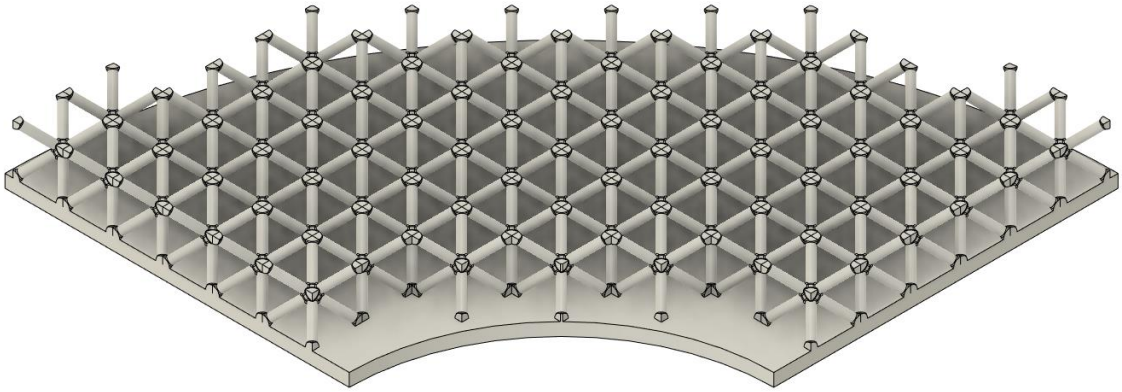

Figure 6.22 BCC 12% Sandwich structure – Orthogonic view without top plate

6.2 Model preparation

6.2.1 Geometry Selection

The lattice geometries previously detailed were transferred into ANSYS for finite element analysis, leveraging the inherent symmetries of the BCC and I-type lattices for computational efficiency. Given their symmetry along the x and y-axis, a quarter-section (90°) model of the disk was utilized for these geometries, reducing the computational load significantly. Conversely, the tetrahedral lattice, exhibiting symmetry at every 180°, was modeled using a half-disk representation to achieve a balance between accuracy and efficiency.

6.2.2 Meshing

Meshing strategies were meticulously designed to optimize the simulation's accuracy and computational efficiency. For the plates, a sweep meshing method was employed, incorporating 40 angular divisions for each 90-degree sector and 3 axial divisions across the 1mm plate thickness, ensuring a detailed representation of the geometry.

Meshing of the lattice structures was approached with a focus on precision, utilizing face sizing to control the mesh granularity. The lattice surface was segregated into two distinct groups: the surface of the struts and that of the nodes and fillets. By exploring various combinations of element sizing within these surfaces, we observed variations in the total number of elements generated and the maximum total deformation. A refinement process was systematically applied to determine the optimal element size, aiming for a variation threshold of less than 0.1% in the maximum total deformation between successive refinements.

6.2.3 Refinement Method

For each model, we provide a diagram below illustrating the relationship between the number of elements and the maximum total deformation. Each point on the plot corresponds to a specific combination of struts' and nodes' element sizes.

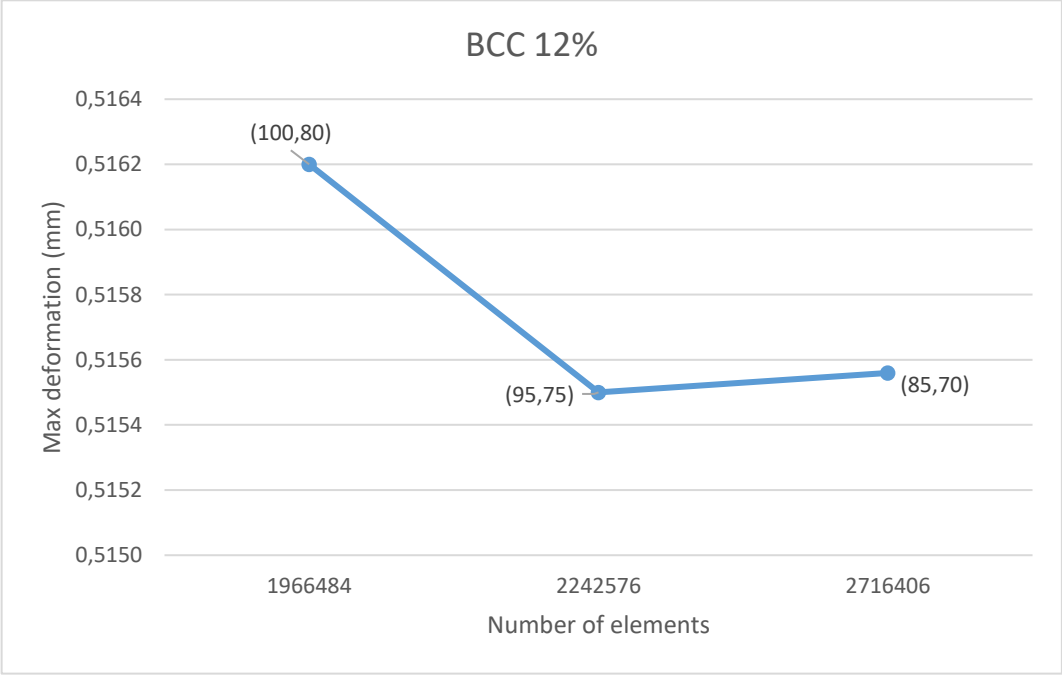

Figure 6.23 Max Total Deformation - Number of Elements diagram for BCC 12%

Figure 6.23 describes the results of the refinement process the BCC 12% model. The initial refinement process revealed a discrepancy of -0.136% in the sequential maximum deformations observed within the model. Employing the value of 100 μm element size for the struts and 80 μm for the nodes, the model comprised a total of 1,966,484 elements, in comparison with the next configuration, utilizing 95 μm for the struts and 75 μm, respectively, resulting in 2,242,576 elements. Subsequently, a second refinement was undertaken to bolster precision, narrowing the deviation to a mere 0.016%, comparing the second one with the more precise model, featuring element size of 85 μm for the struts and 75 μm for the nodes, ensuring heightened accuracy and reliability in the model's performance evaluation.

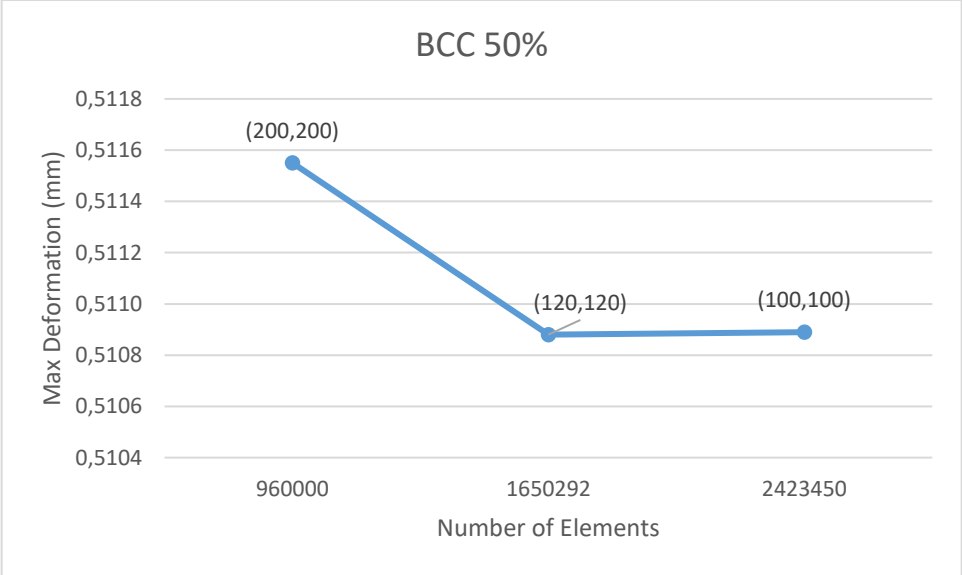

Figure 6.24 Max Total Deformation - Number of elements diagram for BCC 50%

Figure 6.24 presents the same process for the BCC 50% model. The starting refinement revealed a -1.56% discrepancy in the sequential maximum deformations noted within the model. Utilizing 200 μm element sizes for the struts and 200 μm for the nodes resulted in a model comprising 943,484 elements, while an alternative configuration with 120 μm for the struts and 120 μm for the nodes yielded 1,650,292 elements, was used for the comparisons. To enhance accuracy, a second refinement was conducted, reducing the deviation to a mere -0.0156%. This next refinement took place between the previous set of values and a finer one, featuring 100 μm for the struts and 100 μm for the nodes. The later further fortified the optimization process, ensuring heightened precision and reliability in evaluating the model's performance.

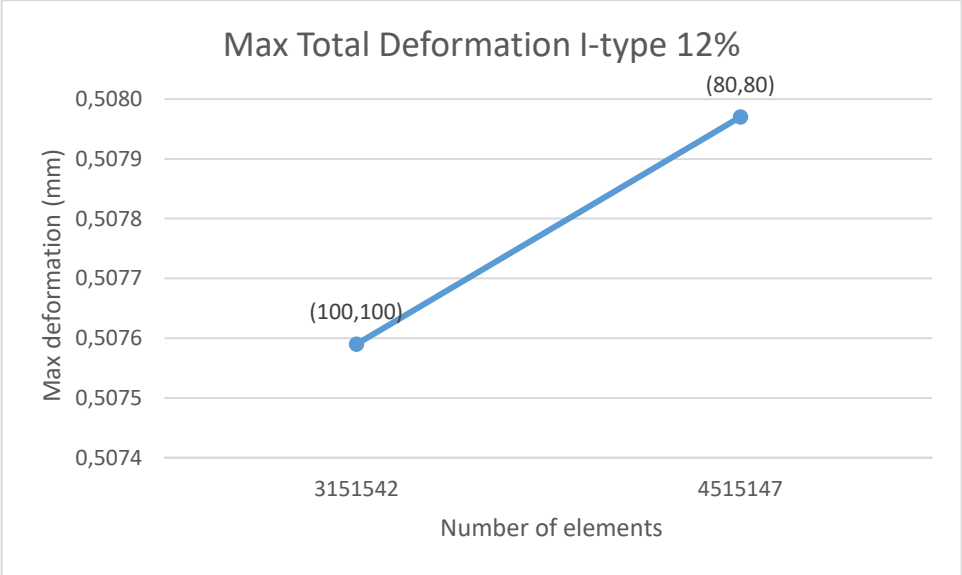

Figure 6.25 Max Total Deformation - Number of elements diagram for I-type 12%

For this scenario *(Figure 6.25)*, after a history of refinements in previous models, a large number of elements was given initially. A single refinement sufficed, with the resulting value obtained approximately at 0.075%. The element sizes for both struts and nodes were established at 80μm each.

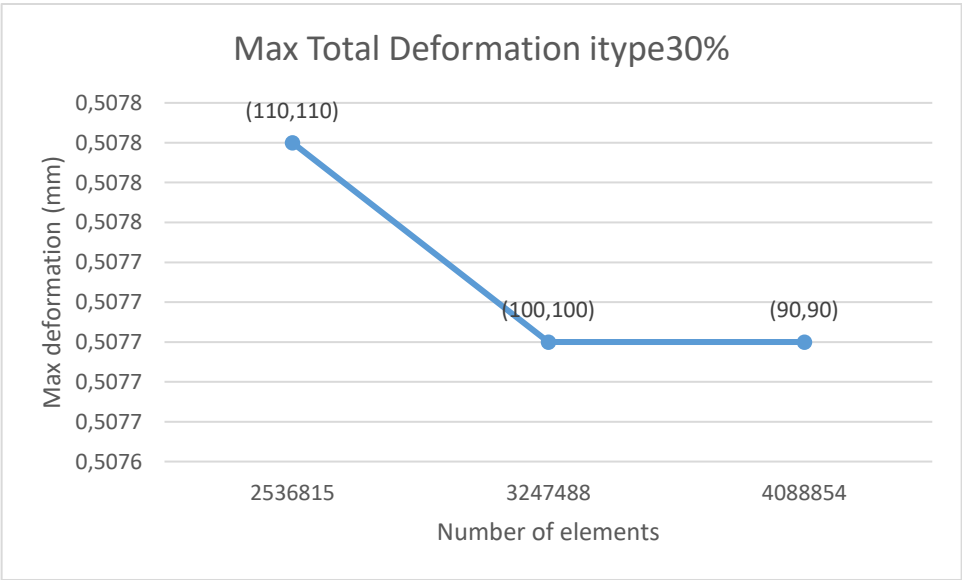

Figure 6.26 Max Total Deformation - Number of elements diagram for I-type 30%

Using again the gained experience, the initial refinement process yielded a reduction in variation to -0.011%, showcasing a notable improvement in accuracy, as seen in *Figure 6.26.* This probably had to do with the low element size chosen again. The three sets of values were (110,110), (100,100) and (90,90) with total number of elements equal to 2536815, 3247488 and 4088854, respectively. Subsequent to this, the second refinement iteration further refined the variation to 0.007%, indicating a continued progression towards enhanced precision. Consequently, to uphold this newfound accuracy, the element sizes for both struts and nodes were meticulously adjusted to 90μm each, ensuring a finely calibrated model that reflects the intricacies of the system under study.

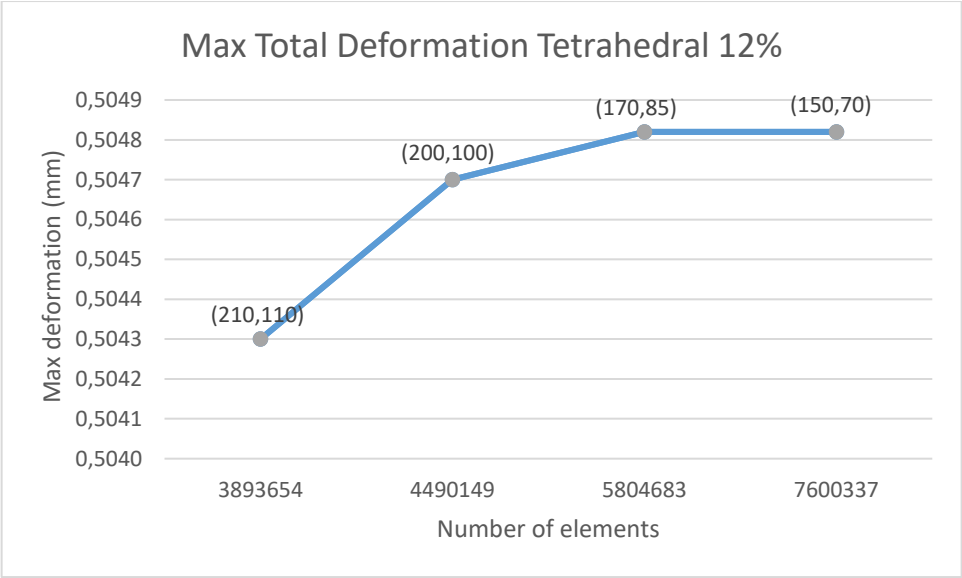

Figure 6.27 Max Total Deformation - Number of elements diagram for tetrahedral 12%

In *Figure 6.27* it is shown that the refinement process started with higher element sizes, because of the volume of the model. Sequential refinements resulted to 0.6%, 0.14% and 0.003%. The number of refinements was determined based on the larger volume of the material. The element sizes for both struts and nodes were established at 150μm for the element size of the struts' element size and 75μm for the nodes'.

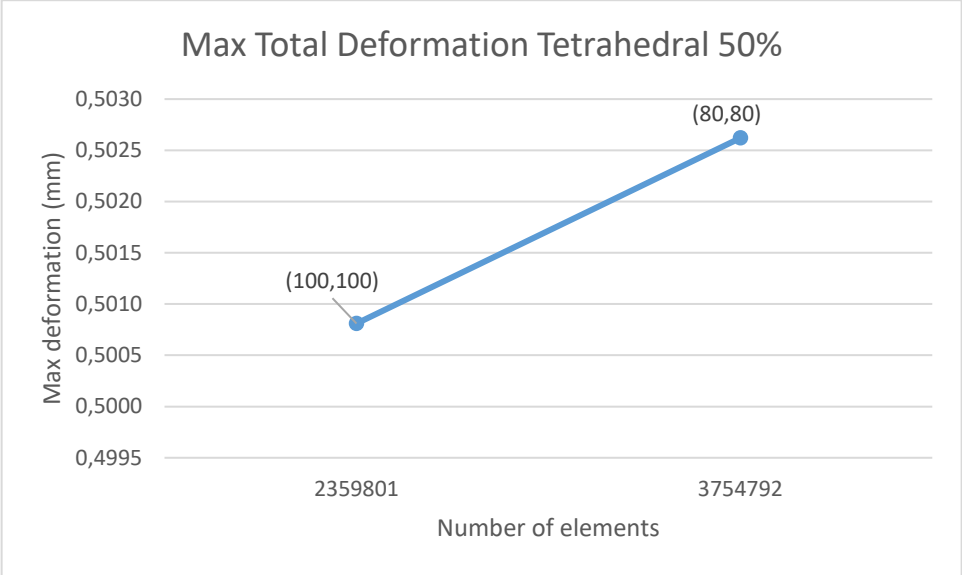

Figure 6.28 Max Total Deformation - Number of elements diagram for tetrahedral 50%

For this scenario *(Figure 6.28)*, after a history of refinements in previous models, a large number of elements was given initially. A single refinement sufficed, with the resulting value obtained approximately at -0.36%. The element sizes for both struts and nodes were established at 80μm each.

For each of the aforementioned scenarios, the final meshing of the model is visually depicted in the images below *(Figure 6.29-6.34).*

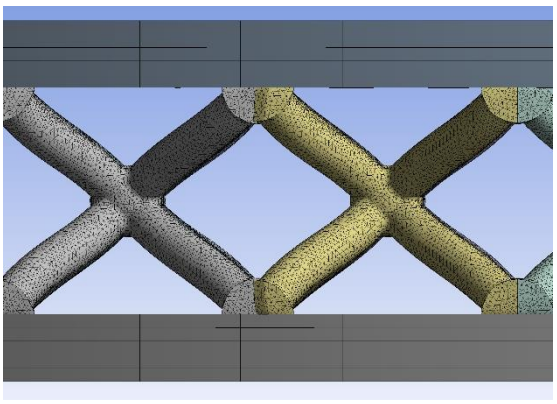

Figure 6.29 BCC 12% face sizing

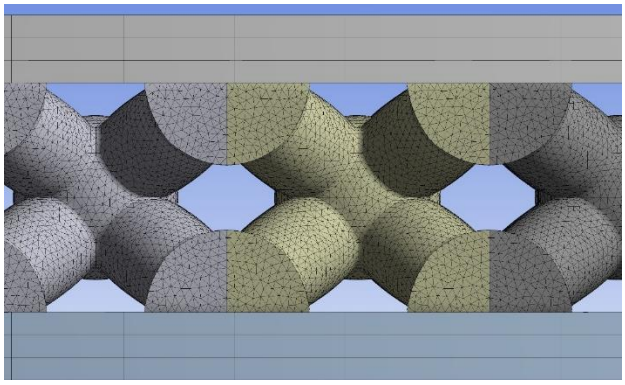

Figure 6.30a BCC 50% face sizing

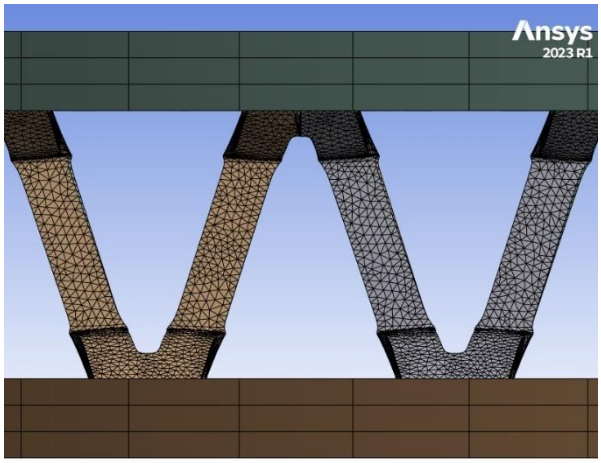

Figure 6.31 I-type 12% face sizing

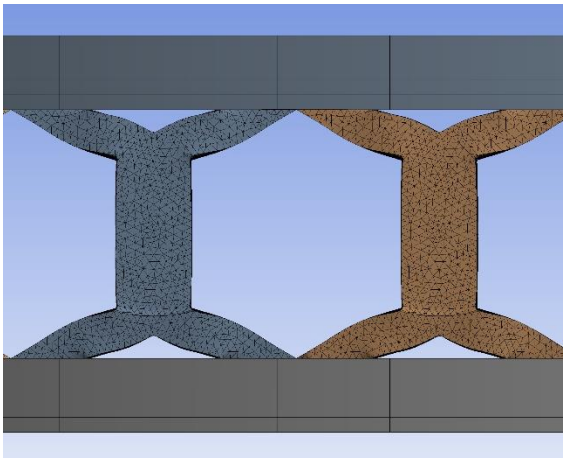

Figure 6.32 I-type 30% face sizing

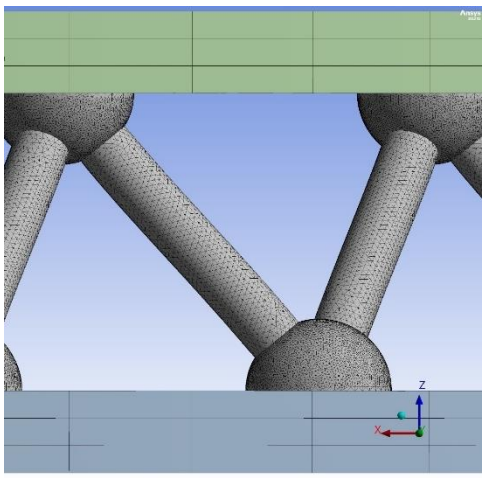

Figure 6.33a Tetrahedral 12% face sizing

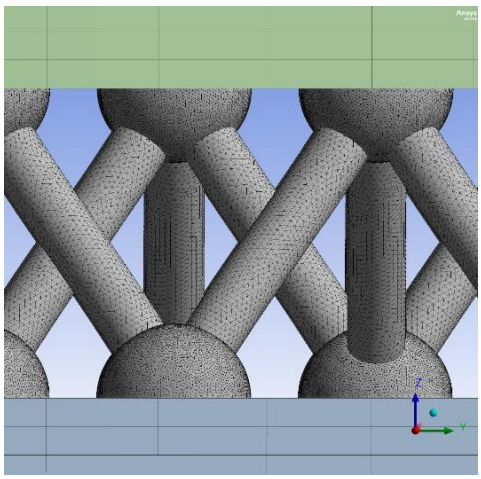

Figure 6.33b Tetrahedral 12% face sizing

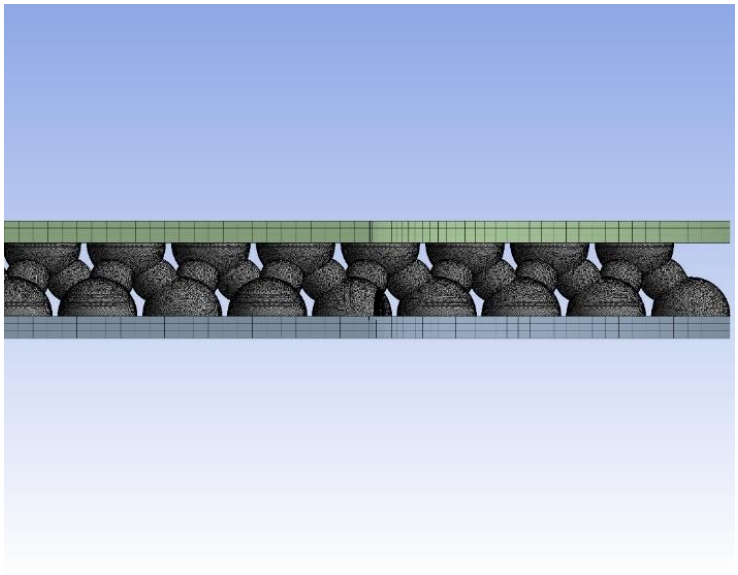

Figure 6.34 Tetrahedral 50% face sizing

6.2.4 Boundary conditions

In defining the boundary conditions for the simulation, each side of the plate was treated as fixed, with the exception of the top surface. The top surface was modeled to undergo a transformation, specifically a displacement of 0.5 mm, to simulate the effects of a compressive load. This approach ensures a realistic representation of the physical behavior under load, capturing the essential stress and deformation responses of the structure.

6.2.5 SS316L (AM) mechanical properties

The material selection process culminated in the choice of Stainless Steel 316L from the additive manufacturing library, renowned for its robustness and corrosion resistance, making it an ideal candidate for engineering applications. Moreover, its compatibility with LPBF technology ensures precise fabrication, contributing to the advancement of clutch disk design and the enhancement of overall performance and efficiency in automotive systems.

After confirming the suitability of SS316L for our innovative approach, a detailed examination of its key properties is pursued through a series of matrices. These matrices are designed to offer comprehensive insights into SS316L's mechanical, thermal, and physical characteristics, crucial for informed decision-making in component design and manufacturing processes. By analyzing these properties across different temperature ranges, a better understanding of SS316L's behavior under varying conditions can be gained, allowing for optimization of its utilization in automotive systems. Each matrix is explored to gain a deeper understanding

of SS316L's performance and its implications for clutch disk design and overall system efficiency. It is pertinent to mention that the data was sourced from the ANSYS library.

1. **Mechanical Properties Matrix (SS316L)**: *Table 6.1a and Table 6.1b* aim to highlight crucial parameters including yield strength, tensile strength, and hardness, offering valuable insights into the material's mechanical behavior across diverse conditions. The data presented has been carefully scrutinized to evaluate SS316L's appropriateness for automotive engineering applications, specifically within the realm of clutch disk design.
2. **Density and Temperature Matrix**: In *Table 6.2* the presented data refers to the density of SS316L alloy at different temperatures. Density is a critical material property that influences various aspects of component design and performance. By examining the relationship between density and temperature, we can better understand how SS316L behaves under different thermal conditions.
3. **Coefficient of Thermal Expansion Matrix**: *Table 6.3* presents data on the coefficient of thermal expansion (CTE) of SS316L over a range of temperatures. CTE is a crucial parameter that describes how a material's dimensions change in response to temperature variations. Understanding the CTE of SS316L is essential for designing components that can withstand thermal cycling without experiencing deformation or failure.
4. **Thermal Conductivity Matrix**: *Table 6.4* displays data on the thermal conductivity of SS316L at different temperatures. Thermal conductivity is a key property that influences the material's ability to conduct heat, which is vital for applications where heat dissipation or thermal management is critical. By examining the thermal conductivity of SS316L across various temperature ranges, we can gain insights into its thermal performance and suitability for automotive engineering applications.
5. **Specific Heat Matrix**: In *Table 6.5*, data on the specific heat capacity of SS316L at different temperatures is provided. Specific heat capacity is a fundamental thermodynamic property that characterizes the amount of heat required to raise the temperature of a material by one degree Celsius. Comprehending the specific heat of SS316L is crucial for precisely anticipating its thermal reactions and crafting components equipped with optimal heat management abilities.

Table 6.1a Mechanical Properties of SS316L

Yield Strength (Pa)	Tangent Modulus (Pa)	Temperature (°C)
2.25e+008	2.091e+009	100
1.68e+008	1.577e+009	300
1.15e+008	7.08e+008	816
3.1e+007	4.05e+008	1040
1.5e+007	2.65e+008	1150

Table 6.1b Mechanical Properties of SS316L

Young's Modulus (Pa)	Poisson's Ratio	Bulk Modulus (Pa)	Shear Modulus (Pa)	Temperature (°C)
1.95e+011	0.25	1.3e+011	7.8e+010	20
1.91e+011	0.26	1.3264e+011	7.5794e+010	100
1.86e+011	0.275	1.3778e+011	7.2941e+010	200
1.8e+011	0.315	1.6216e+011	6.8441e+010	300
1.73e+011	0.33	1.6961e+011	6.5038e+010	400
1.64e+011	0.3	1.3667e+011	6.3077e+010	500
1.55e+011	0.32	1.4352e+011	5.8712e+010	600
1.44e+011	0.31	1.2632e+011	5.4962e+010	700
1.31e+011	0.24	8.3974e+010	5.2823e+010	800
1.17e+011	0.24	7.5e+010	4.7177e+010	900
1.e+011	0.24	6.4103e+010	4.0323e+010	1000
8.1e+010	0.24	5.1923e+010	3.2661e+010	1100
5.1e+010	0.24	3.2692e+010	2.0565e+010	1200

Table 6.2 Density-Temperature relationship

Density (kg/m³)	Temperature (°C)
7954	26.85
7910	126.85
7864	226.85
7818	326.85
7771	426.85
7723	526.85

7674	626.85
7624	726.85
7574	826.85
7523	926.85
7471	1026.8
7419	1126.8
7365	1226.8
7311	1326.8
6979	1426.8
6920	1526.8
6857	1626.8
6791	1726.8
6721	1826.8
6648	1926.8
6571	2026.8

Table 6.3 Coefficient of Thermal Expansion

Coefficient of Thermal Expansion (°C^-1)	Temperature (°C)
1.457e-005	-0.15
1.478e-005	26.85
1.518e-005	76.85
1.561e-005	126.85
1.633e-005	226.85
1.691e-005	326.85

1.742e-005	426.85
1.789e-005	526.85
1.832e-005	626.85
1.871e-005	726.85
1.903e-005	826.85
1.927e-005	926.85
1.945e-005	1026.8
1.961e-005	1126.8
1.977e-005	1226.8
1.99e-005	1326.8

Zero-Thermal-Strain Reference Temperature: 19.85°C

Table 6.4 Thermal Conductivity

Thermal Conductivity (W m^-1 °C^-1)	Temperature (°C)
12.97	-0.15
13.31	19.85
13.44	26.85
14.32	76.85
15.16	126.85
16.8	226.85
18.36	326.85
19.87	426.85
21.39	526.85
22.79	626.85

24.06	726.85
25.46	826.85
26.74	926.85
28.02	1026.8
29.32	1126.8
30.61	1226.8
31.86	1326.8
32.41	1370.8
26.9	1398.8
27.24	1426.8

Table 6.5 Specific heat

Specific Heat (J kg^-1 °C^-1)	Temperature (°C)
498.73	26.85
512.12	126.85
525.51	226.85
538.48	326.85
551.87	426.85
565.26	526.85
578.65	626.85
591.62	726.85
605.01	826.85
618.4	926.85

631.78	1026.8
644.75	1126.8
658.14	1226.8
671.53	1326.8
769.86	1426.8
769.86	1526.8

7. Results

For each disk analyzed in this study, the comparison will focus on five critical metrics: total deformation, equivalent elastic strain, maximum stress, strain energy and force reaction. These parameters are essential for understanding the mechanical behavior of the lattice-structured disks under applied loads and for evaluating their performance. The results for each metric will be discussed below:

1. **Total Deformation**: This metric measures the maximum displacement experienced by the lattice structure when subjected to the specified loading conditions. Total deformation is a key indicator of the structural integrity and the ability of the disk to maintain its shape under load. A lower value of total deformation signifies a stiffer structure that is less susceptible to bending or warping, which is crucial for maintaining the functional integrity of the disk in operational conditions.
2. **Equivalent Elastic Strain**: Equivalent elastic strain provides insight into the material's deformation before yielding. It is a measure of the strain distributed throughout the lattice structure under load, offering an indication of the material's elastic response. This parameter is critical for assessing the resilience of the structure and its ability to return to its original shape after deformation. Lower values of equivalent elastic strain are desirable as they indicate a material that is less likely to undergo permanent deformation.
3. **Maximum Stress**: The maximum stress experienced by the lattice structure under the applied load conditions is a critical factor in determining its strength and durability. This metric identifies the points of highest stress concentration, which are potential sites for the initiation of failure. By evaluating the maximum stress, we can assess the safety and reliability of the structure. A well-designed lattice structure should distribute stress evenly to avoid excessive concentrations that could lead to failure.
4. **Strain Energy**: Strain energy is the energy absorbed by the structure due to deformation, which is indicative of the structure's toughness and its ability to withstand unexpected loads. Higher strain energy values suggest a structure that can absorb more energy before failure, contributing to its overall durability and impact resistance. This metric is particularly important for evaluating the performance of the lattice structure in dynamic or unpredictable operating environments.
5. **Force reaction:** Force reaction is crucial in Finite Element Analysis (FEA) as it ensures equilibrium, provides insights into stress and strain distributions, facilitates load transfer analysis, validates FEA models, and guides performance optimization. By analyzing force reactions, engineers can assess internal forces, stress concentrations, and deformation patterns, enabling informed decisions to enhance structural integrity and performance.

By comparing these five metrics across different disks, comprehensive insights can be derived into their mechanical performance, identifying areas for optimization and helping the decisions about the most suitable lattice configurations for specific applications. This comparative analysis is instrumental in advancing the design of lattice-structured disks, optimizing their performance, and enhancing their application potential in various mechanical systems.

7.1 BCC 12%

7.1.1 Total Deformation

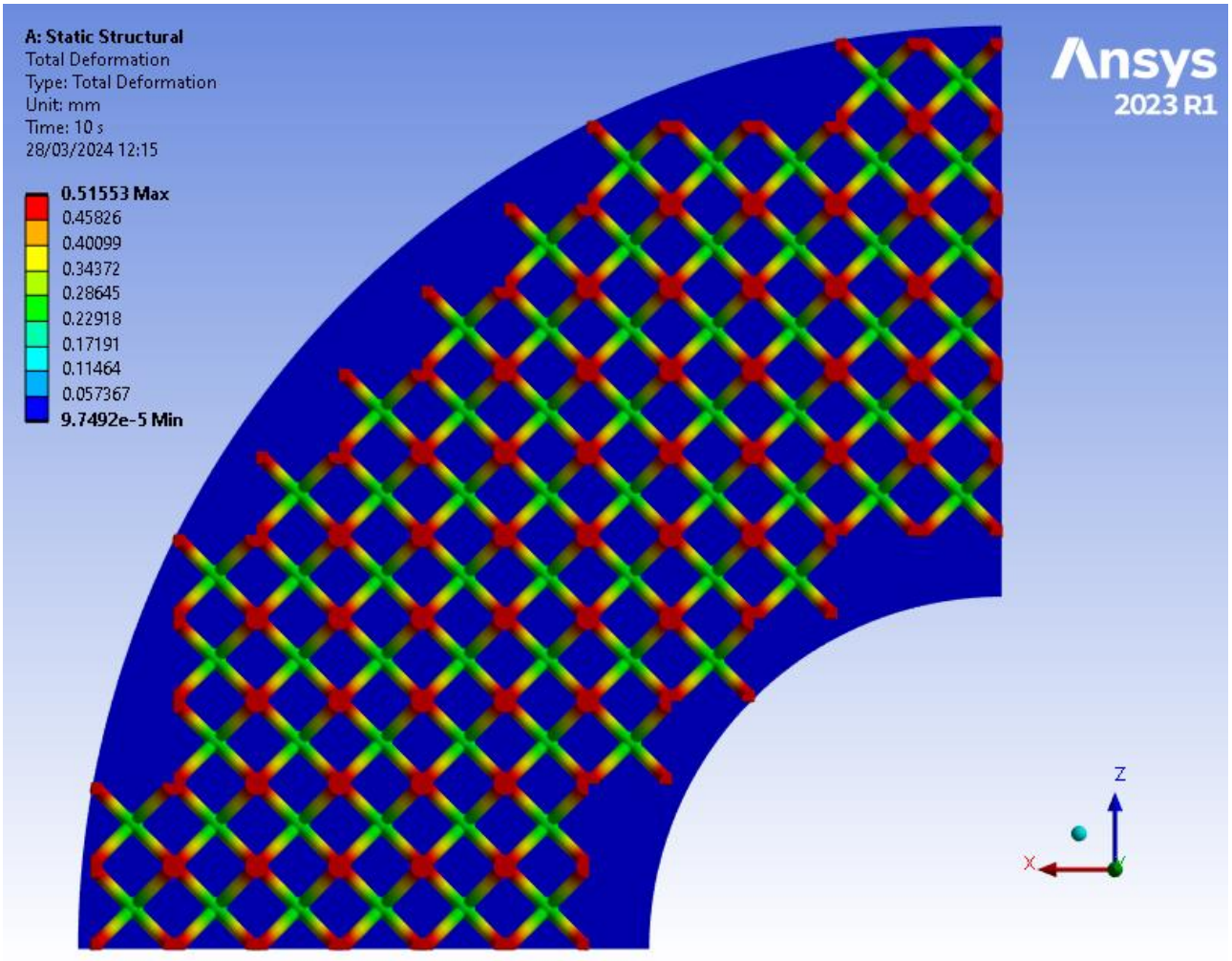

Figure 7.1 Total deformation contour map: BCC 12% – top view

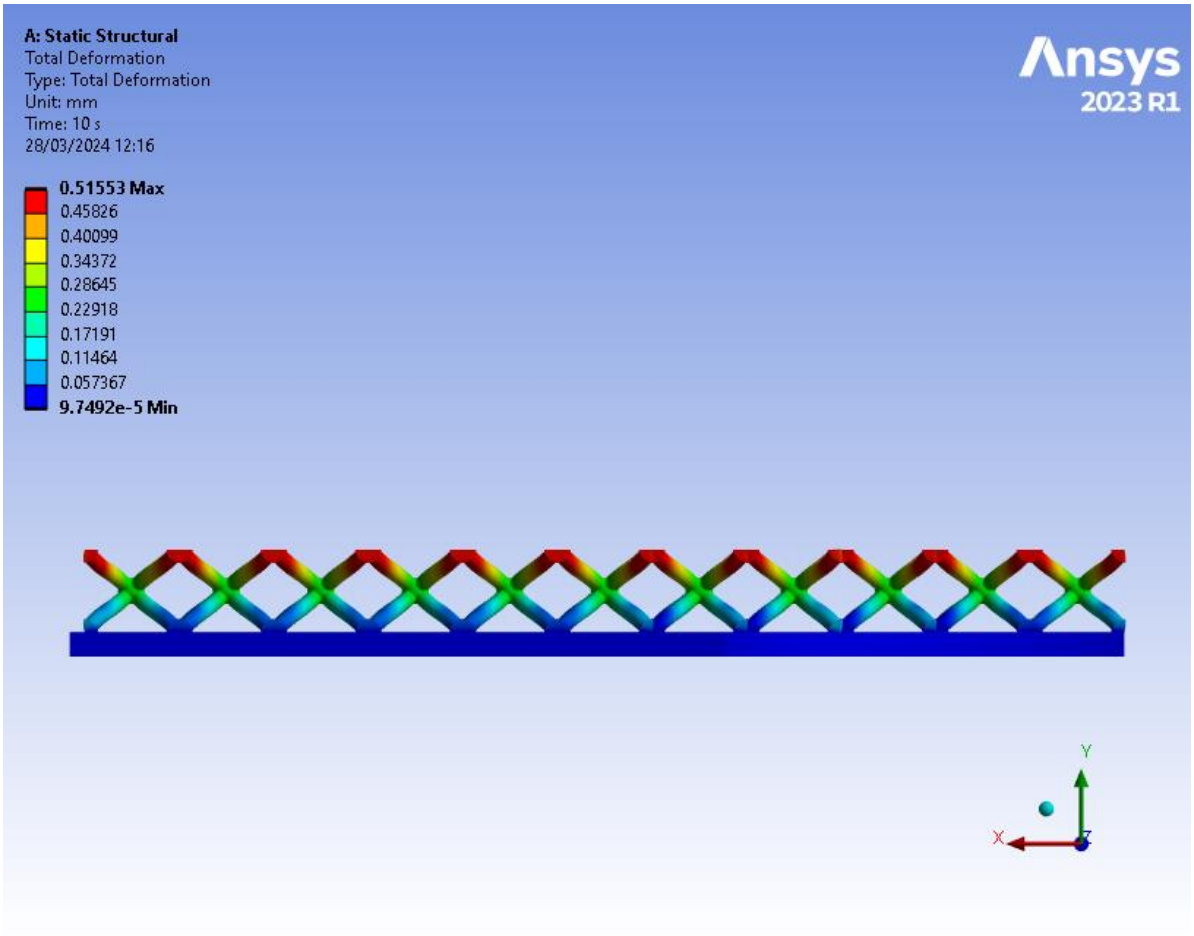

Figure 7.2 Total deformation contour map: BCC 12% – side view

The analysis of *Figure 7.1* and *Figure 7.2* reveals a notable concentration of deformation primarily in the upper region of the lattice structure, corresponding to the expected primary displacement zone. Specifically, at the apex of the node, the maximum total deformation reaches a peak value of 0.51553mm. Moving down the structure to the midpoint of the strut between the upper and central nodes, the total deformation hovers around 0.3mm. In contrast, the central nodes display significantly less deformation, with values averaging around 0.25mm, indicating a comparatively more stable configuration. Additionally, the struts positioned below these central nodes exhibit significantly less deformation, with values between 0.1mm and 0.2mm on the upper half and up to 0.1mm on the lower half of the bottom struts, which underscores their resilience and ability to maintain structural integrity even when subjected to external loads. In general, there is a trend of decreasing deformation moving downwards within the lattice structure. This trend is evident as we observe higher deformation values at the upper sections, gradually decreasing towards the central nodes and further diminishing towards the lower struts.

Table 7.1 presents a detailed compilation of the minimum, maximum, and average deformation values observed throughout the designated time interval. This dataset offers invaluable insights into the structural behavior, enabling us to identify recurring patterns and evolving trends in deformation responses. Through a meticulous examination of this table, we gain the ability to precisely identify the average deformation corresponding to the initial displacement, thereby enhancing our comprehension of the structural dynamics and response mechanisms over time. Specifically, upon scrutiny, we observe that the maximum and average deformation recorded stand at 0.515mm and 0.254mm respectively, shedding light on the extent of structural deformation under varying conditions.

Graphs are showcased in *Figure 7.3.*

Table 7.1 Deformation Data – BCC 12%

t(s)	Min Deformation (m)	Max Deformation (m)	Avg deformation(m)
0.2	1.3285e-007	1.0729e-005	5.6009e-006
0.4	5.0603e-008	2.1927e-005	1.0963e-005
0.7	1.1873e-007	3.8433e-005	1.8778e-005
1.	1.2566e-007	5.4503e-005	2.6532e-005
1.2	1.8397e-007	6.5002e-005	3.1678e-005
1.4	1.3794e-007	7.5399e-005	3.6800e-005
1.7	7.8534e-008	9.0915e-005	4.4468e-005
2.	8.8529e-008	1.0642e-004	5.2120e-005
2.2	1.1876e-007	1.1694e-004	5.7213e-005
2.4	1.1797e-007	1.2728e-004	6.2294e-005
2.7	1.1252e-007	1.4277e-004	6.9907e-005
3.	1.2948e-007	1.5817e-004	7.7511e-005
3.2	1.2273e-007	1.6840e-004	8.2573e-005
3.4	1.0708e-007	1.7864e-004	8.7643e-005
3.7	8.5111e-008	1.9398e-004	9.5238e-005
4.	5.6534e-008	2.0930e-004	1.0283e-004
4.2	5.0125e-008	2.1951e-004	1.0789e-004
4.4	4.5475e-008	2.2973e-004	1.1295e-004
4.7	4.3498e-008	2.4506e-004	1.2054e-004
5.	3.3212e-008	2.6040e-004	1.2813e-004
5.2	2.4630e-008	2.7061e-004	1.3319e-004
5.4	6.0293e-008	2.8085e-004	1.3825e-004
5.7	7.0075e-008	2.9618e-004	1.4584e-004
6.	7.8932e-008	3.1151e-004	1.5342e-004
6.2	8.0901e-008	3.2170e-004	1.5847e-004
6.4	9.6896e-008	3.3193e-004	1.6354e-004

6.7	1.1453e-007	3.4724e-004	1.7112e-004
7.	1.3303e-007	3.6255e-004	1.7870e-004
7.2	1.4355e-007	3.7275e-004	1.8376e-004
7.4	1.4777e-007	3.8296e-004	1.8881e-004
7.7	1.1511e-007	3.9826e-004	1.9640e-004
8.	8.7623e-008	4.1355e-004	2.0398e-004
8.2	8.2285e-008	4.2375e-004	2.0903e-004
8.4	7.2497e-008	4.3394e-004	2.1408e-004
8.7	8.5552e-008	4.4923e-004	2.2167e-004
9.	6.8986e-008	4.6453e-004	2.2924e-004
9.2	5.4304e-008	4.7473e-004	2.3430e-004
9.4	5.4908e-008	4.8493e-004	2.3935e-004
9.7	6.9485e-008	5.0023e-004	2.4693e-004
10	9.7492e-008	5.1553e-004	2.5451e-004

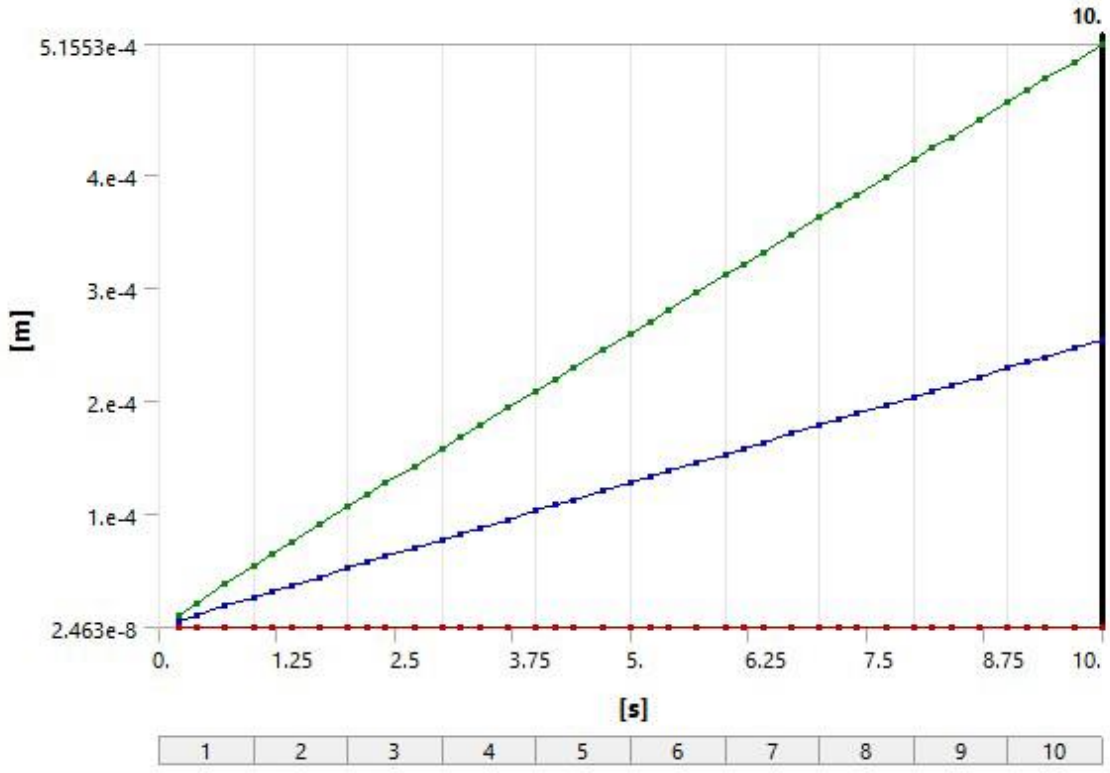

Figure 7.3 Deformation Profiles: BCC 12%

7.1.2 Equivalent Elastic Strain

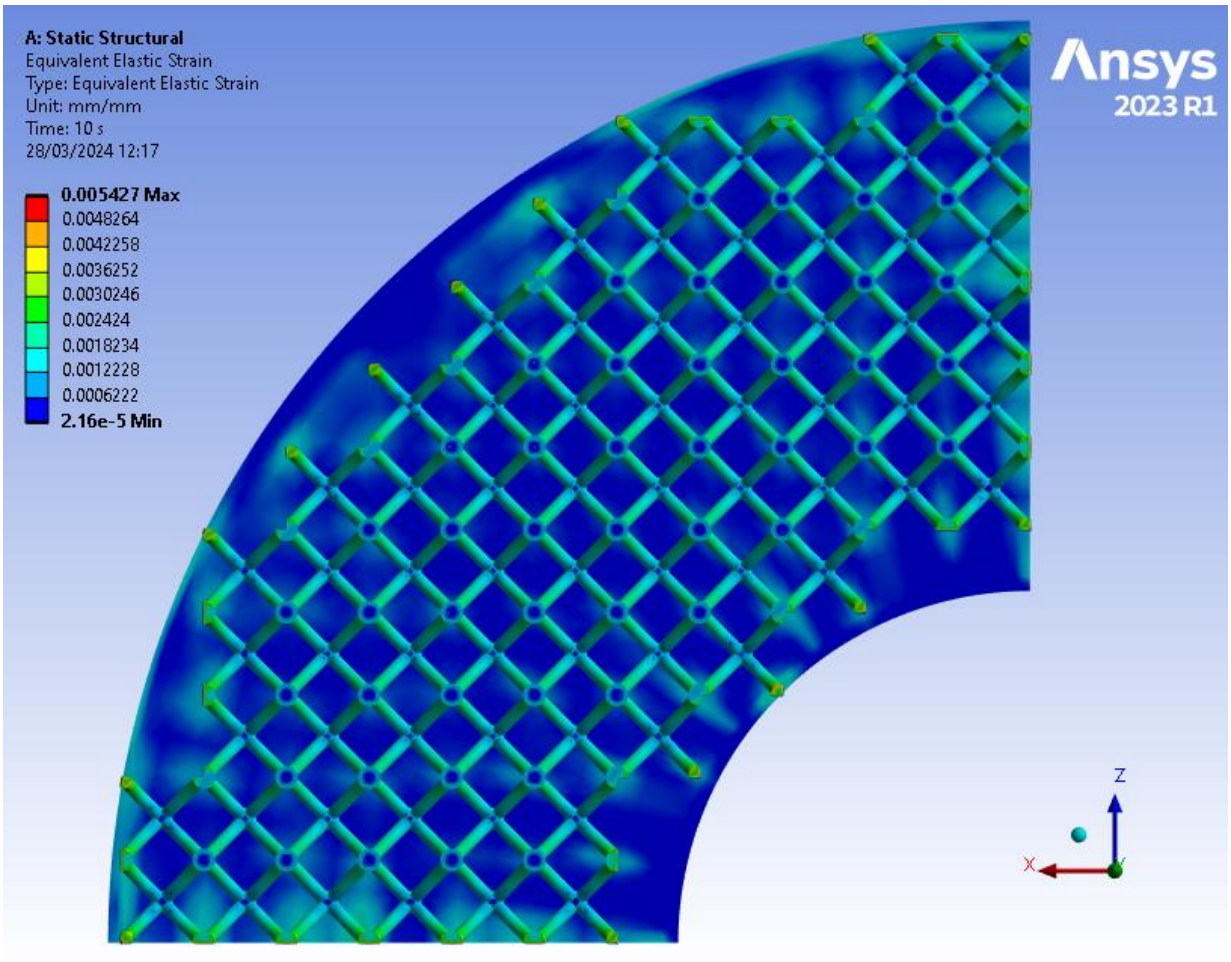

Figure 7.4 Equivalent Elastic Strain contour map: BCC 12% – top view

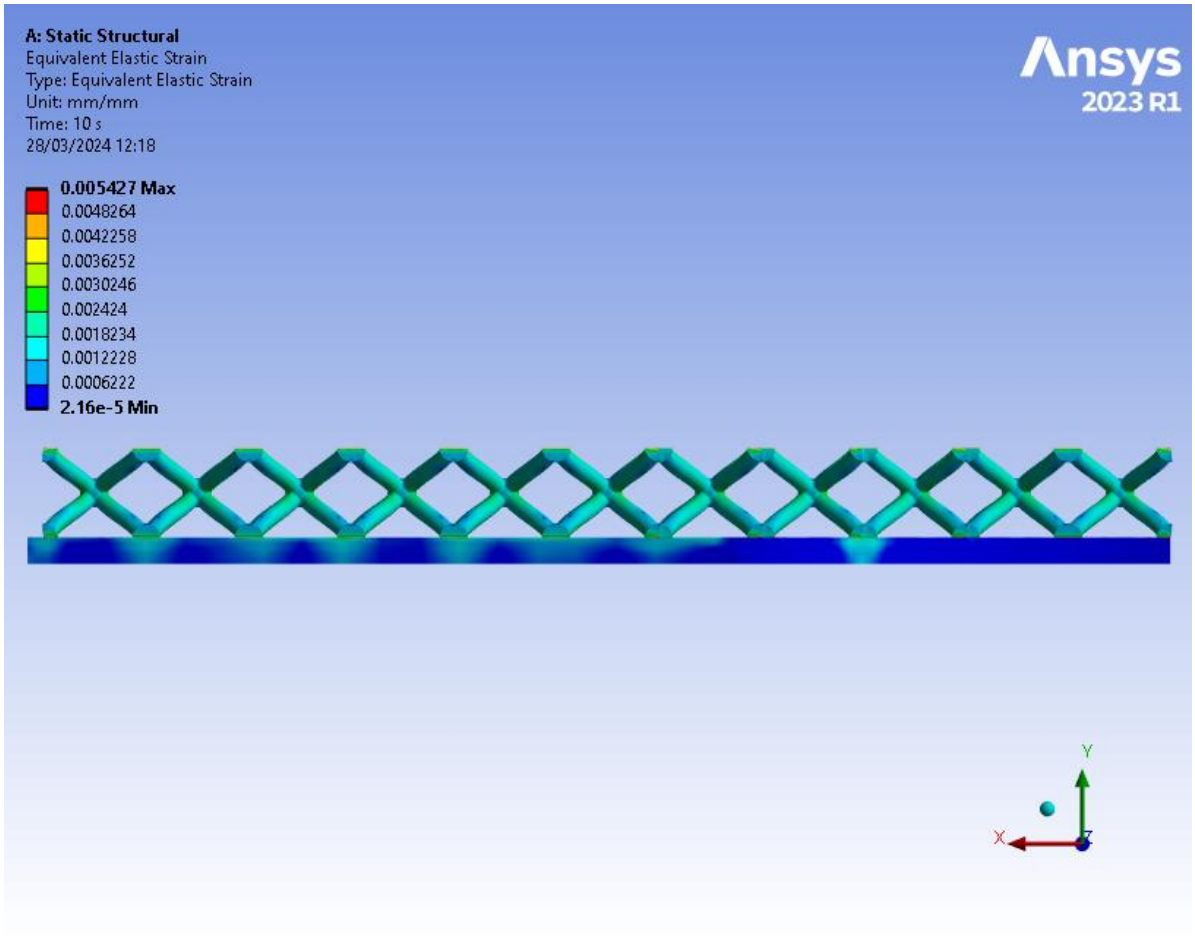

Figure 7.5 Equivalent Elastic Strain contour map: BCC 12% – side view

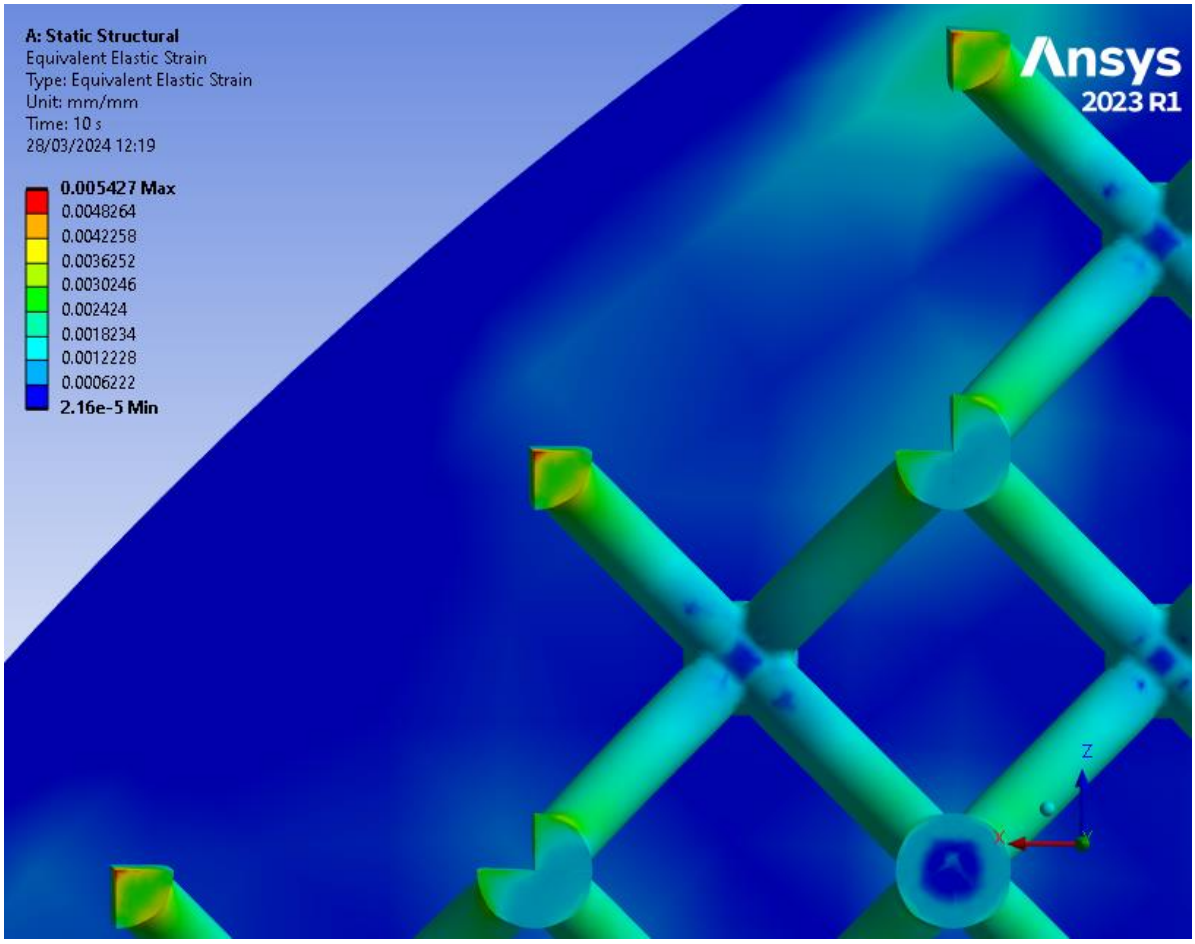

Figure 7.6 Equivalent Elastic Strain contour map: BCC 12% – zoomed-in top view

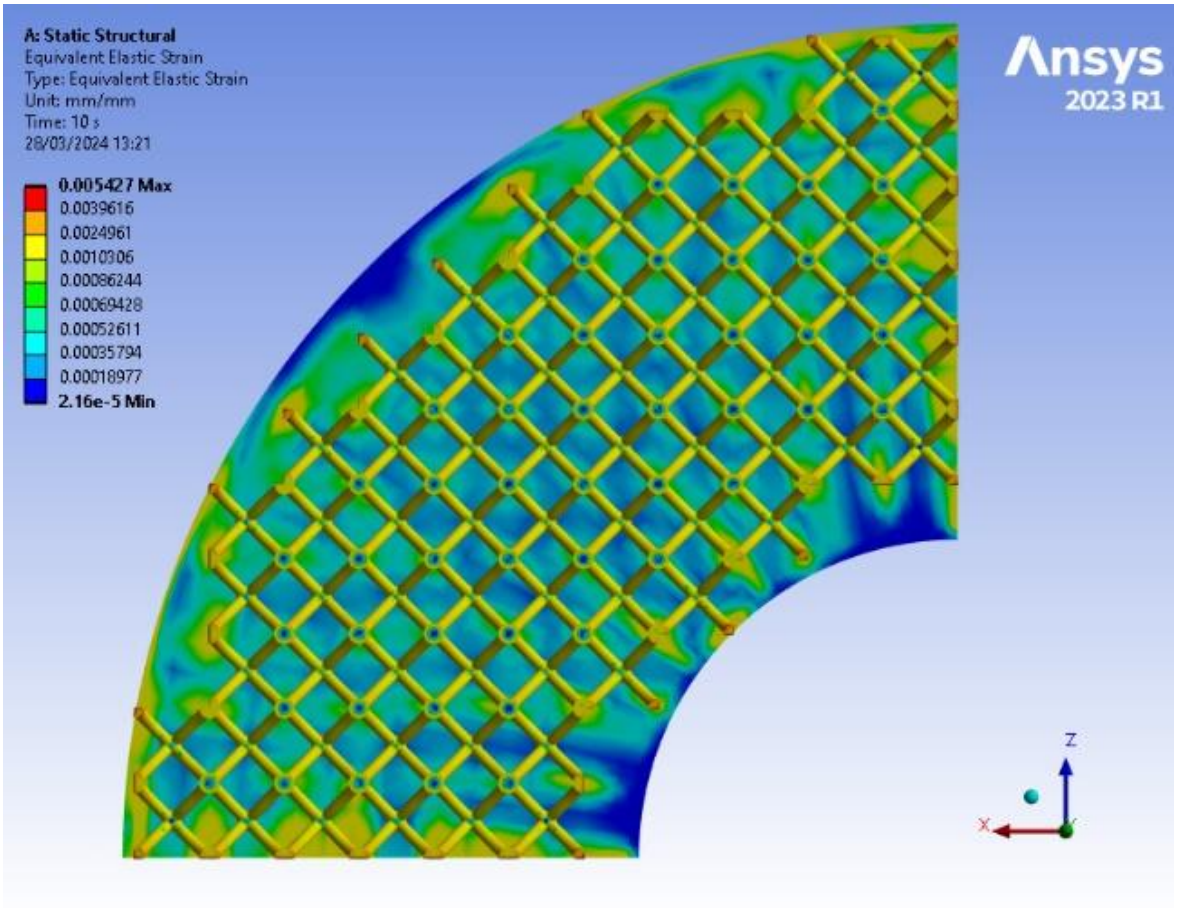

Figure 7.7 Equivalent Elastic Strain filtered contour map: BCC 12% –top view

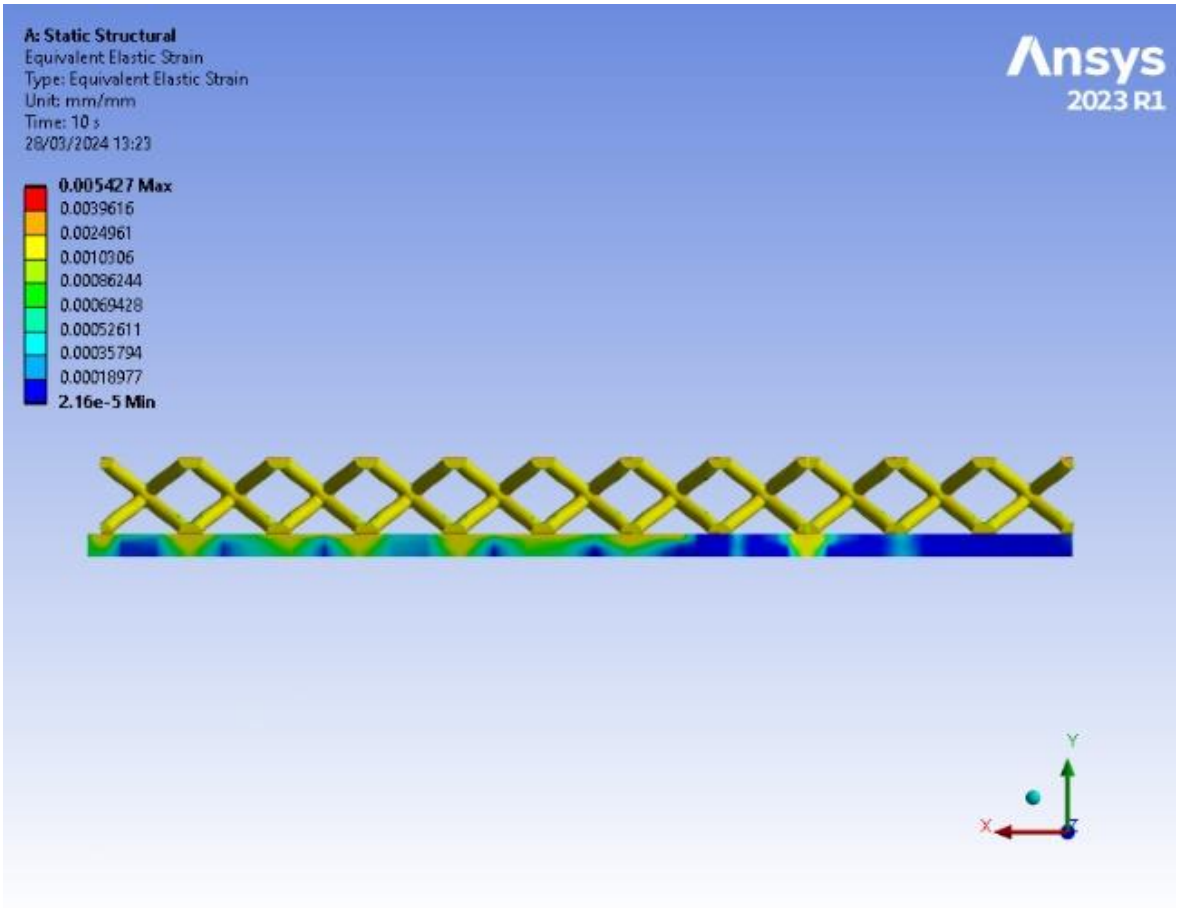

Figure 7.8 Equivalent Elastic Strain filtered contour map: BCC 12% – side view

Figures 7.4 and 7.6 show incomplete nodes manifest as strain concentration corners, displaying significantly higher values up to 0.005mm/mm compared to the surrounding geometry, which measures up to 0.002mm/mm. Furthermore, these incomplete nodes lead to increased elastic strain at the contact areas of the plates, particularly evident in the outer regions of the model, where it measures approximately 0.0025mm/mm in some areas. *Figure 7.7* and *Figure 7.8* provide filtered representations, allowing for clearer observation of this elastic strain phenomenon. This filtration enhances the understanding of the spatial distribution and magnitude of elastic strain within the model, highlighting the sensitivity of the contact areas between the plates and the incomplete nodes. All struts elastic strain range between 0.001mm/mm to 0.002mm/mm, while central nodes' fillets reach up to 0.0025mm/mm.

Within *Table 7.2*, a comprehensive array of data unveils the minimum, maximum, and average elastic strain values documented throughout the designated timeframe. This dataset acts as a reservoir of knowledge, offering valuable glimpses into the intricacies of structural behavior and the evolving nature of deformation responses. By meticulously analyzing this table, we can zero in on the average deformation associated with the

initial displacement, thereby deepening our comprehension of structural dynamics and response mechanisms over time. Notably, upon careful review, we note that the maximum and average elastic strain readings reach 0.005mm and 0.002mm respectively, offering valuable insights into the magnitude of structural deformation under various conditions.

Graphs are showcased in *Figure 7.9.*

Table 7.2: Equivalent Elastic Strain Data – BCC 12%

t(s)	Min Elastic Strain (mm/mm)	Max Elastic Strain (mm/mm)	Avg Elastic Strain (mm/mm)
0.2	6.2288e-006	1.8127e-003	7.6381e-004
0.4	1.1698e-005	1.8188e-003	9.6833e-004
0.7	2.2617e-005	2.2167e-003	1.0375e-003
1.	1.8748e-005	2.507e-003	1.074e-003
1.2	1.8045e-005	2.6706e-003	1.0924e-003
1.4	1.7448e-005	2.8216e-003	1.1085e-003
1.7	1.7609e-005	3.0156e-003	1.13e-003
2.	1.9227e-005	3.1819e-003	1.1498e-003
2.2	1.8998e-005	3.2739e-003	1.1624e-003
2.4	1.8895e-005	3.3564e-003	1.175e-003
2.7	1.8817e-005	3.468e-003	1.1933e-003
3.	1.8797e-005	3.5746e-003	1.2114e-003
3.2	1.8817e-005	3.6413e-003	1.2231e-003
3.4	1.8819e-005	3.7102e-003	1.235e-003
3.7	1.5642e-005	3.807e-003	1.2525e-003
4.	1.2777e-005	3.9006e-003	1.2699e-003
4.2	1.2709e-005	3.9569e-003	1.2813e-003
4.4	1.1783e-005	4.0206e-003	1.2929e-003
4.7	1.3033e-005	4.1088e-003	1.3101e-003
5.	1.6494e-005	4.195e-003	1.3272e-003
5.2	1.8943e-005	4.2463e-003	1.3383e-003
5.4	1.9341e-005	4.3065e-003	1.3498e-003
5.7	1.9434e-005	4.3888e-003	1.3667e-003
6.	1.9544e-005	4.4692e-003	1.3835e-003
6.2	1.9647e-005	4.5171e-003	1.3945e-003
6.4	1.9705e-005	4.573e-003	1.4059e-003
6.7	1.9836e-005	4.65e-003	1.4226e-003
7.	1.9979e-005	4.7253e-003	1.4392e-003

7.2	2.0089e-005	4.7738e-003	1.4503e-003
7.4	2.0185e-005	4.8233e-003	1.4614e-003
7.7	2.0349e-005	4.8949e-003	1.4781e-003
8.	2.0519e-005	4.9654e-003	1.4947e-003
8.2	2.0637e-005	5.0113e-003	1.5058e-003
8.4	2.0736e-005	5.0579e-003	1.5169e-003
8.7	2.0906e-005	5.1259e-003	1.5335e-003
9.	2.1069e-005	5.1964e-003	1.5501e-003
9.2	2.1191e-005	5.2411e-003	1.5611e-003
9.4	2.1285e-005	5.2892e-003	1.5722e-003
9.7	2.1447e-005	5.3583e-003	1.5889e-003
10	2.16e-005	5.427e-003	1.6055e-003

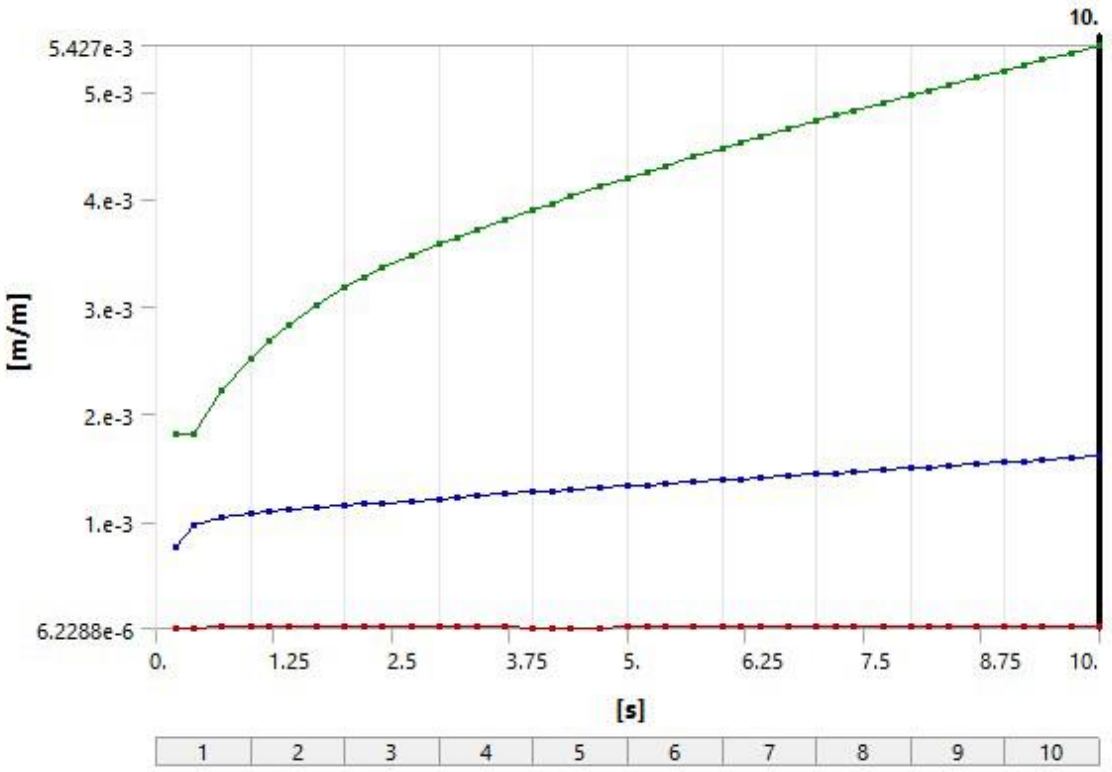

Figure 7.9 Elastic Strain Profiles: BCC 12%

7.1.3 Equivalent Stress

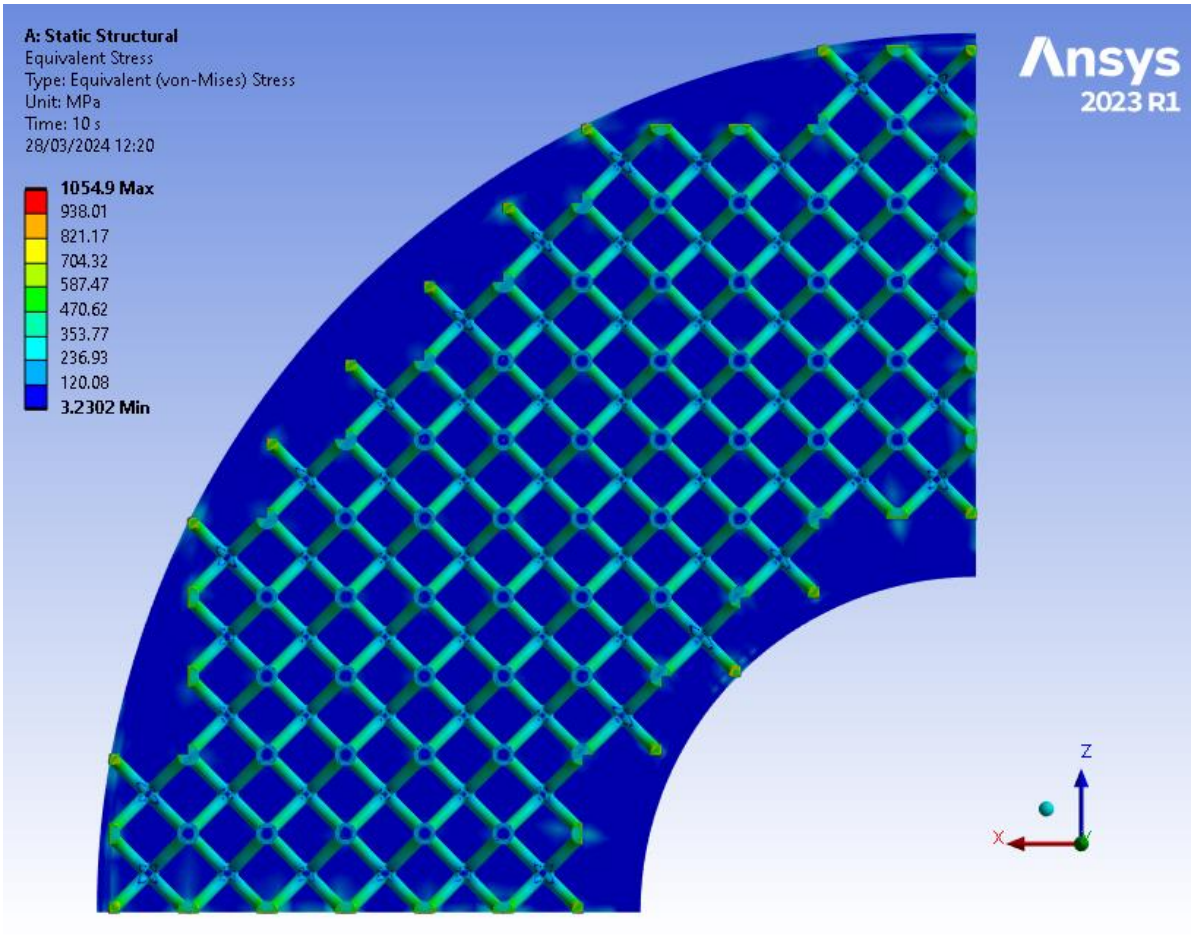

Figure 7.10 Equivalent (von-Mises) Stress contour map: BCC 12% – top view

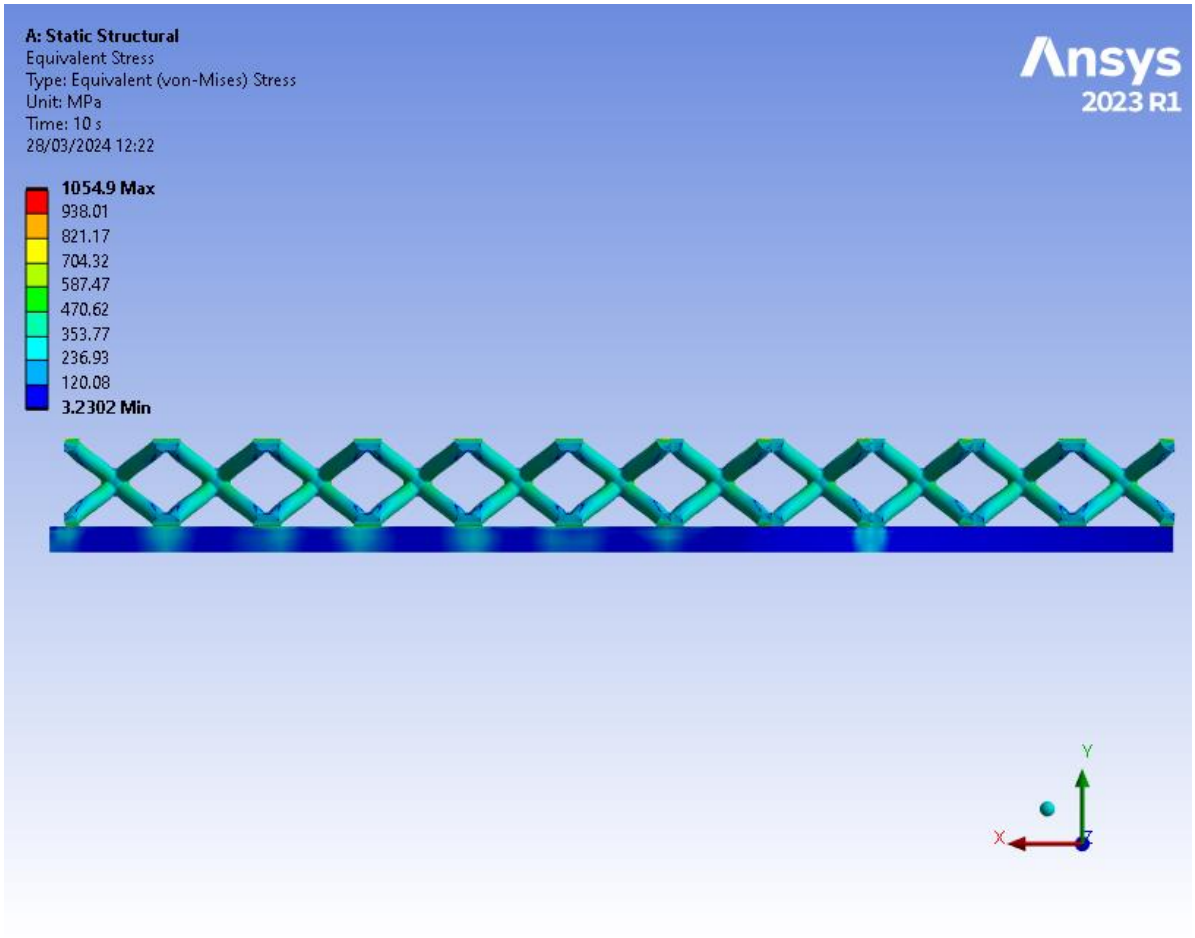

Figure 7.11 Equivalent (von-Mises) Stress contour map: BCC 12% – zoomed-in top view

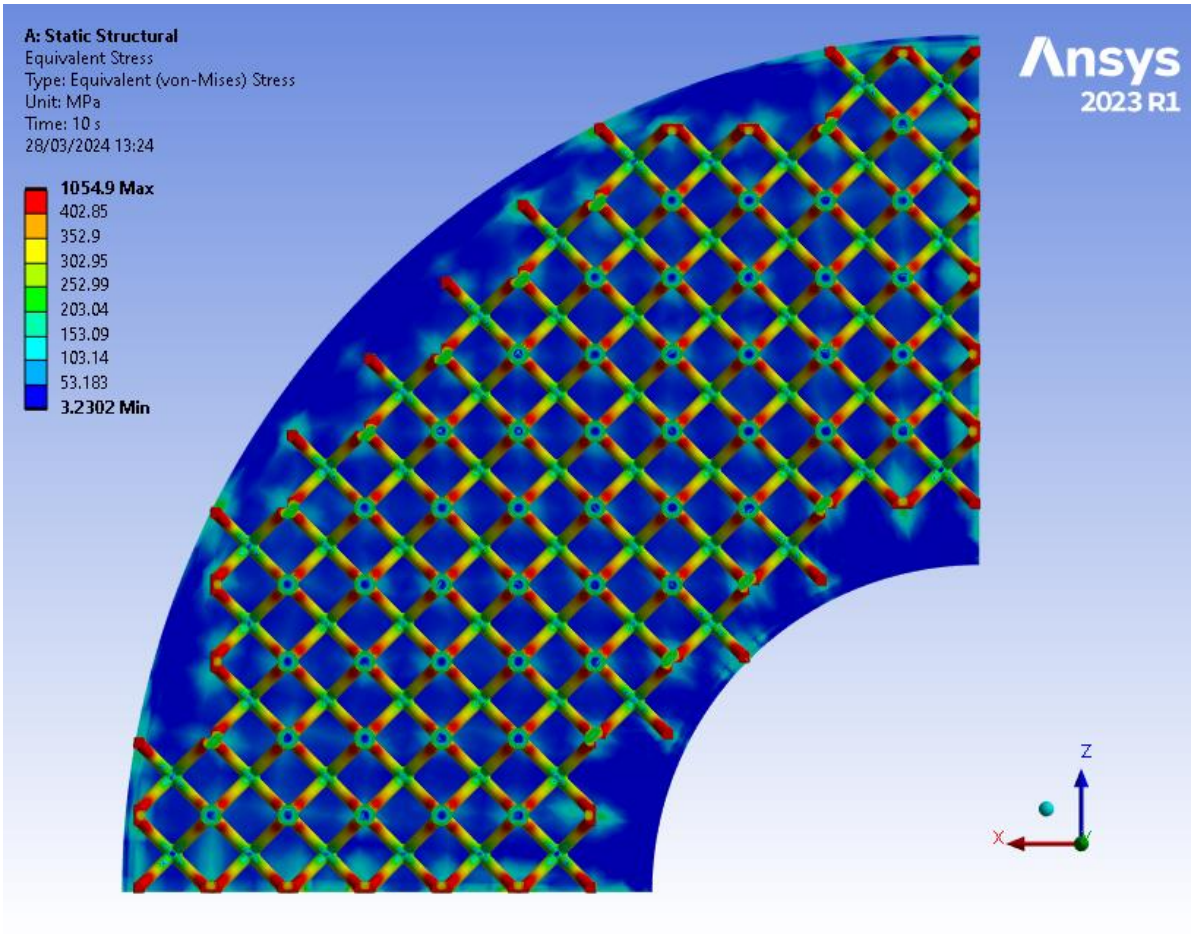

Figure 7.12 Equivalent (von-Mises) Stress filtered contour map: BCC 12% – top view

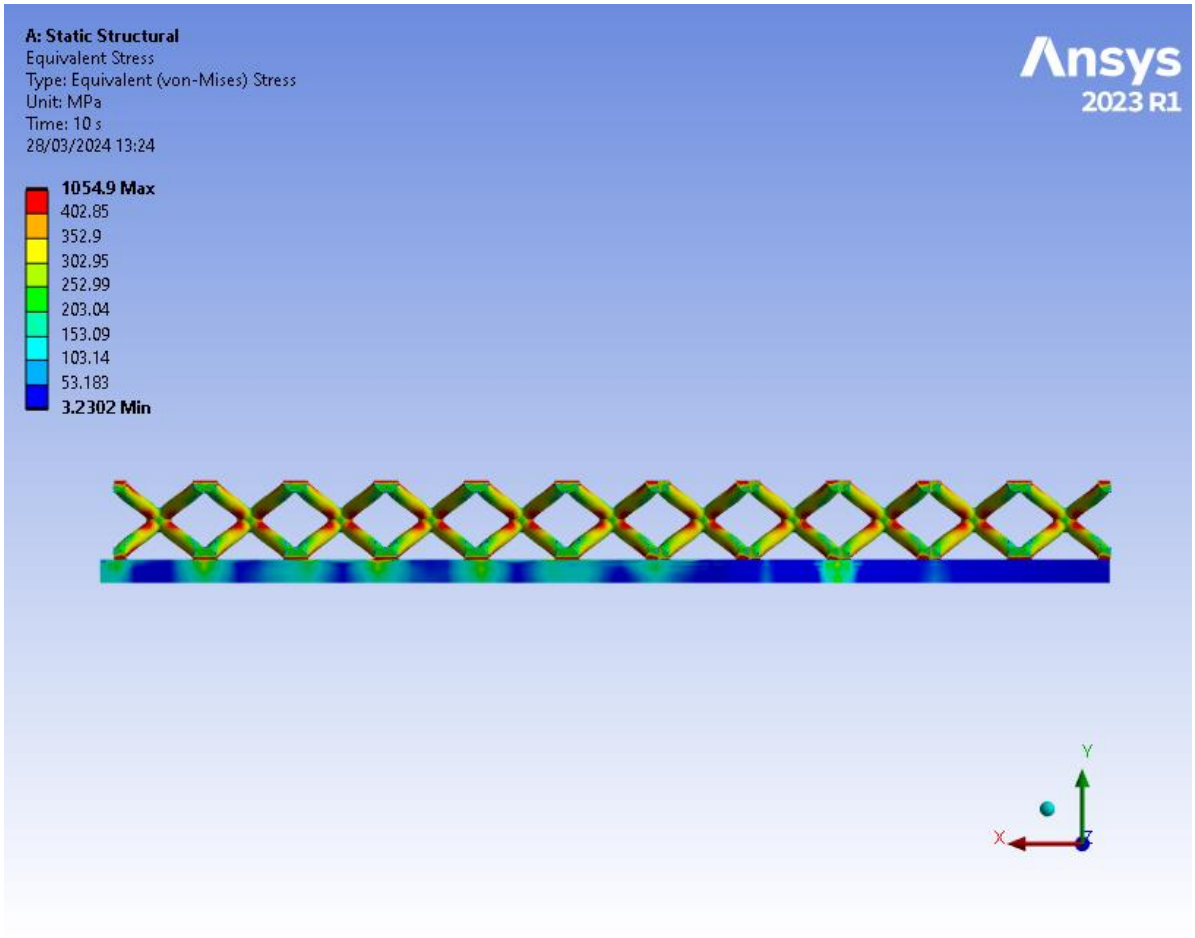

Figure 7.13 Equivalent Stress filtered contour map: BCC 12% – side view

Upon detailed scrutiny of *Figures 7.10 and 7.11*, it is discernible that the lattice structure generally lacks prominent stress concentration regions, apart from the corners associated with incomplete nodes. Areas near the central node gather stresses up to 400MPa, as evidenced in *Figure 7.12*, with stress levels measuring. To enhance visual clarity, a filter was applied to the legend, resulting in the refined depictions observed in *Figures 7.12 and 7.13*. Upon closer examination, the primary stress concentration zones are found to align closely with the nodes, as anticipated. Notably, at the contact points of the top nodes with the plate, stress levels hover around 200MPa for complete nodes, whereas for incomplete nodes, the stress can soar up to 1054 MPa, underscoring the significance of incomplete nodes in influencing stress distribution within the lattice structure.

Table 7.6 offers a comprehensive overview of the minimum, maximum, and average stress values recorded over the designated time period. This data provides invaluable insights into the structural behavior, allowing us to discern patterns and trends in displacement responses. By analyzing this table, we can pinpoint the average and maximum stress that corresponds to the initial displacement, facilitating a deeper understanding

of the structural dynamics and response mechanisms over time. Specifically, upon scrutiny, we observe that the maximum and average deformation recorded stand at 1055.42MPa and 306.67, respectively.

Graphs are showcased in *Figure 7.14.*

Table 7.3 Equivalent Stress Data – BCC 12%

t(s)	Minimum Stress (Pa)	Maximum Stress (Pa)	Average Stress (Pa)
0.2	9.1421e+005	3.2901e+008	1.4702e+008
0.4	5.7387e+005	3.5372e+008	1.8583e+008
0.7	2.3724e+006	4.3043e+008	1.9861e+008
1.	1.875e+006	4.8696e+008	2.0527e+008
1.2	1.8421e+006	5.1921e+008	2.0862e+008
1.4	2.0166e+006	5.4859e+008	2.1159e+008
1.7	2.5968e+006	5.8633e+008	2.1558e+008
2.	2.5167e+006	6.1864e+008	2.193e+008
2.2	1.9624e+006	6.3654e+008	2.2169e+008
2.4	1.6622e+006	6.5258e+008	2.2407e+008
2.7	1.9364e+006	6.7427e+008	2.2755e+008
3.	2.0816e+006	6.9453e+008	2.3098e+008
3.2	1.8925e+006	7.0622e+008	2.332e+008
3.4	2.118e+006	7.1998e+008	2.3549e+008
3.7	1.281e+006	7.3845e+008	2.3883e+008
4.	6.5307e+005	7.5641e+008	2.4216e+008
4.2	1.1276e+006	7.6593e+008	2.4433e+008
4.4	1.7261e+006	7.7937e+008	2.4656e+008
4.7	1.785e+006	7.9645e+008	2.4985e+008
5.	1.6445e+006	8.1312e+008	2.5312e+008
5.2	1.9073e+006	8.2121e+008	2.5526e+008
5.4	2.4989e+006	8.3443e+008	2.5747e+008
5.7	2.9272e+006	8.5042e+008	2.6072e+008
6.	2.9348e+006	8.6608e+008	2.6395e+008
6.2	2.9391e+006	8.7389e+008	2.6606e+008
6.4	2.1499e+006	8.8607e+008	2.6825e+008
6.7	1.441e+006	9.0115e+008	2.7146e+008
7.	1.6091e+006	9.1601e+008	2.7467e+008
7.2	2.149e+006	9.2527e+008	2.768e+008
7.4	2.8104e+006	9.3536e+008	2.7895e+008
7.7	3.007e+006	9.4969e+008	2.8215e+008

8.	3.0254e+006	9.6388e+008	2.8535e+008
8.2	3.038e+006	9.7279e+008	2.8748e+008
8.4	3.0498e+006	9.8248e+008	2.8962e+008
8.7	3.0738e+006	9.9632e+008	2.9282e+008
9.	3.1015e+006	1.01e+009	2.9601e+008
9.2	2.9085e+006	1.0188e+009	2.9813e+008
9.4	2.7759e+006	1.0281e+009	3.0027e+008
9.7	2.9481e+006	1.0415e+009	3.0347e+008
10	3.2302e+006	1.0549e+009	3.0667e+008

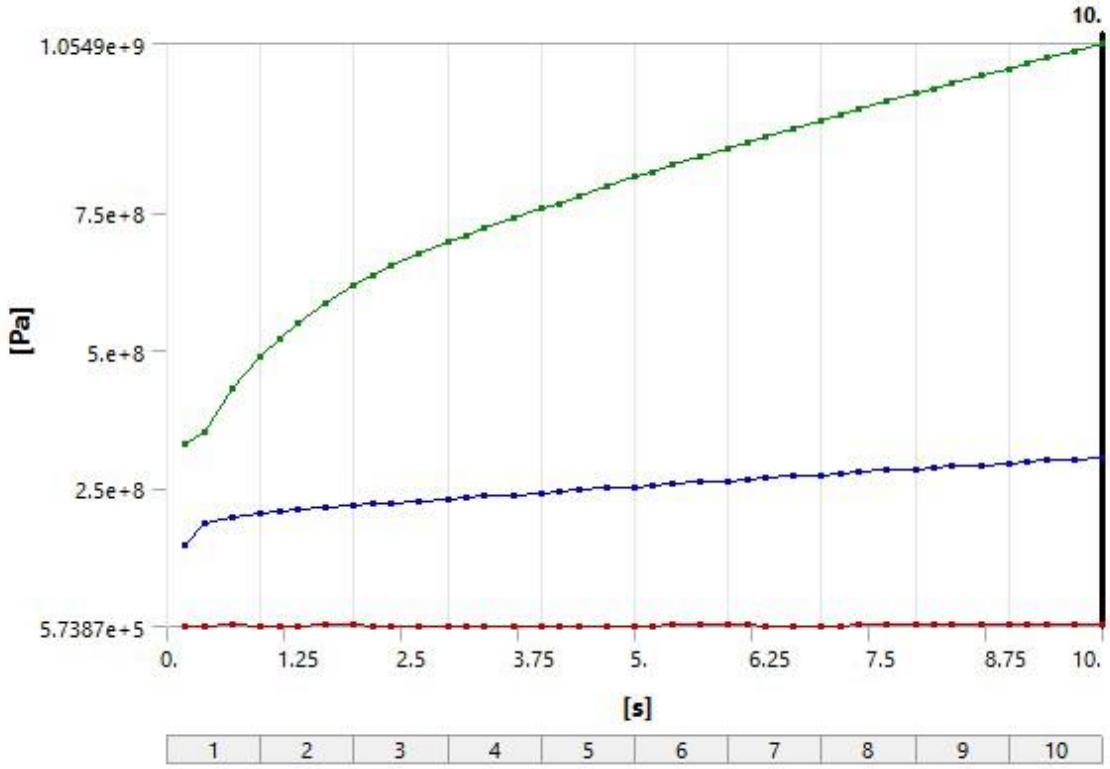

Figure 7.14 Equivalent (Von Mises) Stress Profiles: BCC 12%

7.1.4 Strain Energy

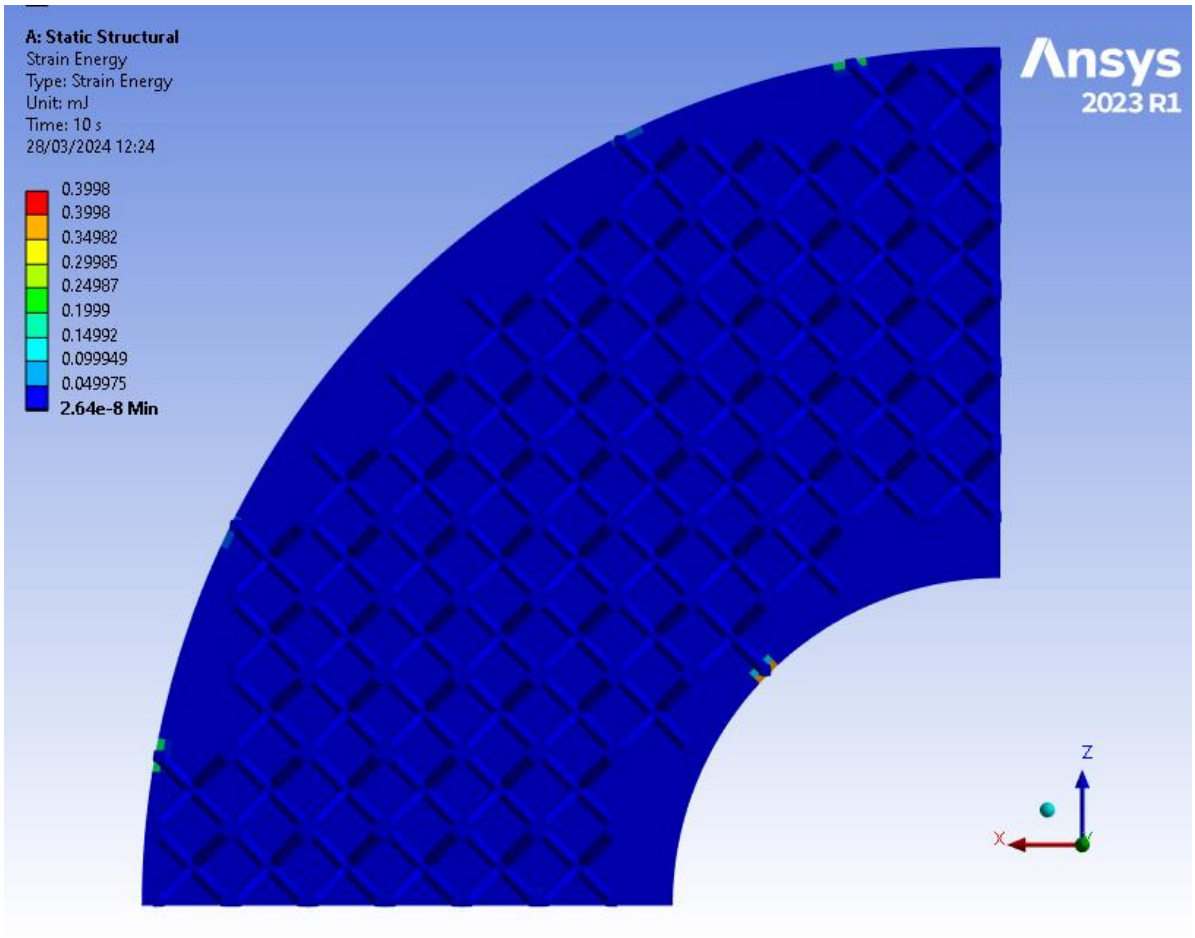

Figure 7.15 Strain Energy contour map: BCC 12% – top view

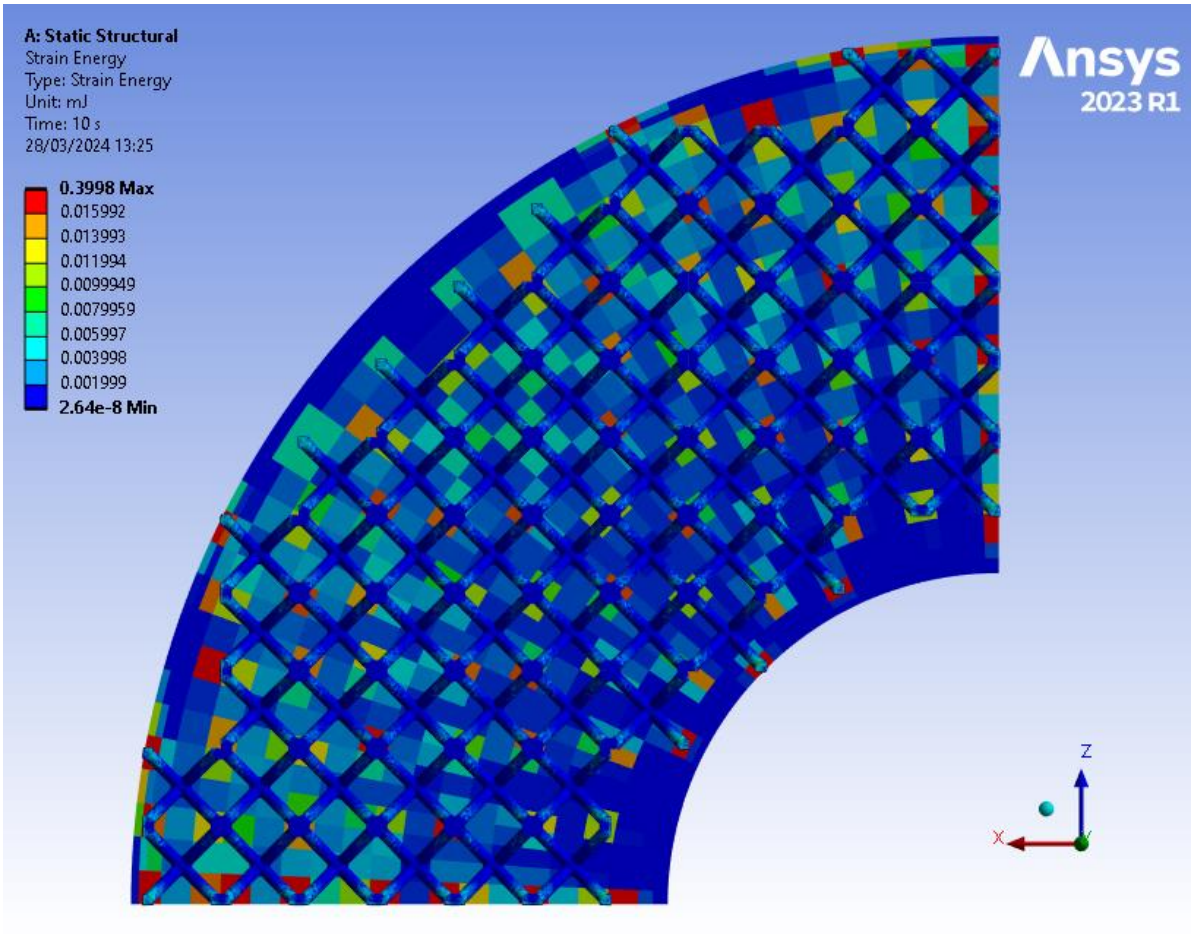

Figure 7.16 Strain Energy filtered contour map: BCC 12% – top view

Figure 7.15 depicts areas of heightened strain energy, particularly notable in regions where the nodes are less than one-fourth of their original size due to cutting. Moving forward to *Figure 7.16*, a symmetrical distribution of strain energy across the area is evident, with noticeably higher concentrations, averaging around 0.016 mJ, observed towards the outer boundaries of the model. Notably, contact areas featuring incomplete nodes exhibit strain energy levels around 0.006 mJ, while those with complete nodes also demonstrate similar strain energy levels around 0.016 mJ. While these values are not exceptionally high, they underscore the insignificance of the distinction between complete and incomplete nodes within the interior of the disk.

Within *Table 7.4*, a comprehensive array of data unveils the minimum, maximum, and total strain energy values documented throughout the designated timeframe. This dataset acts as a reservoir of knowledge, offering valuable glimpses into the intricacies of structural behavior and the evolving nature of deformation responses. By meticulously analyzing this table, we can zero in on the total strain energy associated with the initial displacement, thereby deepening our comprehension of structural dynamics and response mechanisms over time. Notably, upon careful review, we note that the maximum and total strain energy readings reach 0.4mJ

and 6940.2mJ respectively, offering valuable insights into the magnitude of structural deformation under various conditions.

Graphs are showcased in *Figure 7.17.*

Table 7.4 Strain Energy – BCC 12%

t(s)	Minimum Strain Energy (J)	Maximum Strain Energy (J)	Total Strain Energy (J)
0.2	4.8496e-013	4.5204e-006	4.4109e-002
0.4	1.6735e-012	7.8511e-006	0.14267
0.7	6.0394e-012	1.8875e-005	0.3033
1.	7.942e-012	3.1303e-005	0.46944
1.2	7.6828e-012	4.0354e-005	0.58258
1.4	9.4175e-012	4.7485e-005	0.69739
1.7	9.8635e-012	5.9306e-005	0.87258
2.	5.3704e-012	7.1059e-005	1.0512
2.2	4.2133e-012	7.9888e-005	1.1721
2.4	3.9013e-012	8.722e-005	1.2944
2.7	4.3248e-012	9.8358e-005	1.4806
3.	5.4333e-012	1.0895e-004	1.6698
3.2	6.9402e-012	1.1581e-004	1.7977
3.4	7.7449e-012	1.23e-004	1.927
3.7	9.9394e-012	1.3368e-004	2.1234
4.	1.1557e-011	1.4455e-004	2.3229
4.2	1.2956e-011	1.5165e-004	2.4576
4.4	1.3112e-011	1.593e-004	2.5937
4.7	1.4329e-011	1.7068e-004	2.8002
5.	1.564e-011	1.8222e-004	3.0098
5.2	1.7306e-011	1.8974e-004	3.1512
5.4	1.7549e-011	1.9786e-004	3.2939
5.7	1.9052e-011	2.0982e-004	3.5105
6.	2.0496e-011	2.2193e-004	3.7301
6.2	2.2116e-011	2.2975e-004	3.8781
6.4	2.2289e-011	2.3826e-004	4.0274
6.7	2.349e-011	2.5072e-004	4.2539
7.	2.4613e-011	2.6331e-004	4.4834
7.2	2.5465e-011	2.7178e-004	4.638

7.4	2.6027e-011	2.8051e-004	4.794
7.7	2.7042e-011	2.9363e-004	5.0303
8.	2.7658e-011	3.0692e-004	5.2697
8.2	2.8055e-011	3.1579e-004	5.4308
8.4	2.7874e-011	3.2486e-004	5.5933
8.7	2.7623e-011	3.3857e-004	5.8395
9.	2.7307e-011	3.5245e-004	6.0886
9.2	2.712e-011	3.6174e-004	6.2564
9.4	2.6894e-011	3.712e-004	6.4254
9.7	2.6614e-011	3.8542e-004	6.6813
10	2.64e-011	3.998e-004	6.9402

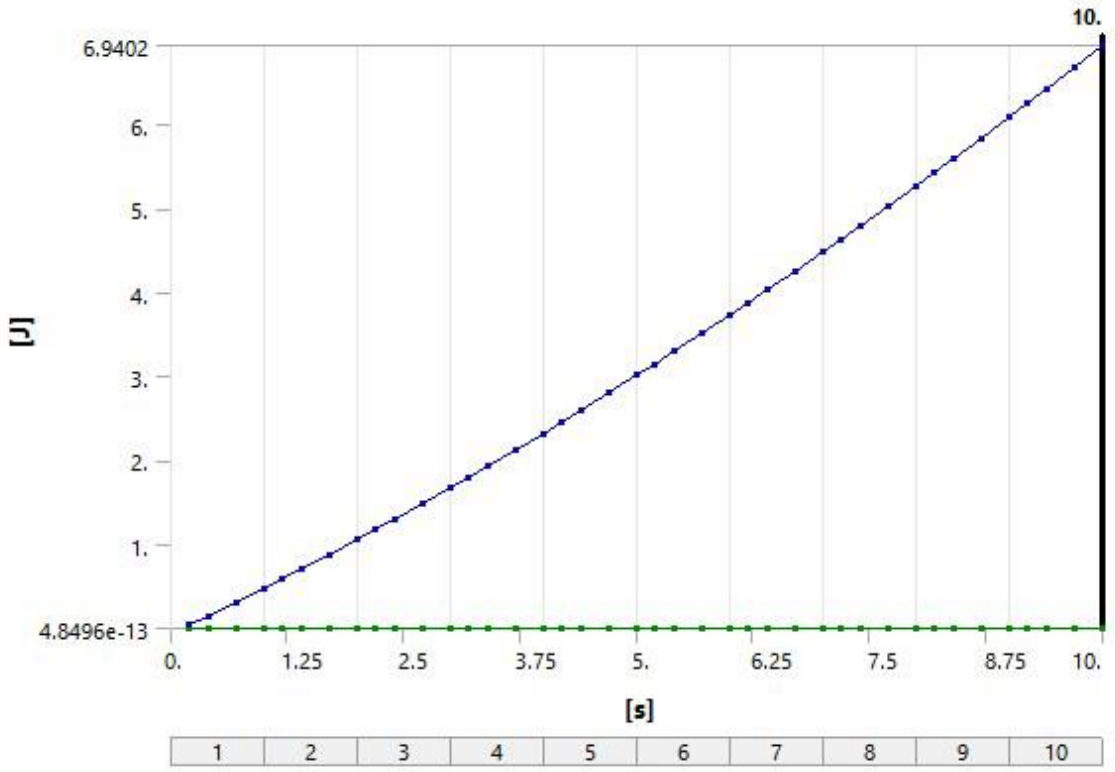

Figure 7.17 Strain Energy Profiles: BCC 12%

7.1.5 Force Reaction

Table 7.5 portrays the application of force (F) over a duration of time (t), where negative values denote compressive force. Over the course of time, there's a progressive escalation in the magnitude of compressive force equaling up to 17362N, indicative of sustained pressure exertion. This implies an ongoing deformation or compression within the material or structure under examination. The consistent trajectory underscores the stability and uniformity of the applied force throughout the designated time frame. Further investigation could delve into associating these force magnitudes with particular mechanical reactions or structural responses. Correspondingly, *Figure 7.18* visually depicts the force reaction trend across time.

Table 7.5 Force Reaction Data– BCC 12%

t(s)	F(N)
0.2	-8557.7
0.4	-10455
0.7	-10923
1.	-11229
1.2	-11412
1.4	-11566
1.7	-11798
2.	-12022
2.2	-12168
2.4	-12308
2.7	-12517
3.	-12725
3.2	-12863
3.4	-12998
3.7	-13202
4.	-13405
4.2	-13541
4.4	-13675
4.7	-13876
5.	-14076
5.2	-14211
5.4	-14343
5.7	-14542
6.	-14741
6.2	-14876
6.4	-15006
6.7	-15204

7.	-15401
7.2	-15533
7.4	-15664
7.7	-15861
8.	-16058
8.2	-16189
8.4	-16319
8.7	-16515
9.	-16711
9.2	-16842
9.4	-16972
9.7	-17167
10	-17362

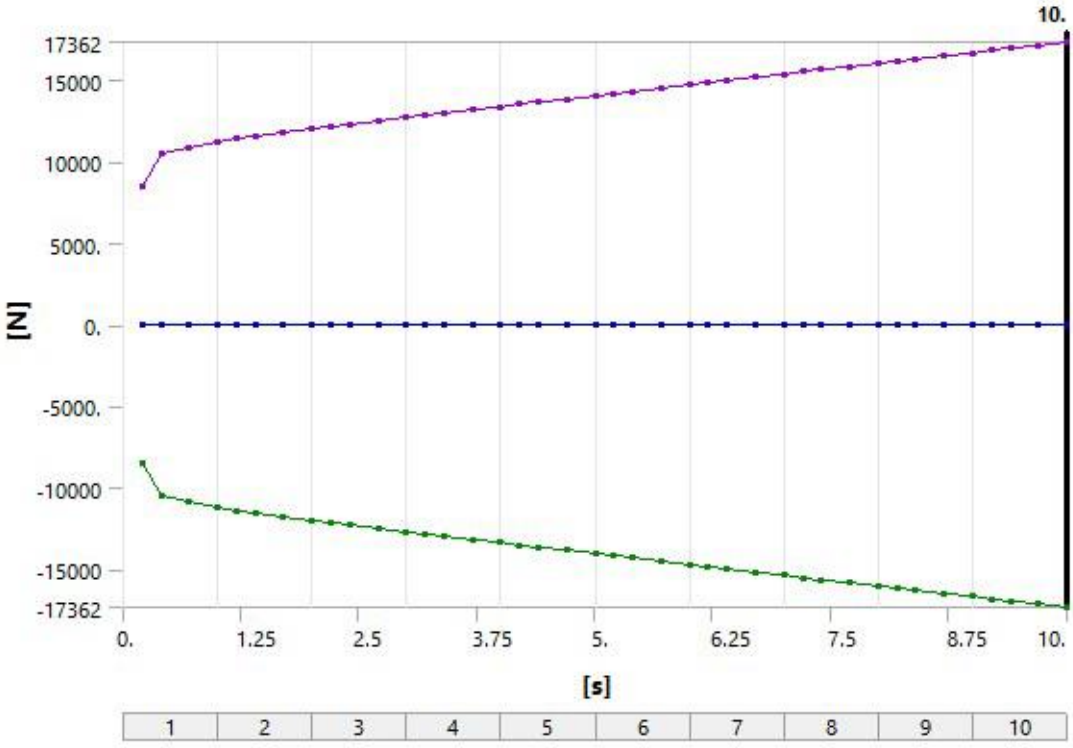

Figure 7.18 Force Reaction Profiles: BCC 12%

7.2 BCC 50%

7.2.1 Total Deformation

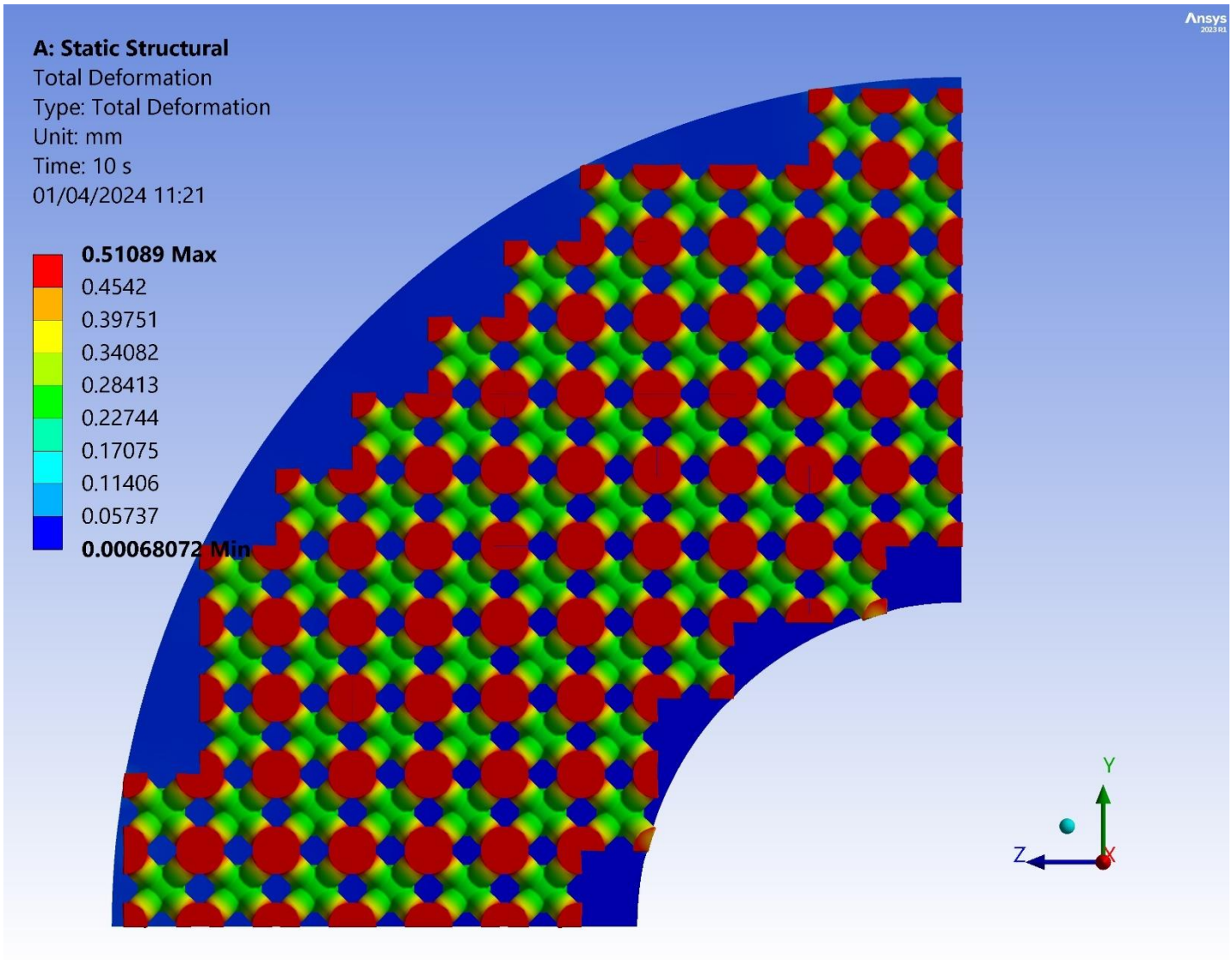

Figure 7.19 Total deformation contour map: BCC 50% – top view

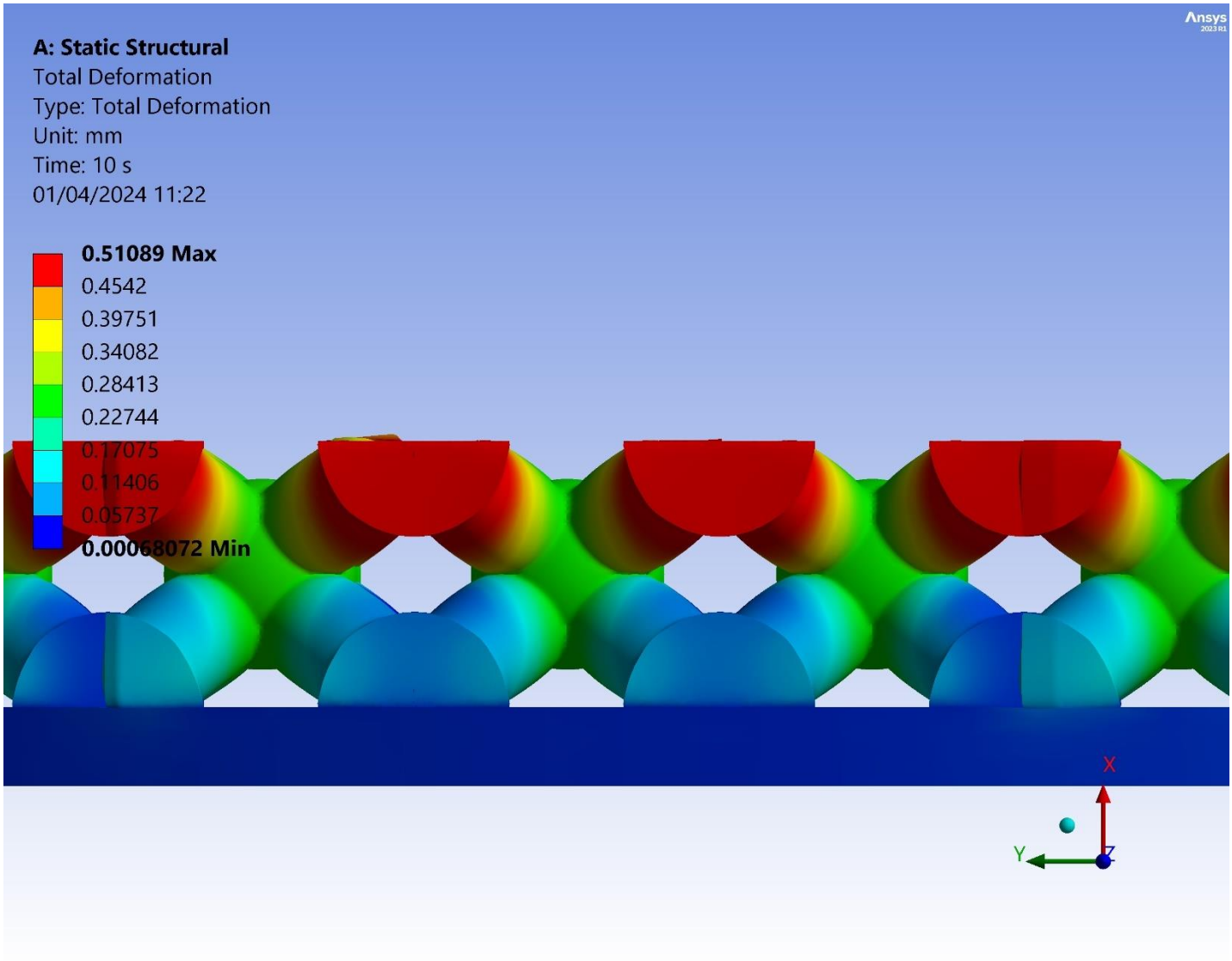

Figure 7.20 Total deformation contour map: BCC 50% – side view

Observing *Figures 7.19 and 7.20*, it's evident that the most pronounced deformation occurs in the upper section of the lattice structure, mirroring the primary displacement zone observed in the BCC 12% model, with a peak value of 0.511mm. Closer to the central node of the unit cell, the total deformation ranges between 0.34mm and 0.4mm. The central nodes exhibit notably less deformation, averaging around 0.25mm, signifying a relatively stable configuration. Moreover, the struts positioned below these central nodes show deformation ranging between 0.2mm and 0.05mm or lower. Further comparison with the BCC 12% model reveals larger deformations in the central nodes and the top struts. Additionally, a consistent trend of decreasing deformation is observed moving downwards within the lattice structure.

Table 7.6 offers a comprehensive overview of the minimum, maximum, and average deformation values recorded over the designated time period. This data provides invaluable insights into the structural behavior, allowing us to discern patterns and trends in deformation responses. By analyzing this table, we can pinpoint the average deformation that corresponds to the initial displacement, facilitating a deeper understanding of the structural dynamics and response mechanisms over time. Specifically, upon scrutiny, we observe that the maximum and average deformation recorded stand at 0.511mm and 0.262mm respectively, shedding light on the extent of structural deformation under varying conditions.

Graphs are showcased in *Figure 7.6.*

Table 7.6 Deformation Data – BCC 50%

t (s)	Min Deformation (mm)	Max Deformation (mm)	Average Deformation(mm)
0.2	2.7472e-003	1.4482e-002	9.1492e-003
0.4	4.1141e-003	2.7861e-002	1.7451e-002
0.7	3.7953e-003	4.2999e-002	2.5566e-002
1.	3.7438e-003	5.7470e-002	3.2960e-002
1.2	3.2485e-003	6.7226e-002	3.7904e-002
1.4	2.8178e-003	7.7024e-002	4.2848e-002
1.7	2.4496e-003	9.1789e-002	5.0270e-002
2.	2.3692e-003	0.10664	5.7720e-002
2.2	2.4643e-003	0.11657	6.2703e-002
2.4	2.3854e-003	0.12653	6.7696e-002
2.7	2.1337e-003	0.1415	7.5201e-002
3.	1.3572e-003	0.15651	8.2726e-002
3.2	1.0253e-003	0.16654	8.7754e-002
3.4	1.0250e-003	0.17657	9.2791e-002
3.7	9.8563e-004	0.19165	0.10036
4.	8.1070e-004	0.20674	0.10794
4.2	1.0481e-003	0.21681	0.113
4.4	1.1657e-003	0.2269	0.11807
4.7	1.1339e-003	0.24203	0.12568
5.	1.4161e-003	0.25718	0.13331
5.2	1.2332e-003	0.26729	0.13839
5.4	1.1322e-003	0.2774	0.14349
5.7	1.1779e-003	0.29257	0.15113
6.	1.4191e-003	0.30776	0.15879
6.2	1.6437e-003	0.31789	0.1639
6.4	1.6414e-003	0.32802	0.16901

6.7	1.4939e-003	0.34322	0.17668
7.	1.4429e-003	0.35843	0.18437
7.2	1.4665e-003	0.36857	0.18949
7.4	1.4780e-003	0.37872	0.19462
7.7	1.4625e-003	0.39394	0.20232
8.	1.5449e-003	0.40917	0.21002
8.2	8.2285e-004	0.41933	0.21516
8.4	7.2497e-004	0.42949	0.2203
8.7	8.5552e-004	0.44473	0.22802
9.	6.8986e-004	0.45999	0.23575
9.2	5.4304e-004	0.47016	0.24091
9.4	5.4908e-004	0.48033	0.24607
9.7	6.9485e-004	0.49561	0.25382
10	9.7492e-004	0.51089	0.26158

Graphs are showcased in *Figure 7.21.*

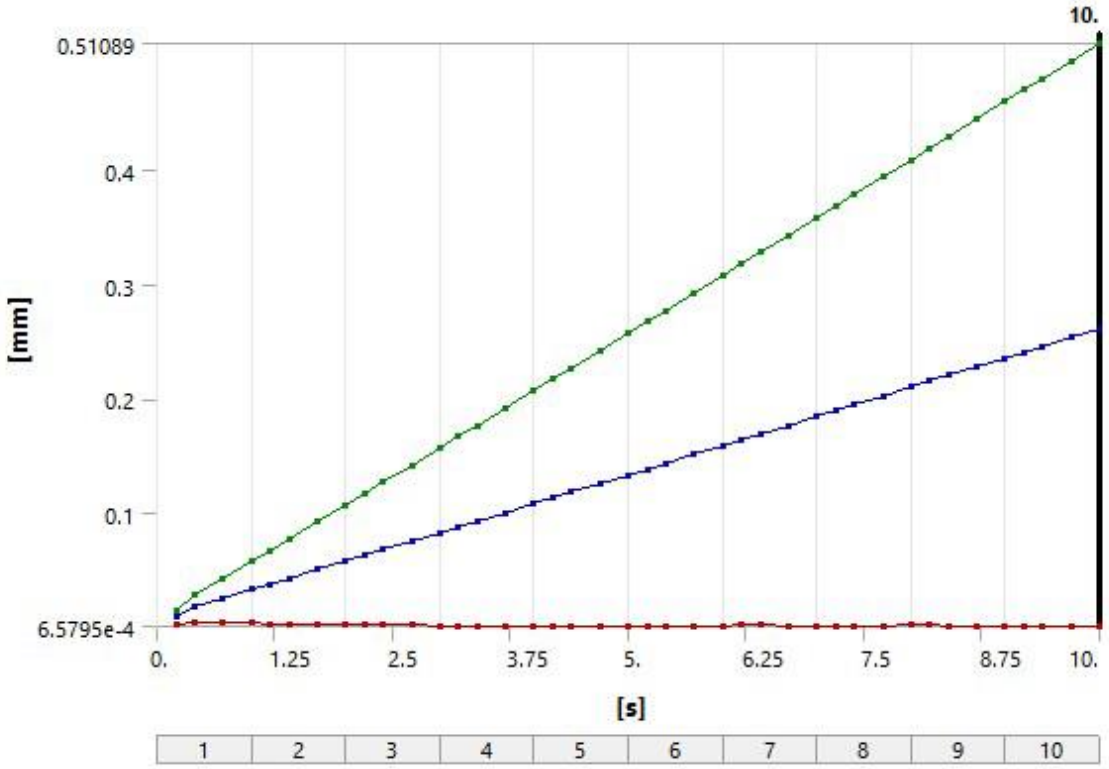

Figure 7.21 Deformation Profiles: BCC 50%

7.2.2 Equivalent Elastic Strain

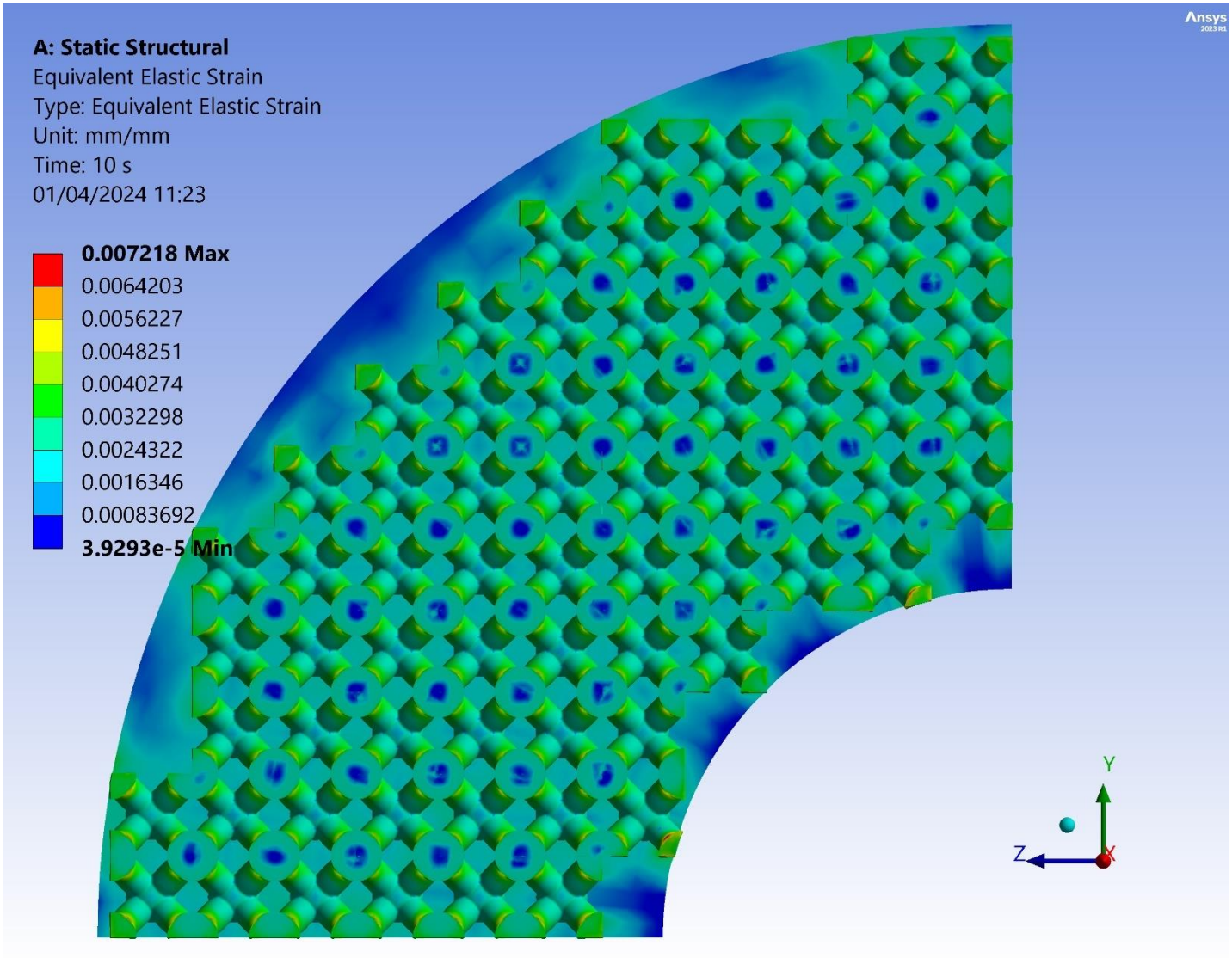

Figure 7.22 Equivalent Elastic Strain contour map: BCC 50% – top view

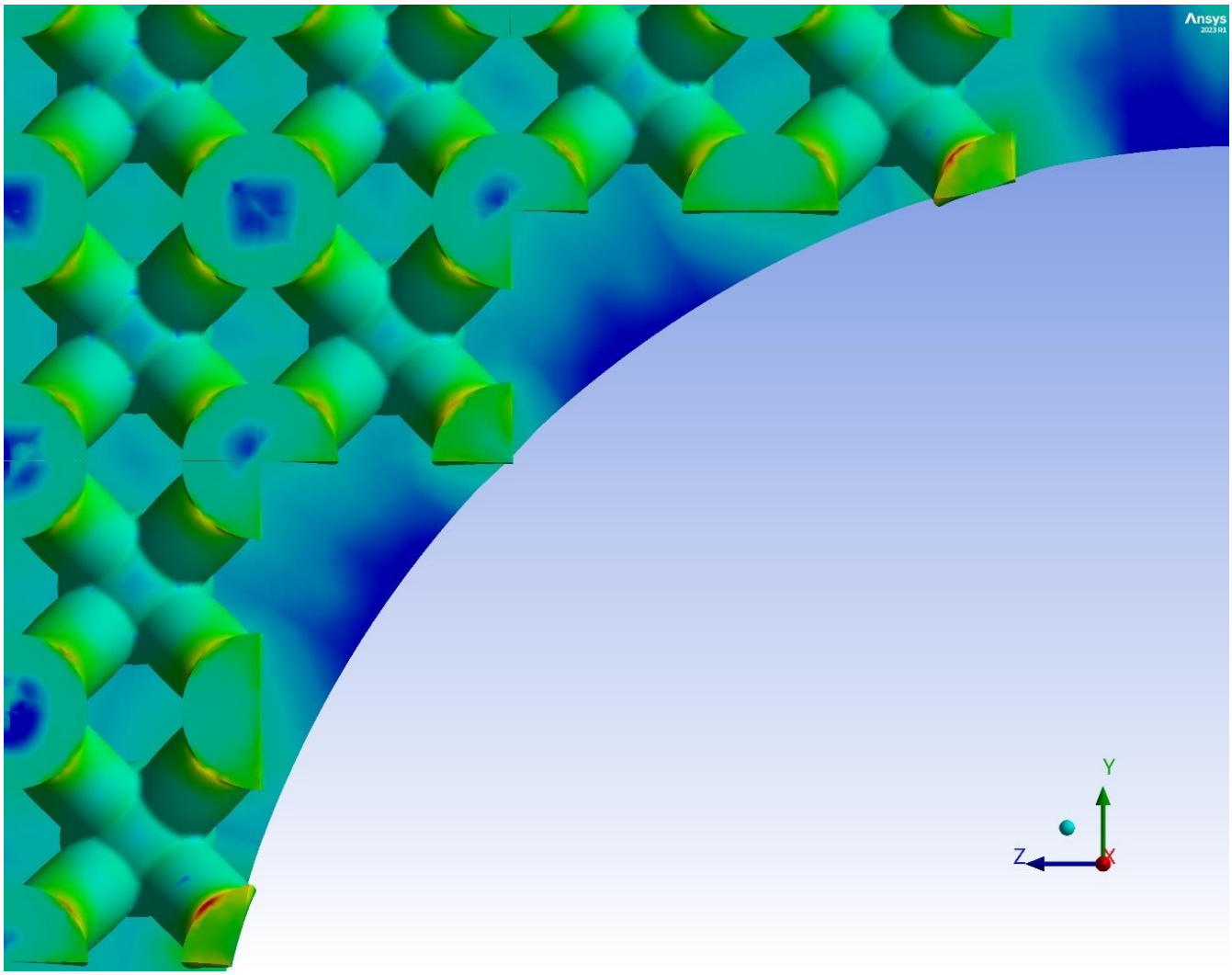

Figure 7.23 Equivalent Elastic Strain contour map: BCC 50% – zoomed-in top view

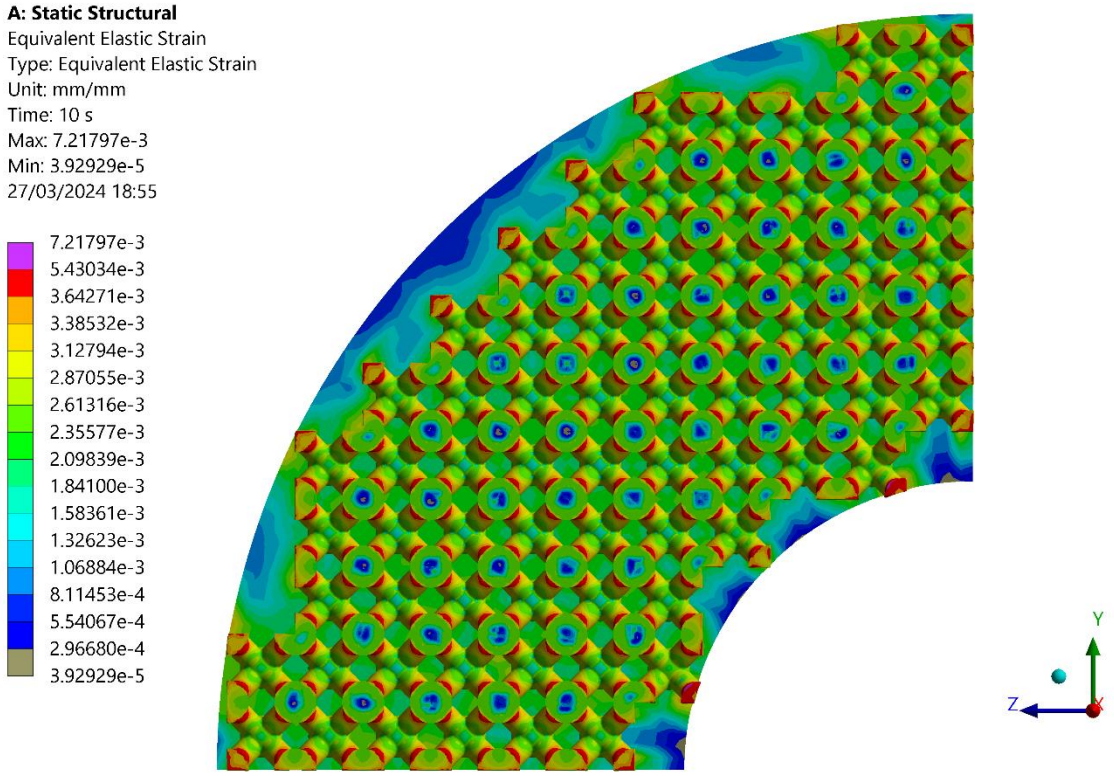

Figure 7.24 Equivalent Elastic Strain filtered contour map: BCC 50% –top view

Figures 7.22 and 7.23 reaffirm the presence of strain concentration points at incomplete nodes, exhibiting an Equivalent Elastic strain of approximately 0.007mm/mm. *Figure 7.24* offers a filtered representation, enhancing the clarity of the elastic strain phenomenon and facilitating a better understanding of its spatial distribution and magnitude within the model. This filtration process helps identify areas for further analysis and refinement. Similar to the BCC 12% scenario, higher struts between top nodes and central nodes exhibit values ranging from 0.0054mm/mm to 0.0026mm/mm, while central nodes maintain a value of approximately 0.0023mm/mm.

Table 7.6 offers a comprehensive overview of the minimum, maximum, and average elastic strain values recorded over the designated time period. This data provides invaluable insights into the structural behavior, allowing us to discern patterns and trends in deformation responses. By analyzing this table, we can pinpoint the average elastic strain that corresponds to the initial displacement, facilitating a deeper understanding of the structural dynamics and response mechanisms over time. Specifically, upon scrutiny, we observe that the maximum and average elastic strain recorded stand at 0.007mm/mm and 0.003mm/mm respectively.

Graphs are showcased in *Figure 7.25.*

Table 7.7 Elastic Strain Data – BCC 50%

t(s)	Min Elastic Strain (mm/mm)	Max Elastic Strain(mm/mm)	Avg Elastic Strain (mm/mm)
0.2	4.7947e-006	2.8491e-003	1.0063e-003
0.4	1.2577e-005	3.4757e-003	1.6827e-003
0.7	2.4567e-005	3.6130e-003	1.9281e-003
1.	3.2530e-005	3.7094e-003	2.0206e-003
1.2	3.7289e-005	3.7633e-003	2.0705e-003
1.4	3.8071e-005	3.9699e-003	2.1127e-003
1.7	3.8284e-005	4.2529e-003	2.1636e-003
2.	3.9512e-005	4.5040e-003	2.2033e-003
2.2	3.9439e-005	4.0999e-003	2.2256e-003
2.4	4.0658e-005	4.2106e-003	2.2455e-003
2.7	3.9158e-005	4.3681e-003	2.2719e-003
3.	3.4042e-005	4.5188e-003	2.2959e-003
3.2	3.1750e-005	4.6166e-003	2.3110e-003
3.4	3.0456e-005	4.7121e-003	2.3255e-003
3.7	2.9619e-005	4.8507e-003	2.3462e-003
4.	2.9639e-005	4.9853e-003	2.3658e-003
4.2	2.9867e-005	5.0733e-003	2.3785e-003
4.4	3.0200e-005	5.1599e-003	2.3909e-003
4.7	3.0963e-005	5.2864e-003	2.4088e-003
5.	3.1849e-005	5.4099e-003	2.4261e-003
5.2	3.2610e-005	5.4911e-003	2.4373e-003
5.4	3.3466e-005	5.5711e-003	2.4484e-003
5.7	3.3448e-005	5.6887e-003	2.4647e-003
6.	3.3777e-005	5.8038e-003	2.4806e-003
6.2	3.4187e-005	5.8798e-003	2.4911e-003
6.4	3.4806e-005	5.9546e-003	2.5015e-003
6.7	3.5890e-005	6.0650e-003	2.5170e-003
7.	3.7444e-005	6.1736e-003	2.5322e-003
7.2	3.8701e-005	6.2453e-003	2.5422e-003
7.4	3.9749e-005	6.3162e-003	2.5522e-003
7.7	3.9652e-005	6.4209e-003	2.5672e-003
8.	3.6751e-005	6.5243e-003	2.5819e-003
8.2	3.5330e-005	6.5924e-003	2.5917e-003
8.4	3.4181e-005	6.6599e-003	2.6016e-003
8.7	3.3524e-005	6.7599e-003	2.6162e-003

9.	3.3640e-005	6.8669e-003	2.6308e-003
9.2	3.4190e-005	6.9383e-003	2.6405e-003
9.4	3.4613e-005	7.0091e-003	2.6502e-003
9.7	3.6245e-005	7.1141e-003	2.6646e-003
10	3.9293e-005	7.2180e-003	2.6791e-003

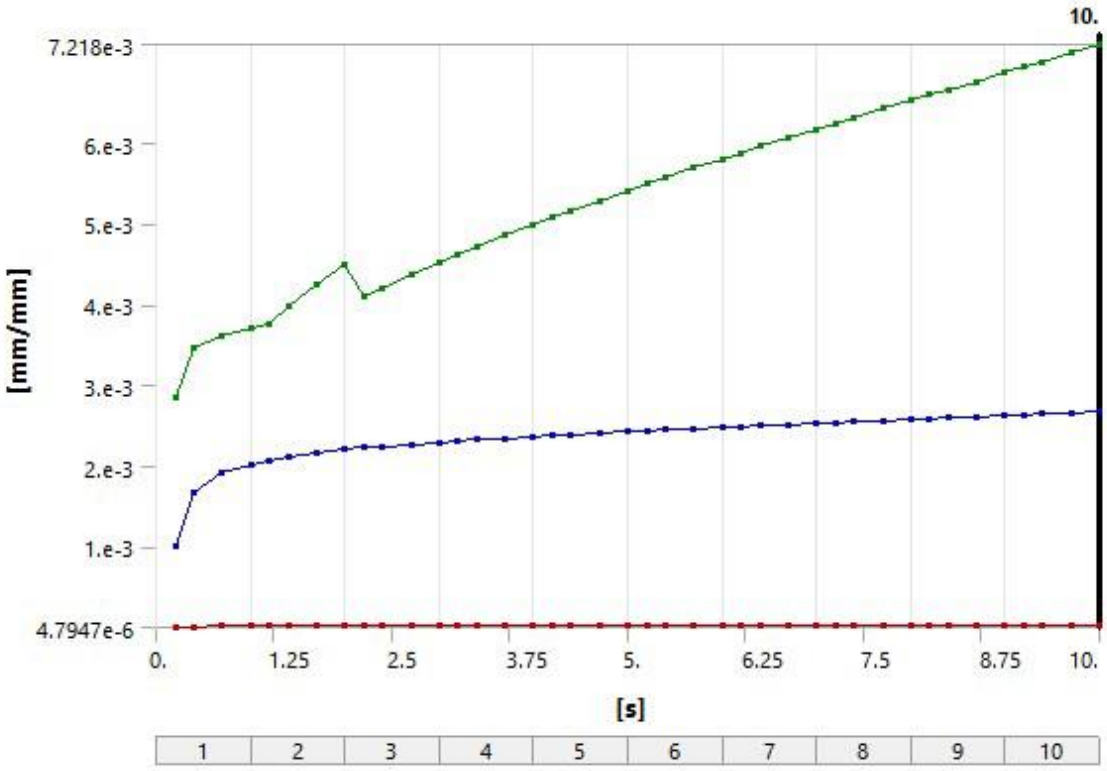

Figure 7.25 Elastic Strain Profiles: BCC 50%

7.2.3 Equivalent Stress

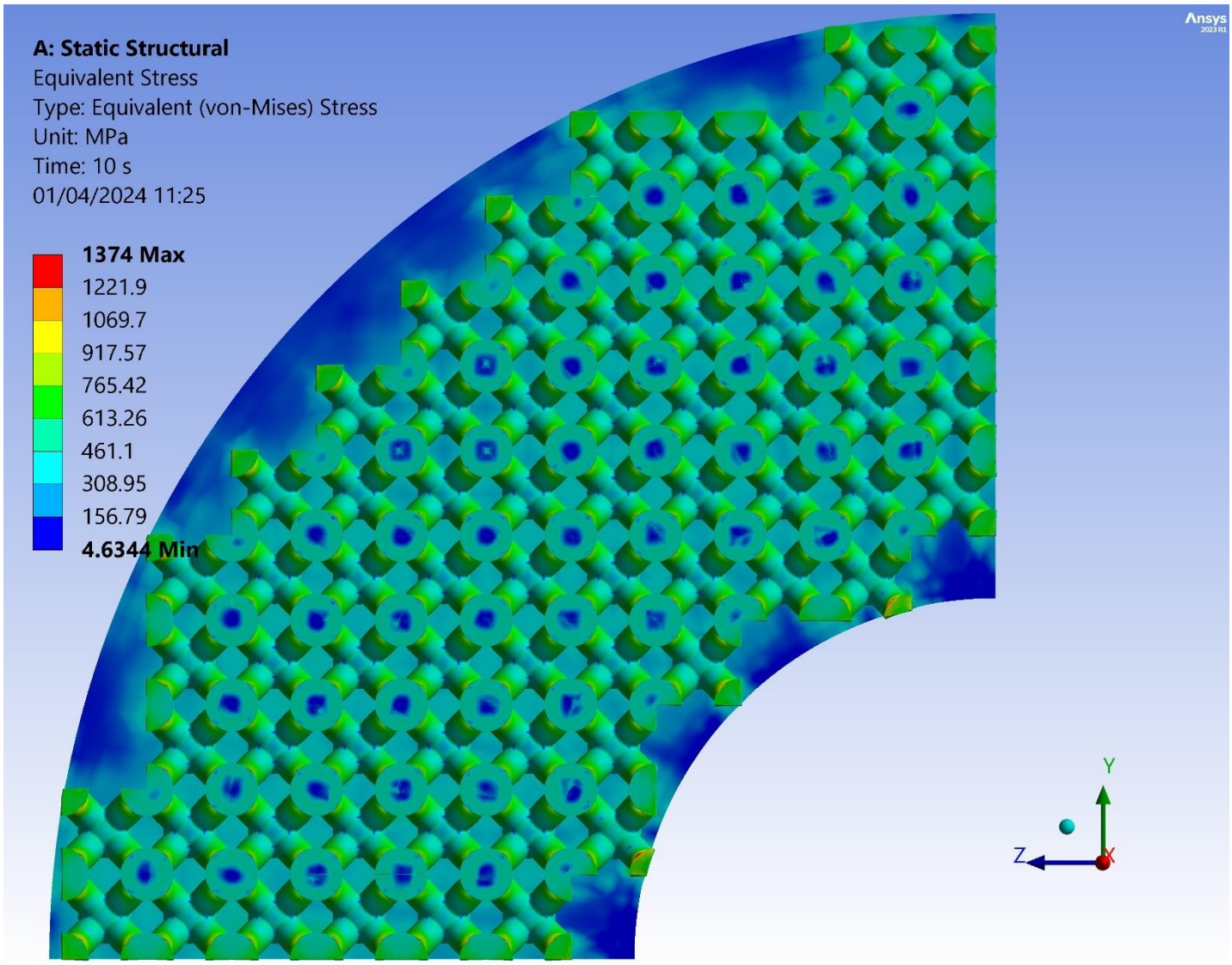

Figure 7.26 Equivalent Stress contour map: BCC 50% – top view

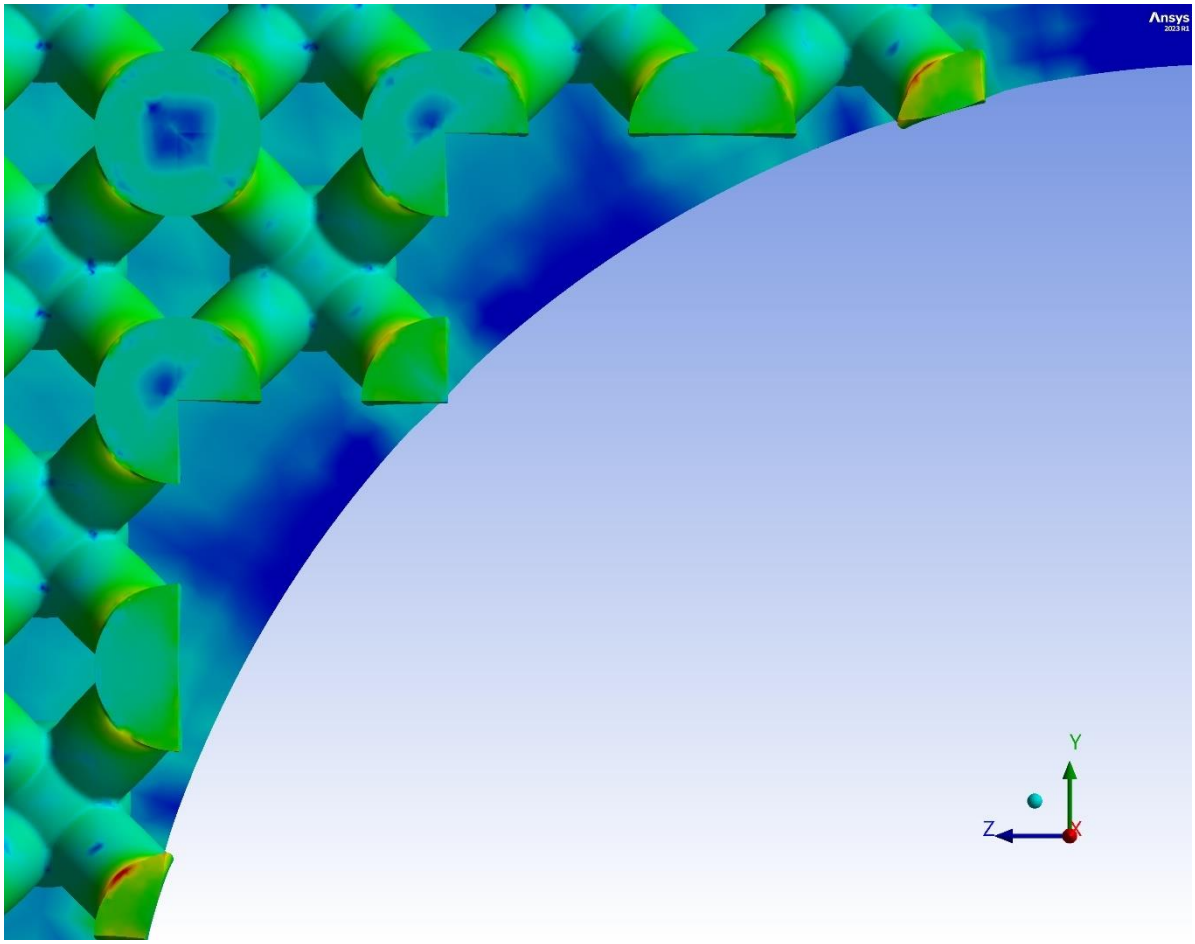

Figure 7.27 Equivalent Stress contour map: BCC 50% – zoomed in top view

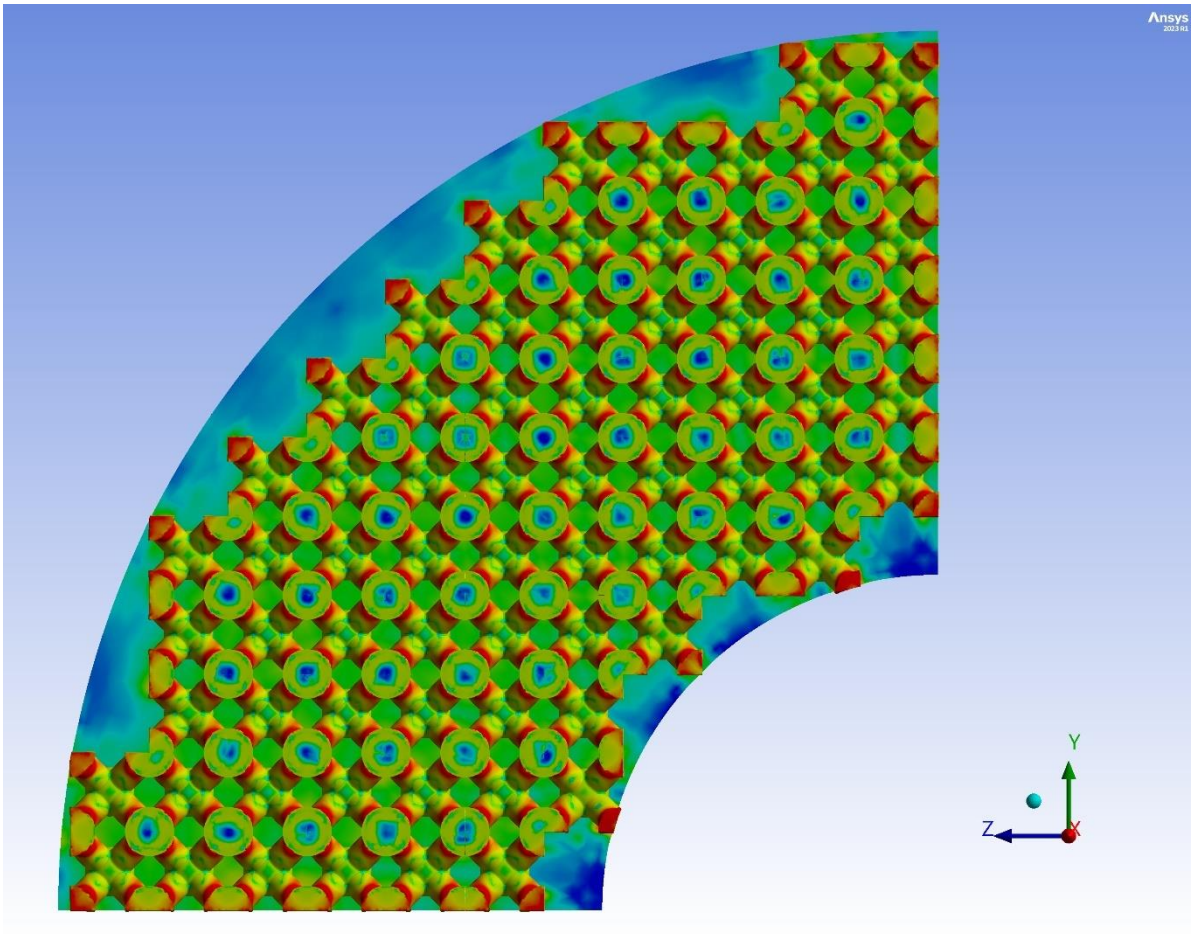

Figure 7.28 Equivalent Stress filtered contour map: BCC 50% – top view

Upon initial inspection of *Figure 7.26* and *Figure 7.27*, it's evident that the lattice structure exhibits prominent stress concentration areas, notably at the corners associated with incomplete nodes and along the edges between the nodes and the struts. To enhance clarity, filtering techniques were applied to the legend. Upon closer examination, it's apparent that the primary stress concentration zones align with the nodes, as anticipated. These stress values can reach up to 1374MPa, particularly at the corners of incomplete nodes, while the struts surrounding the central node typically experience stresses around 500MPa, as seen in the *Figure 7.28*. Furthermore, it's noteworthy that stress tends to increase with decreasing node size.

Table 7.8 offers a comprehensive overview of the minimum, maximum, and average stress values recorded over the designated time period. This data provides invaluable insights into the structural behavior, allowing us to discern patterns and trends in deformation responses. By analyzing this table, we can pinpoint the average and maximum stress that corresponds to the initial displacement, facilitating a deeper understanding

of the structural dynamics and response mechanisms over time. Specifically, upon scrutiny, we observe that the maximum and average stress recorded stand at 1374MPa and 495.22MPa, respectively.

Graphs are showcased in *Figure 7.29.*

Table 7.8 Equivalent (von-Mises) Stress Data – BCC 50%

t(s)	Minimum Stress (MPa)	Maximum Stress (MPa)	Average Stress (MPa)
0.2	0.93449	547.45	190.52
0.4	2.2389	594.61	318.07
0.7	2.8397	697.41	363.15
1.	3.7154	707.69	379.22
1.2	3.8522	669.97	387.71
1.4	4.6315	697.38	394.83
1.7	4.8982	734.71	403.35
2.	4.9298	769.17	409.98
2.2	2.639	790.78	413.72
2.4	3.0795	811.42	417.09
2.7	4.395	840.71	421.59
3.	3.8678	868.66	425.71
3.2	2.9916	886.72	428.31
3.4	2.4349	904.4	430.82
3.7	2.0761	930.15	434.41
4.	2.2062	955.18	437.85
4.2	2.5157	971.59	440.07
4.4	2.8445	987.78	442.25
4.7	3.3829	1011.5	445.43
5.	3.6852	1034.8	448.51
5.2	3.9387	1050.1	450.53
5.4	4.2155	1065.3	452.52
5.7	4.6704	1087.6	455.46
6.	4.751	1109.5	458.36
6.2	4.5867	1123.9	460.27
6.4	4.4522	1138.2	462.18
6.7	4.2693	1159.3	465.01
7.	4.1018	1180.1	467.81
7.2	3.9816	1193.8	469.67
7.4	3.9343	1207.4	471.52

7.7	3.8765	1227.5	474.29
8.	3.8816	1247.4	477.04
8.2	3.9143	1260.4	478.85
8.4	3.989	1273.6	480.69
8.7	4.1187	1292.9	483.43
9.	4.2806	1312	486.16
9.2	4.4062	1324.6	487.96
9.4	4.5275	1337.1	489.79
9.7	4.6166	1355.7	492.5
10	4.6344	1374	495.22

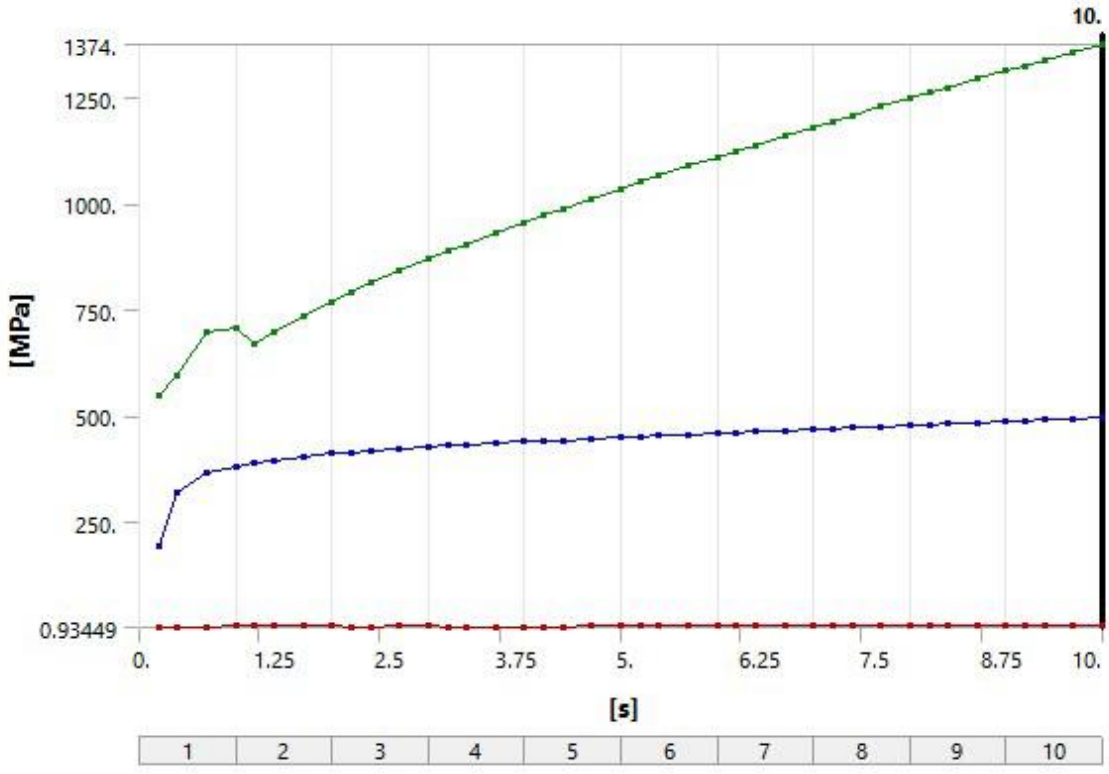

Figure 7.29 Equivalent (von-Mises) Stress Profiles: BCC 50%

7.2.4 Strain Energy

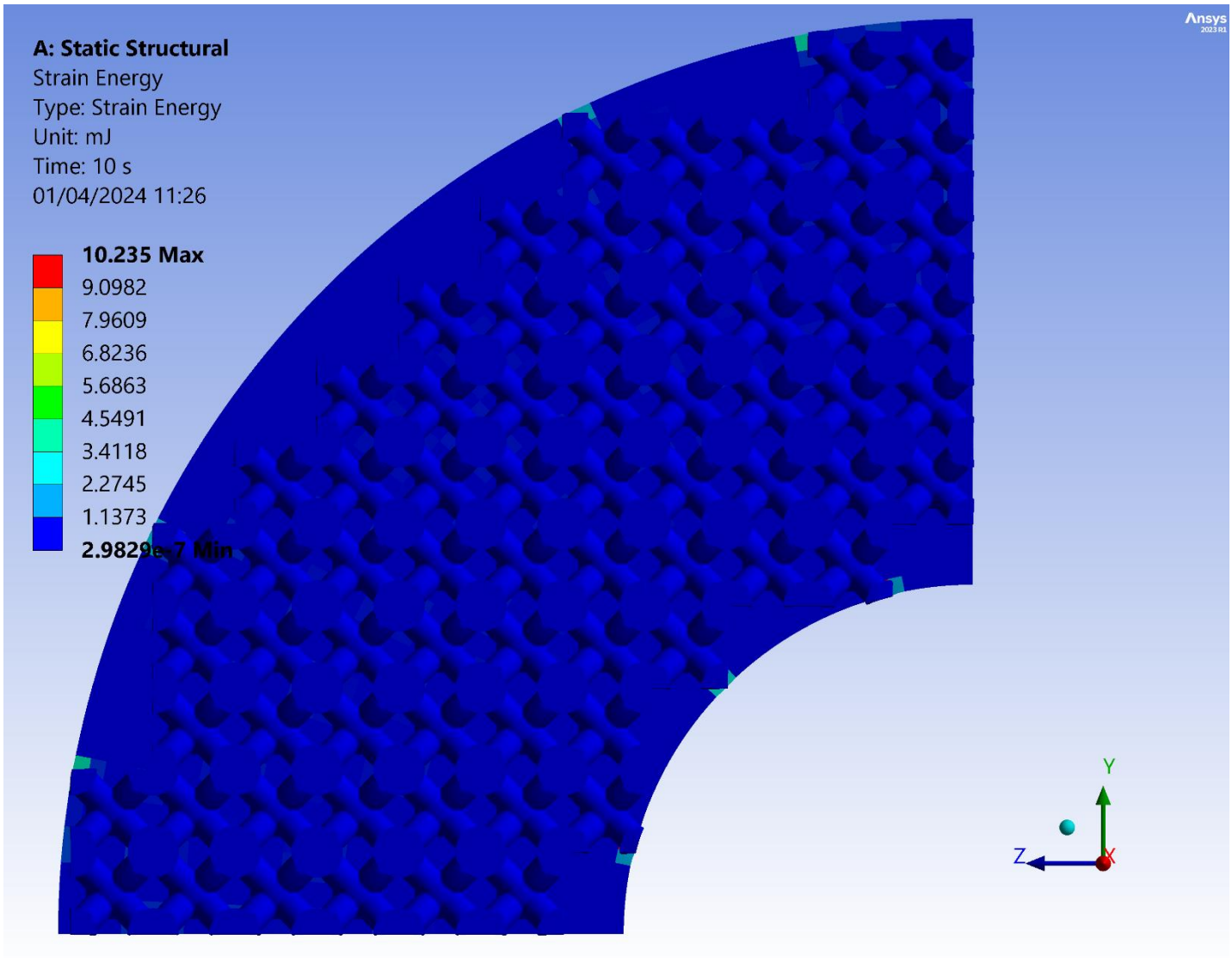

Figure 7.30 Strain Energy contour map: BCC 50% – top view

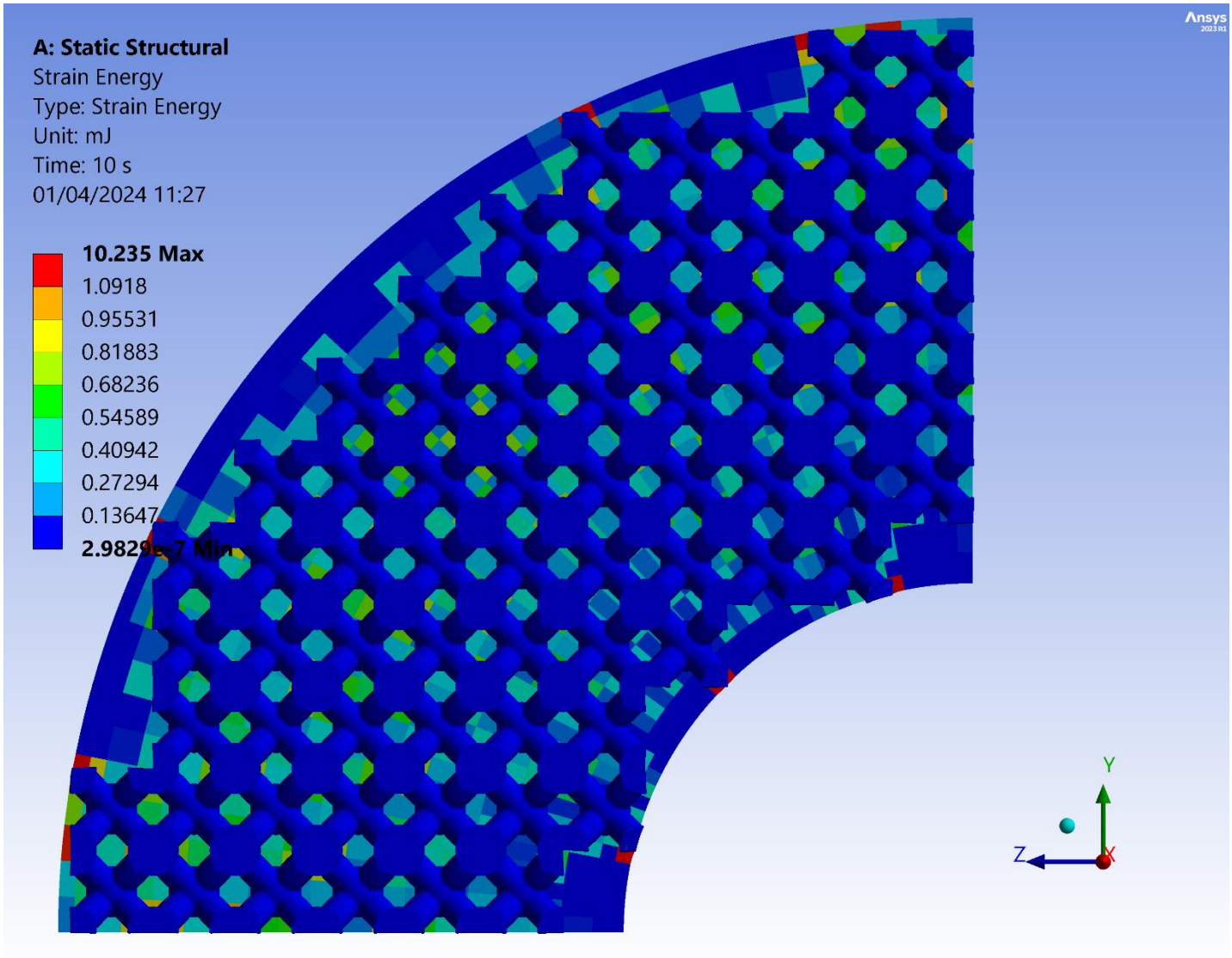

Figure 7.31 Strain Energy filtered contour map: BCC 50% – top view

Within *Table 7.9*, a comprehensive array of data unveils the minimum, maximum, and total strain energy values documented throughout the designated timeframe. This dataset acts as a reservoir of knowledge, offering valuable glimpses into the intricacies of structural behavior and the evolving nature of deformation responses. By meticulously analyzing this table, we can zero in on the total strain energy associated with the initial displacement, thereby deepening our comprehension of structural dynamics and response mechanisms over time. Notably, upon careful review, we note that the maximum and total strain energy readings reach 10.235mJ and 82484mJ respectively, offering valuable insights into the magnitude of structural deformation under various conditions.

Graphs are showcased in *Figure 7.33.*

Table 7.9 Strain Energy – BCC 50%

t(s)	Min Strain Energy (mJ)	Max Strain Energy (mJ)	Total Strain Energy (mJ)
0.2	9.1218e-010	8.5007e-002	380.01
0.4	5.046e-009	0.27183	1428.3
0.7	1.7164e-008	0.61362	3506.8
1.	3.1429e-008	0.99613	5680.2
1.2	3.9226e-008	1.232	7154.1
1.4	4.3301e-008	1.4562	8643.8
1.7	5.0398e-008	1.7765	10904
2.	6.6473e-008	2.088	13193
2.2	8.5913e-008	2.2917	14733
2.4	1.1305e-007	2.4924	16284
2.7	1.4717e-007	2.7892	18632
3.	1.6949e-007	3.0827	21003
3.2	1.839e-007	3.2776	22597
3.4	1.9512e-007	3.4714	24201
3.7	2.0181e-007	3.7616	26627
4.	2.0795e-007	4.0518	29075
4.2	2.1223e-007	4.2461	30720
4.4	2.1582e-007	4.4413	32374
4.7	2.2106e-007	4.7347	34874
5.	2.256e-007	5.0322	37395
5.2	2.2818e-007	5.232	39088
5.4	2.3108e-007	5.4322	40791
5.7	2.355e-007	5.7333	43363
6.	2.4003e-007	6.0359	45955
6.2	2.4351e-007	6.2391	47696
6.4	2.4627e-007	6.4423	49445
6.7	2.5031e-007	6.7488	52087
7.	2.5356e-007	7.0569	54749
7.2	2.564e-007	7.2633	56535
7.4	2.5882e-007	7.4699	58331
7.7	2.6336e-007	7.7813	61041
8.	2.6759e-007	8.0949	63771
8.2	2.7121e-007	8.3051	65603
8.4	2.7362e-007	8.5159	67443

8.7	2.7761e-007	8.8342	70220
9.	2.8153e-007	9.1544	73017
9.2	2.8458e-007	9.3691	74893
9.4	2.8769e-007	9.5845	76778
9.7	2.928e-007	9.909	79621
10	2.9829e-007	10.235	82484

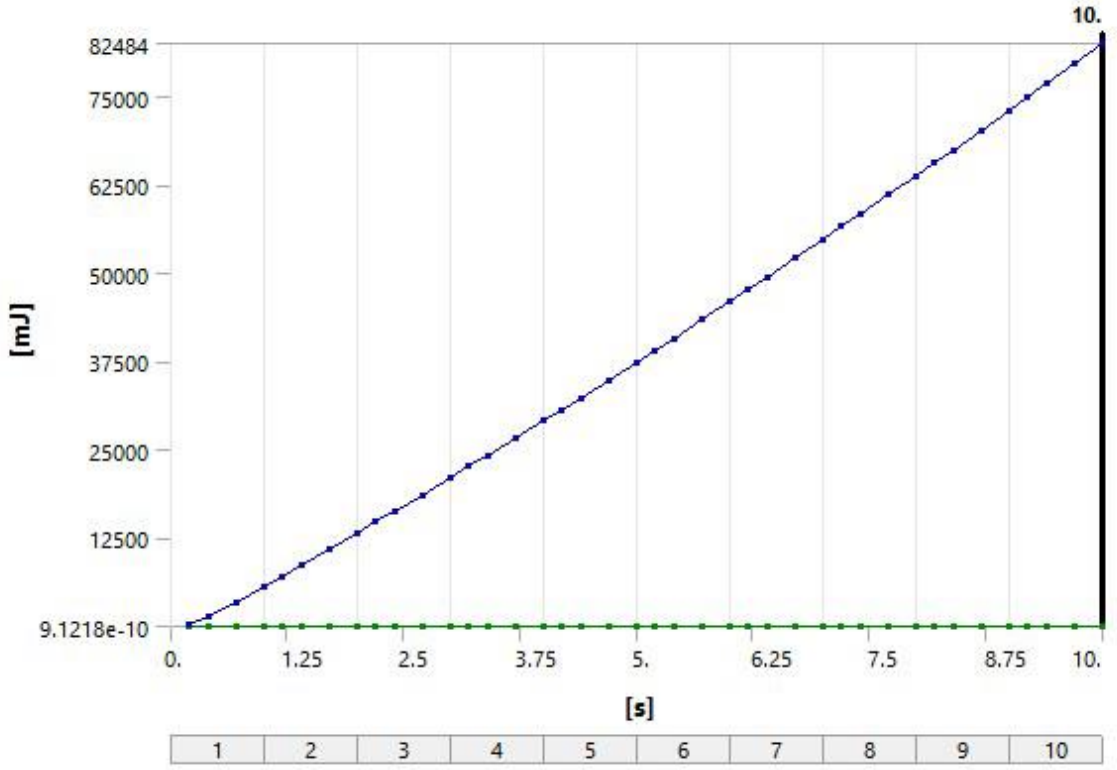

Figure 7.33 Strain Energy Profiles: BCC 50%

7.2.5 Force Reaction

Table 7.5 portrays the application of force (F) over a duration of time (t), where negative values denote compressive force. Over the course of time, there's a progressive escalation in the magnitude of compressive force equaling up to 191610N, indicative of sustained pressure exertion. This implies an ongoing deformation or compression within the material or structure under examination. The consistent trajectory underscores the stability and uniformity of the applied force throughout the designated time frame. Further investigation could delve into associating these force magnitudes with particular mechanical reactions or structural responses. Correspondingly, *Figure 7.18* visually depicts the force reaction trend across time.

Table 7.10 Force Reaction Data – BCC 50%

t(s)	F(N)
0.2	-76222
0.4	-1.288e+005
0.7	-1.4297e+005
1.	-1.4657e+005
1.2	-1.483e+005
1.4	-1.4977e+005
1.7	-1.5172e+005
2.	-1.5352e+005
2.2	-1.5465e+005
2.4	-1.5576e+005
2.7	-1.5738e+005
3.	-1.5896e+005
3.2	-1.6e+005
3.4	-1.6102e+005
3.7	-1.6254e+005
4.	-1.6403e+005
4.2	-1.6502e+005
4.4	-1.66e+005
4.7	-1.6746e+005
5.	-1.6891e+005
5.2	-1.6987e+005
5.4	-1.7082e+005
5.7	-1.7223e+005
6.	-1.7364e+005
6.2	-1.7457e+005
6.4	-1.755e+005
6.7	-1.7688e+005

7.	-1.7826e+005
7.2	-1.7917e+005
7.4	-1.8008e+005
7.7	-1.8144e+005
8.	-1.8279e+005
8.2	-1.8366e+005
8.4	-1.8457e+005
8.7	-1.8591e+005
9.	-1.8723e+005
9.2	-1.8812e+005
9.4	-1.8899e+005
9.7	-1.903e+005
10	-1.9161e+005

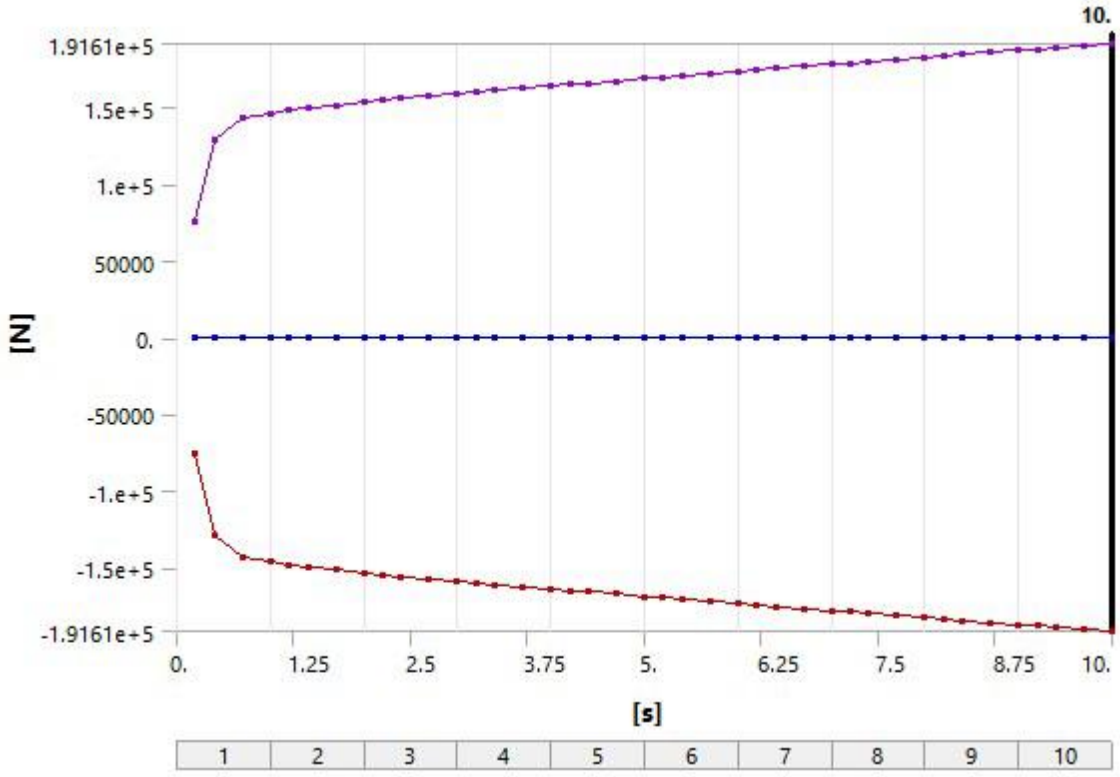

Figure 7.34 Force Reaction Profiles: BCC 50%

7.3 I-type 12%

7.3.1 Total Deformation

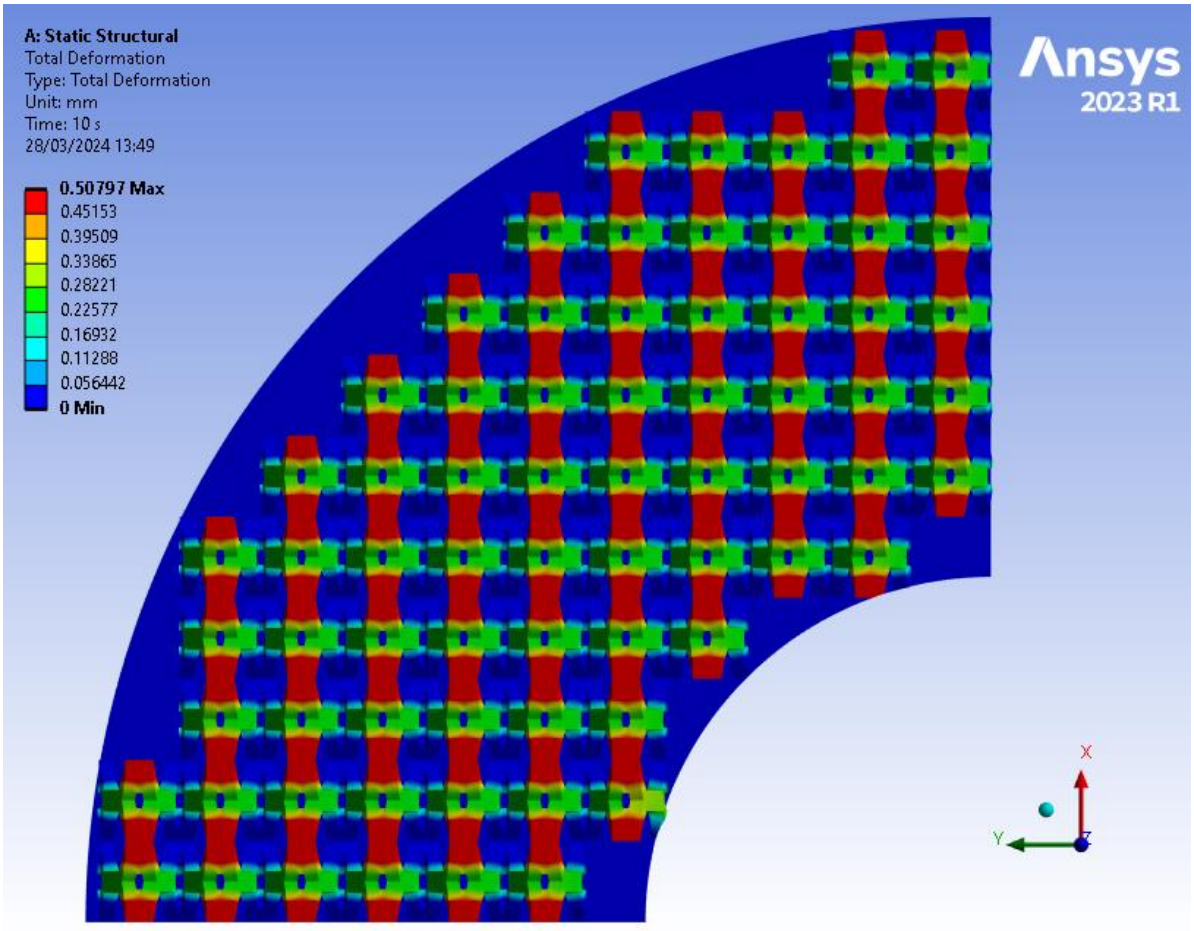

Figure 7.35 Total deformation contour map: I-type 12% – top view

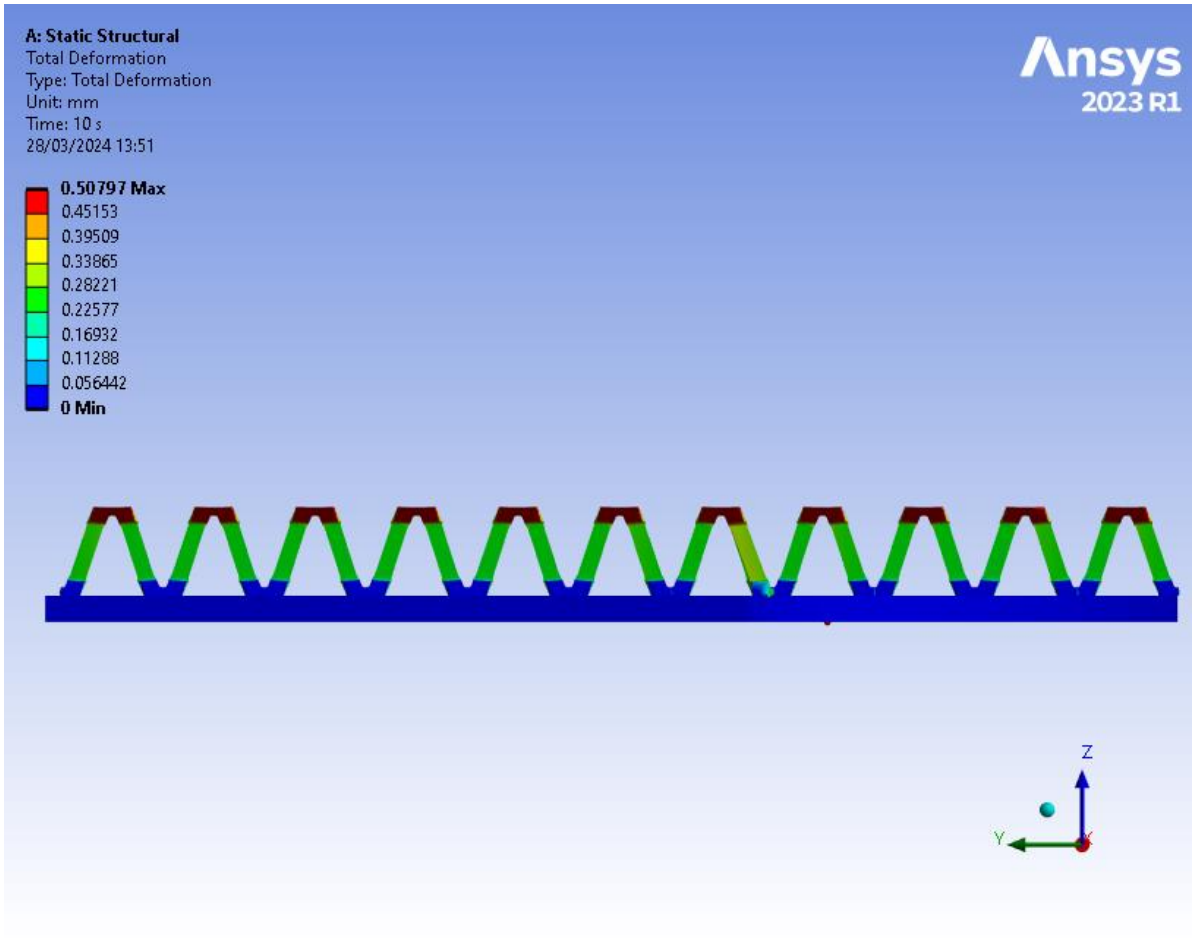

Figure 7.36 Total deformation contour map: I-type 12% – side view

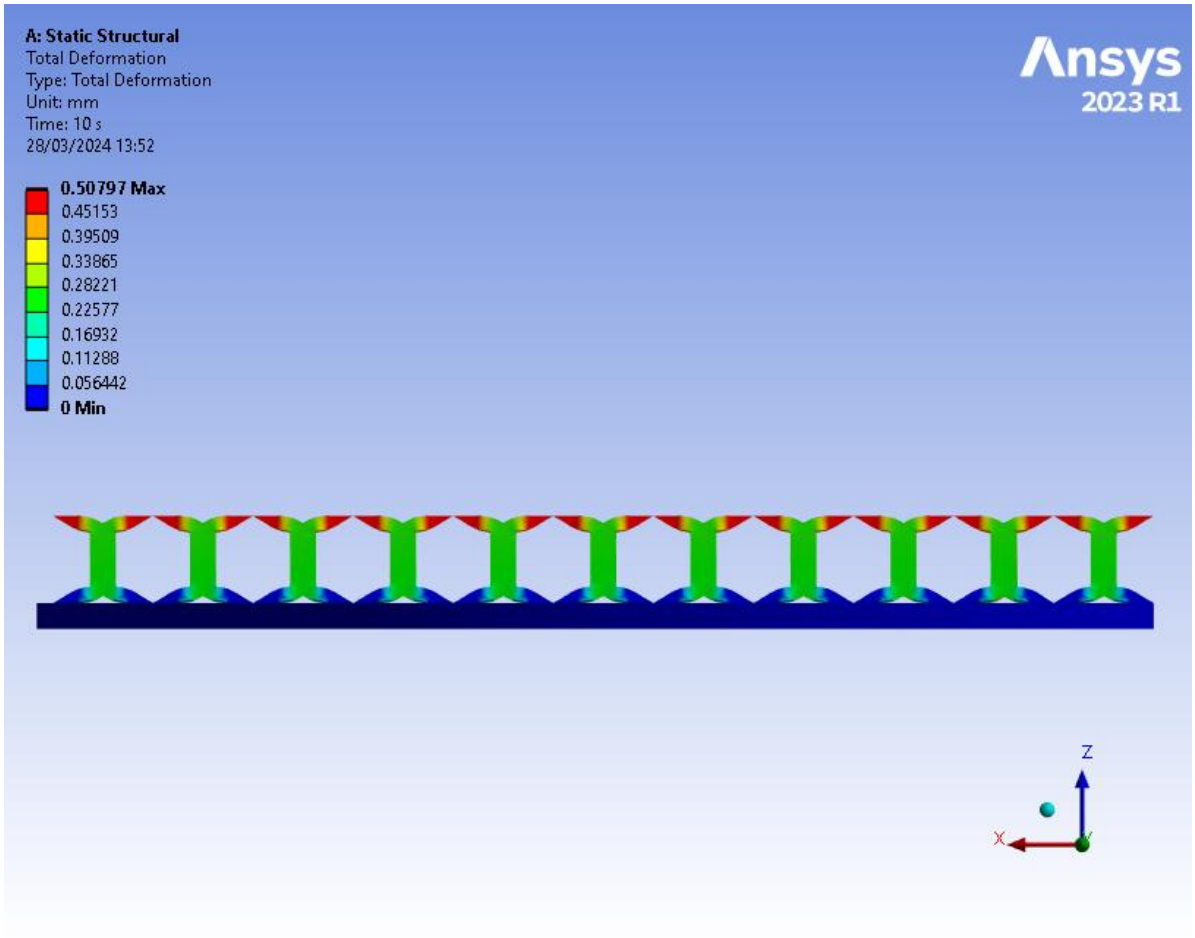

Figure 7.37 Total deformation contour map: I-type 12% – side view

The analysis of *Figures 7.35, 7.36, and 7.37* reveals a consistent concentration of the highest deformation predominantly within the upper struts, which corresponds to the anticipated primary displacement zone. The deformation values observed in this region start at approximately 0.34mm and quickly escalate to a range between 0.45mm and 0.5mm over a short distance. In contrast, the central struts display significantly less deformation, averaging around 0.25mm, indicating a comparatively stable structural configuration. Moreover, the lower struts demonstrate minimal deformation, in most of their volume, with maximum deformation reaching up to 0.15mm near the fillets. This pattern suggests a well-distributed load-bearing capacity across the lattice structure, with the upper struts absorbing the majority of the deformation due to the applied load while maintaining stability and structural integrity.

Displayed in *Table 7.11* are meticulous records of the minimum, maximum, and average deformation values witnessed during the specified time span. This dataset serves as a treasure trove of insights into the structural dynamics, enabling the discernment of recurring patterns and evolving trends in deformation responses. Delving into this table with precision allows us to pinpoint the average deformation linked to the initial displacement, thus enriching our understanding of the structural behavior and response mechanisms over time. Upon closer examination, it becomes evident that the maximum and average deformation measures stand at 0.508mm and 0.253mm respectively, providing clarity on the extent of structural deformation across different scenarios.

Graphs are showcased in *Figure 7.11.*

Table 7.11 Deformation Data – I-type 12%

t(s)	Min Deformation (m)	Max Deformation(m)	Avg Deformation (m)
0.2	0	1.0295e-005	5.0161e-006
0.4	0	2.0807e-005	1.0097e-005
0.7	0	3.5881e-005	1.7914e-005
1.	0	5.0773e-005	2.5658e-005
1.2	0	6.0793e-005	3.0774e-005
1.4	0	7.0851e-005	3.5866e-005
1.7	0	8.5983e-005	4.3473e-005
2.	0	1.0114e-004	5.1061e-005
2.2	0	1.1125e-004	5.6113e-005
2.4	0	1.2137e-004	6.1164e-005
2.7	0	1.3655e-004	6.8734e-005
3.	0	1.5175e-004	7.6299e-005
3.2	0	1.6189e-004	8.1342e-005
3.4	0	1.7203e-004	8.6383e-005
3.7	0	1.8726e-004	9.3944e-005
4.	0	2.0249e-004	1.015e-004
4.2	0	2.1264e-004	1.0654e-004
4.4	0	2.228e-004	1.1158e-004
4.7	0	2.3804e-004	1.1914e-004
5.	0	2.5329e-004	1.267e-004
5.2	0	2.6346e-004	1.3174e-004
5.4	0	2.7363e-004	1.3677e-004
5.7	0	2.8889e-004	1.4433e-004
6.	0	3.0415e-004	1.5189e-004
6.2	0	3.1433e-004	1.5693e-004
6.4	0	3.2451e-004	1.6196e-004

6.7	0	3.3978e-004	1.6952e-004
7.	0	3.5506e-004	1.7708e-004
7.2	0	3.6524e-004	1.8211e-004
7.4	0	3.7543e-004	1.8715e-004
7.7	0	3.9071e-004	1.9471e-004
8.	0	4.06e-004	2.0226e-004
8.2	0	4.1619e-004	2.073e-004
8.4	0	4.2638e-004	2.1234e-004
8.7	0	4.4168e-004	2.1989e-004
9.	0	4.5697e-004	2.2745e-004
9.2	0	4.6717e-004	2.3249e-004
9.4	0	4.7737e-004	2.3753e-004
9.7	0	4.9267e-004	2.4508e-004
10	0	5.0797e-004	2.5264e-004

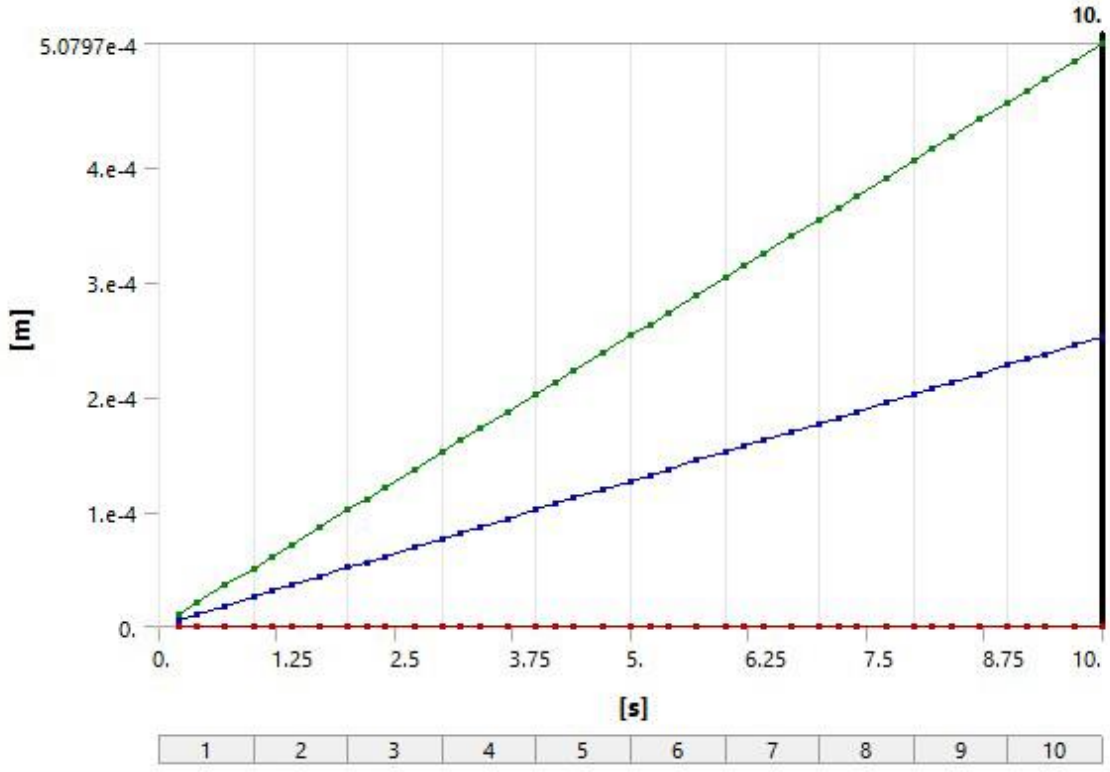

Figure 7.38 Deformation Profiles: I-type 12%

7.3.2 Equivalent elastic strain

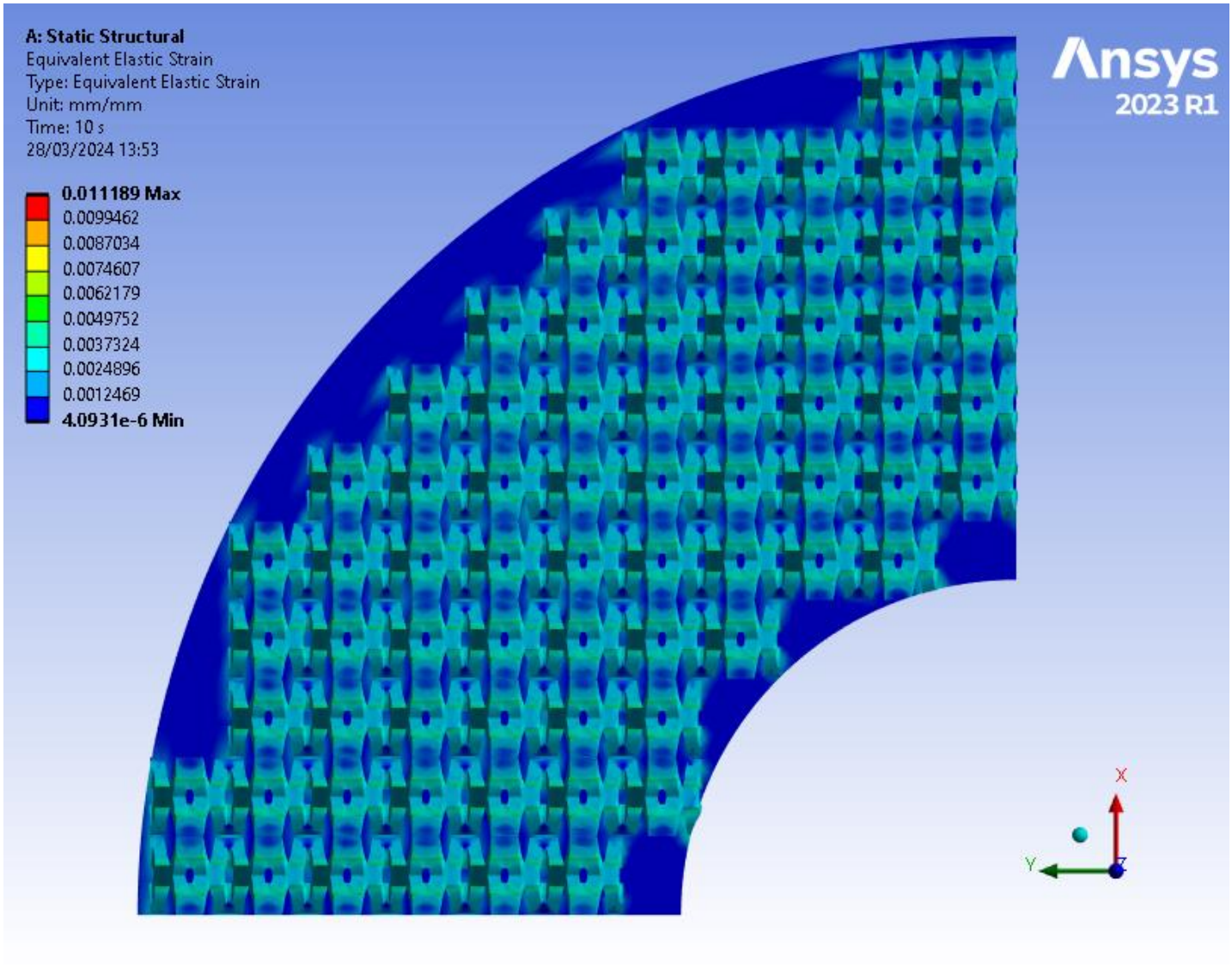

Figure 7.39 Equivalent Elastic Strain contour map: I-type 12% – top view

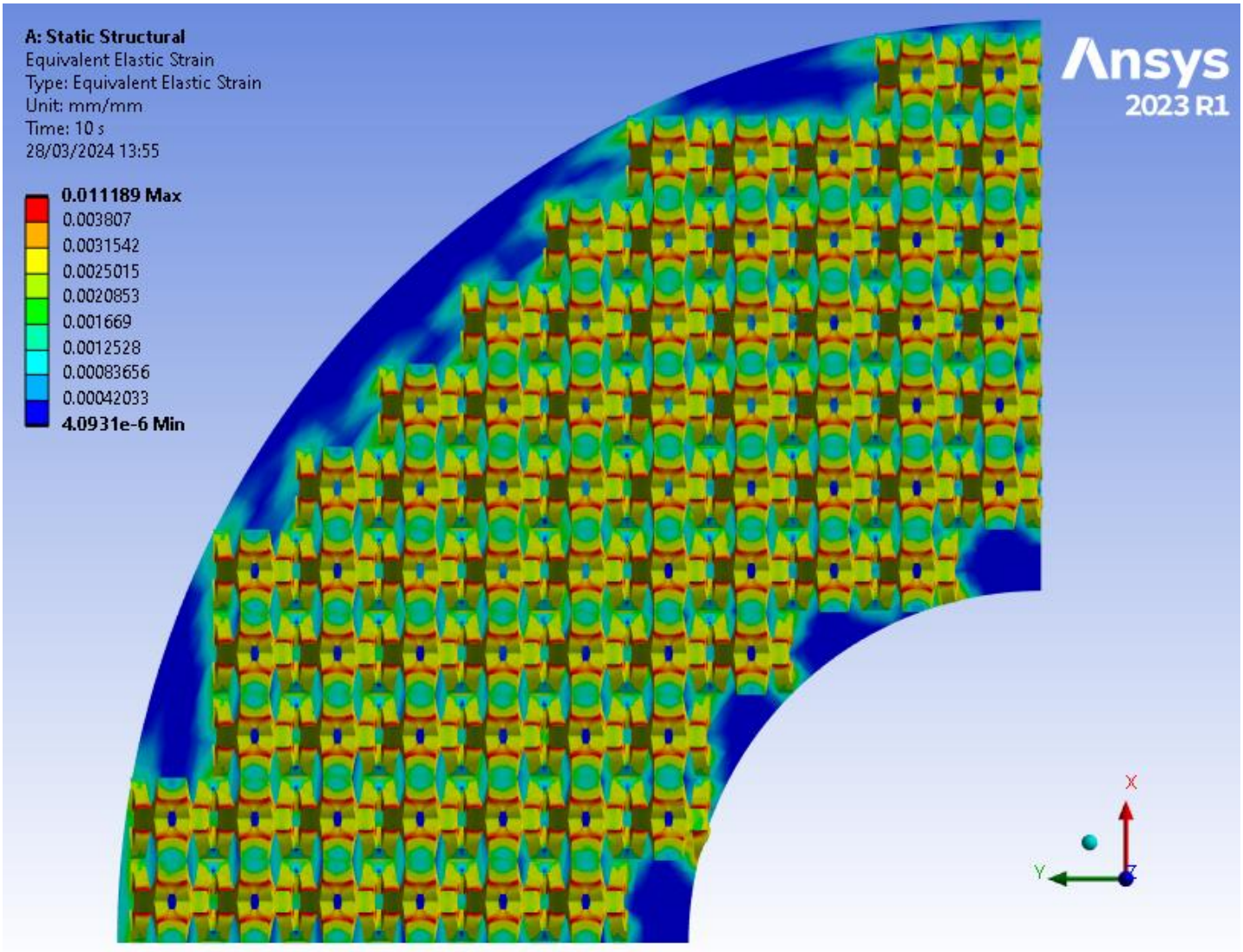

Figure 7.40 Equivalent Elastic Strain filtered contour map: I-type 12% – top view

Figure 7.39 illustrates a localized region of heightened strain energy equal to 0.011mm/mm in the area of an incomplete node. For the rest of the lattice, it is visible that strain energy reaches up to 0.004mm/mm in the top contact points. Subsequently, *Figure 7.40* provides a refined depiction, enhancing the clarity of the elastic strain phenomenon, showing elastic strains up to 0.0031mm/mm for the higher struts and up to 0.0017mm/mm for the central struts. This improved visualization aids in understanding the spatial distribution and magnitude of elastic strain within the model, highlighting a consistent and uniform distribution along the surface of the plate. Unlike the BCC design, the outer regions do not demonstrate any pronounced increase in elastic strain, because of the geometry of the unit cells.

Table 7.12 presents a detailed compilation of the minimum, maximum, and average elastic strain values observed throughout the designated time interval. This dataset offers invaluable insights into the structural behavior, enabling us to identify recurring patterns and evolving trend. Through a meticulous examination of this table, we gain the ability to precisely identify the average elastic strain corresponding to the initial displacement, thereby enhancing our comprehension of the structural dynamics and response mechanisms over time. Specifically, upon scrutiny, we observe that the maximum and average deformation recorded stand at 0.011mm and 0.003mm respectively, shedding light on the extent of structural deformation under varying conditions.

Graphs are showcased in *Figure 7.41.*

Table 7.12 Elastic Strain Data – I-type 12 %

t(s)	Min Elastic Strain (m/m)	Max Elastic Strain (m/m)	Average Elastic Strain (m/m)
0.2	1.253e-006	0.0029514	0.0010218
0.4	2.0756e-006	0.0030805	0.0016117
0.7	1.9944e-006	0.0034011	0.0018473
1.	1.9571e-006	0.00391	0.0019538
1.2	1.9478e-006	0.0042257	0.0019997
1.4	1.9458e-006	0.0045253	0.0020341
1.7	1.9536e-006	0.0049427	0.0020743
2.	1.97e-006	0.005321	0.0021072
2.2	1.9847e-006	0.0055542	0.0021268
2.4	2.0105e-006	0.005777	0.0021452
2.7	2.0831e-006	0.0060876	0.0021717
3.	2.1544e-006	0.0063771	0.002197
3.2	2.1976e-006	0.0065615	0.0022131
3.4	2.2522e-006	0.006739	0.0022289
3.7	2.3393e-006	0.006993	0.0022517
4.	2.4294e-006	0.0072365	0.0022737
4.2	2.491e-006	0.0073941	0.0022882
4.4	2.5546e-006	0.0075483	0.0023023
4.7	2.6524e-006	0.0077733	0.0023232
5.	2.756e-006	0.0079927	0.0023435
5.2	2.8211e-006	0.0081365	0.0023567
5.4	2.9022e-006	0.008279	0.00237
5.7	3.0195e-006	0.0084886	0.0023895
6.	3.1415e-006	0.0086943	0.0024087
6.2	3.2101e-006	0.0088295	0.0024211

6.4	3.3047e-006	0.0089638	0.0024337
6.7	3.4327e-006	0.0091622	0.0024523
7.	3.5586e-006	0.0093577	0.0024705
7.2	3.6244e-006	0.0094865	0.0024824
7.4	3.7211e-006	0.0096147	0.0024945
7.7	3.7686e-006	0.0098046	0.0025123
8.	3.8018e-006	0.0099921	0.00253
8.2	3.8259e-006	0.010116	0.0025415
8.4	3.8498e-006	0.010239	0.0025531
8.7	3.8862e-006	0.010422	0.0025702
9.	3.9254e-006	0.010603	0.0025871
9.2	3.9539e-006	0.010723	0.0025981
9.4	3.9843e-006	0.010841	0.0026093
9.7	4.0339e-006	0.011016	0.0026257
10	4.0931e-006	0.011189	0.0026419

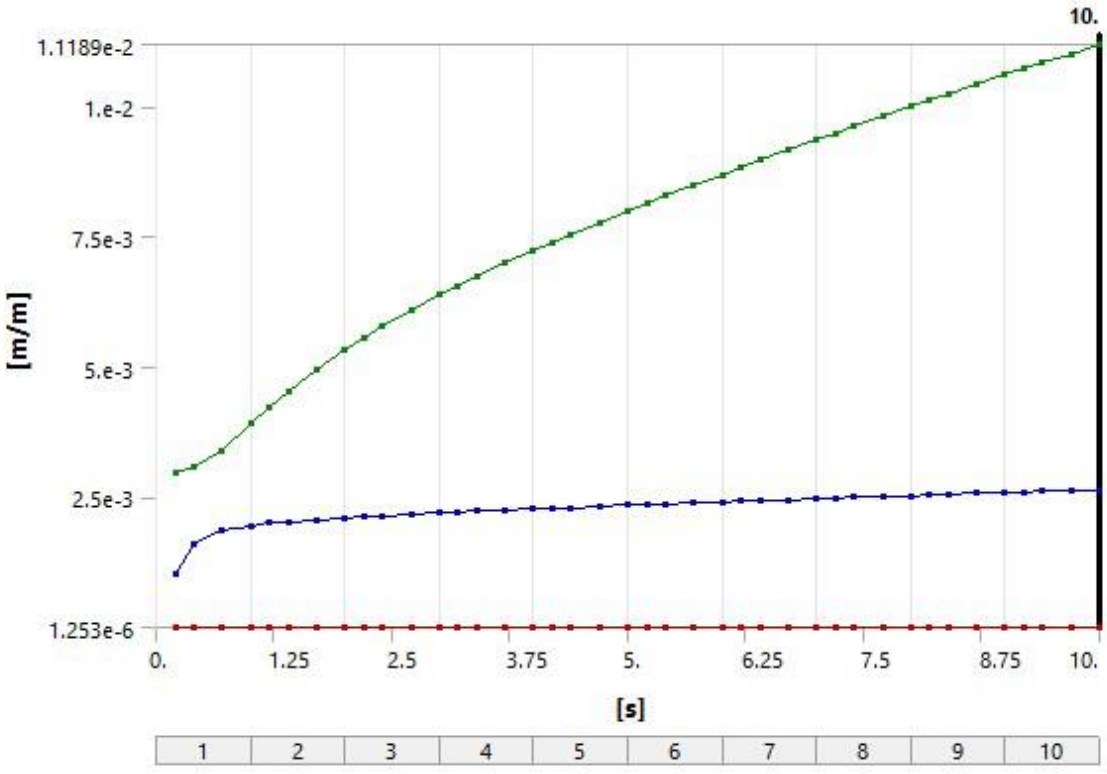

Figure 7.41 Elastic Strain Profiles: I-type 12%

7.3.3 Equivalent stress

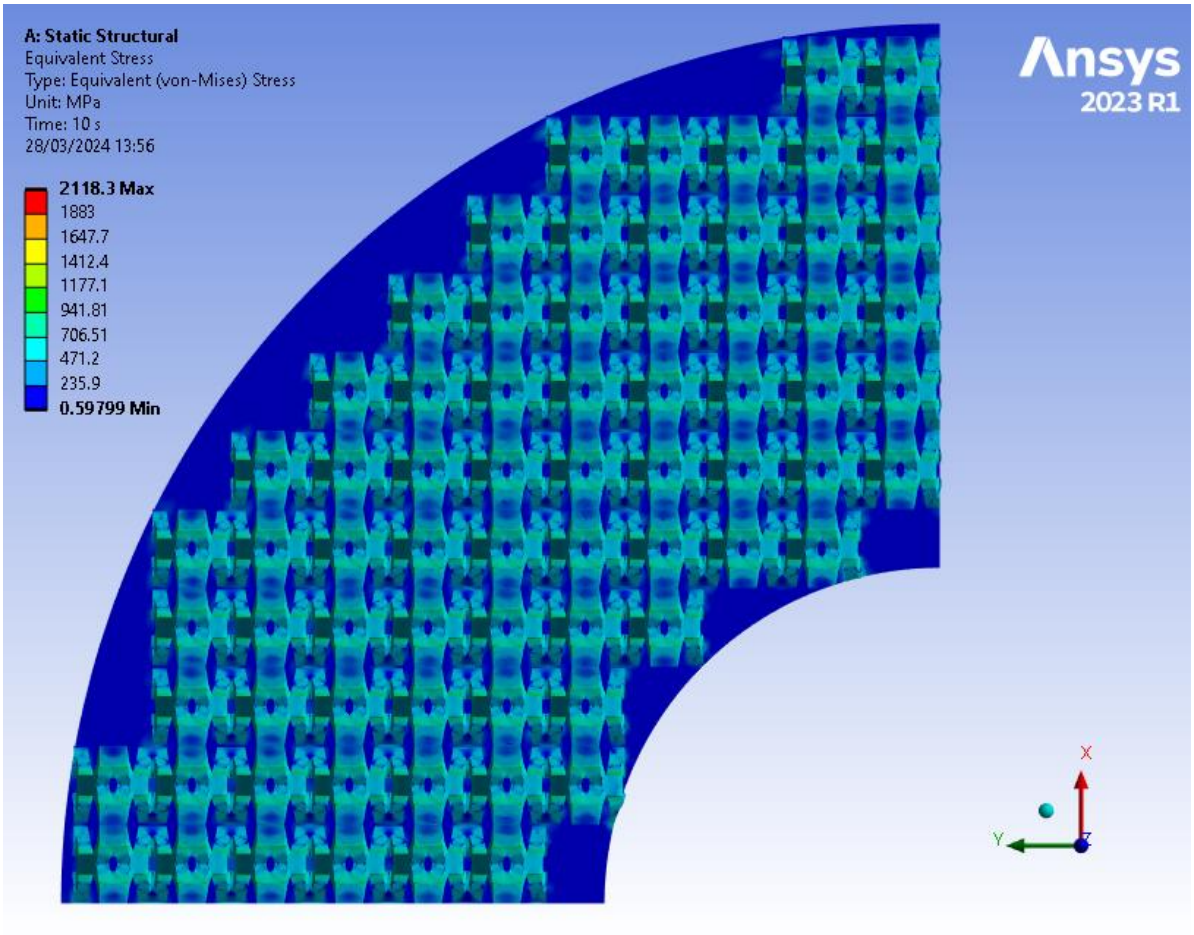

Figure 7.42 Equivalent Stress (von-Mises) contour map: I-type 12% – top view

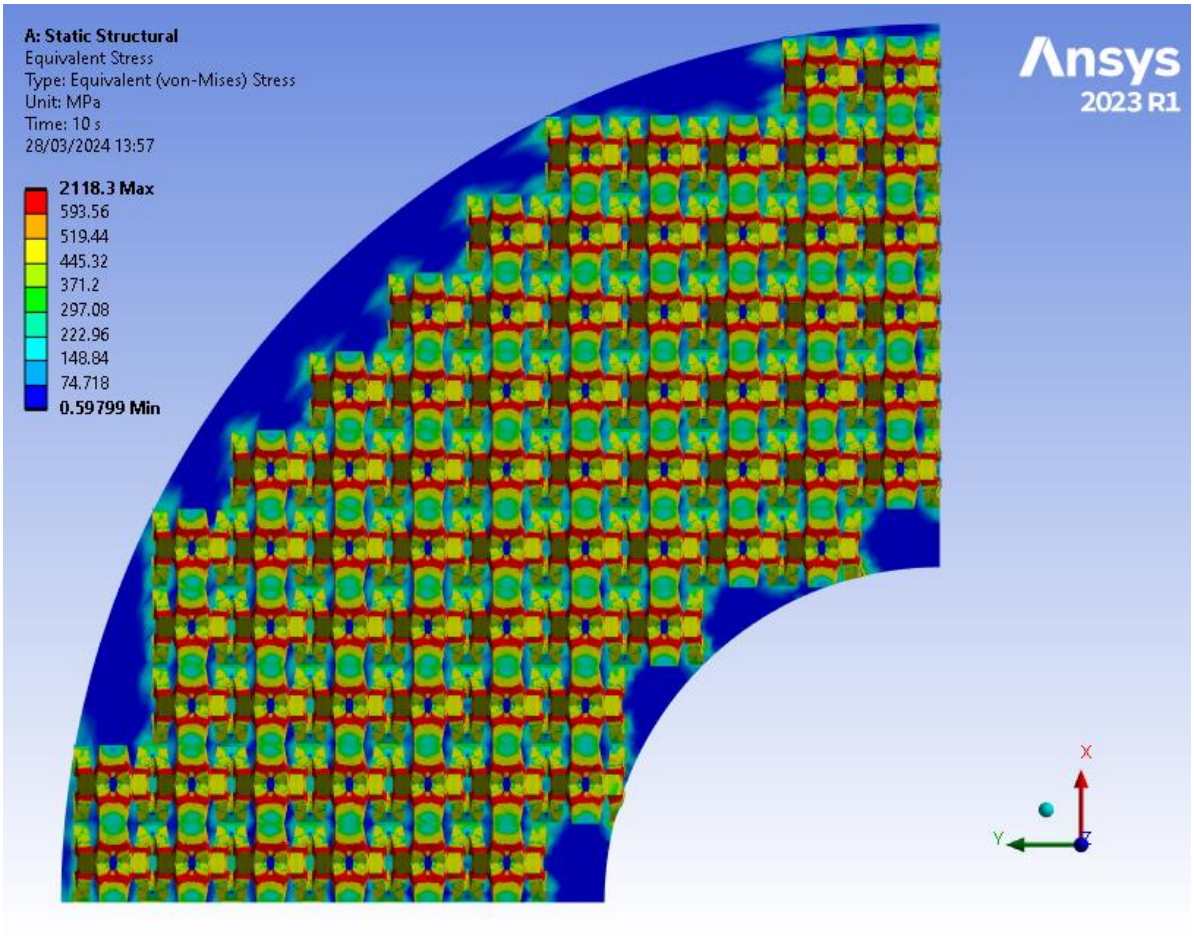

Figure 7.43 Equivalent (von-Mises) Stress filtered contour map: I-type 12% – top view

Upon initial examination of *Figure 7.42*, it's evident that the stresses on the lattice do not pose any risk of failure. To enhance clarity, filtering techniques were applied to the legend, resulting in refined representations depicted in *Figure 7.43*. Upon closer scrutiny, it's apparent that the primary stress concentration zones are the higher struts, exhibiting stresses ranging from 600MPa, near the top to 400MPa, near the central strut, showcasing good uniformity. Central struts show stress around 300MPa, while the lower ones demonstrate null stress. The lower contact areas of the lattice with the disk can experience stresses up to 300MPa. Additionally, areas with incomplete nodes display higher stresses, consistent with expectations.

Table 7.13 offers a comprehensive overview of the minimum, maximum, and average stress values recorded over the designated time period. This data provides invaluable insights into the structural behavior, allowing us to discern patterns and trends in deformation responses. By analyzing this table, we can pinpoint the average and maximum stress that corresponds to the initial displacement, facilitating a deeper understanding

of the structural dynamics and response mechanisms over time. Specifically, upon scrutiny, we observe that the maximum and average stress recorded stand at 2118.3MPa and 491.1MPa, respectively.

Graphs are showcased in *Figure 7.44.*

Table 7.13 Stress Data – I-type 12%

t(s)	Min Stress (Pa)	Max Stress (Pa)	Average Stress (Pa)
0.2	1.9493e+005	5.7183e+008	1.9513e+008
0.4	3.2167e+005	5.9061e+008	3.0619e+008
0.7	3.6525e+005	6.5078e+008	3.4731e+008
1.	3.7704e+005	7.4519e+008	3.6505e+008
1.2	3.7962e+005	8.0419e+008	3.7278e+008
1.4	3.7923e+005	8.6023e+008	3.7862e+008
1.7	3.8075e+005	9.3864e+008	3.8554e+008
2.	3.8396e+005	1.0099e+009	3.9129e+008
2.2	3.8682e+005	1.054e+009	3.9476e+008
2.4	3.9186e+005	1.096e+009	3.9803e+008
2.7	4.06e+005	1.1546e+009	4.0275e+008
3.	4.199e+005	1.2092e+009	4.0727e+008
3.2	4.2832e+005	1.2439e+009	4.1017e+008
3.4	4.3588e+005	1.2775e+009	4.1306e+008
3.7	4.4409e+005	1.3254e+009	4.1721e+008
4.	4.5244e+005	1.3713e+009	4.2127e+008
4.2	4.5804e+005	1.4011e+009	4.2393e+008
4.4	4.6367e+005	1.4302e+009	4.2655e+008
4.7	4.7216e+005	1.4727e+009	4.3043e+008
5.	4.8076e+005	1.5142e+009	4.3424e+008
5.2	4.8625e+005	1.5413e+009	4.367e+008
5.4	4.9229e+005	1.5684e+009	4.3922e+008
5.7	5.0095e+005	1.6079e+009	4.4289e+008
6.	5.0959e+005	1.6468e+009	4.4651e+008
6.2	5.1487e+005	1.6722e+009	4.4886e+008
6.4	5.2086e+005	1.6977e+009	4.5127e+008
6.7	5.2952e+005	1.7352e+009	4.5479e+008
7.	5.3762e+005	1.7721e+009	4.5827e+008
7.2	5.4161e+005	1.7964e+009	4.6053e+008

7.4	5.464e+005	1.8207e+009	4.6285e+008
7.7	5.5323e+005	1.8566e+009	4.6626e+008
8.	5.5979e+005	1.8921e+009	4.6964e+008
8.2	5.6356e+005	1.9154e+009	4.7182e+008
8.4	5.6801e+005	1.9387e+009	4.7407e+008
8.7	5.7443e+005	1.9734e+009	4.7735e+008
9.	5.8076e+005	2.0076e+009	4.8059e+008
9.2	5.8476e+005	2.0302e+009	4.8269e+008
9.4	5.8915e+005	2.0525e+009	4.8485e+008
9.7	5.9485e+005	2.0857e+009	4.8801e+008
10	5.9799e+005	2.1183e+009	4.9113e+008

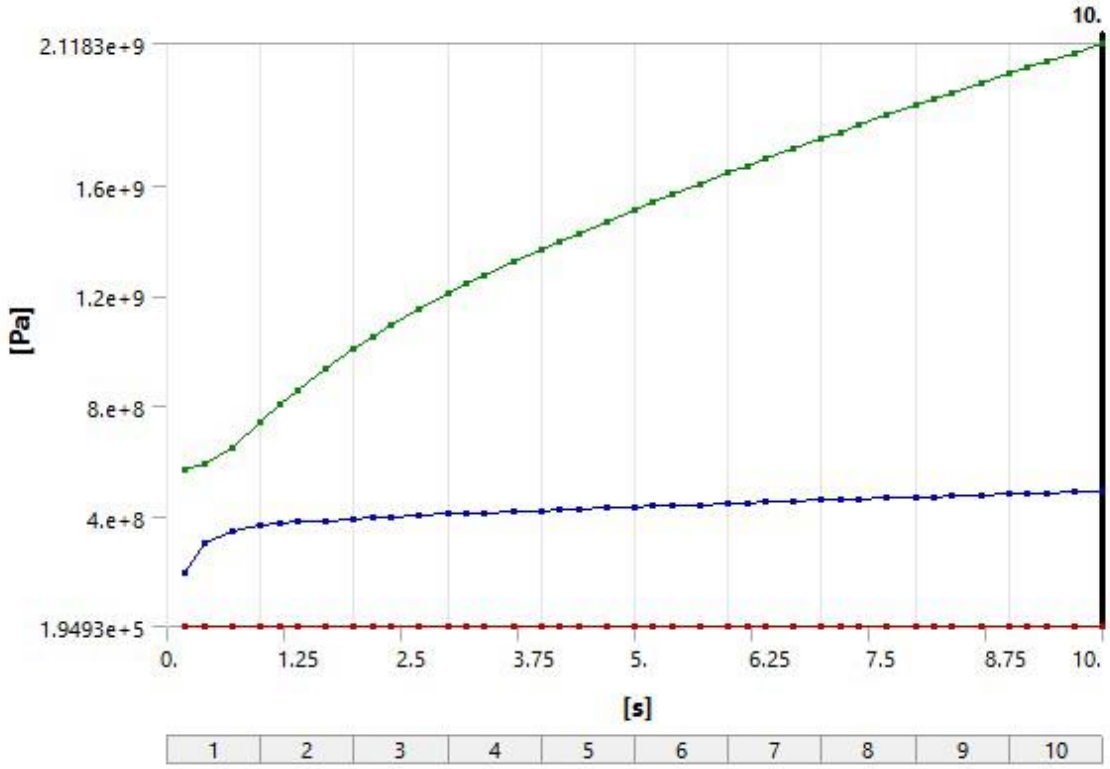

Figure 7.44 Equivalent (Von Mises) Stress Profiles: I-type 12%

7.3.4 Strain energy

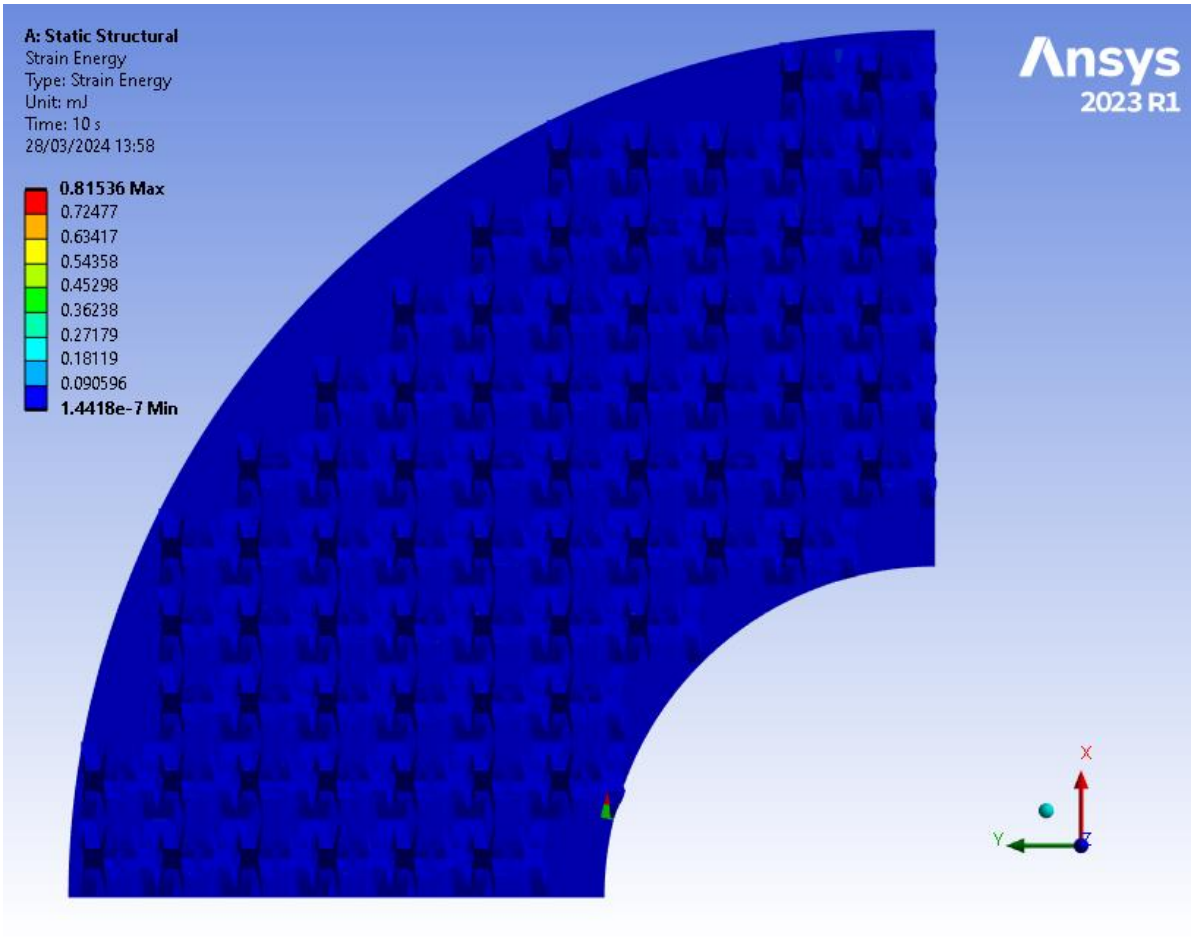

Figure 7.45 Strain Energy contour map: I-type 12% – top view

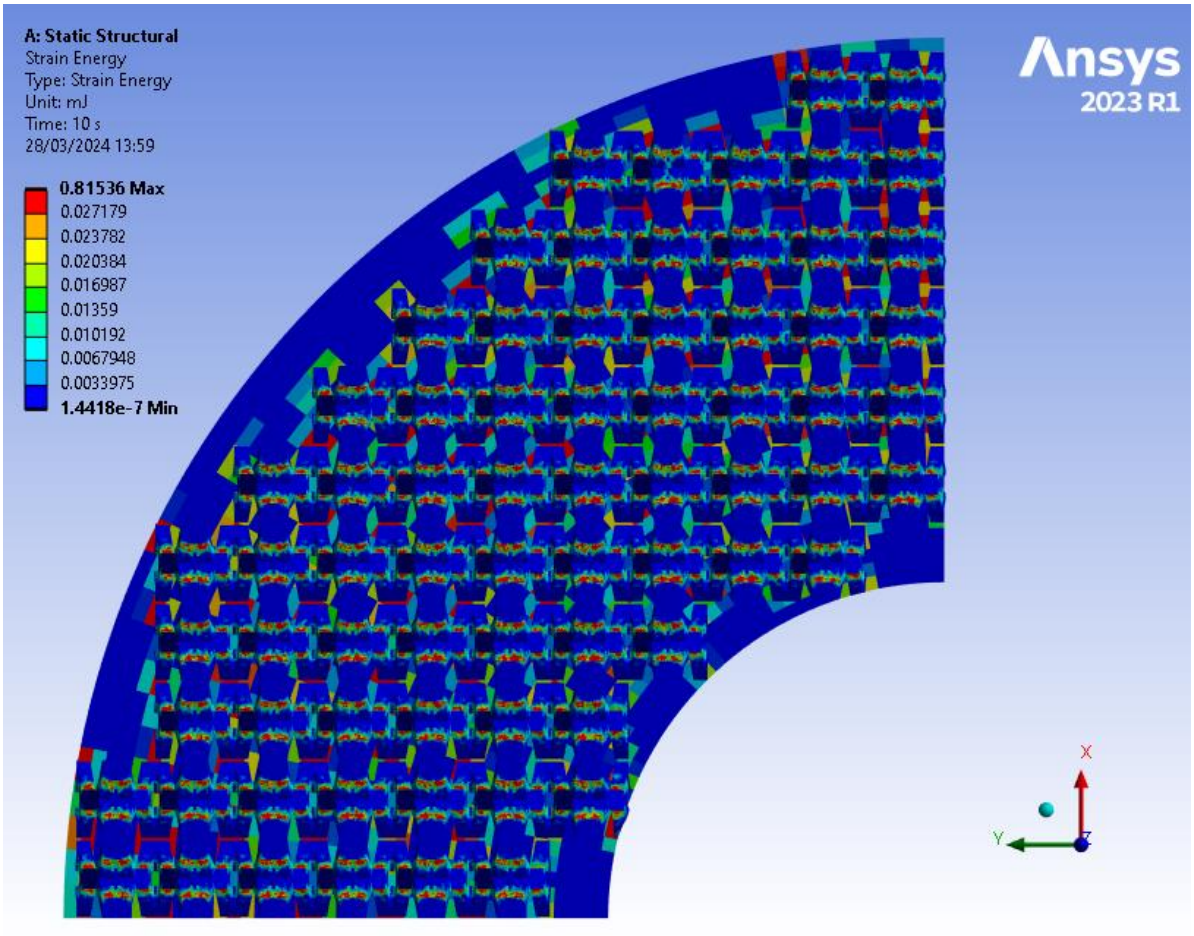

Figure 7.46 Strain Energy filtered contour map: I-type 12% – top view

In *Figure 7.46* presented above, it's evident that the distribution of strain energy across the area follows a symmetrical pattern, showcasing impressive uniformity along the surface, with values reaching up to 0.27 mJ. Additionally, in *Figure 7.47*, a small area stands out with strain energy equal to 0.81 mJ, attributed to a cut node. This localized region of heightened strain energy is notable within an otherwise uniformly distributed pattern, emphasizing the impact of structural irregularities on strain energy distribution

Within *Table 7.14*, a comprehensive array of data unveils the minimum, maximum, and total strain energy values documented throughout the designated timeframe. This dataset acts as a reservoir of knowledge, offering valuable glimpses into the intricacies of structural behavior and the evolving nature of deformation responses. By meticulously analyzing this table, we can zero in on the total strain energy associated with the initial displacement, thereby deepening our comprehension of structural dynamics and response mechanisms over time. Notably, upon careful review, we note that the maximum and total strain energy readings reach

0.81mJ and 15654mJ respectively, offering valuable insights into the magnitude of structural deformation under various conditions.

Graphs are showcased in *Figure 7.47.*

Table 7.14 Strain energy – I-type 12%

t(s)	Min Strain Energy (J)	Max Strain Energy (J)	Total Strain Energy (J)
0.2	3.7263e-012	1.4509e-005	8.1342e-002
0.4	2.5187e-011	3.3865e-005	0.29326
0.7	3.5008e-011	4.2263e-005	0.68041
1.	5.3858e-011	6.019e-005	1.083
1.2	3.5953e-011	7.3477e-005	1.3562
1.4	2.8319e-011	8.5841e-005	1.6326
1.7	2.7324e-011	1.0349e-004	2.0524
2.	3.1158e-011	1.2359e-004	2.4781
2.2	3.4598e-011	1.3626e-004	2.765
2.4	3.8348e-011	1.4874e-004	3.0544
2.7	4.3931e-011	1.6662e-004	3.4929
3.	4.9369e-011	1.8372e-004	3.9367
3.2	5.2901e-011	1.9485e-004	4.2354
3.4	5.6553e-011	2.0569e-004	4.5364
3.7	6.2218e-011	2.2258e-004	4.9921
4.	6.8503e-011	2.3998e-004	5.4527
4.2	7.295e-011	2.5309e-004	5.7626
4.4	7.779e-011	2.6634e-004	6.0747
4.7	8.5724e-011	2.8715e-004	6.5468
5.	9.4707e-011	3.094e-004	7.0238
5.2	1.0103e-010	3.2439e-004	7.3444
5.4	1.085e-010	3.3957e-004	7.6672
5.7	1.2065e-010	3.6267e-004	8.1553
6.	1.3433e-010	3.87e-004	8.6481
6.2	1.4358e-010	4.0404e-004	8.9793
6.4	1.5533e-010	4.2128e-004	9.3125
6.7	1.736e-010	4.4761e-004	9.8161
7.	1.7911e-010	4.7584e-004	10.324
7.2	1.754e-010	4.9532e-004	10.666
7.4	1.7239e-010	5.1511e-004	11.009
7.7	1.6952e-010	5.454e-004	11.528

8.	1.693e-010	5.7667e-004	12.051
8.2	1.7064e-010	5.9788e-004	12.403
8.4	1.7339e-010	6.1936e-004	12.756
8.7	1.6728e-010	6.5283e-004	13.29
9.	1.5345e-010	6.8714e-004	13.828
9.2	1.4702e-010	7.1045e-004	14.189
9.4	1.424e-010	7.3542e-004	14.553
9.7	1.4006e-010	7.7445e-004	15.101
10	1.4418e-010	8.1536e-004	15.654

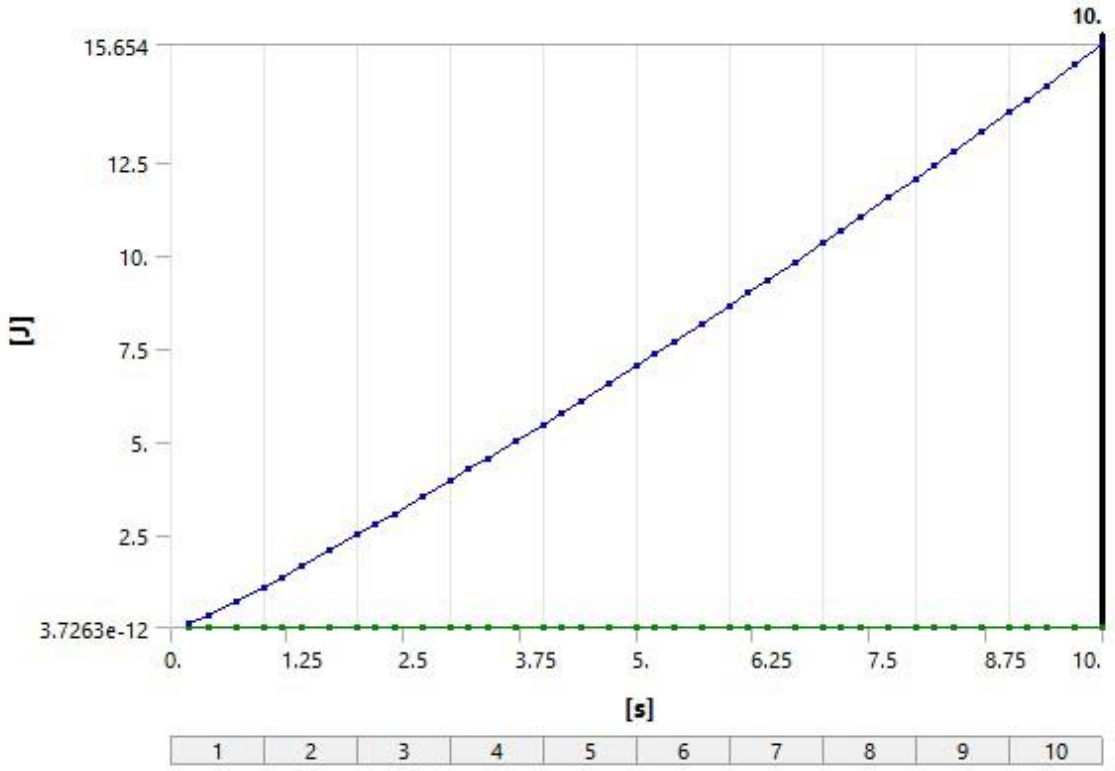

Figure 7.47 Strain Energy Profiles: I-type 12%

7.3.5 Force reaction

Table 7.15 provides a visual representation of the force (F) exerted over a period of time (t), where negative values indicate compressive force. As time advances, there's a gradual increase in the compressive force magnitude, up to 37034N indicating a continuous application of pressure. This suggests an ongoing deformation or compression process within the material or structure under examination. The consistent trend

observed underscores the uniformity and stability of the applied force throughout the specified time interval. Further investigation may involve establishing correlations between these force values and specific mechanical responses or structural behaviors. Correspondingly, *Figure 7.48* presents a graphical depiction illustrating the force reaction pattern across the temporal domain.

Table 7.15 Force reaction – I-type 12%

t(s)	F(N)
0.2	-16524
0.4	-24748
0.7	-26551
1.	-27199
1.2	-27530
1.4	-27824
1.7	-28229
2.	-28609
2.2	-28854
2.4	-29094
2.7	-29447
3.	-29793
3.2	-30022
3.4	-30248
3.7	-30583
4.	-30914
4.2	-31134
4.4	-31351
4.7	-31675
5.	-31996
5.2	-32210
5.4	-32420
5.7	-32735
6.	-33048
6.2	-33256
6.4	-33461
6.7	-33769
7.	-34075
7.2	-34279
7.4	-34479
7.7	-34780

8.	-35080
8.2	-35280
8.4	-35477
8.7	-35772
9.	-36066
9.2	-36262
9.4	-36455
9.7	-36746
10	-37034

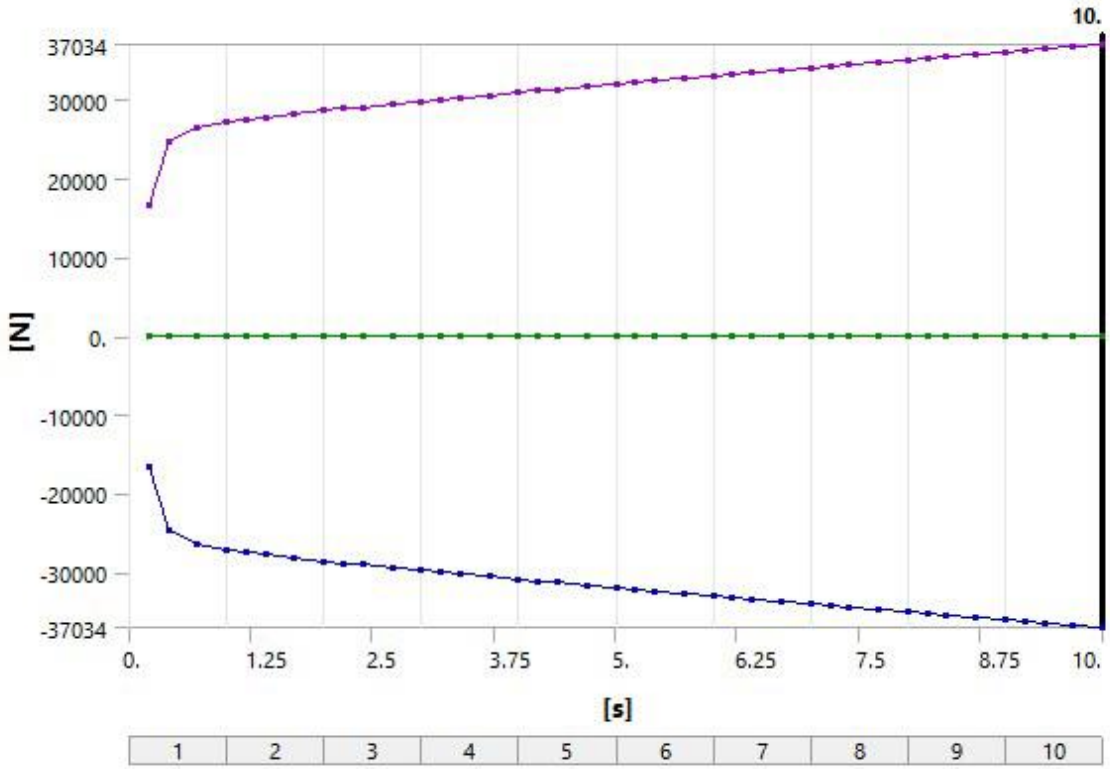

Figure 7.48 Force Reaction Profiles: I-type 12%

The provided data presents force (F) values corresponding to different time intervals (t). The force values remain negative. As time progresses from 0.2 seconds to 10 seconds, the force values exhibit a consistent increase in magnitude, starting from -16524 N and reaching 37034 N at the end of the observation period. This dataset likely represents a force-time relationship or a force response under certain conditions, providing insights into the behavior of the system being studied over time.

7.4 I-type 30%

7.4.1 Total deformation

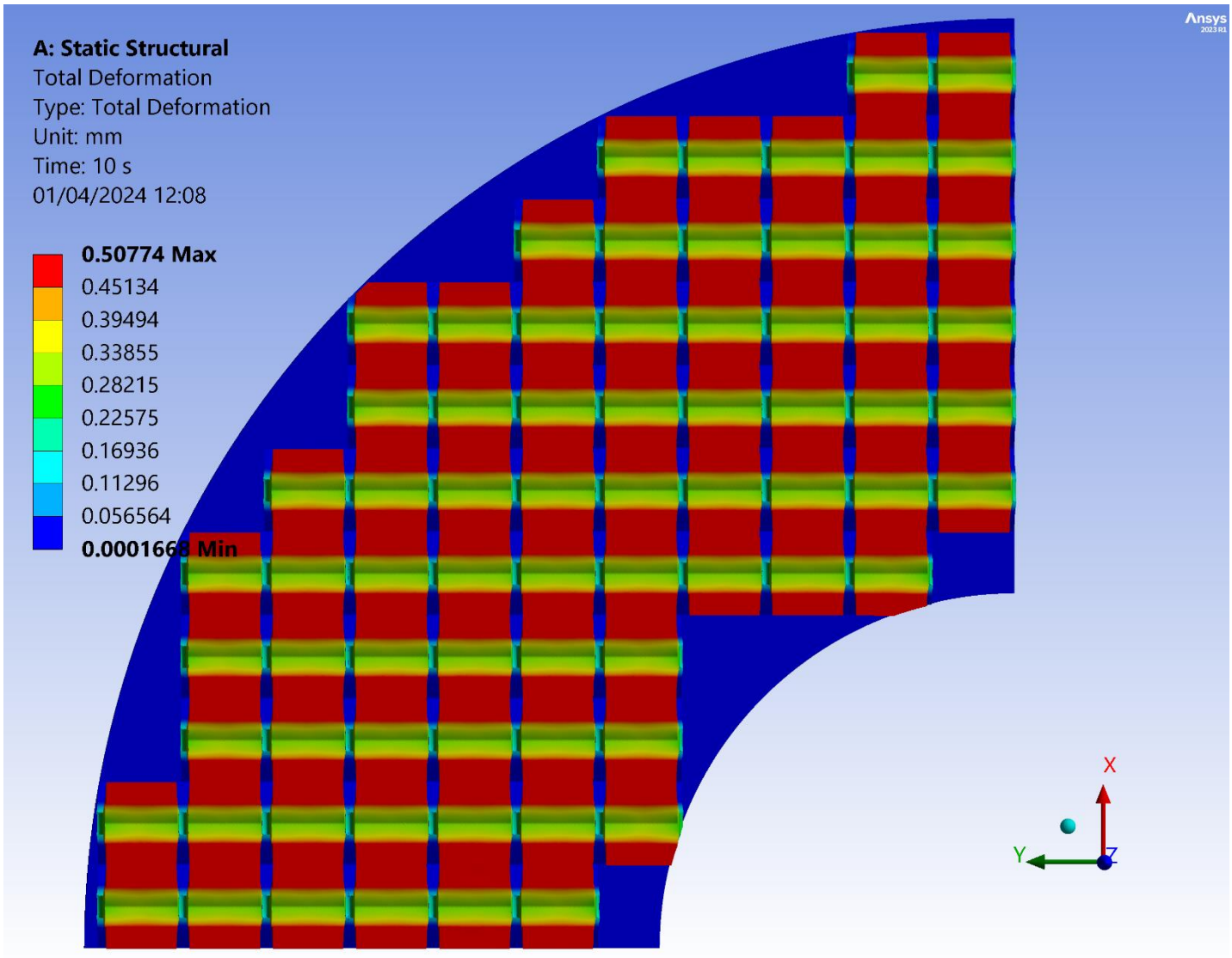

Figure 7.50 Total deformation contour map: I-type 30% – top view (No plate)

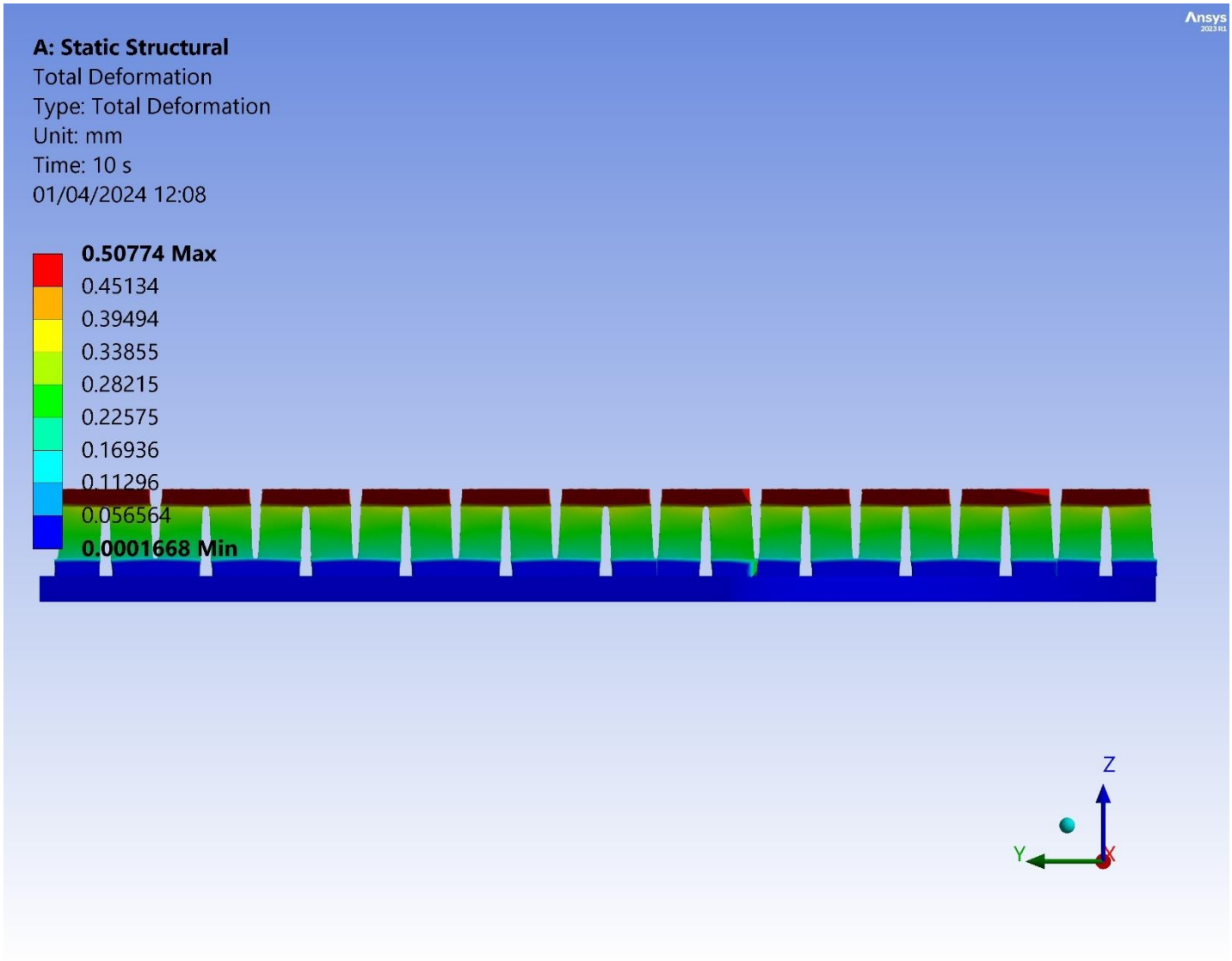

Figure 7.51 Total deformation contour map: I-type 30% – side view

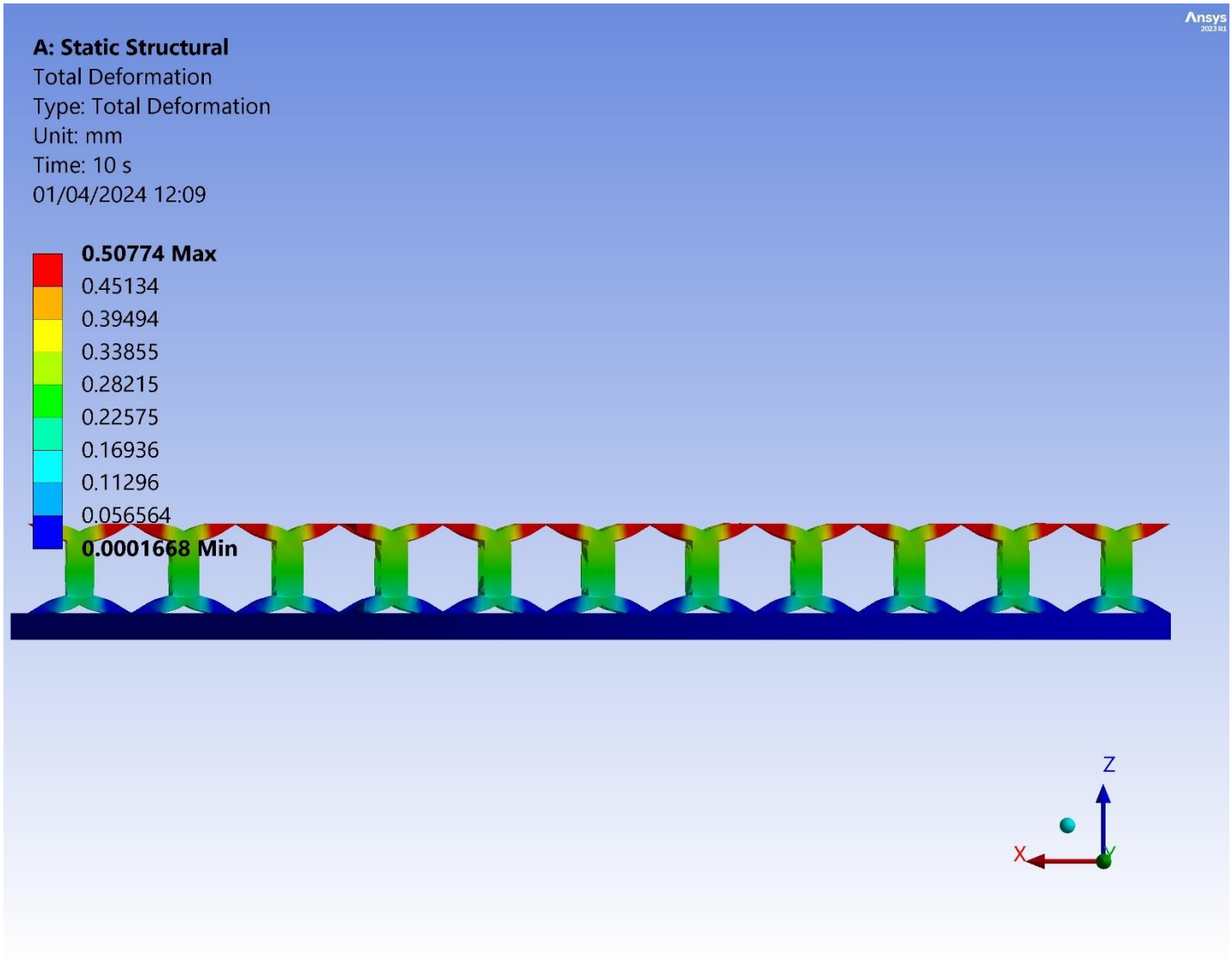

Figure 7.52 Total deformation contour map: I-type 30% – side view

The results obtained from the *Figures 7.49-7.52*, for the I-type 30% configuration align closely with the anticipated outcomes observed in the patterns of the I-type 12% configuration. Notably, the highest deformations are consistently observed in the upper struts of the lattice, ranging from 0.5mm to 0.4mm for the most of their volume. Near the fillets deformation reaches up to 0.35mm. In contrast, the central strut exhibits a relatively stable displacement of approximately 0.25mm, while the lower struts experience minimal deformation, typically less than 0.15mm. This consistent distribution of deformations suggests an effective distribution of load-bearing capacity throughout the lattice structure. Specifically, the upper struts bear the brunt of the applied load, highlighting their crucial role in maintaining stability and structural integrity, mirroring the behavior observed in the I-type 12% density design.

Within *Table 7.1*, a comprehensive array of data unveils the minimum, maximum, and average deformation values documented throughout the designated timeframe. This dataset acts as a reservoir of knowledge, offering valuable glimpses into the intricacies of structural behavior and the evolving nature of deformation responses. By meticulously analyzing this table, we can zero in on the average deformation associated with the initial displacement, thereby deepening our comprehension of structural dynamics and response mechanisms over time. Notably, upon careful review, we note that the maximum and average deformation readings reach 0.508mm and 0.250mm respectively, offering valuable insights into the magnitude of structural deformation under various conditions.

Table 7.16 Deformation Data – I-type 30%

t(s)	Min Deformation (mm)	Max Deformation (mm)	Avg Deformation (mm)
0.2	2.18E-04	1.28E-02	6.63E-03
0.4	1.77E-04	2.21E-02	1.16E-02
0.7	3.96E-05	3.67E-02	1.89E-02
1	8.72E-05	5.16E-02	2.63E-02
1.2	4.76E-05	6.16E-02	3.13E-02
1.4	5.09E-05	7.17E-02	3.63E-02
1.7	9.02E-05	8.69E-02	4.37E-02
2	7.89E-05	0.10208	5.12E-02
2.2	6.38E-05	0.11223	5.62E-02
2.4	7.95E-05	0.12238	6.12E-02
2.7	2.99E-05	0.13759	6.86E-02
3	3.17E-05	0.1528	7.61E-02
3.2	1.73E-05	0.16292	8.10E-02
3.4	8.36E-05	0.17305	8.60E-02
3.7	5.62E-05	0.18824	9.34E-02
4	1.06E-05	0.20343	0.10088
4.2	5.65E-05	0.21356	0.10584
4.4	5.31E-05	0.22369	0.11081
4.7	1.03E-04	0.2389	0.11826
5	1.07E-04	0.2541	0.12571
5.2	1.25E-04	0.26424	0.13068
5.4	1.34E-04	0.27438	0.13565

5.7	1.05E-04	0.28959	0.1431
6	9.58E-05	0.3048	0.15056
6.2	9.52E-05	0.31494	0.15553
6.4	1.06E-04	0.32508	0.16051
6.7	1.04E-04	0.3403	0.16797
7	6.44E-05	0.35551	0.17544
7.2	8.04E-05	0.36566	0.18041
7.4	9.72E-05	0.3758	0.18539
7.7	1.68E-04	0.39102	0.19286
8	1.80E-04	0.40624	0.20033
8.2	2.14E-04	0.41638	0.20532
8.4	1.74E-04	0.42653	0.2103
8.7	8.87E-05	0.44175	0.21777
9	2.15E-05	0.45698	0.22525
9.2	4.28E-05	0.46713	0.23024
9.4	1.04E-04	0.47728	0.23523
9.7	1.64E-04	0.49251	0.24271
10	1.67E-04	0.50774	0.2502

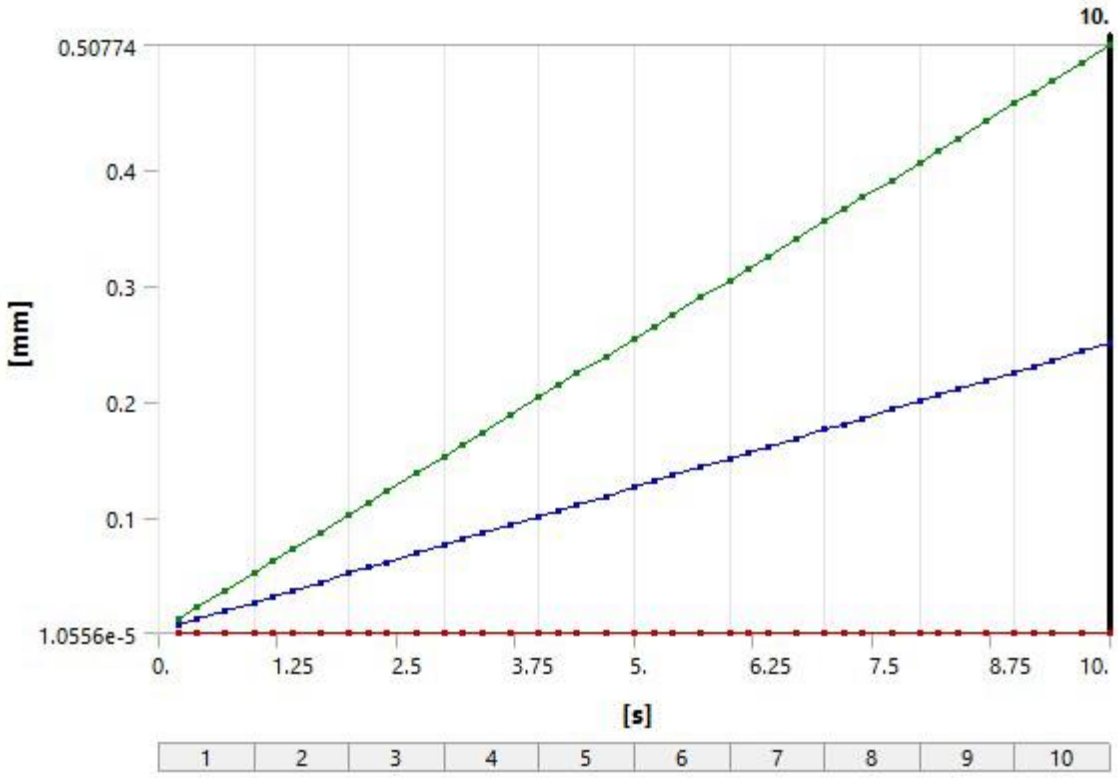

Figure 7.53 Deformation Profiles: I-type 30%

7.4.2 Equivalent elastic strain

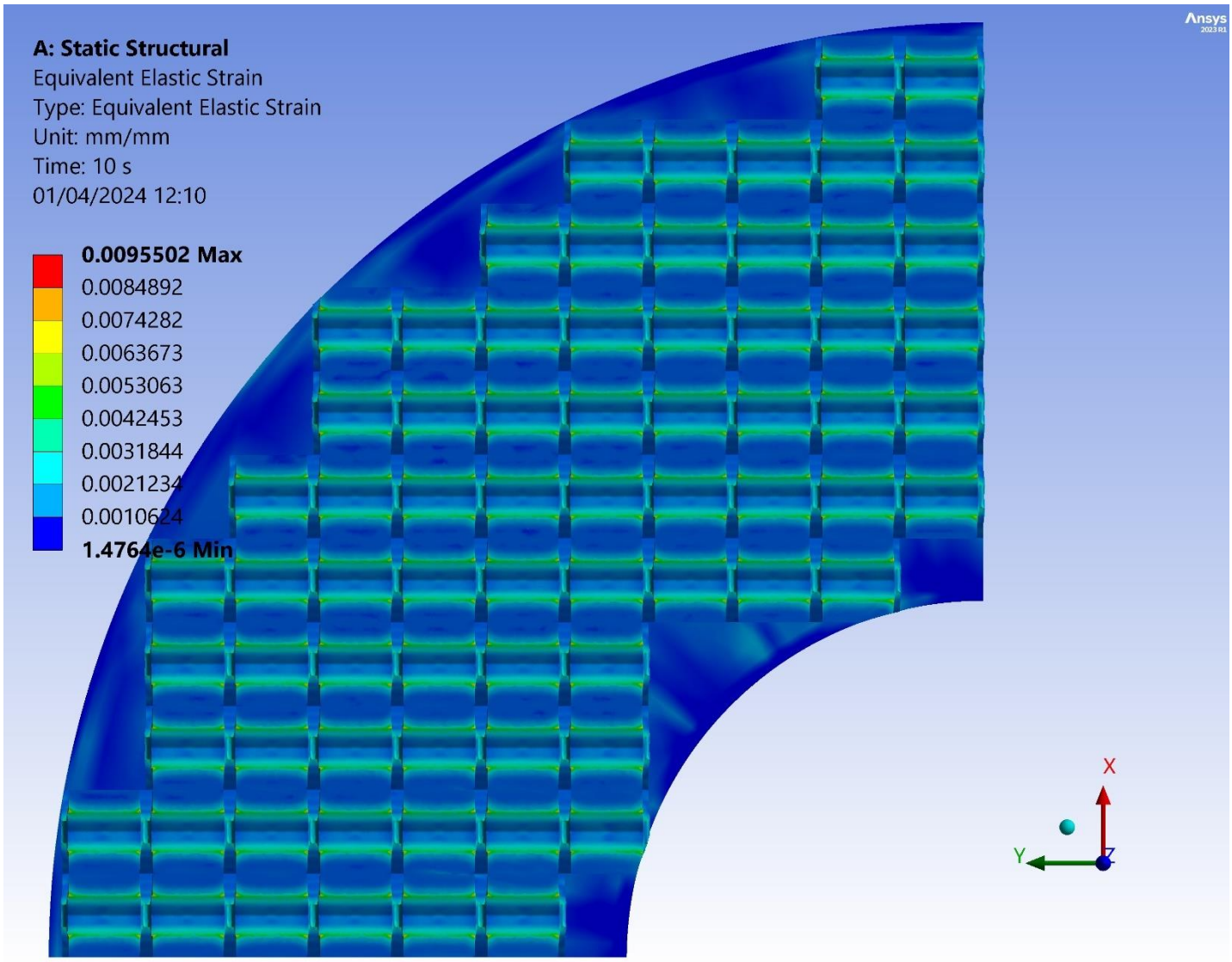

Figure 7.54 Equivalent Elastic Strain contour map: I-type 30% – top view

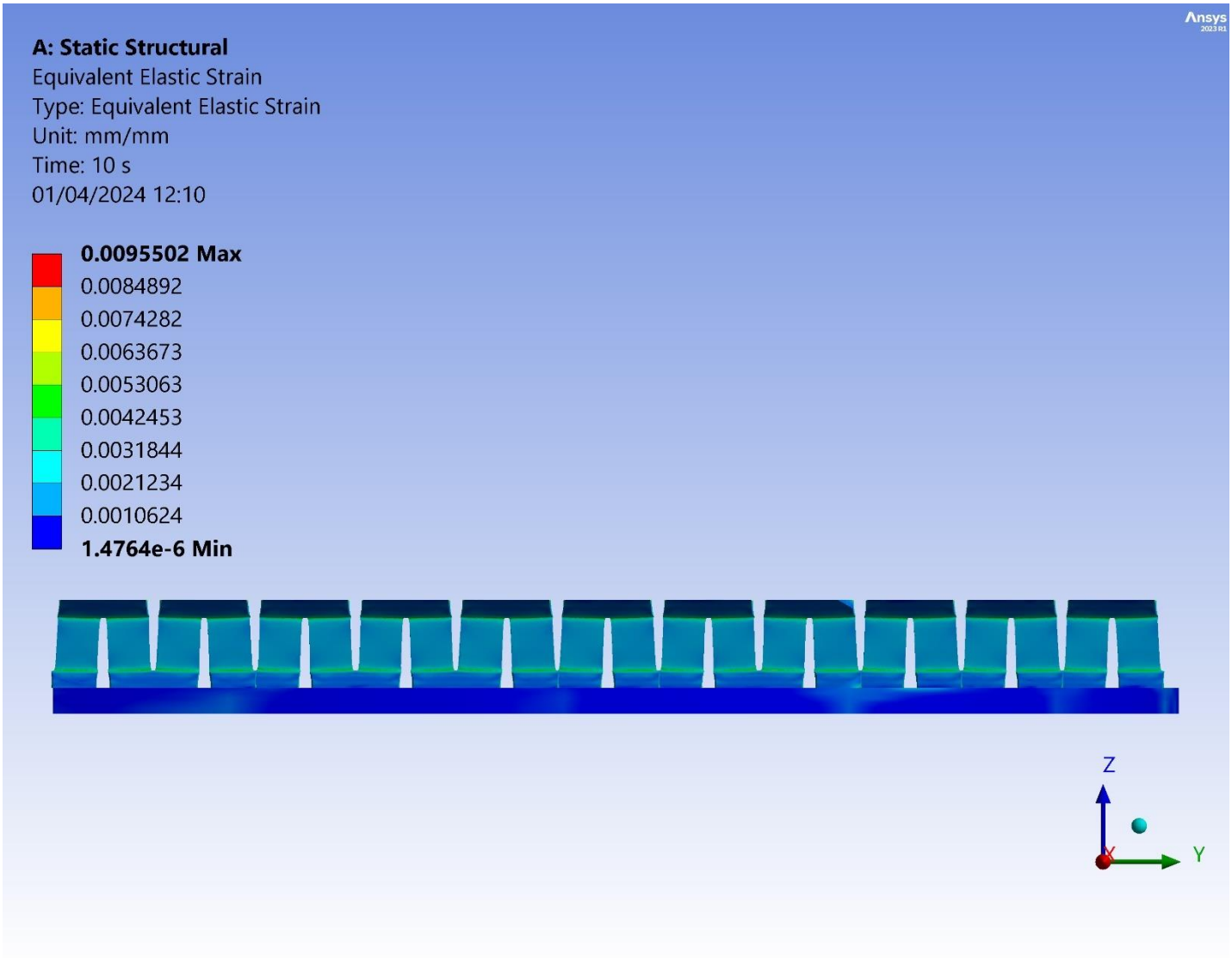

Figure 7.55 Equivalent Elastic Strain contour map: I-type 30% – side view

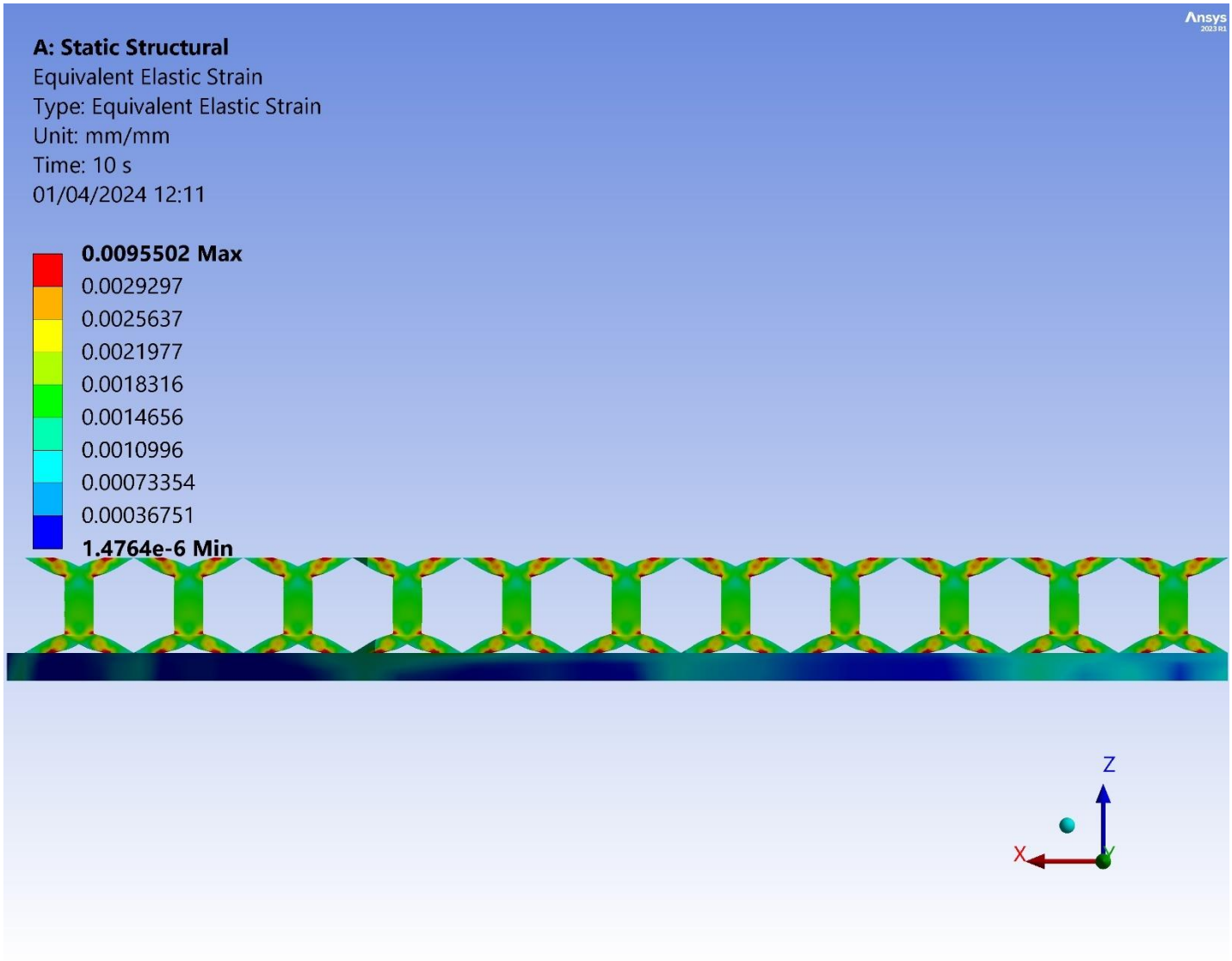

Figure 7.56 Equivalent Elastic Strain filtered contour map: I-type 30% – side view

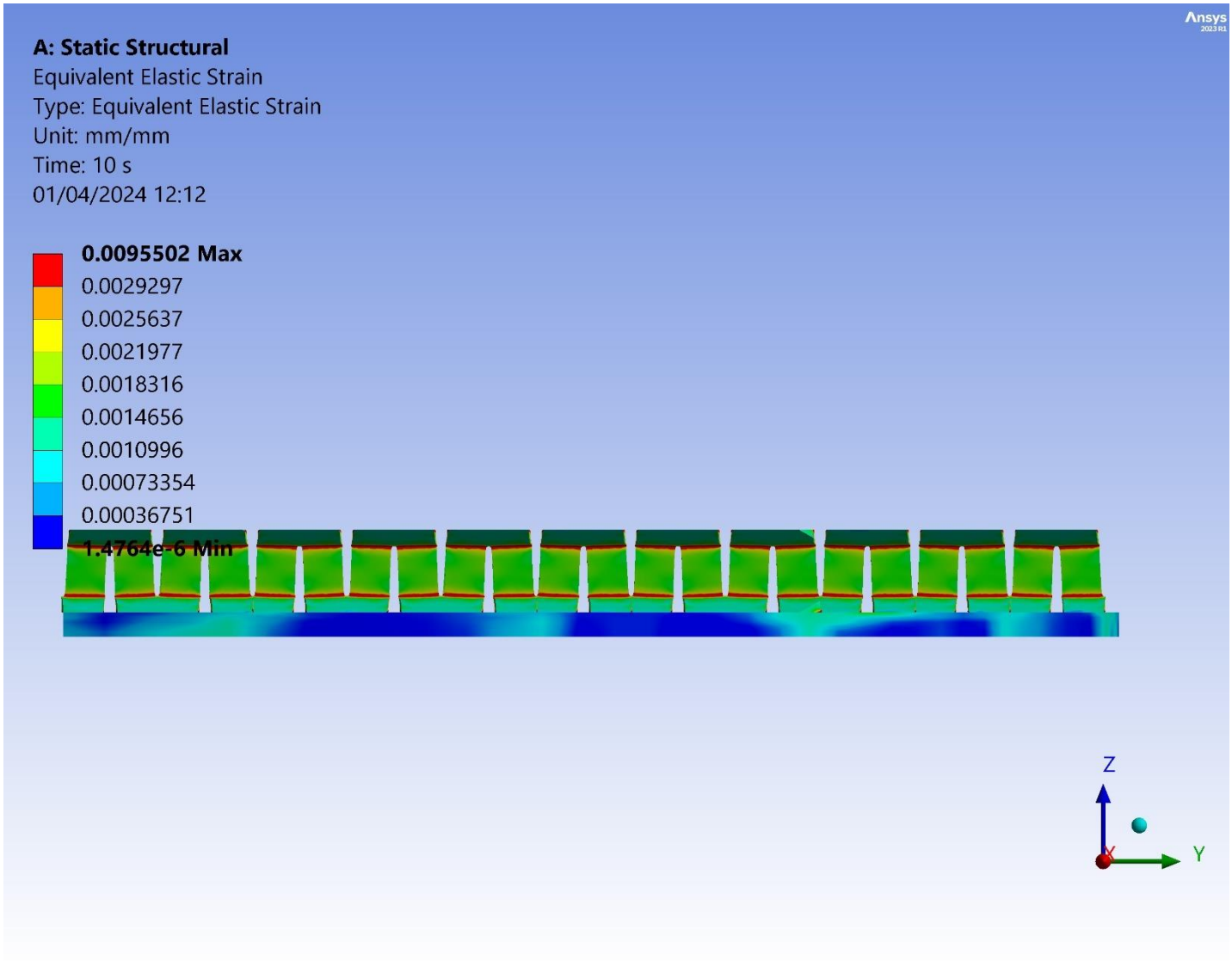

Figure 7.57 Equivalent Elastic Strain filtered contour map: I-type 30% – side view

Figures 7.54 and 7.55 initially exhibit a striking resemblance between the 12% and 30% models, suggesting similarities in their structural behavior. Once again, a localized region of heightened strain energy is discernible, primarily attributed to the presence of incomplete nodes, a recurring phenomenon observed in the 12% model. Furthermore, upon closer examination facilitated by a legend filter in *Figures 4.56 and 4.57, i*t becomes apparent that the edges the of unit cells approach 0.003mm/mm elastic strain. The same applies for the volume between the top and bottom edge of every strut. This observation underscores the significance of corners' fillets and robustness in influencing overall strain distribution within the lattice structure.

Table 7.17 offers a comprehensive overview of the minimum, maximum, and average elastic strain values recorded over the designated time period. This data provides invaluable insights into the structural behavior, allowing us to discern patterns and trends in deformation responses. By analyzing this table, we can pinpoint the average elastic strain that corresponds to the initial displacement, facilitating a deeper understanding of the structural dynamics and response mechanisms over time. Specifically, upon scrutiny, we observe that the maximum and average elastic strain recorded stand at 0.010mm/mm and 0.002mm/mm respectively.

Graphs are showcased in *Figure 7.58.*

Table 7.17 Equivalent Elastic Strain – I-type 30%

t(s)	Min Elastic Strain (mm/mm)	Max Elastic Strain (mm/mm)	Avg Elastic Strain (mm/mm)
0.2	1.27E-06	1.63E-03	7.52E-04
0.4	8.08E-07	1.69E-03	9.06E-04
0.7	1.77E-06	2.09E-03	9.96E-04
1	1.92E-06	2.45E-03	1.06E-03
1.2	1.83E-06	2.68E-03	1.09E-03
1.4	1.64E-06	2.90E-03	1.13E-03
1.7	1.17E-06	3.21E-03	1.17E-03
2	9.10E-07	3.51E-03	1.21E-03
2.2	9.53E-07	3.68E-03	1.24E-03
2.4	1.22E-06	3.88E-03	1.27E-03
2.7	8.36E-07	4.15E-03	1.30E-03
3	1.08E-06	4.39E-03	1.33E-03
3.2	1.44E-06	4.55E-03	1.35E-03
3.4	1.77E-06	4.72E-03	1.37E-03
3.7	2.07E-06	4.96E-03	1.39E-03
4	2.24E-06	5.19E-03	1.42E-03
4.2	1.77E-06	5.35E-03	1.44E-03
4.4	1.39E-06	5.50E-03	1.45E-03
4.7	1.41E-06	5.74E-03	1.48E-03
5	2.03E-06	5.96E-03	1.50E-03
5.2	2.69E-06	6.11E-03	1.52E-03

5.4	3.19E-06	6.27E-03	1.53E-03
5.7	4.24E-06	6.49E-03	1.56E-03
6	5.41E-06	6.71E-03	1.58E-03
6.2	5.75E-06	6.86E-03	1.60E-03
6.4	5.55E-06	7.01E-03	1.62E-03
6.7	5.17E-06	7.22E-03	1.64E-03
7	4.74E-06	7.44E-03	1.66E-03
7.2	4.48E-06	7.58E-03	1.68E-03
7.4	4.28E-06	7.73E-03	1.70E-03
7.7	3.87E-06	7.94E-03	1.72E-03
8	3.43E-06	8.15E-03	1.74E-03
8.2	3.12E-06	8.30E-03	1.76E-03
8.4	2.79E-06	8.44E-03	1.78E-03
8.7	2.46E-06	8.65E-03	1.80E-03
9	2.22E-06	8.86E-03	1.82E-03
9.2	2.19E-06	8.99E-03	1.84E-03
9.4	2.28E-06	9.13E-03	1.85E-03
9.7	9.43E-07	9.34E-03	1.88E-03
10	1.48E-06	9.55E-03	1.90E-03

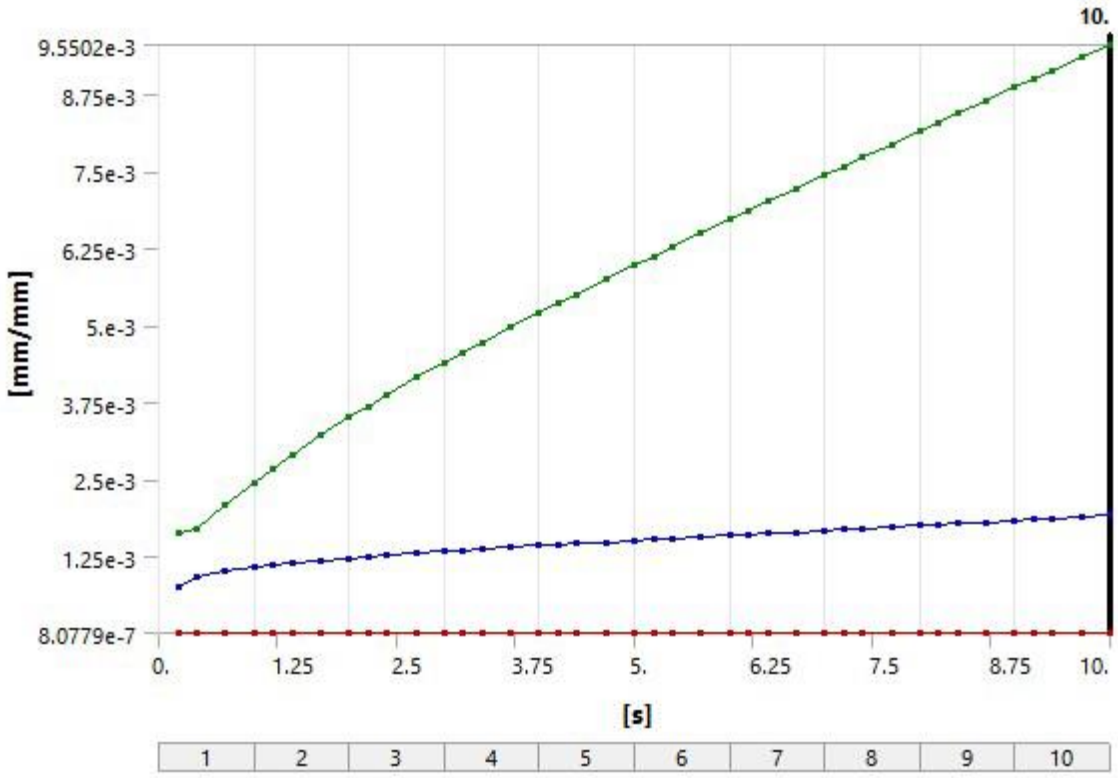

Figure 7.58 Elastic Strain Profiles: I-type 30%

7.4.3 Equivalent stress

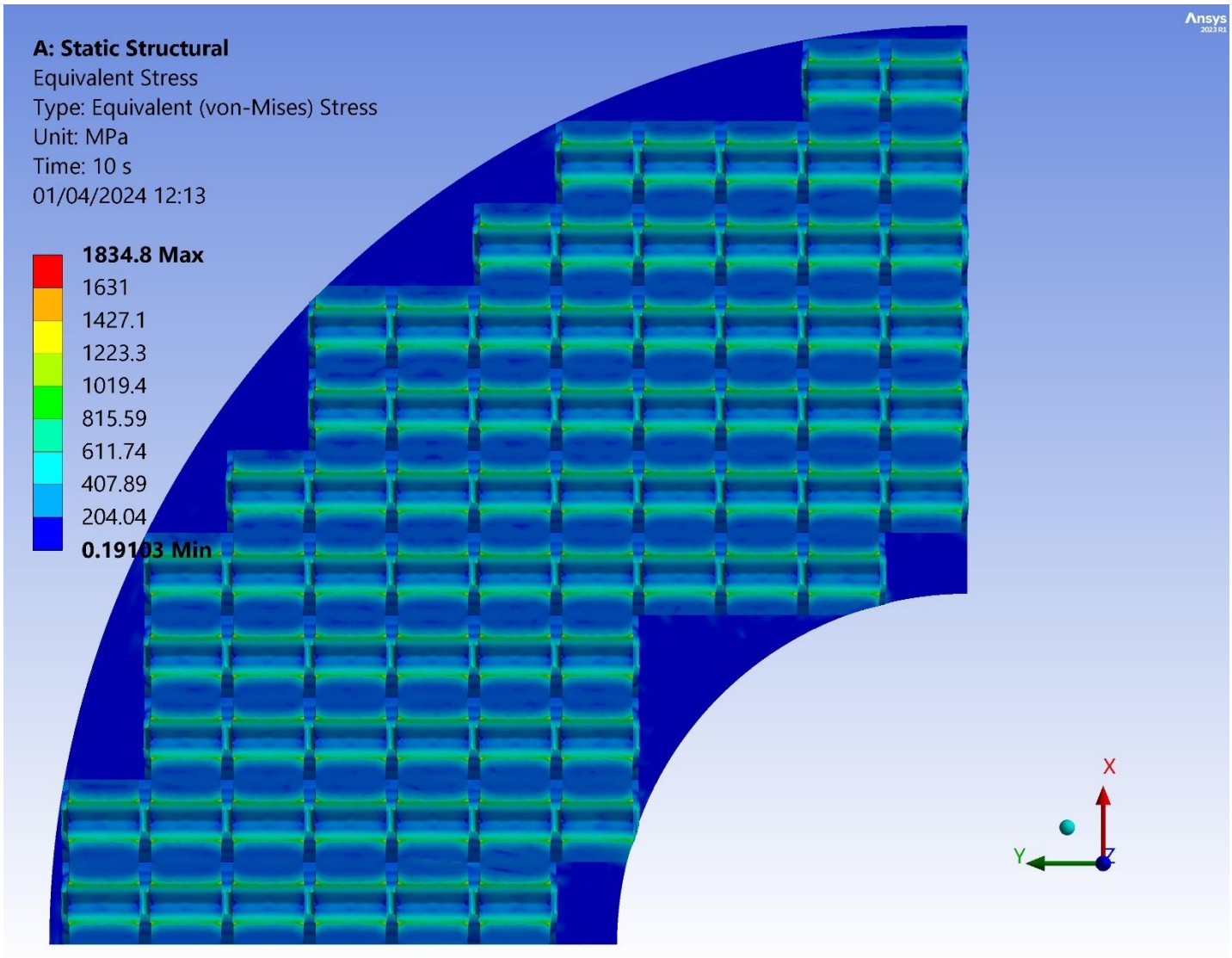

Figure 7.59 Equivalent (von-Mises) Stress contour map: I-type 30% – top view

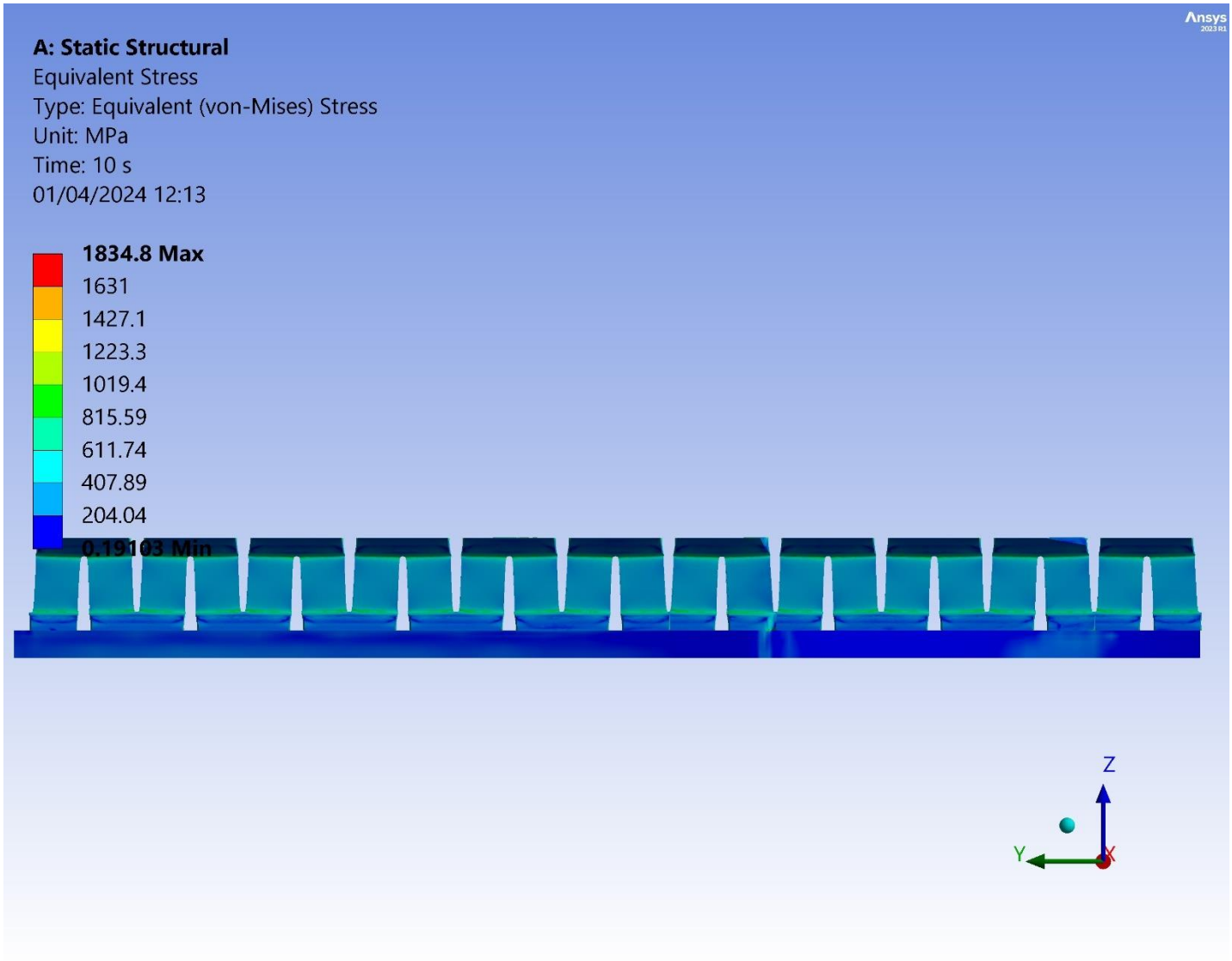

Figure 7.60 Equivalent (von-Mises) Stress contour map: I-type 30% – side view

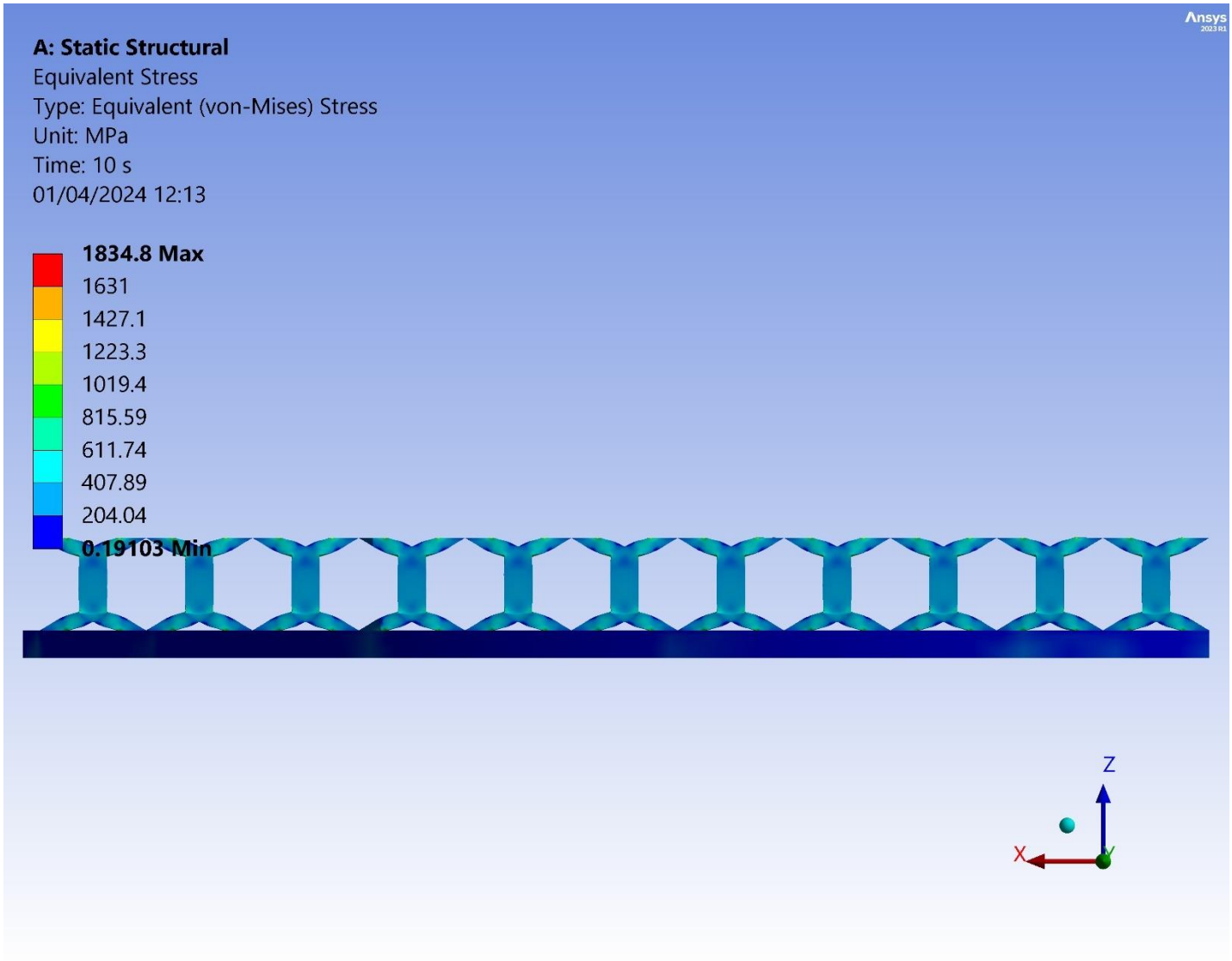

Figure 7.61 Equivalent (von-Mises) Stress contour map: I-type 30% – side view

Upon initial examination of *Figure 7.59 and 7.60*, it's evident that the stresses on the lattice do not pose any risk of failure. To enhance clarity, filtering techniques were applied to the legend, resulting in refined representations depicted in *Figure 7.61*. Upon closer scrutiny, it's apparent that the primary stress concentration zones are the higher struts, exhibiting stresses up to 1200MPa. This number is almost the double comparing to the BCC 12%. Central struts show stress up to 400Mpa. The lower contact areas of the lattice with the disk can experience stresses up to 300MPa.

Table 7.18 offers a comprehensive overview of the minimum, maximum, and average stress values recorded over the designated time period. This data provides invaluable insights into the structural behavior, allowing

us to discern patterns and trends in deformation responses. By analyzing this table, we can pinpoint the average and maximum stress that corresponds to the initial displacement, facilitating a deeper understanding of the structural dynamics and response mechanisms over time. Specifically, upon scrutiny, we observe that the maximum and average stress recorded stand at 1834.8MPa and 358.56MPa, respectively.

Graphs are showcased in *Figure 7.64.*

Table 7.18 Equivalent stress – I-type 30%

t(s)	Min Stress (MPa)	Max Stress (MPa)	Avg Stress (MPa)
0.2	7.41E-02	265.57	141.5
0.4	0.14948	320.75	168.62
0.7	0.23125	395.74	185.09
1	0.26083	464.32	196.78
1.2	0.17104	507.96	203.54
1.4	0.21786	549.82	209.92
1.7	0.2179	609.48	218.72
2	0.1581	666.22	226.88
2.2	0.16012	705.24	231.97
2.4	0.19898	744.61	236.64
2.7	0.14216	796.36	242.99
3	0.18377	844.39	248.87
3.2	0.20769	876.04	252.55
3.4	0.13532	907.48	256.09
3.7	0.20384	953.73	261.2
4	0.36632	999.32	266.14
4.2	0.29362	1029.2	269.35
4.4	0.20658	1059.4	272.59
4.7	0.22096	1103.7	277.36
5	0.34791	1147.6	282.09
5.2	0.37843	1176.2	285.21
5.4	0.3197	1205.5	288.35
5.7	0.27509	1248.5	293.03

6	0.27089	1291	297.69
6.2	0.2998	1318.5	300.77
6.4	0.33357	1347.4	303.88
6.7	0.4057	1389.2	308.52
7	0.50378	1430.8	313.14
7.2	0.5781	1457.3	316.19
7.4	0.64421	1485.8	319.27
7.7	0.67455	1526.7	323.87
8	0.5961	1567.5	328.44
8.2	0.56347	1594.6	331.48
8.4	0.53963	1621.5	334.52
8.7	0.48025	1661.8	339.05
9	0.43177	1702	343.57
9.2	0.42744	1727.6	346.56
9.4	0.44451	1755.3	349.58
9.7	0.17558	1795.1	354.08
10	0.19103	1834.8	358.56

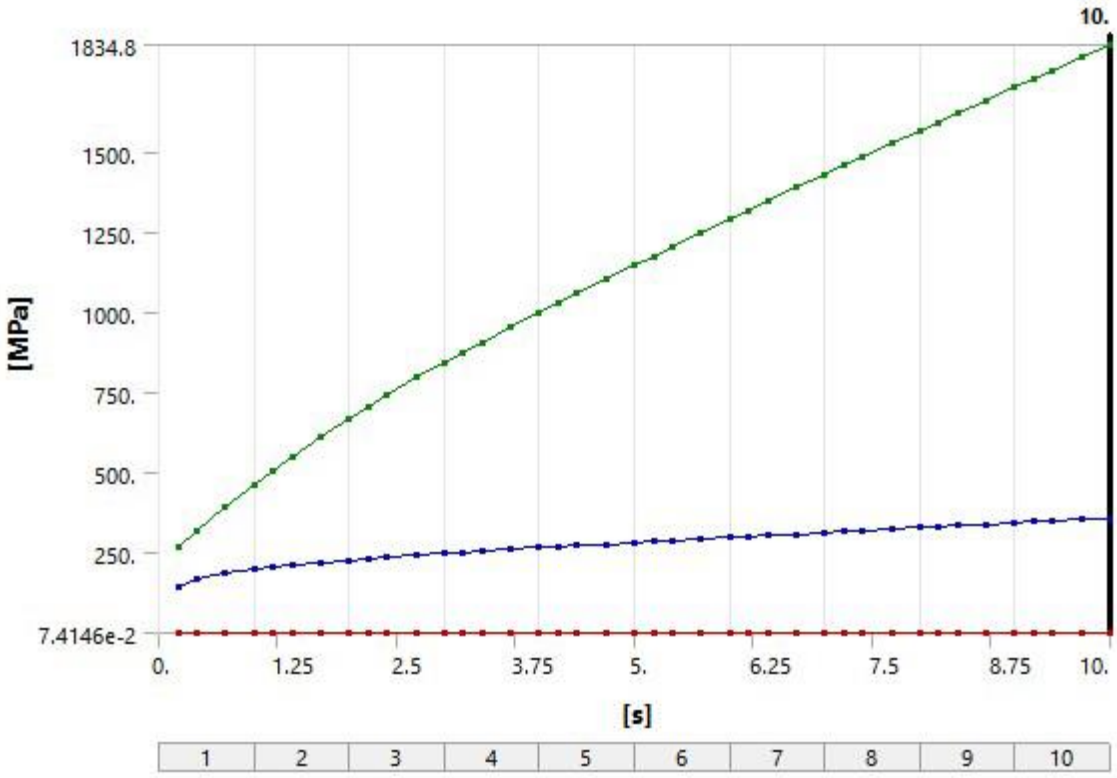

Figure 7.64 Equivalent (Von Mises) Stress Profiles: I-type 30%

7.4.4 Strain energy

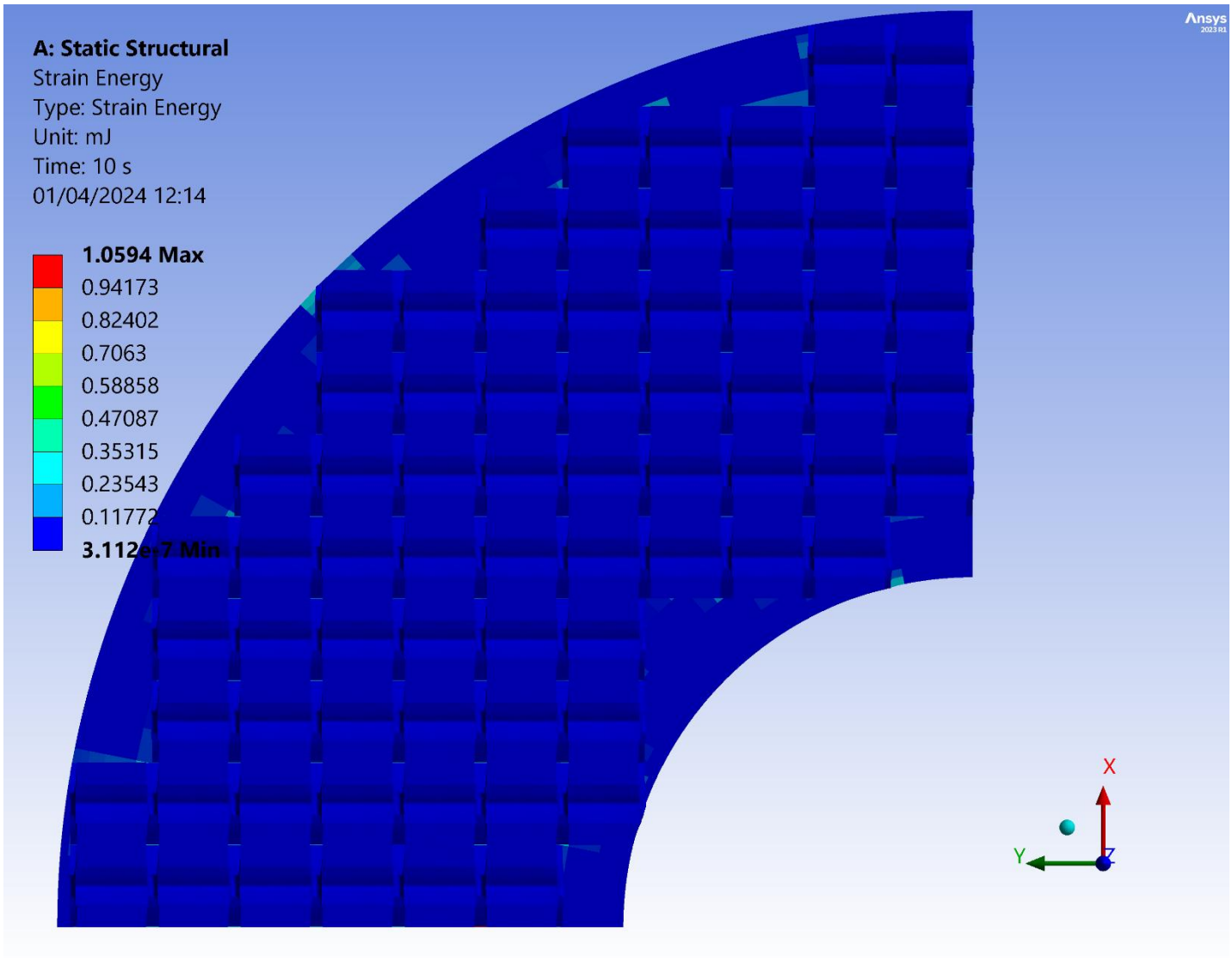

Figure 7.65 Strain Energy contour map: I-type 30% – top view

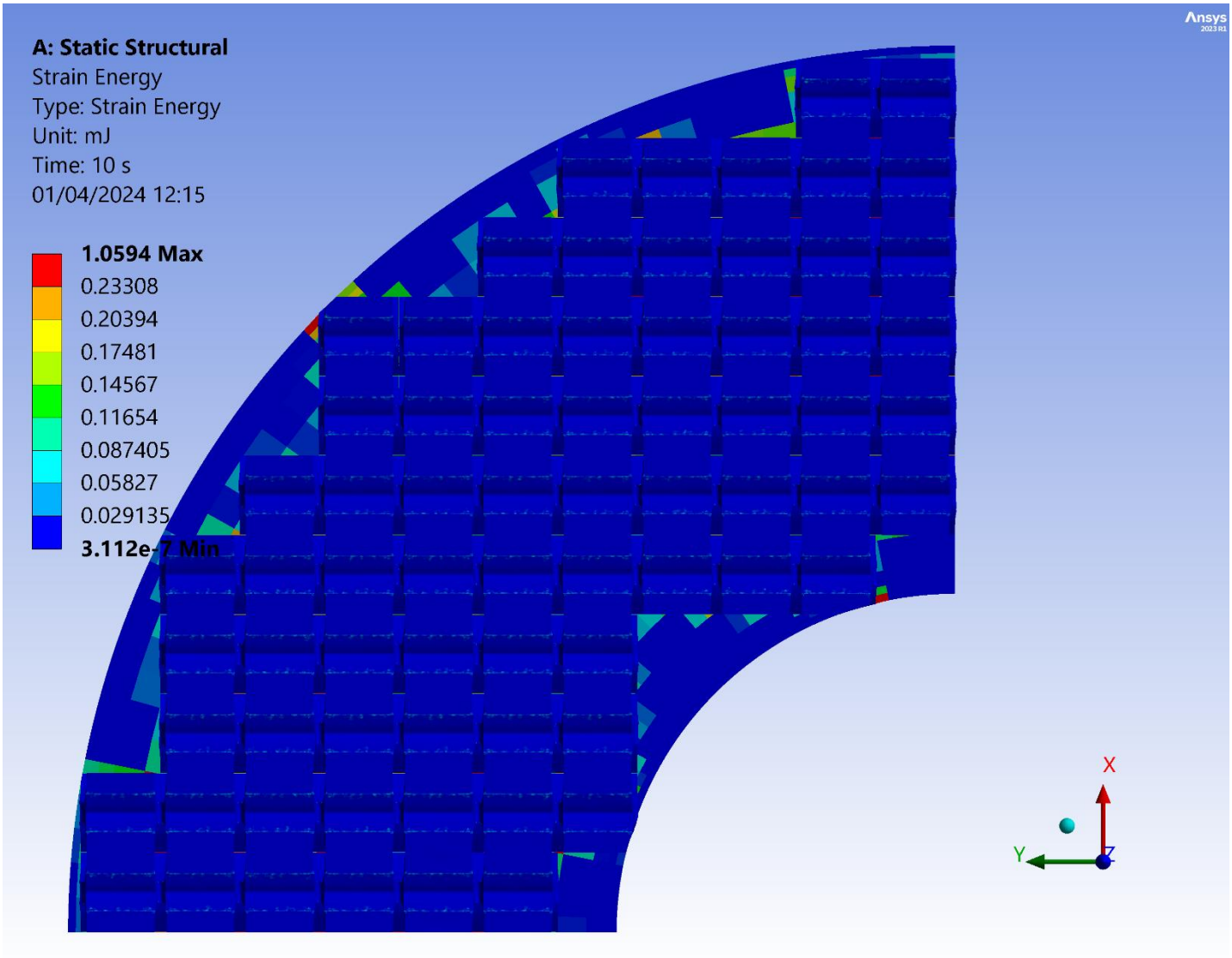

Figure 7.66 Strain Energy filtered contour map: I-type 30% – top view

In *Figure 7.65* presented above, it's evident that the distribution of strain energy across the area follows a symmetrical pattern, showcasing impressive uniformity along the surface, with values reaching up to 0.11 mJ. Additionally, in *Figure 7.66*, a small area stands out with strain energy equal to 1.05 mJ, attributed to a cut node. This localized region of heightened strain energy is notable within an otherwise uniformly distributed pattern, emphasizing the impact of structural irregularities on strain energy distribution. There also some spread areas of strain energy equal to 0.15mJ.

Within *Table 7.19*, a comprehensive array of data unveils the minimum, maximum, and total strain energy values documented throughout the designated timeframe. This dataset acts as a reservoir of knowledge,

offering valuable glimpses into the intricacies of structural behavior and the evolving nature of deformation responses. By meticulously analyzing this table, we can zero in on the total strain energy associated with the initial displacement, thereby deepening our comprehension of structural dynamics and response mechanisms over time. Notably, upon careful review, we note that the maximum and total strain energy readings reach 1.05mJ and 28698mJ respectively, offering valuable insights into the magnitude of structural deformation under various conditions.

Graphs are showcased in *Figure 7.67.*

Table 7.19 Strain Energy – I-type 30%

t(s)	Min Strain Energy (mJ)	Max Strain Energy (mJ)	Total Strain Energy (mJ)
0.2	8.57E-09	1.51E-02	181.21
0.4	1.81E-08	2.00E-02	513.44
0.7	2.33E-08	2.38E-02	1054
1	2.89E-08	3.00E-02	1630.2
1.2	3.53E-08	3.82E-02	2032.5
1.4	4.47E-08	4.72E-02	2448.2
1.7	6.05E-08	6.29E-02	3096.3
2	8.53E-08	8.07E-02	3772.4
2.2	8.97E-08	9.73E-02	4237.7
2.4	1.05E-07	0.10806	4713.9
2.7	4.51E-08	0.1299	5447.4
3	3.87E-08	0.15278	6201.1
3.2	4.23E-08	0.16883	6714.2
3.4	5.11E-08	0.18383	7235.5
3.7	7.16E-08	0.2072	8032.4
4	1.02E-07	0.23116	8847
4.2	1.31E-07	0.24733	9399.7
4.4	1.69E-07	0.26374	9960.2
4.7	2.00E-07	0.2888	10815
5	2.06E-07	0.31461	11687
5.2	2.10E-07	0.33213	12278
5.4	2.14E-07	0.35004	12877

5.7	2.21E-07	0.3777	13789
6	2.28E-07	0.40617	14717
6.2	2.33E-07	0.42548	15346
6.4	2.36E-07	0.4453	15982
6.7	2.42E-07	0.47582	16950
7	2.47E-07	0.50722	17935
7.2	2.51E-07	0.5285	18601
7.4	2.55E-07	0.55038	19274
7.7	2.63E-07	0.59517	20298
8	2.71E-07	0.64492	21338
8.2	2.75E-07	0.67915	22041
8.4	2.78E-07	0.71436	22751
8.7	2.82E-07	0.77319	23831
9	2.87E-07	0.8348	24926
9.2	2.91E-07	0.87698	25666
9.4	2.95E-07	0.92104	26413
9.7	3.02E-07	0.98903	27548
10	3.11E-07	1.0594	28698

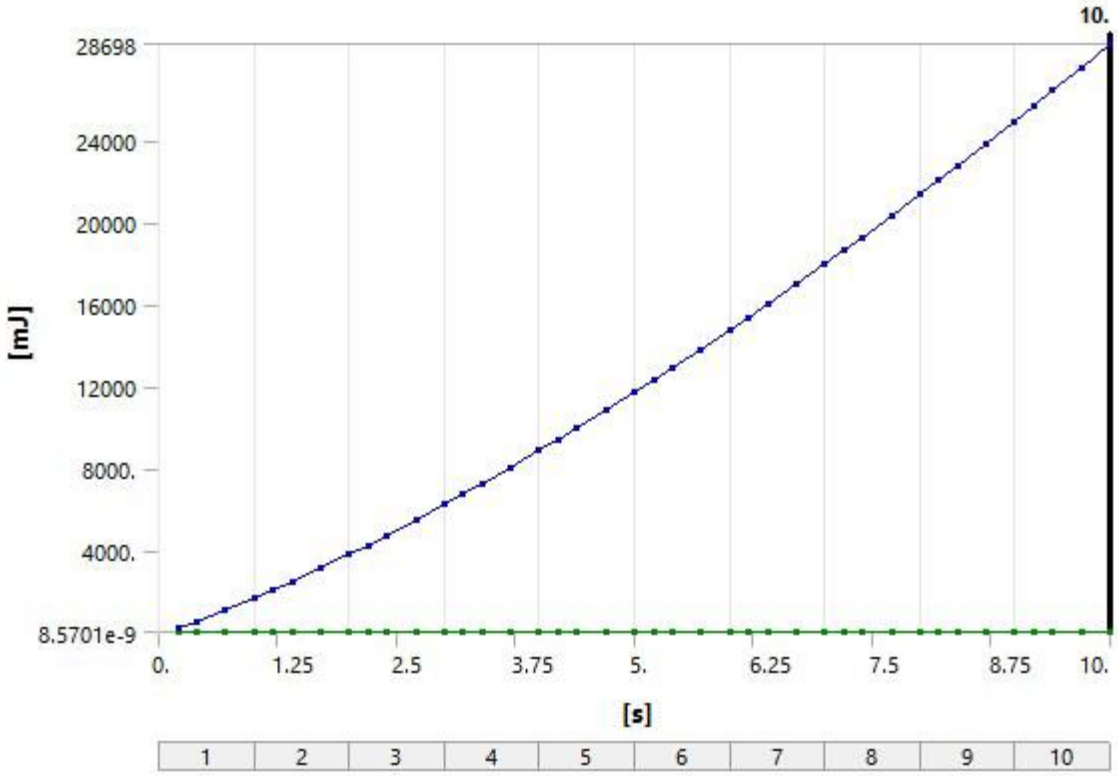

Figure 7.67 Strain Energy Profiles: I-type 30%

7.4.5 Force reaction

The data presented in *Table 7.20* delineates the application of force (F) as a function of time (t), where negative values denote compressive force. Over the duration of time, there's a progressive increase in the magnitude of compressive force, reaching up to 77375N, indicating a sustained exertion of pressure. This implies an ongoing deformation or compression phenomenon within the material or structure under scrutiny. The consistent trend observed underscores the stability and uniformity of the applied force throughout the designated time frame. Further exploration could entail examining the relationship between these force values and specific mechanical reactions or structural responses. Additionally, *Figure 7.68* visually illustrates the force reaction trend over time, providing complementary insight into the observed phenomenon.

Table 7.20 Force reaction – I-type 30%

t(s)	F(N)
0.2	-31170
0.4	-34787
0.7	-37421
1	-39660
1.2	-41033
1.4	-42368
1.7	-44283
2	-46067
2.2	-47200
2.4	-48261
2.7	-49694
3	-50985
3.2	-51805
3.4	-52611
3.7	-53798
4	-54968
4.2	-55747
4.4	-56510
4.7	-57657
5	-58797
5.2	-59561
5.4	-60311
5.7	-61441
6	-62568
6.2	-63327
6.4	-64067
6.7	-65187
7	-66306

7.2	-67060
7.4	-67794
7.7	-68906
8	-70017
8.2	-70757
8.4	-71496
8.7	-72602
9	-73707
9.2	-74452
9.4	-75177
9.7	-76277
10	-77375

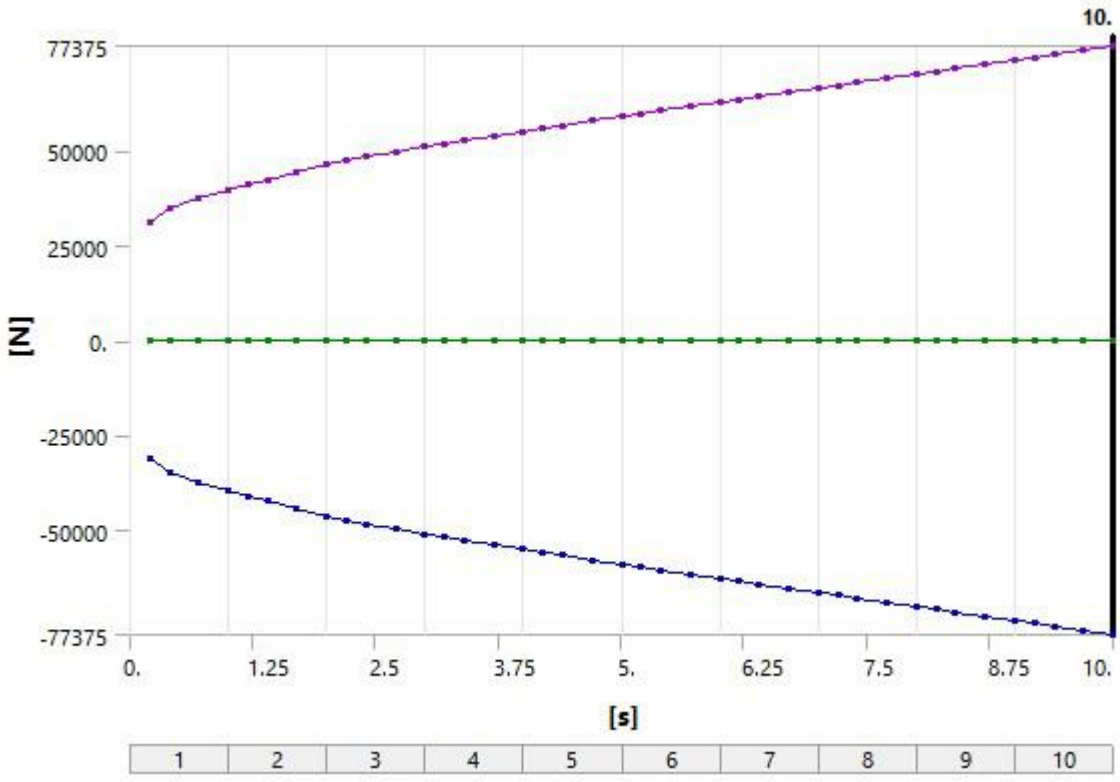

Figure 7.68 Force Reaction Profiles: I-type 30%

7.5 Tetrahedral 12%

7.5.1 Total deformation

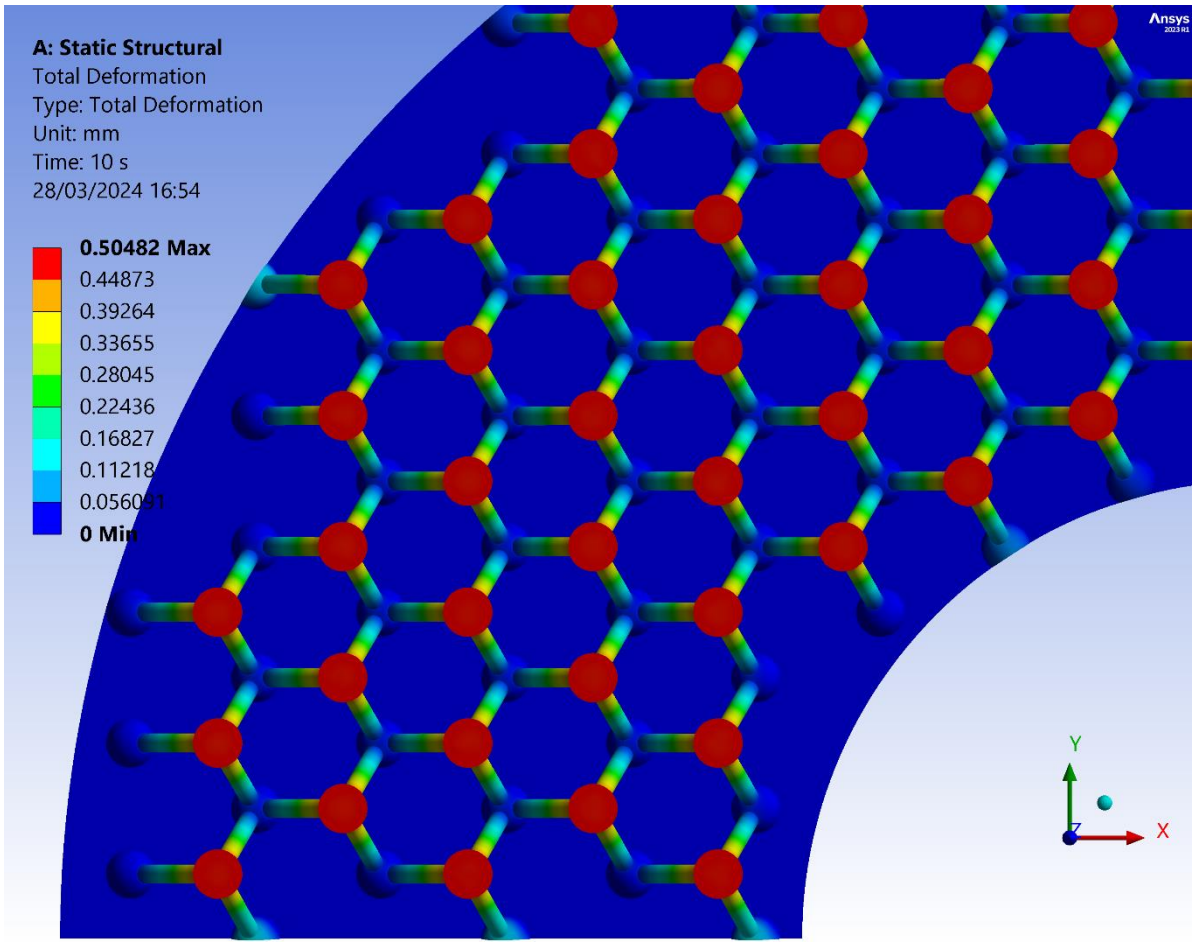

Figure 7.69 Total deformation contour map: Tetrahedral 12% – top view

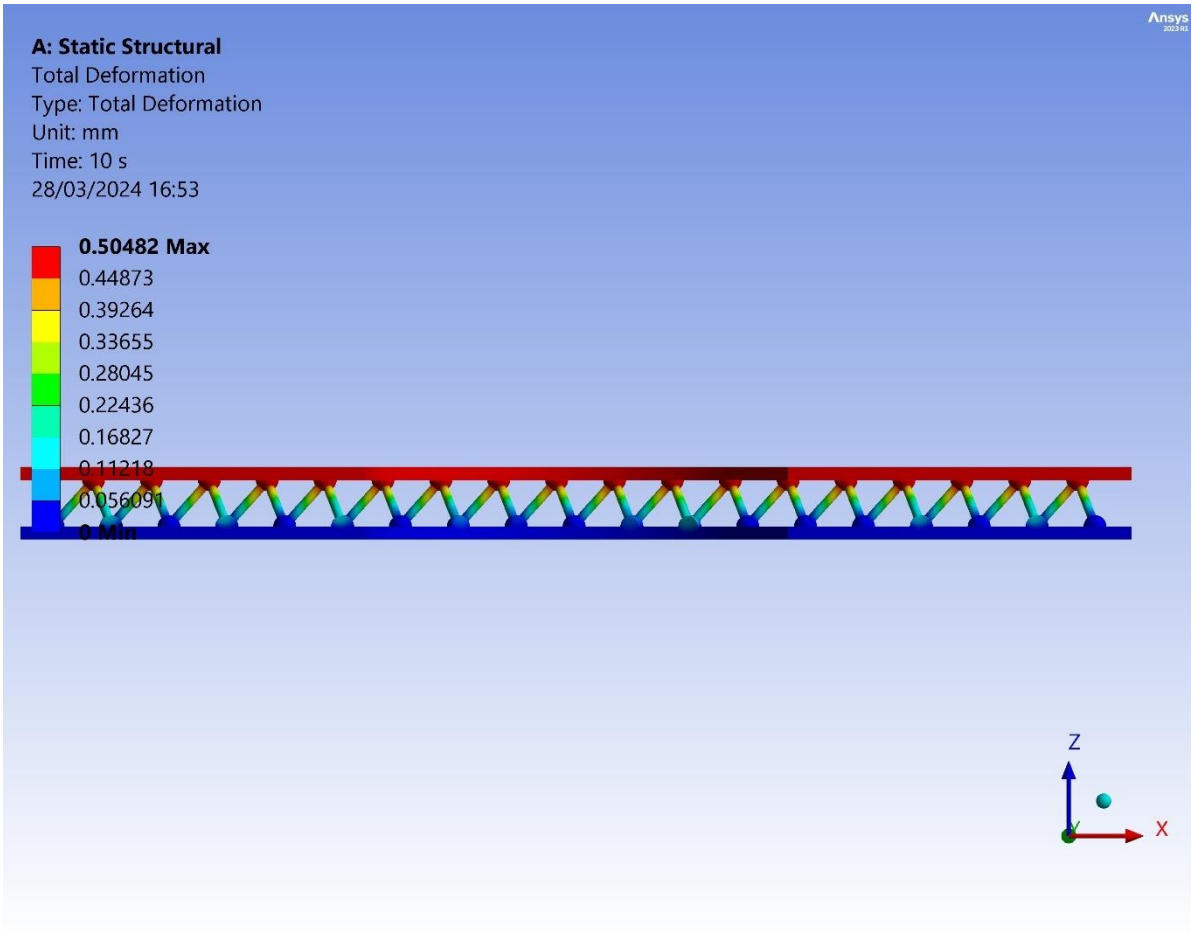

Figure 7.70 Total deformation contour map: Tetrahedral 12% – side view

Upon observing *Figures 7.69 and 7.70*, it's evident that the most significant deformation is concentrated in the upper nodes of the lattice structure, consistent with expectations regarding the primary displacement zone. Additionally, it's notable that the deformation levels in the struts between the nodes range from 0.4mm to 0.05mm in an almost linear way. This emphasizes the robustness of these struts, underscoring their capacity to uphold structural integrity even under applied loads.

Table 7.21 lays out a detailed exposition of the minimum, maximum, and average deformation metrics observed across the specified duration. This dataset serves as a rich source of information, unveiling nuances in structural behavior and the nuanced shifts in deformation responses. Through a meticulous examination of this table, we unravel the average deformation tied to the initial displacement, thus enriching our understanding of structural dynamics and response mechanisms over time. Noteworthy is the observation that upon thorough scrutiny, the maximum and average deformation values stand at 0.503mm and 0.231mm respectively, providing a comprehensive view of structural deformation across different contexts.

Graphs are showcased in *Figure 7.71.*

Table 7.21 Deformation Data – Tetrahedral 12%

t	Min Deformation (mm)	Max Deformation (mm)	Avg Deformation (mm)
1	0	5.0482e-005	2.3102e-005
2	0	1.0096e-004	4.6204e-005
3	0	1.5145e-004	6.9306e-005
4	0	2.0193e-004	9.2408e-005
5	0	2.5241e-004	1.1551e-004
6	0	3.0289e-004	1.3861e-004
7	0	3.5337e-004	1.6171e-004
8	0	4.0385e-004	1.8482e-004
9	0	4.5434e-004	2.0792e-004
10	0	5.0482e-004	2.3102e-004

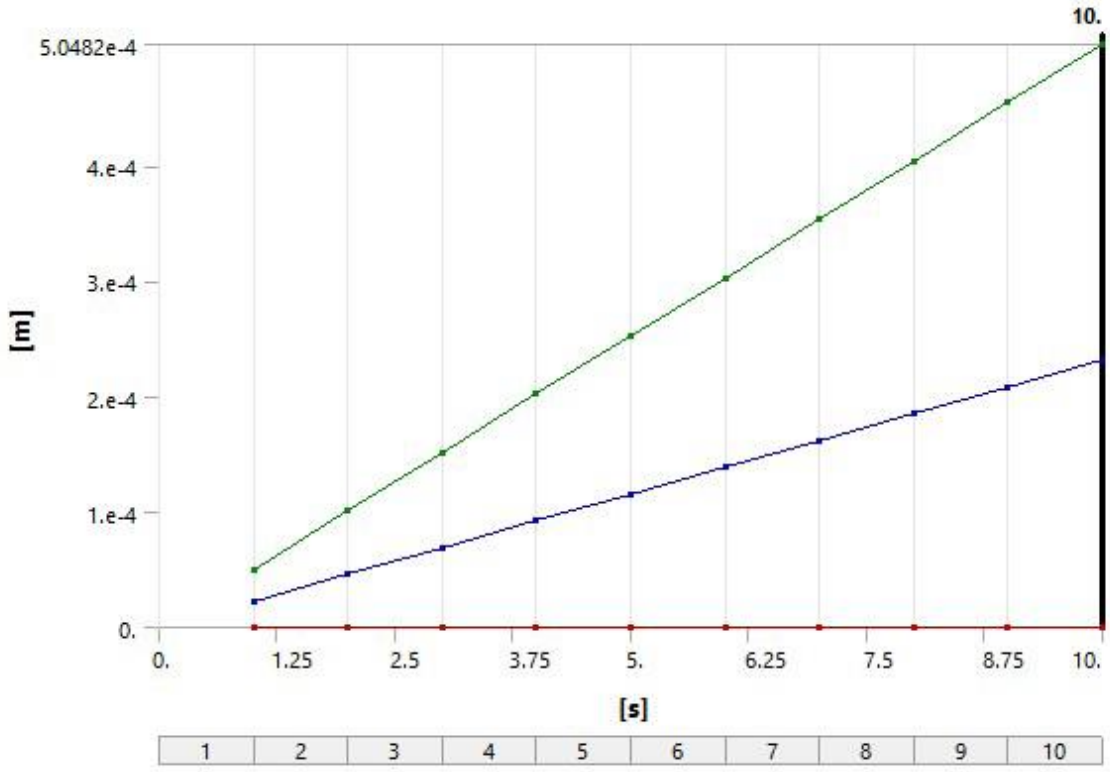

Figure 7.71 Deformation Profiles: Tetrahedral 12%

7.5.2 Equivalent elastic strain

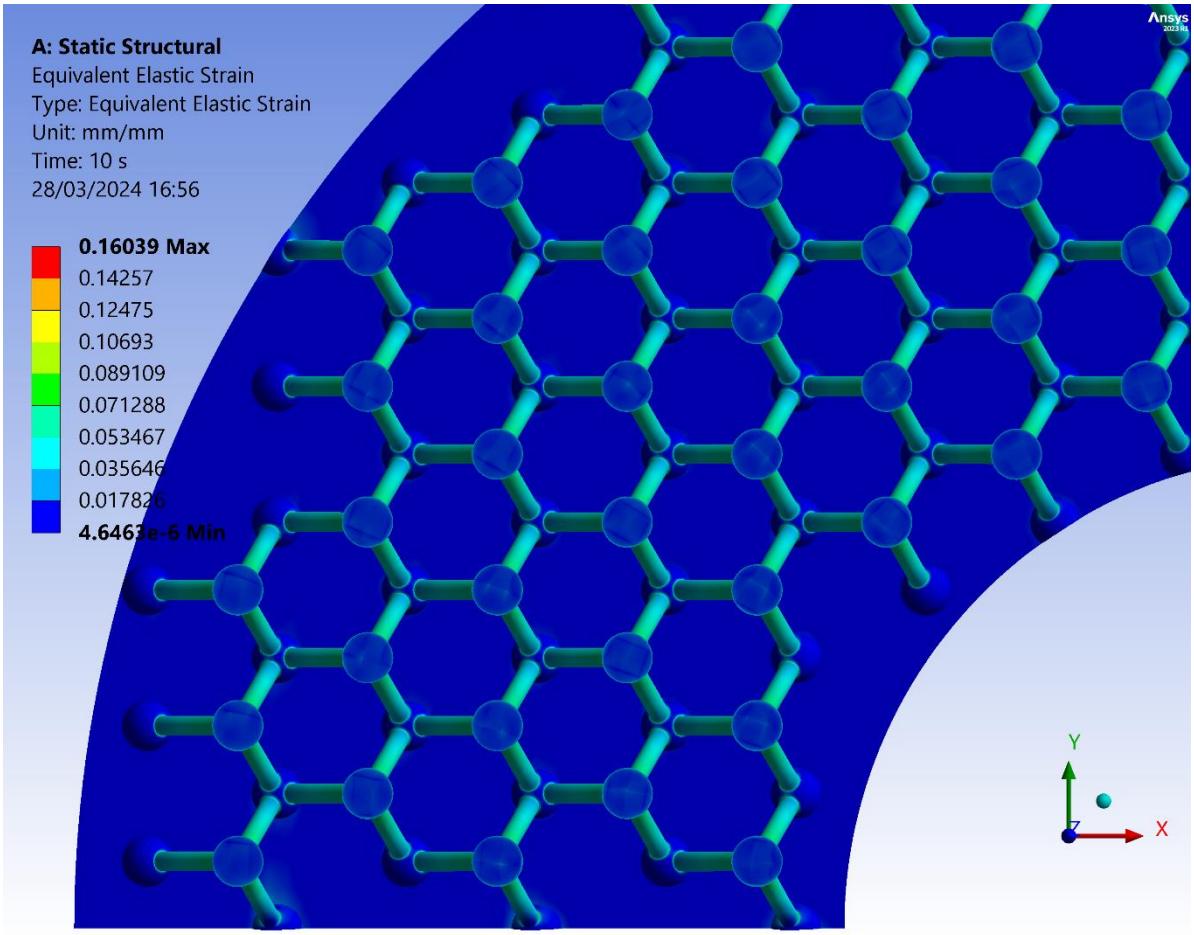

Figure 7.72 Equivalent Elastic Strain contour map: Tetrahedral 12% – top view

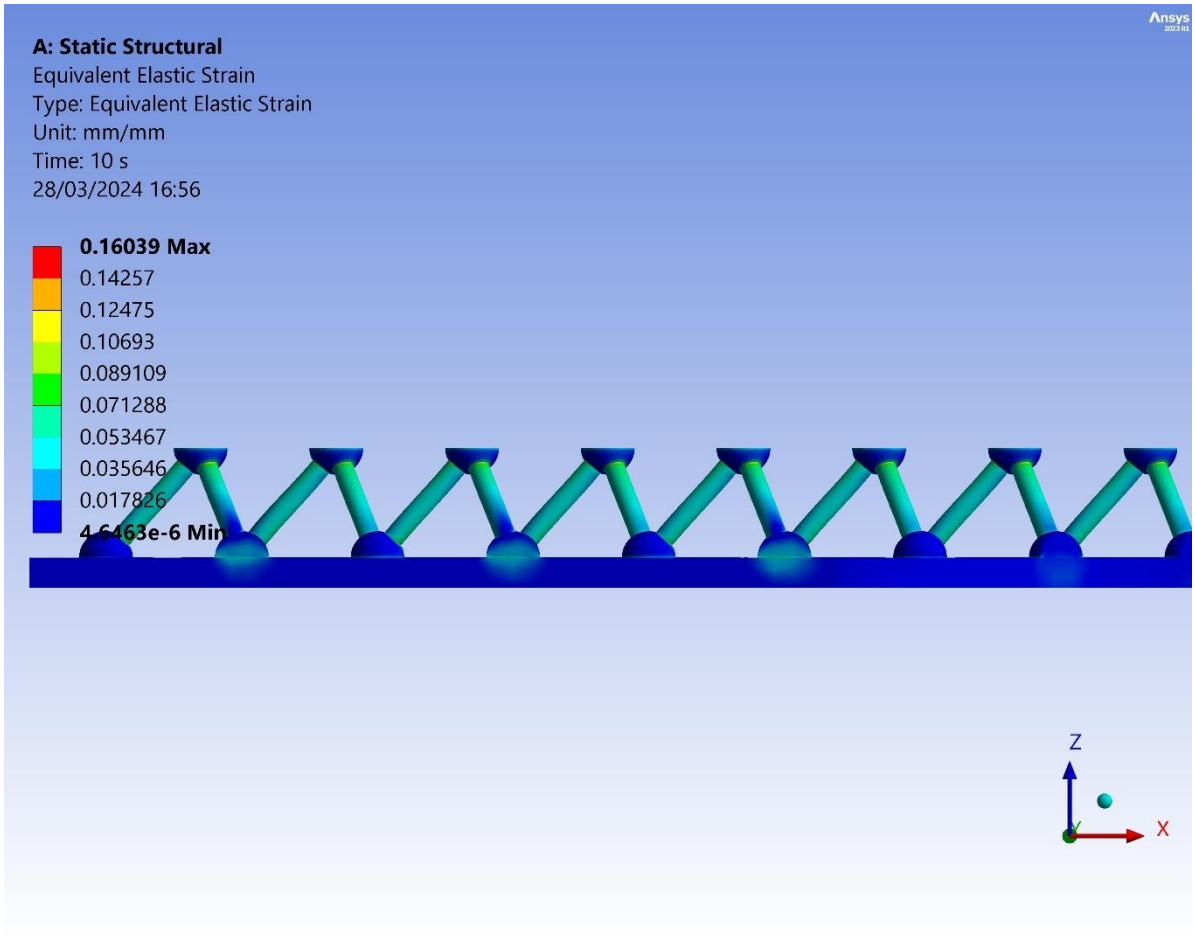

Figure 7.73 Equivalent Elastic Strain contour map: Tetrahedral 12% – side view

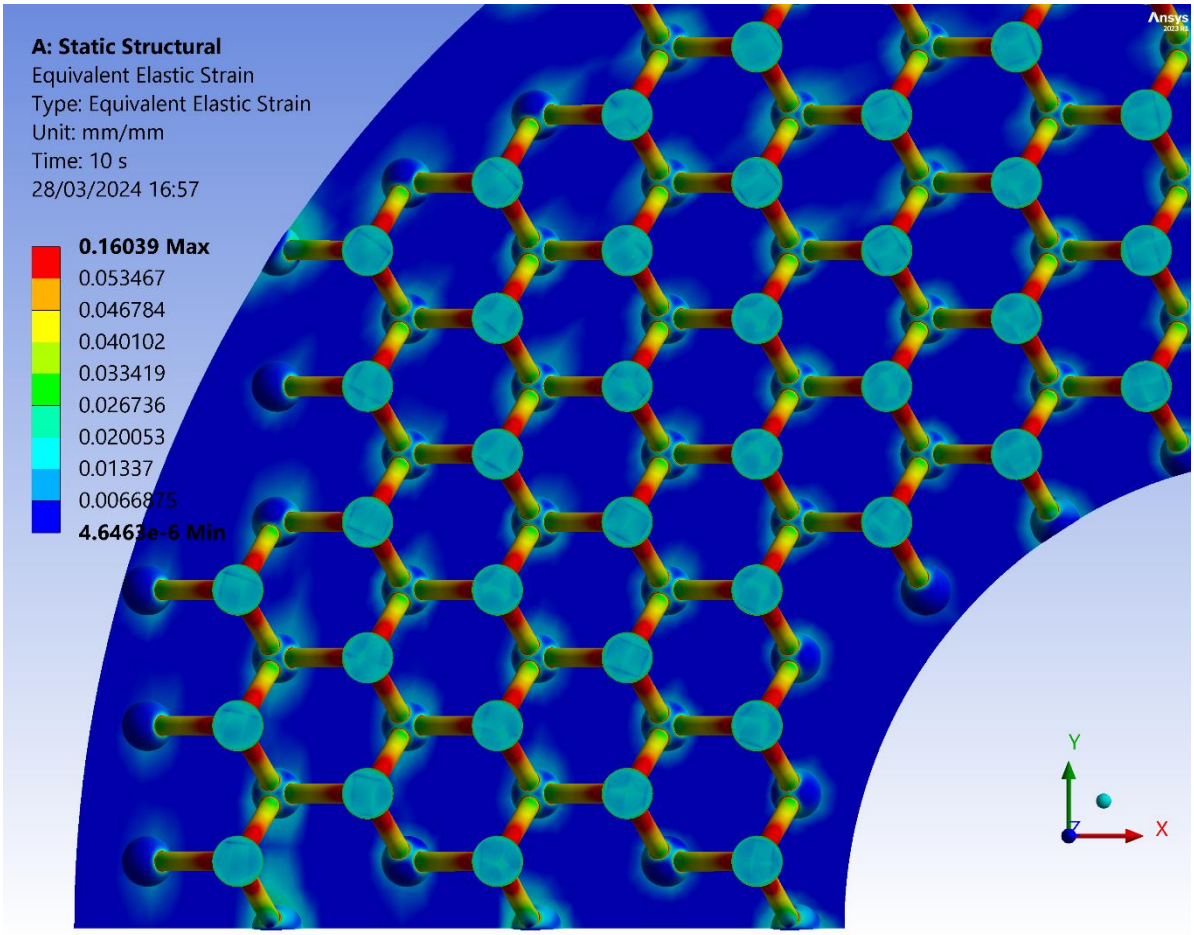

Figure 7.74 Equivalent Elastic Strain filtered contour map: Tetrahedral 12% – top view

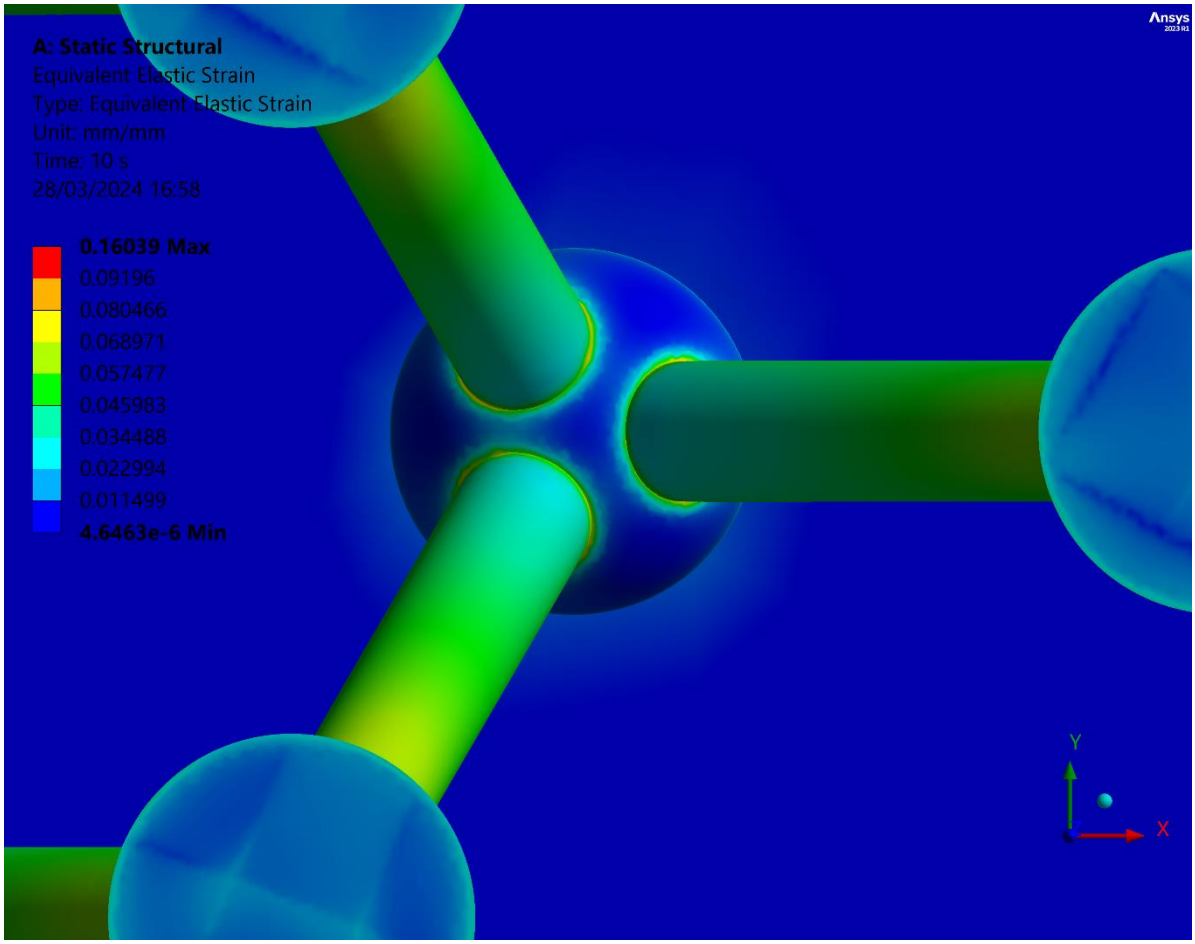

Figure 7.75 Equivalent Elastic Strain contour map: Tetrahedral 12% – zoomed in top view

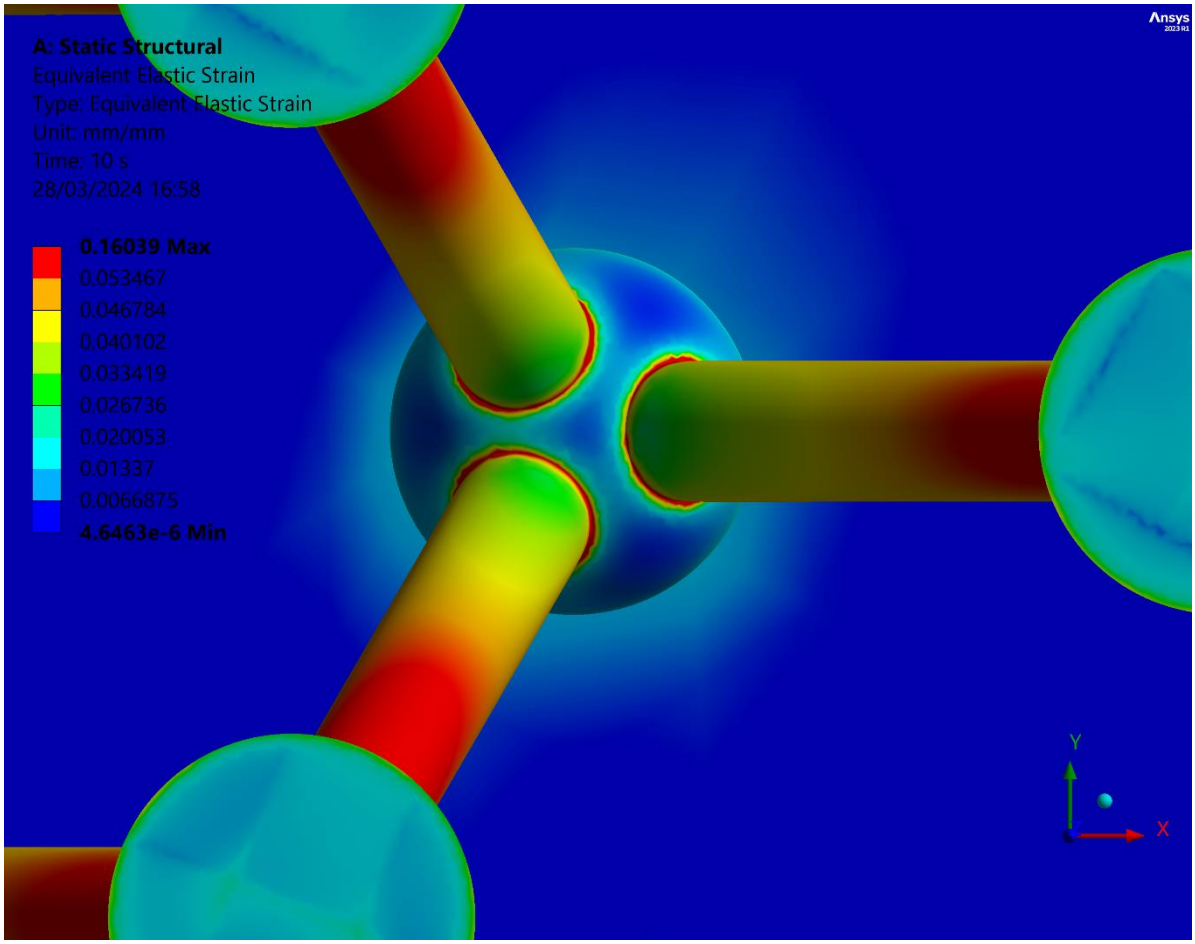

Figure 7.76 Equivalent Elastic Strain filtered contour map: Tetrahedral 12% – zoomed in top view

Once again, *Figure 7.72 and Figure 7.73* highlight the presence of incomplete nodes, evident through concentrated strain along the edges, resulting in notably higher values, as seen in *Figure 7.74*, reaching up to 0.16mm/mm. This strain concentration consequently leads to increased elastic strain at the contact areas of the plates, particularly prominent in the outer regions of the model. *Figures 7.74 and 7.76* indicate significant elastic strain concentration in the upper sections of the struts and along the edges between struts and nodes, ranging from 0.16mm/mm near the nodes to 0.03mm/mm. The lower part of the struts have an elastic strain between 0.0026mm/mm and 0.0046mm/mm.

Table 7.22 presents a detailed compilation of the minimum, maximum, and average elastic strain values observed throughout the designated time interval. This dataset offers invaluable insights into the structural behavior, enabling us to identify recurring patterns and evolving trend. Through a meticulous examination of this table, we gain the ability to precisely identify the average elastic strain corresponding to the initial displacement, thereby enhancing our comprehension of the structural dynamics and response mechanisms

over time. Specifically, upon scrutiny, we observe that the maximum and average deformation recorded stand at 0.160mm and 0.025mm respectively, shedding light on the extent of structural deformation under varying conditions.

Graphs are showcased in *Figure 7.77.*

Table 7.22 Equivalent elastic strain – Tetrahedral 12%

t (s)	Min Elastic Strain (mm/mm)	Max Elastic Strain (mm/mm)	Avg Elastic Strain (mm/mm)
1	4.6472e-007	1.6039e-002	2.4617e-003
2	9.2944e-007	3.2079e-002	4.9233e-003
3	1.3939e-006	4.8118e-002	7.3850e-003
4	1.8589e-006	6.4157e-002	9.8467e-003
5	2.3231e-006	8.0196e-002	1.2308e-002
6	2.7885e-006	9.6236e-002	1.4770e-002
7	3.2524e-006	0.11227	1.7232e-002
8	3.7178e-006	0.12831	1.9693e-002
9	4.1825e-006	0.14435	2.2155e-002
10	4.6463e-006	0.16039	2.4617e-002

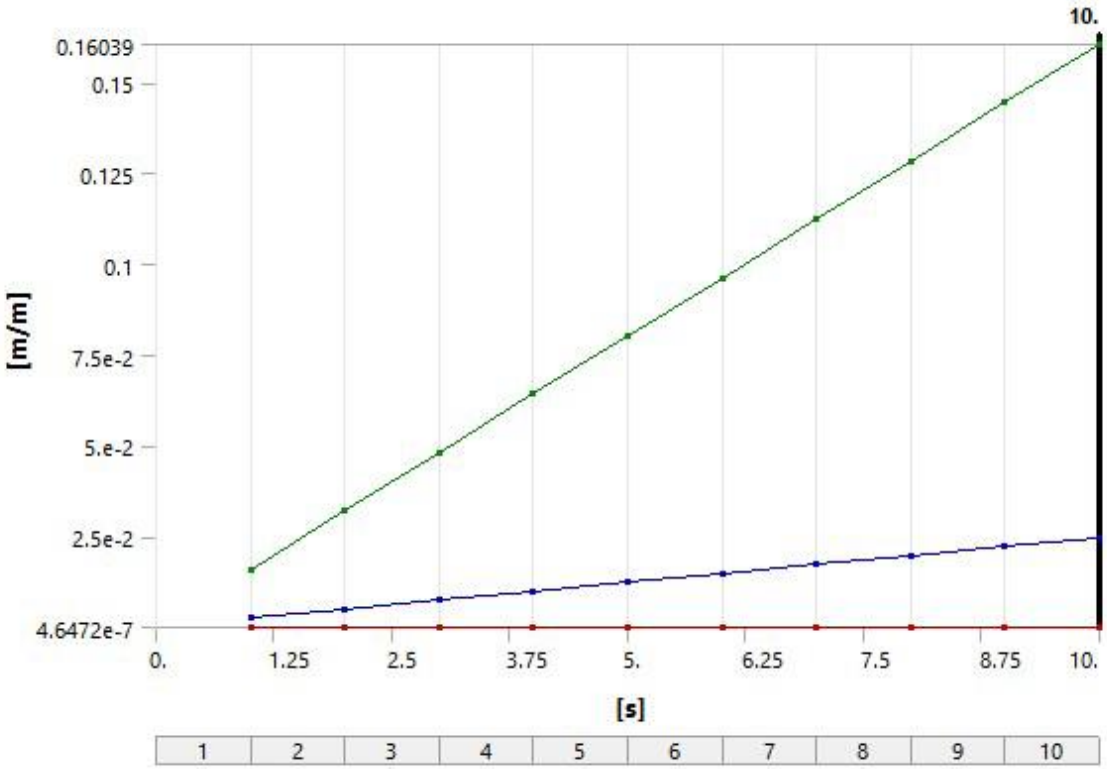

Figure 7.77 Elastic Strain Profiles: Tetrahedral 12%

7.5.3 Equivalent stress

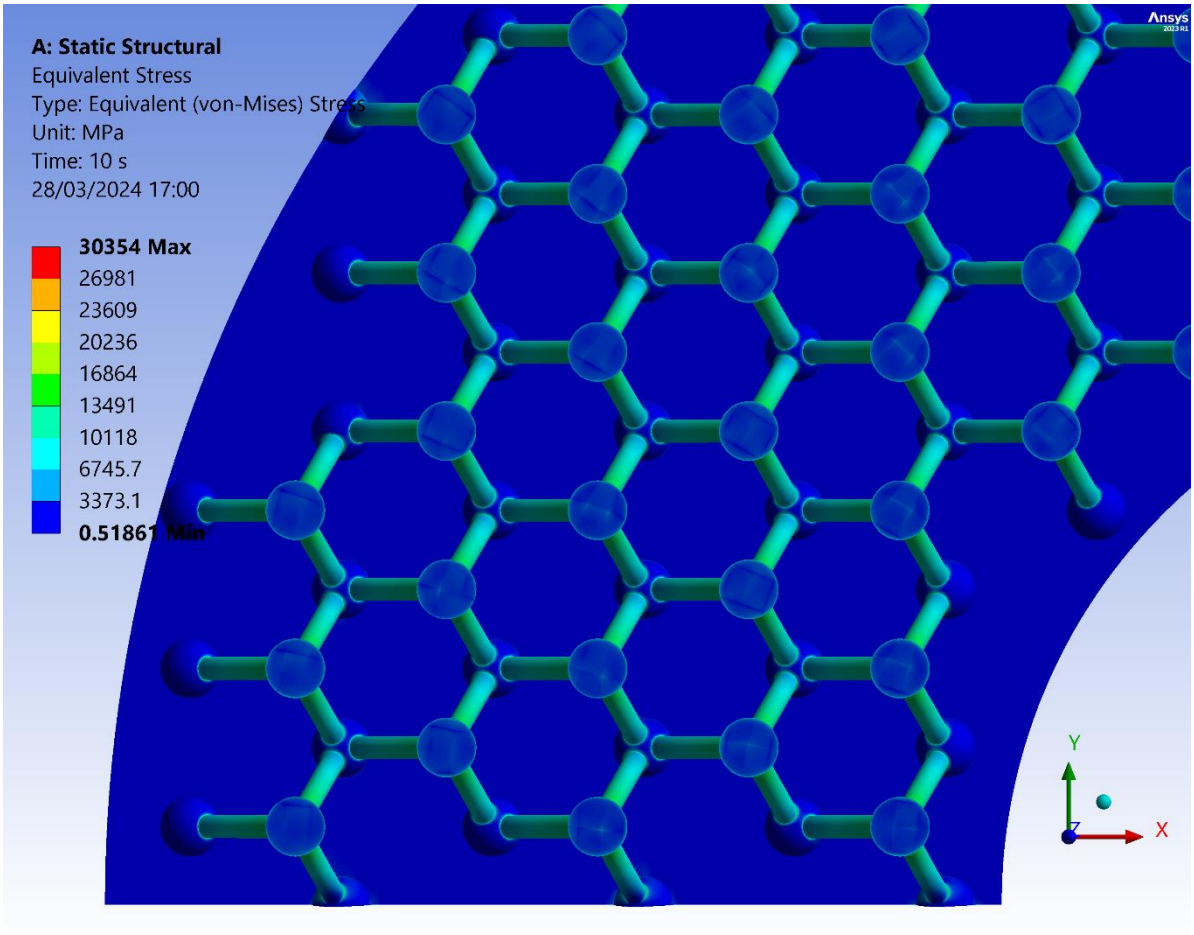

Figure 7.78 Equivalent (von-Mises) Stress contour map: Tetrahedral 12% – top view

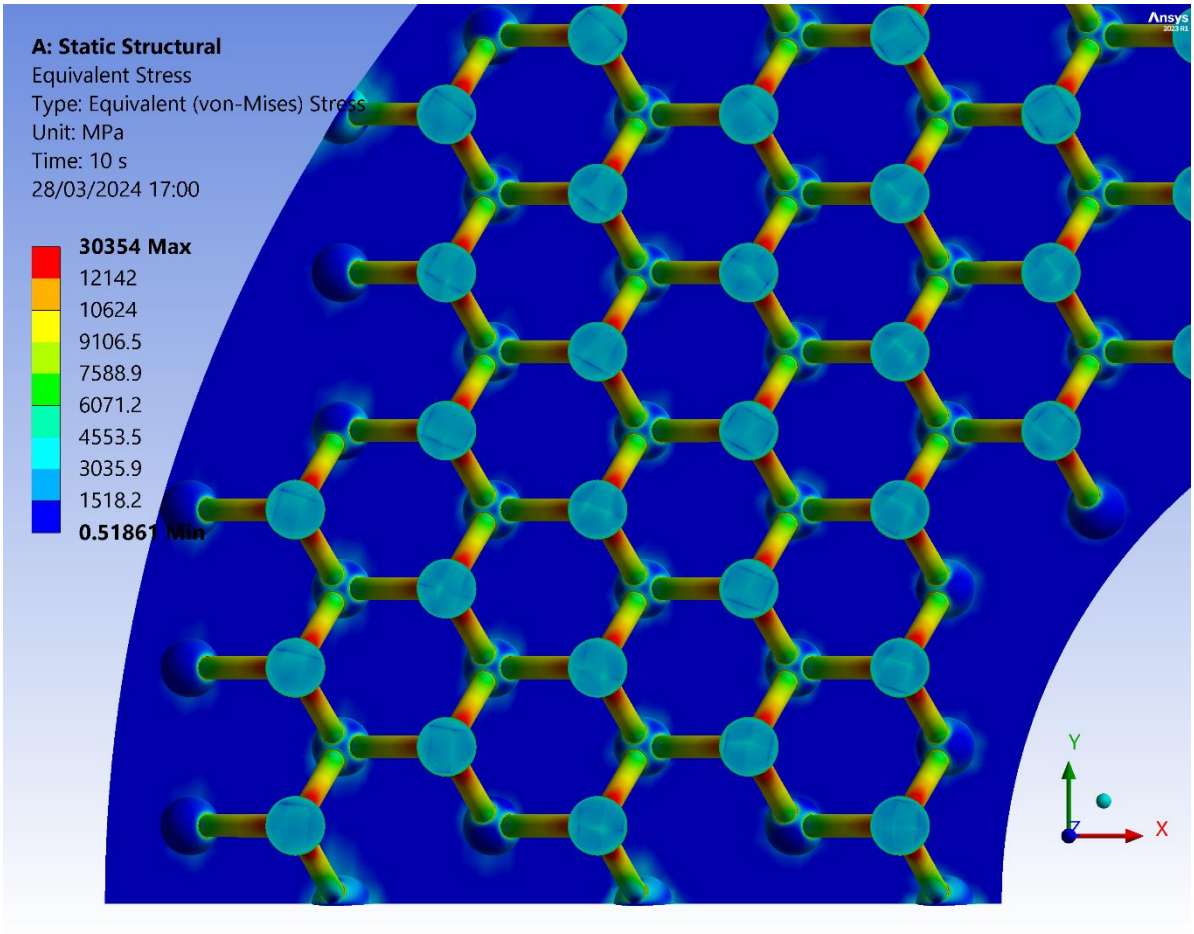

Figure 7.79 Equivalent (von-Mises) Stress filtered contour map: Tetrahedral 12% – top view

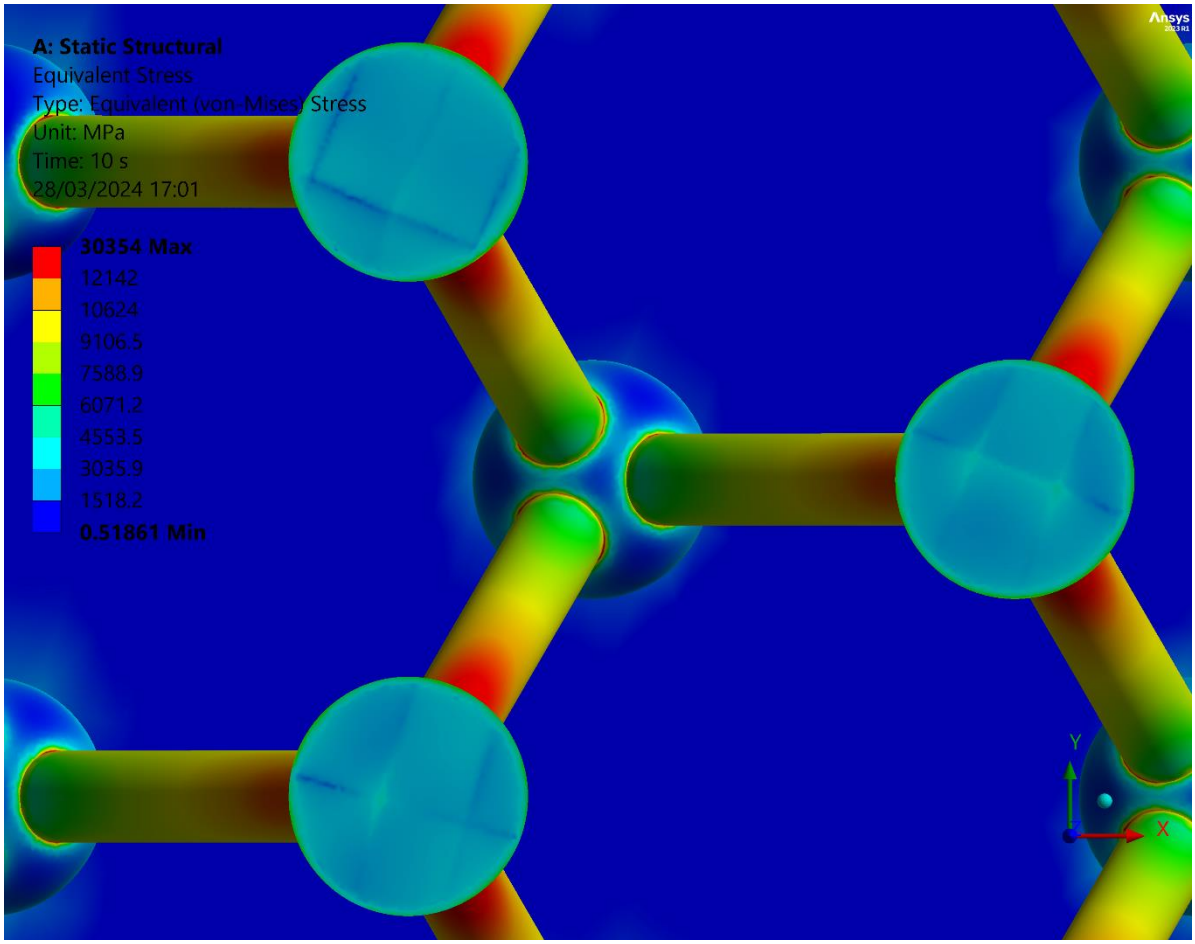

Figure 7.80 Equivalent (von-Mises) Stress filtered contour map: Tetrahedral 12% – zoomed in top view

Upon initial examination of *Figures 7.78 - 7.80*, it becomes apparent that the primary stress concentration zones are observed at the higher sections of the struts and at the edges between the nodes and the struts with values ranging from 12GPa to 6GPa, for both. This suggests that these regions experience higher stress levels compared to the nodes, and the higher the strut area, the higher the stress, too.

Table 7.23 offers a comprehensive overview of the minimum, maximum, and average stress values recorded over the designated time period. This data provides invaluable insights into the structural behavior, allowing us to discern patterns and trends in deformation responses. By analyzing this table, we can pinpoint the average and maximum stress that corresponds to the initial displacement, facilitating a deeper understanding of the structural dynamics and response mechanisms over time. Specifically, upon scrutiny, we observe that the maximum and average stress recorded stand at 30.35GPa and 4866.4MPa, respectively.

Graphs are showcased in *Figure 7.81.*

Table 7.23 Equivalent Stress – Tetrahedral 12%

t (s)	Min Stress (Pa)	Max Stress (Pa)	Avg (Pa)
1	51869	3.0354e+009	4.8664e+008
2	1.0374e+005	6.0708e+009	9.7328e+008
3	1.5558e+005	9.1062e+009	1.4599e+009
4	2.0748e+005	1.2142e+010	1.9466e+009
5	2.5930e+005	1.5177e+010	2.4332e+009
6	3.1109e+005	1.8212e+010	2.9199e+009
7	3.6295e+005	2.1248e+010	3.4065e+009
8	4.1495e+005	2.4283e+010	3.8931e+009
9	4.6681e+005	2.7319e+010	4.3798e+009
10	5.1861e+005	3.0354e+010	4.8664e+009

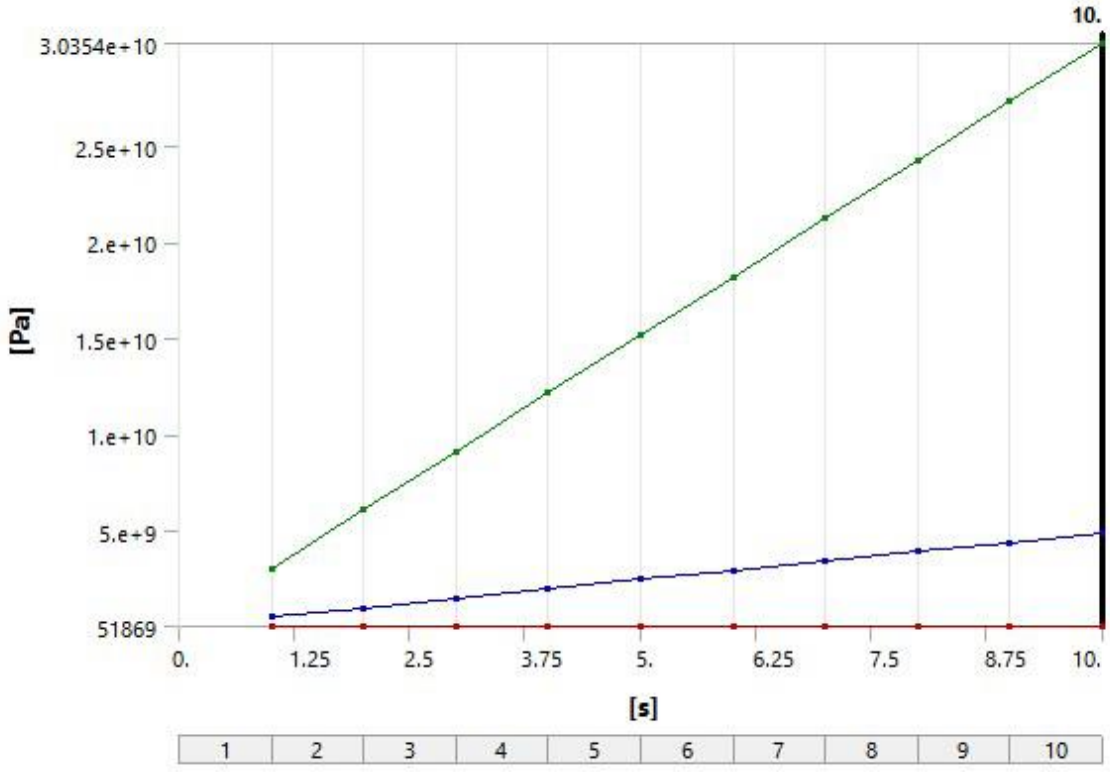

Figure 7.81 Equivalent (Von Mises) Stress Profiles: Tetrahedral 12%

7.5.4 Force reaction

Table 7.24 portrays the application of force (F) over a duration of time (t), where negative values denote compressive force. Over the course of time, there's a progressive escalation in the magnitude of compressive force equaling up to 3.44GN, indicative of sustained pressure exertion. This implies an ongoing deformation or compression within the material or structure under examination. The consistent trajectory underscores the stability and uniformity of the applied force throughout the designated time frame. Further investigation could delve into associating these force magnitudes with particular mechanical reactions or structural responses. Correspondingly, *Figure 7.82* visually depicts the force reaction trend across time.

Table 7.24 Force reaction – tetrahedral 12%

t (s)	F(N)
1	-3,44E+05
2	-6,88E+05
3	-1,03E+05
4	-1,38E+05
5	-1,72E+06
6	-2,06E+06
7	-2,41E+06
8	-2,75E+06
9	-3,10E+06
10	-3,44E+06

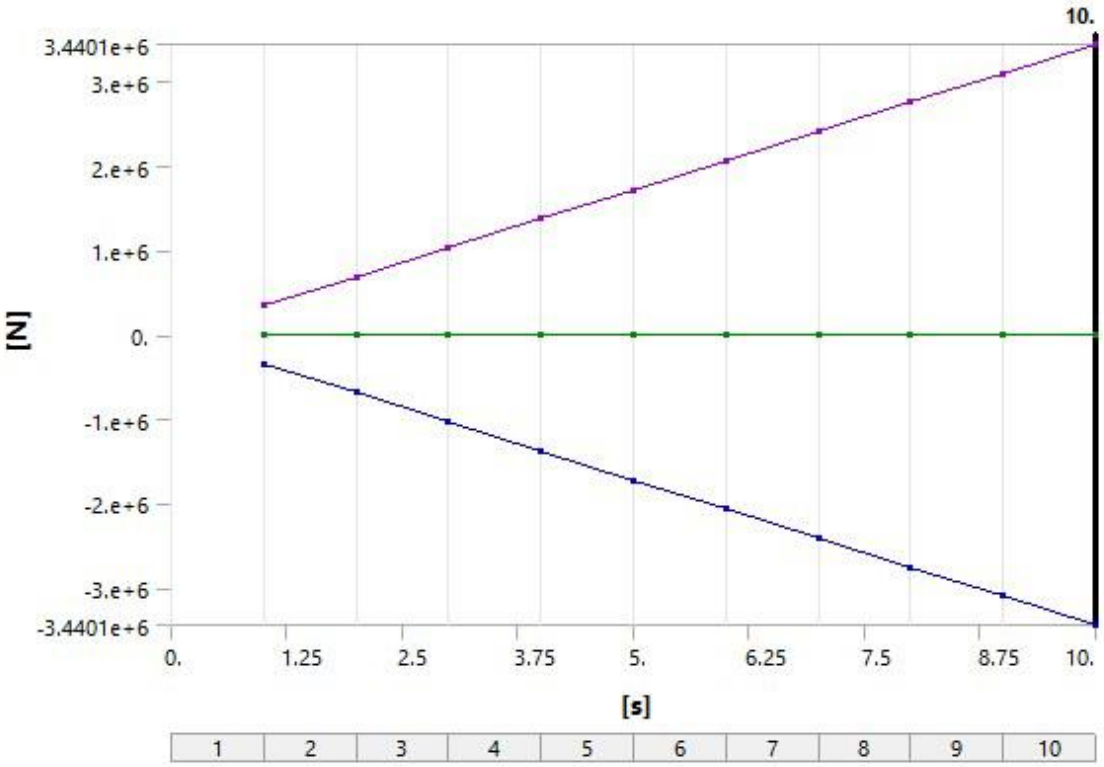

Figure 7.82 Force Reaction Profiles: Tetrahedral 12%

7.6 Tetrahedral 50%

7.6.1 Total deformation

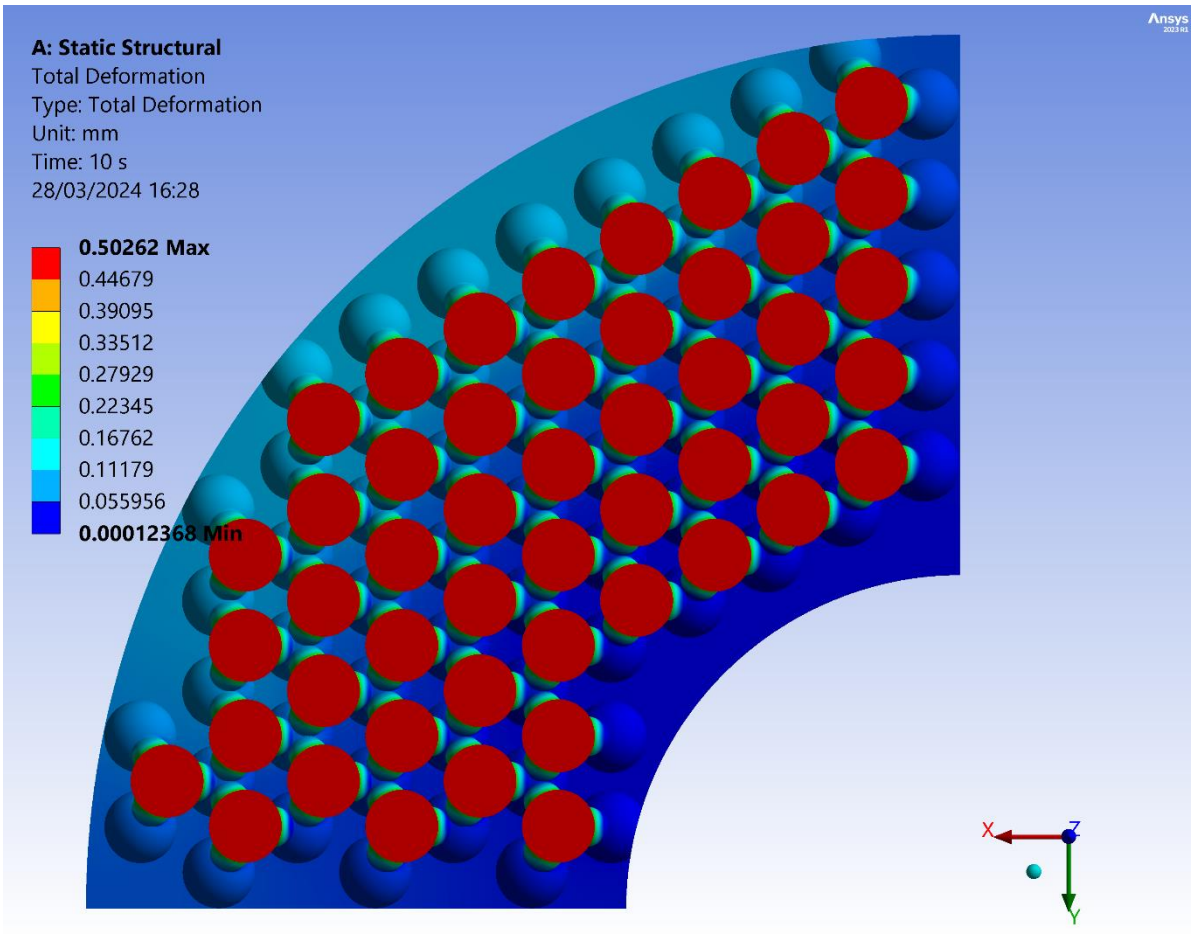

Figure 7.83 Total deformation contour map: Tetrahedral 50% – top view

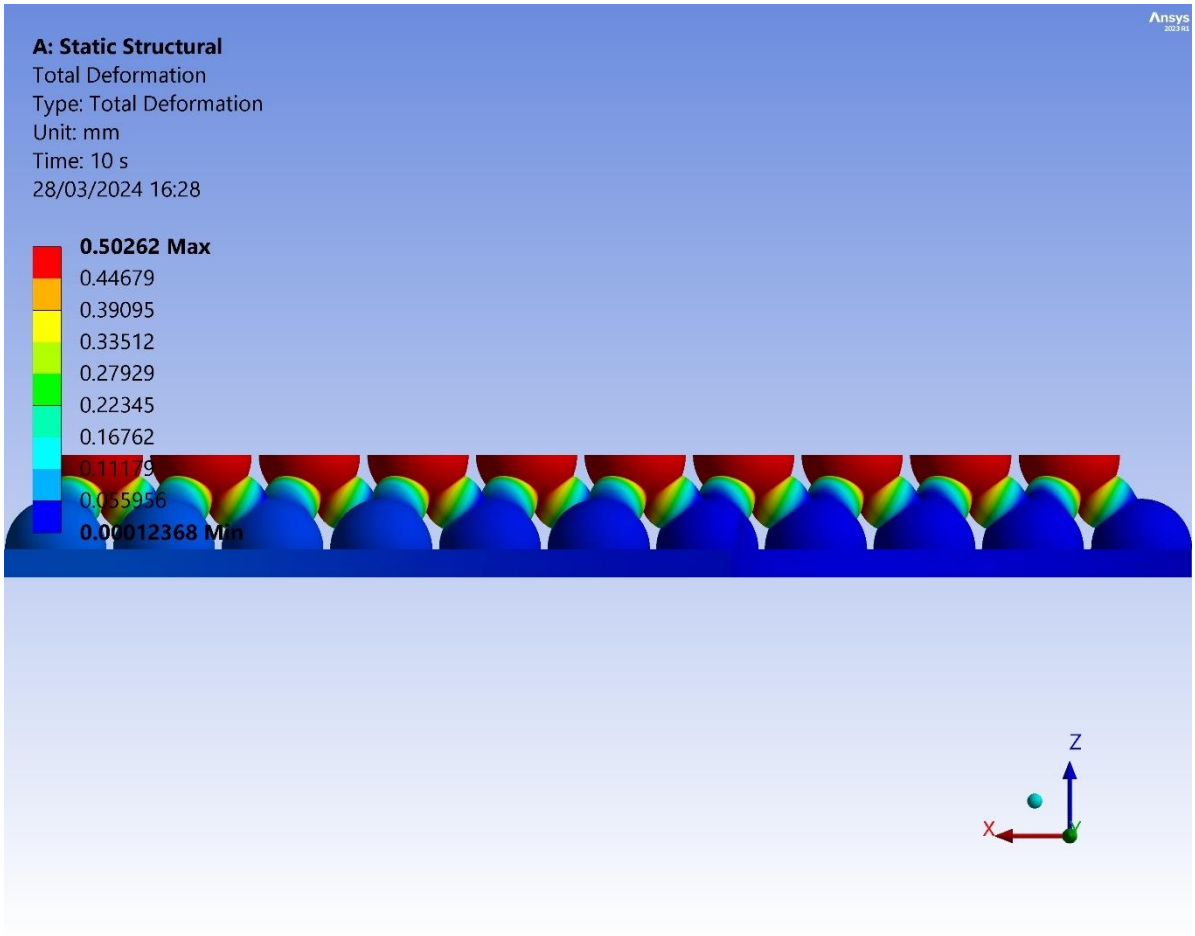

Figure 7.84 Total deformation contour map: Tetrahedral 50% – side view

Upon examining *Figure 7.83* and *Figure 7.84*, it's evident that the upper nodes within the lattice structure undergo substantial deformation, consistent with previous models. The struts positioned between the top and bottom nodes display a gradient deformation ranging from 0.45mm to 0, demonstrating a decreasing trend towards the lower nodes. Noteworthy is also the fact that the gradient deformation is not perpendicular to the direction of the strut but from fillet to filet diagonally. The thickness of the struts is the reason behind this phenomenon and also, behind the minimal deformation of the bottom nodes. The similar phenomenon could not easily be observed because of the thinner struts.

Table 7.6 offers a comprehensive overview of the minimum, maximum, and average deformation values recorded over the designated time period. This data provides invaluable insights into the structural behavior, allowing us to discern patterns and trends in deformation responses. By analyzing this table, we can pinpoint the average deformation that corresponds to the initial displacement, facilitating a deeper understanding of the structural dynamics and response mechanisms over time. Specifically, upon scrutiny, we observe that the

maximum and average deformation recorded stand at 0.503mm and 0.249mm respectively, shedding light on the extent of structural deformation under varying conditions.

Graphs are showcased in *Figure 7.85.*

Table 7.25 Total deformation – Tetrahedral 50%

t(s)	Min Deformation (m)	Max Deformation (m)	Avg deformation (m)
0.2	2.7947e-006	1.4541e-005	9.5256e-006
0.4	3.5389e-006	2.4659e-005	1.546e-005
0.6	3.5761e-006	3.3691e-005	2.0082e-005
0.9	3.5875e-006	4.7625e-005	2.6803e-005
1.	3.5007e-006	5.2379e-005	2.9058e-005
1.2	3.3693e-006	6.1995e-005	3.3581e-005
1.4	3.2777e-006	7.1711e-005	3.8115e-005
1.7	3.2276e-006	8.6419e-005	4.4959e-005
2.	3.0374e-006	1.0122e-004	5.1832e-005
2.2	2.9145e-006	1.1112e-004	5.6427e-005
2.4	2.8242e-006	1.2104e-004	6.1027e-005
2.6	2.7844e-006	1.3097e-004	6.5636e-005
2.9	2.8388e-006	1.4589e-004	7.256e-005
3.	2.7911e-006	1.5087e-004	7.4872e-005
3.2	2.7006e-006	1.6083e-004	7.9498e-005
3.4	2.5984e-006	1.708e-004	8.4136e-005
3.7	2.5125e-006	1.8576e-004	9.1102e-005
4.	2.4234e-006	2.0073e-004	9.8087e-005
4.2	2.282e-006	2.1071e-004	1.0275e-004
4.4	2.1697e-006	2.207e-004	1.0743e-004
4.7	2.0851e-006	2.3568e-004	1.1448e-004
5	2.0461e-006	2.5067e-004	1.2155e-004
5.2	1.9318e-006	2.6067e-004	1.2629e-004
5.4	1.8649e-006	2.7068e-004	1.3104e-004
5.7	1.8376e-006	2.8569e-004	1.3819e-004
6.	1.649e-006	3.007e-004	1.4539e-004
6.2	1.597e-006	3.1072e-004	1.5021e-004
6.4	1.643e-006	3.2074e-004	1.5506e-004
6.7	1.8394e-006	3.3577e-004	1.6239e-004
7.	1.9277e-006	3.5082e-004	1.698e-004
7.2	1.8387e-006	3.6086e-004	1.7479e-004

7.4	1.9414e-006	3.709e-004	1.7981e-004
7.7	1.974e-006	3.8598e-004	1.8743e-004
8.	2.1309e-006	4.0108e-004	1.9513e-004
8.2	2.1251e-006	4.1117e-004	2.0033e-004
8.4	2.1731e-006	4.2127e-004	2.0557e-004
8.7	1.8205e-006	4.3643e-004	2.1354e-004
9.	7.9508e-007	4.5163e-004	2.2164e-004
9.2	1.6277e-007	4.6178e-004	2.2711e-004
9.4	1.1255e-007	4.7196e-004	2.3263e-004
9.6	1.9741e-007	4.8216e-004	2.382e-004
9.9	1.164e-007	4.975e-004	2.4668e-004
10.	1.2368e-007	5.0262e-004	2.4953e-004

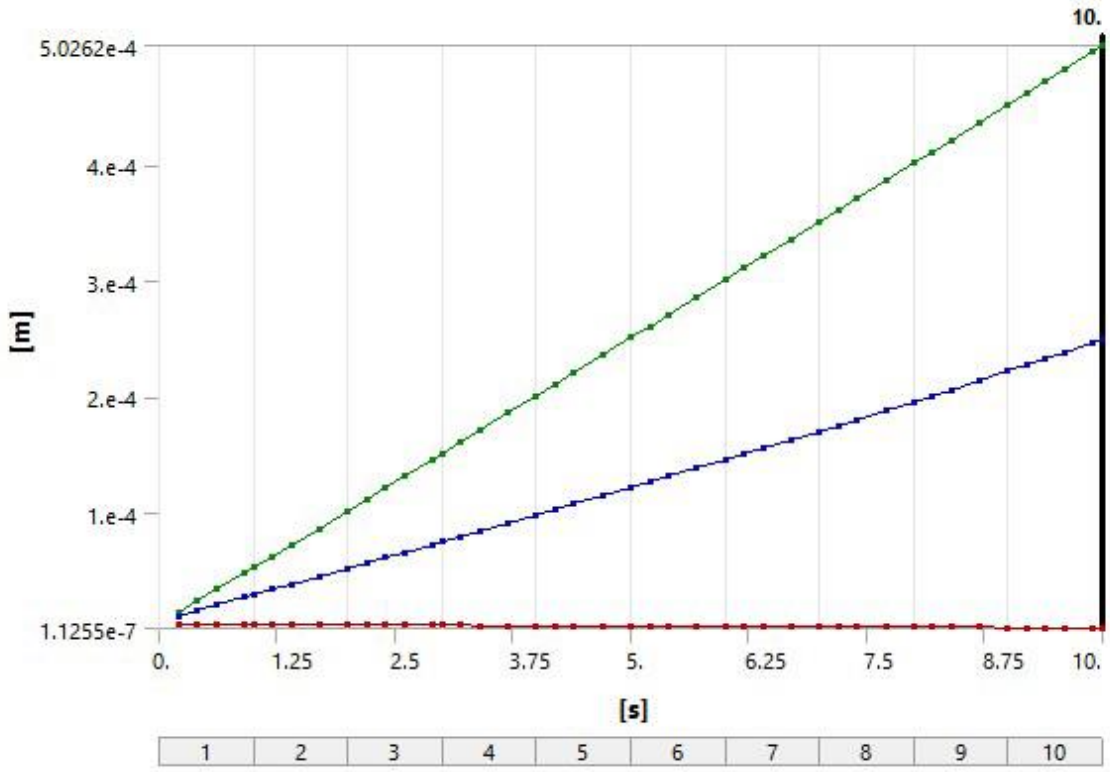

Figure 7.85 Deformation Profiles: Tetrahedral 50%

7.6.2 Equivalent elastic strain

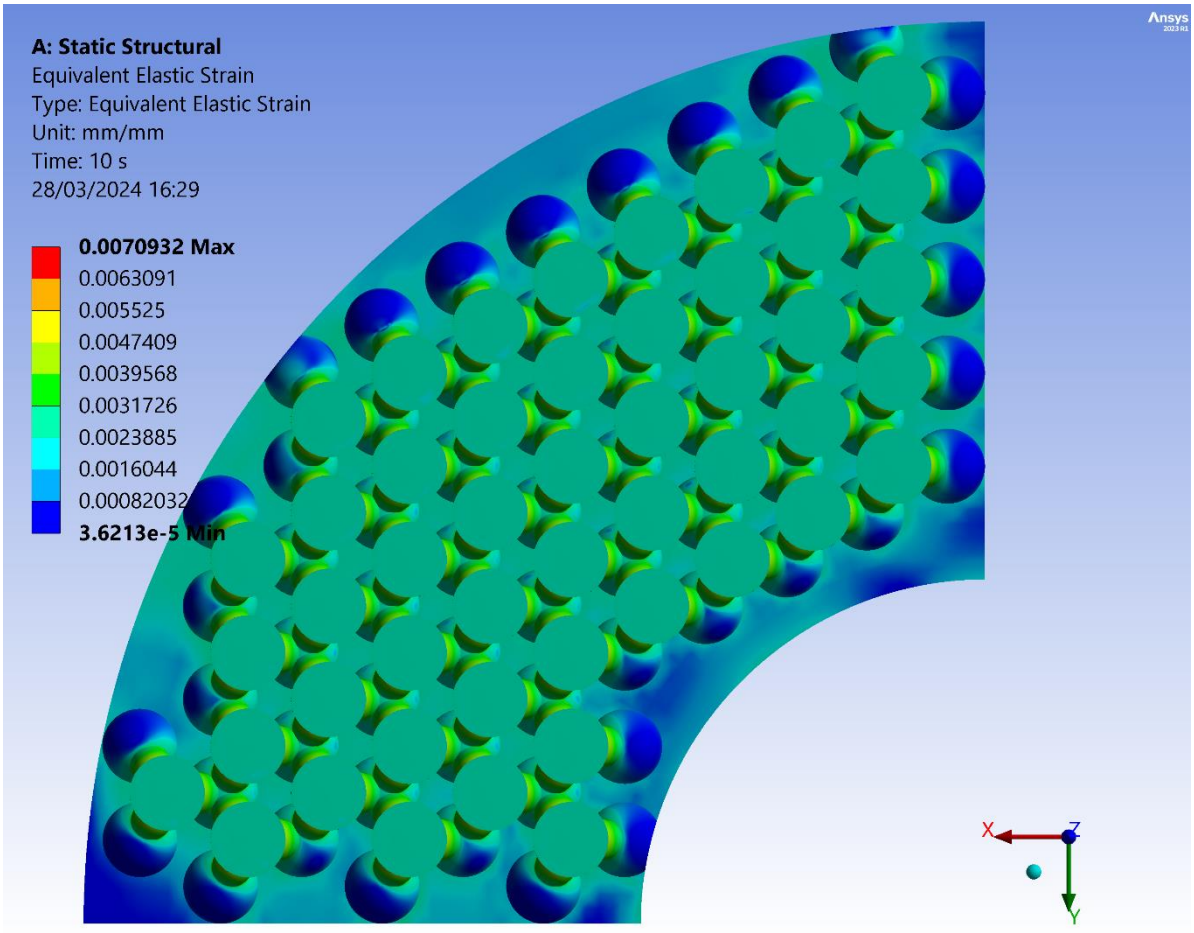

Figure 7.86 Equivalent Elastic Strain contour map: Tetrahedral 50% – top view

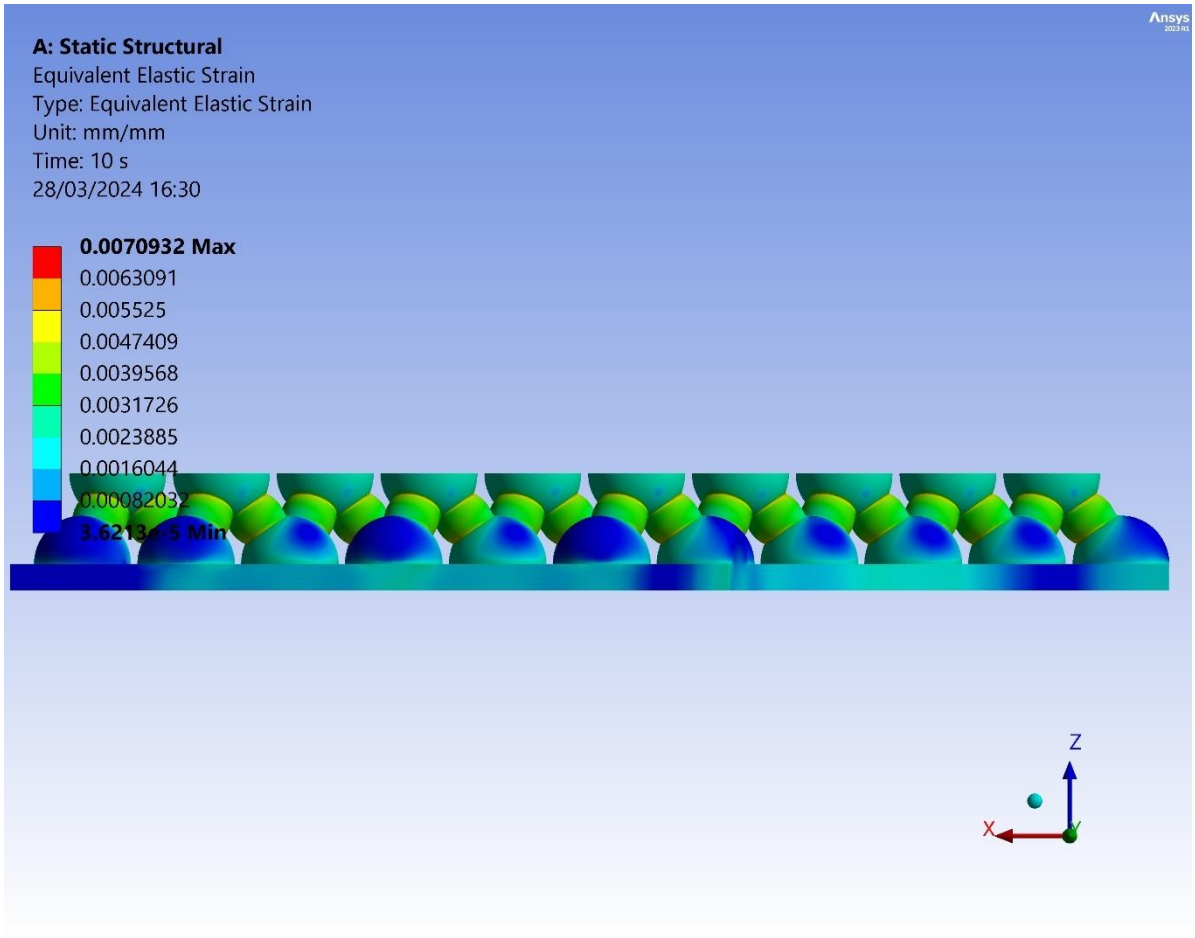

Figure 7.87 Equivalent Elastic Strain contour map: Tetrahedral 50% – side view

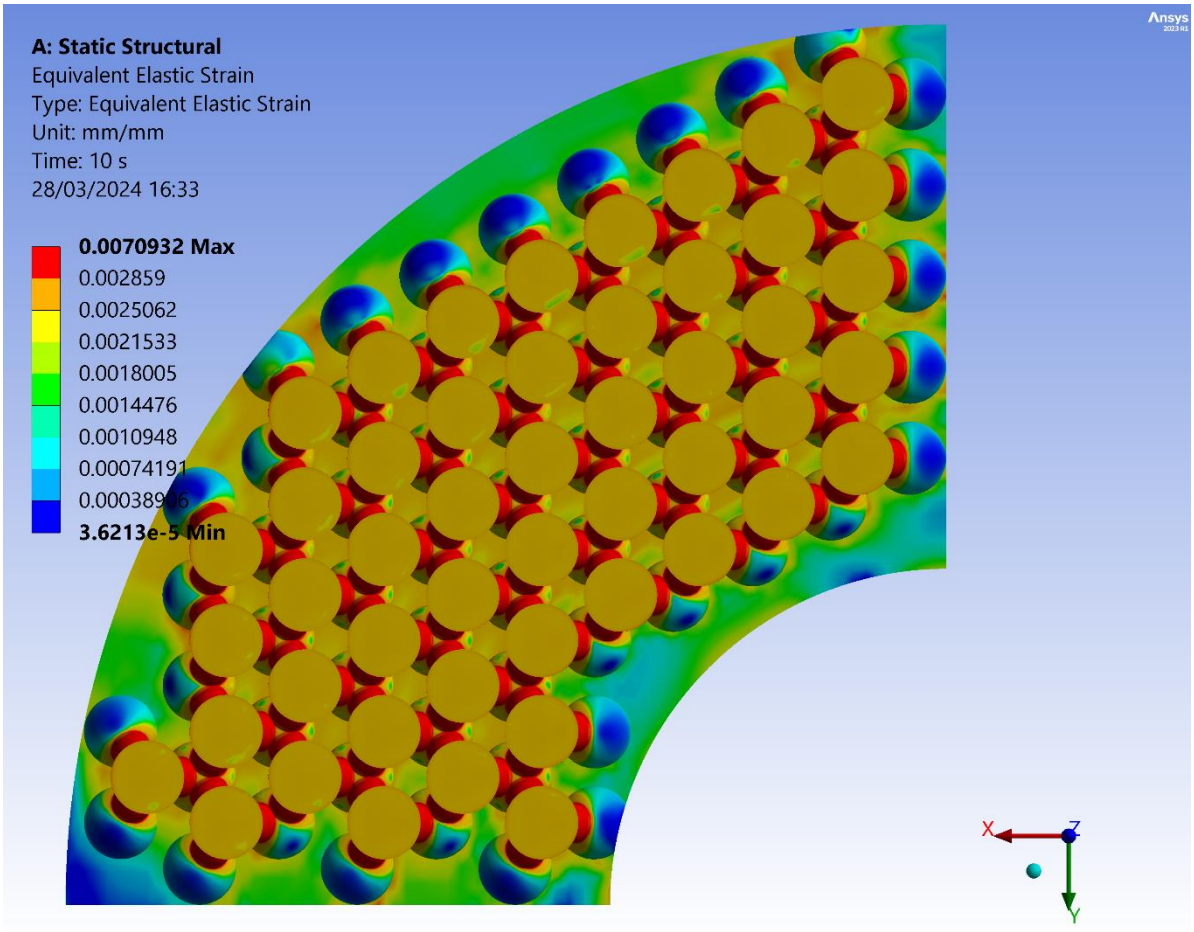

Figure 7.88 Equivalent Elastic Strain contour map: Tetrahedral 50% – top view

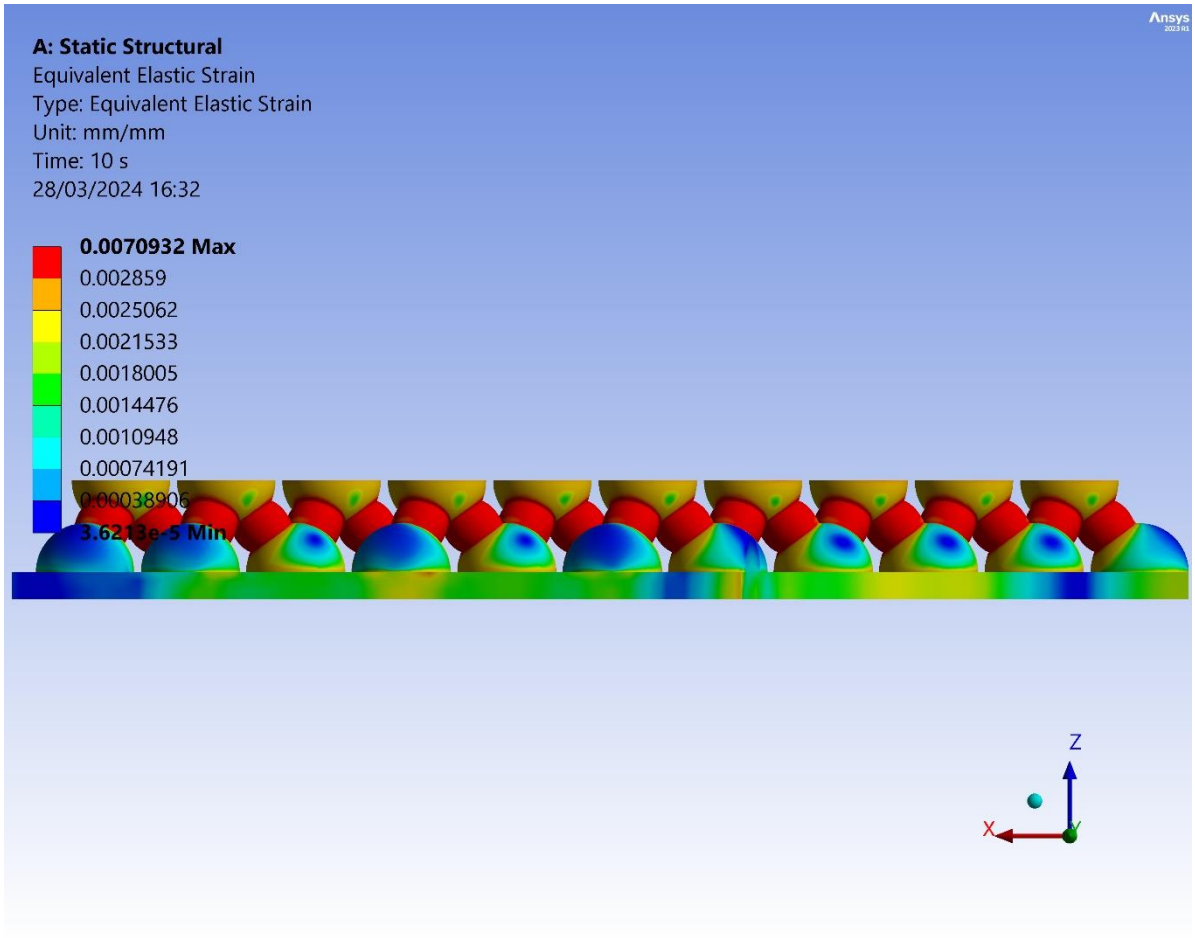

Figure 7.89 Equivalent Elastic Strain filtered contour map: Tetrahedral 50% – side view

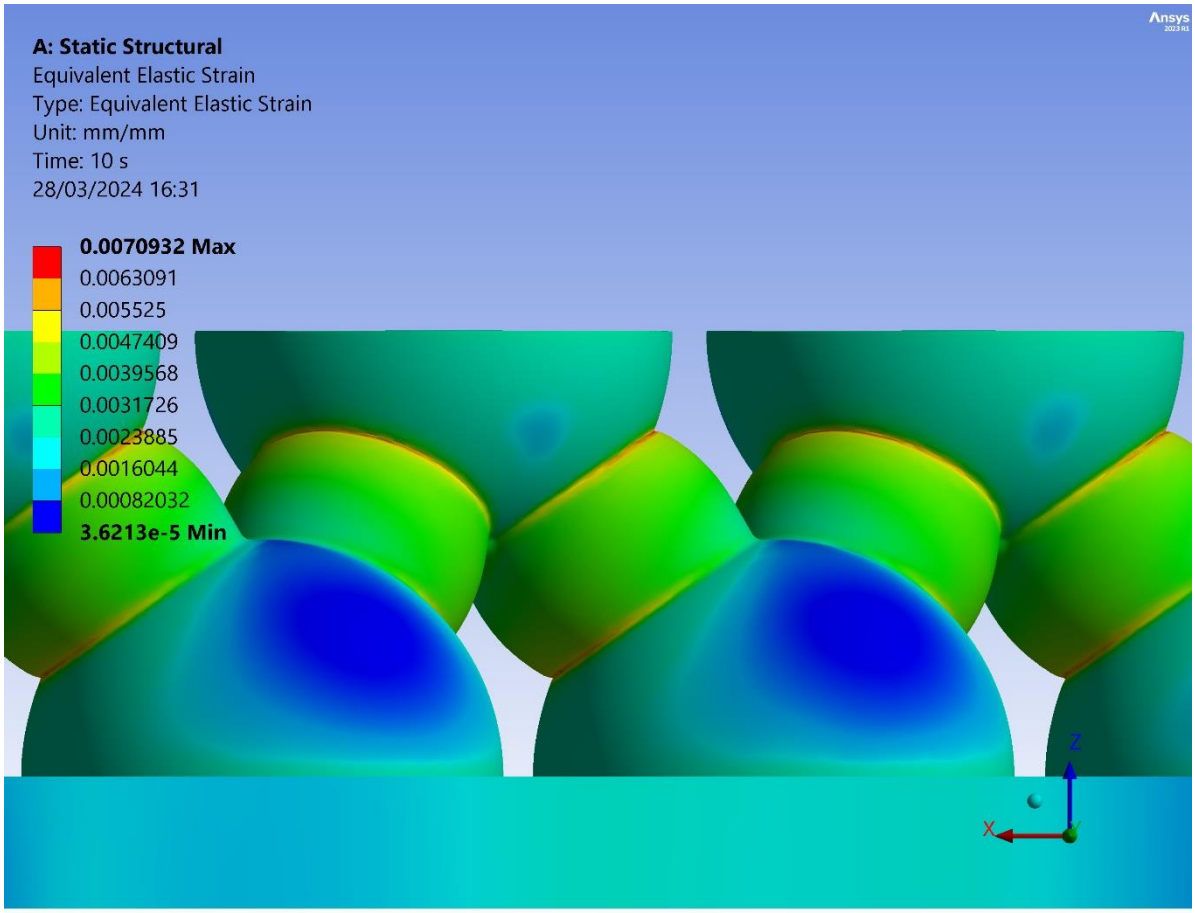

Figure 7.90 Equivalent Elastic Strain filtered contour map: Tetrahedral 50% – zoomed in side view

Like the previous model, *Figures 7.86-7.88* highlight the significance of incomplete nodes as focal points for strain concentration, showcasing notably elevated values compared to the surrounding geometry, while areas without support display null strain. This localized strain concentration results in heightened elastic strain at the contact areas of the plates, especially noticeable in the outer regions of the model. The filtered views provided in *Figures 7.87 and 7.89* offer improved clarity regarding this elastic strain phenomenon. Notably, the struts exhibit higher strain energy compared to the nodes, with values ranging from 0.003mm/mm to 0.004mm/mm and 0.001mm/mm to 0.003mm/mm, respectively. Moreover, *Figure 7.90* illustrates that the edges between struts and nodes act as regions where higher elastic strain is concentrated, with values reaching up to 0.0065mm/mm, closely resembling those observed in the Tetrahedral 12% configuration.

Table 7.26 offers a comprehensive overview of the minimum, maximum, and average elastic strain values recorded over the designated time period. This data provides invaluable insights into the structural behavior, allowing us to discern patterns and trends in deformation responses. By analyzing this table, we can pinpoint

the average elastic strain that corresponds to the initial displacement, facilitating a deeper understanding of the structural dynamics and response mechanisms over time. Specifically, upon scrutiny, we observe that the maximum and average elastic strain recorded stand at 0.007mm/mm and 0.003mm/mm respectively.

Graphs are showcased in *Figure 7.91.*

Table 7.26 Elastic Strain Data – Tetrahedral 50%

t	Min Elastic Strain (mm/mm)	Max Elastic Strain (mm/mm)	Average Elastic Strain (mm/mm)
0.2	2.9507e-006	2.8184e-003	1.317e-003
0.4	2.0029e-006	2.8523e-003	1.6327e-003
0.6	4.2459e-006	2.9298e-003	1.7303e-003
0.9	7.3603e-006	3.0053e-003	1.8074e-003
1.	7.5607e-006	3.0635e-003	1.827e-003
1.2	6.4671e-006	3.1857e-003	1.8617e-003
1.4	5.1914e-006	3.2898e-003	1.8938e-003
1.7	3.2768e-006	3.4542e-003	1.9397e-003
2.	3.3569e-006	3.6145e-003	1.9843e-003
2.2	4.4091e-006	3.7195e-003	2.0133e-003
2.4	5.5008e-006	3.823e-003	2.0423e-003
2.6	6.7129e-006	3.9252e-003	2.0711e-003
2.9	8.3952e-006	4.0752e-003	2.1136e-003
3.	8.911e-006	4.1248e-003	2.1276e-003
3.2	9.9097e-006	4.2228e-003	2.155e-003
3.4	1.0659e-005	4.3195e-003	2.1827e-003
3.7	1.1713e-005	4.462e-003	2.2232e-003
4.	1.252e-005	4.602e-003	2.2627e-003
4.2	1.2932e-005	4.6941e-003	2.2884e-003
4.4	1.3211e-005	4.7854e-003	2.3137e-003
4.7	1.3301e-005	4.9202e-003	2.3504e-003
5	1.3022e-005	5.0531e-003	2.3854e-003
5.2	1.276e-005	5.1408e-003	2.4078e-003
5.4	1.266e-005	5.2277e-003	2.43e-003
5.7	1.2682e-005	5.3563e-003	2.4623e-003
6.	1.2936e-005	5.4832e-003	2.4936e-003
6.2	1.3186e-005	5.567e-003	2.514e-003
6.4	1.1002e-005	5.6503e-003	2.534e-003
6.7	1.4201e-005	5.7738e-003	2.5633e-003
7.	1.4718e-005	5.8962e-003	2.5916e-003

7.2	1.4719e-005	5.9771e-003	2.6098e-003
7.4	1.5053e-005	6.0575e-003	2.6277e-003
7.7	1.5292e-005	6.1768e-003	2.6536e-003
8.	1.4966e-005	6.2949e-003	2.6786e-003
8.2	1.4495e-005	6.373e-003	2.6948e-003
8.4	1.3402e-005	6.4507e-003	2.7106e-003
8.7	9.4858e-006	6.5661e-003	2.7335e-003
9.	5.1241e-006	6.6802e-003	2.7556e-003
9.2	9.3513e-006	6.7556e-003	2.7699e-003
9.4	1.6468e-005	6.8319e-003	2.7838e-003
9.6	2.137e-005	6.9191e-003	2.7975e-003
9.9	4.4278e-005	7.0497e-003	2.8175e-003
10.	3.6213e-005	7.0932e-003	2.8241e-003

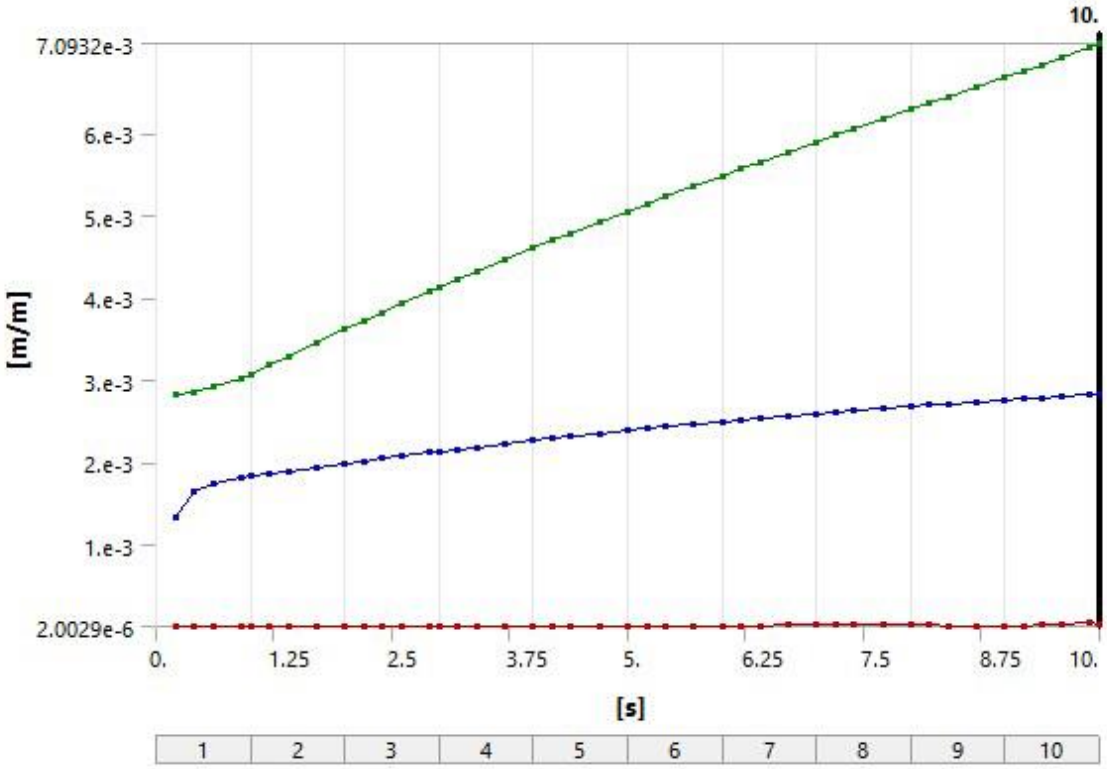

Figure 7.91 Elastic Strain Profiles: Tetrahedral 50%

7.6.3 Equivalent stress

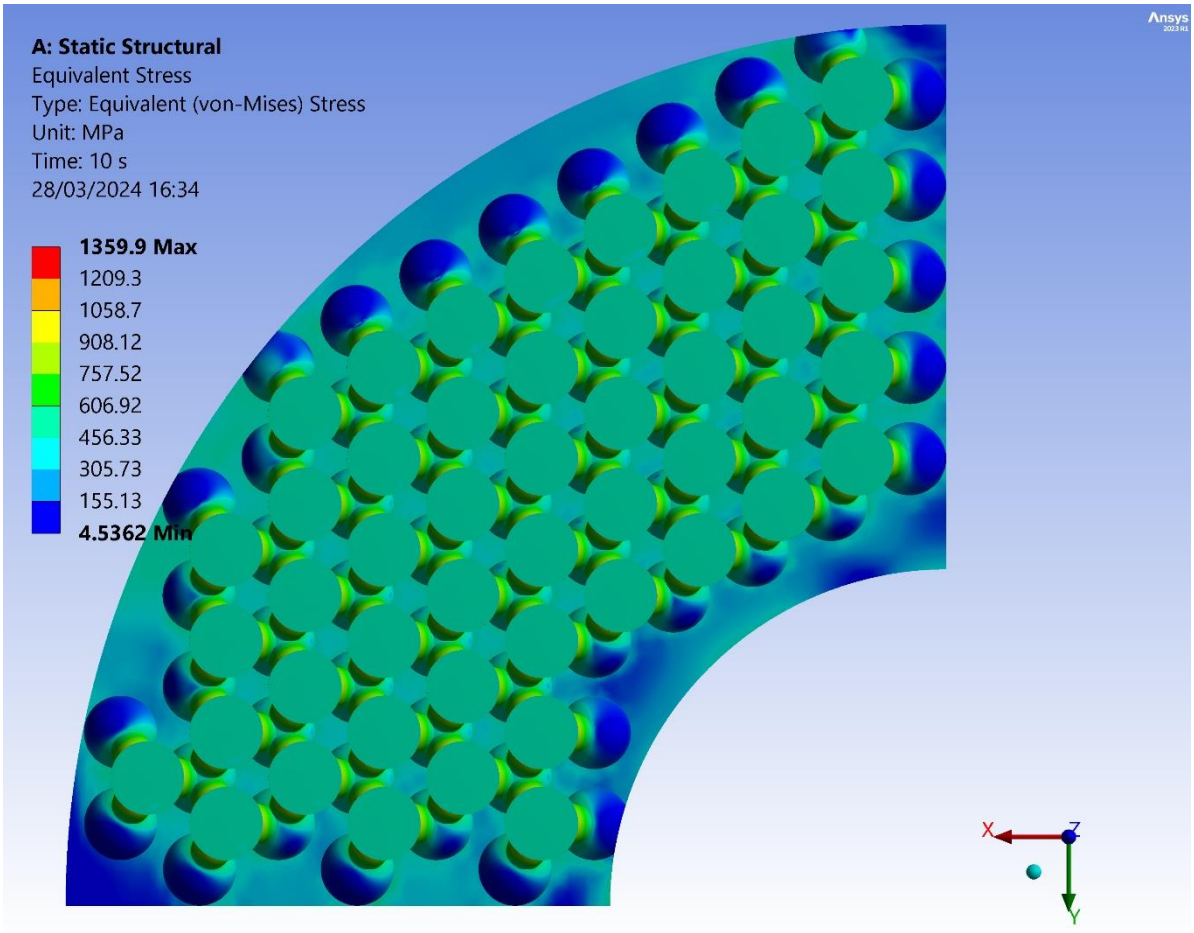

Figure 7.92 Equivalent (von-Mises) Stress contour map: Tetrahedral 50% – top view

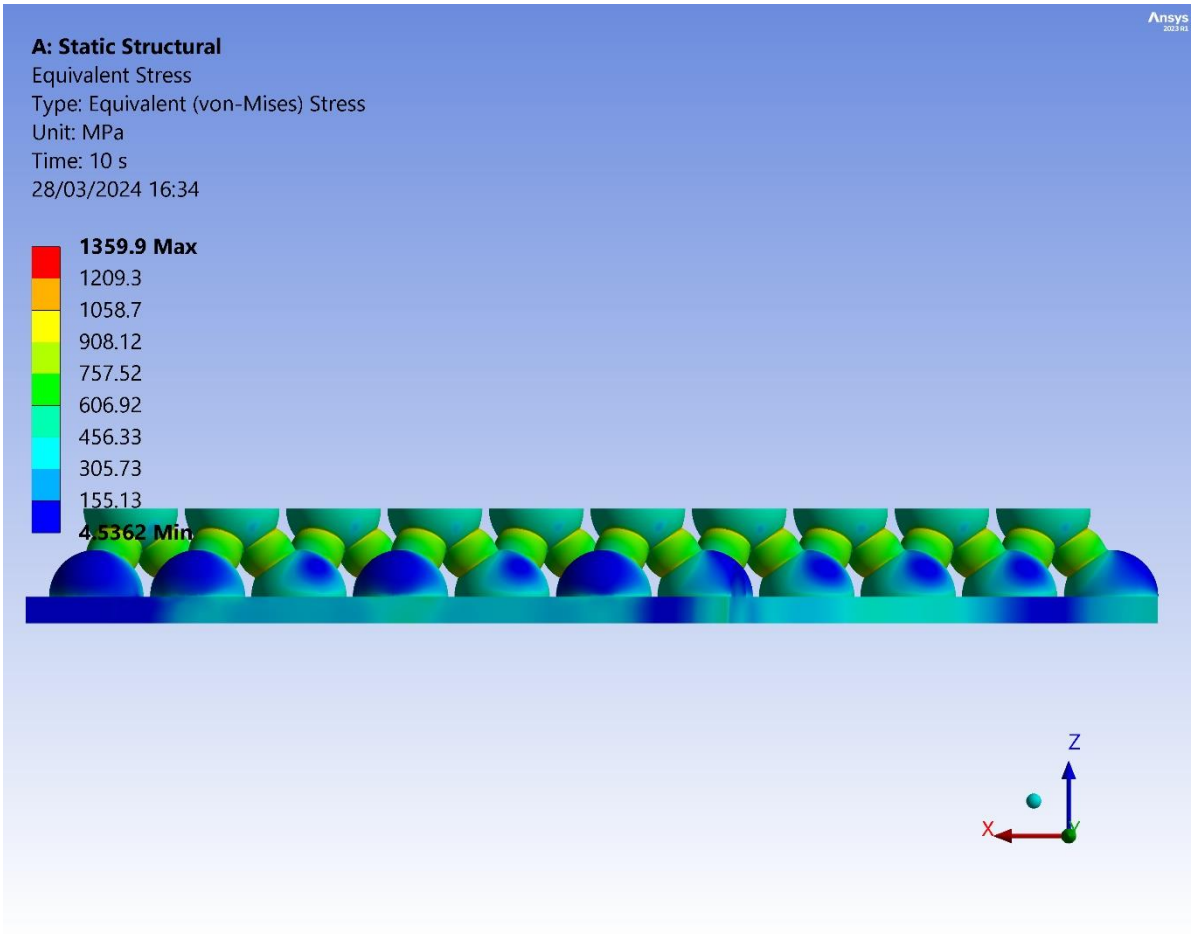

Figure 7.93 Equivalent (von-Mises) Stress contour map: Tetrahedral 50% – side view

Upon initial scrutiny of *Figures 7.92 and 7.93*, it's apparent that the primary stress concentration zones coincide with the struts and the edges between the struts and nodes, with stress ranges spanning from 600MPa to 900MPa and 1000MPa to 1200MPa, respectively. However, it's crucial to note that these stress levels do not reach critical thresholds. In contrast with the tetrahedral 12% model, struts accept significantly less stress, because of the strut's diameter. This suggests that while stress concentrations are present in these regions, they remain within acceptable bounds and can be limited by thickening the struts.

Table 7.27 offers a comprehensive overview of the minimum, maximum, and average stress values recorded over the designated time period. This data provides invaluable insights into the structural behavior, allowing us to discern patterns and trends in deformation responses. By analyzing this table, we can pinpoint the average and maximum stress that corresponds to the initial displacement, facilitating a deeper understanding of the structural dynamics and response mechanisms over time. Specifically, upon scrutiny, we observe that the maximum and average stress recorded stand at 1359.9MPa and 543.3MPa, respectively.

Graphs are showcased in *Figure 7.94.*

Table 7.27 Stress Data – Tetrahedral 50%

t(s)	Min Stress (Pa)	Max Stress (Pa)	Average (Pa)
0.2	4.9528e+005	5.4272e+008	2.546e+008
0.4	3.824e+005	5.4425e+008	3.1511e+008
0.6	7.7068e+005	5.6982e+008	3.3352e+008
0.9	1.2926e+006	5.772e+008	3.4817e+008
1.	1.1909e+006	5.8769e+008	3.5191e+008
1.2	9.5026e+005	6.0965e+008	3.5851e+008
1.4	9.6787e+005	6.3146e+008	3.647e+008
1.7	5.4991e+005	6.634e+008	3.7353e+008
2.	5.201e+005	6.9452e+008	3.8211e+008
2.2	7.4663e+005	7.1493e+008	3.877e+008
2.4	9.8958e+005	7.3499e+008	3.9333e+008
2.6	1.0659e+006	7.5478e+008	3.9888e+008
2.9	1.1568e+006	7.8385e+008	4.0711e+008
3.	1.1812e+006	7.9347e+008	4.0982e+008
3.2	1.2116e+006	8.1244e+008	4.1512e+008
3.4	1.2076e+006	8.3116e+008	4.2049e+008
3.7	1.1793e+006	8.5872e+008	4.2832e+008
4.	1.1375e+006	8.858e+008	4.3598e+008
4.2	1.1152e+006	9.0361e+008	4.4095e+008
4.4	1.1285e+006	9.2124e+008	4.4585e+008
4.7	1.2574e+006	9.4729e+008	4.5293e+008
5	1.4611e+006	9.7296e+008	4.5971e+008
5.2	1.4234e+006	9.8991e+008	4.6402e+008
5.4	1.5008e+006	1.0067e+009	4.6831e+008
5.7	1.8825e+006	1.0315e+009	4.7452e+008
6.	2.4813e+006	1.056e+009	4.8055e+008
6.2	2.5293e+006	1.0722e+009	4.8443e+008
6.4	2.1245e+006	1.0883e+009	4.8828e+008
6.7	2.7257e+006	1.1121e+009	4.9389e+008
7.	2.8229e+006	1.1357e+009	4.993e+008
7.2	2.82e+006	1.1514e+009	5.0275e+008

7.4	2.8782e+006	1.1669e+009	5.0616e+008
7.7	2.9064e+006	1.1899e+009	5.1109e+008
8.	2.8438e+006	1.2127e+009	5.1584e+008
8.2	2.748e+006	1.2278e+009	5.1889e+008
8.4	2.5275e+006	1.2428e+009	5.2189e+008
8.7	1.7144e+006	1.265e+009	5.2623e+008
9.	8.8866e+005	1.2871e+009	5.304e+008
9.2	1.7511e+006	1.3016e+009	5.3309e+008
9.4	2.3206e+006	1.3161e+009	5.3573e+008
9.6	3.1385e+006	1.3305e+009	5.3831e+008
9.9	5.2708e+006	1.3519e+009	5.421e+008
10.	4.5362e+006	1.3599e+009	5.4335e+008

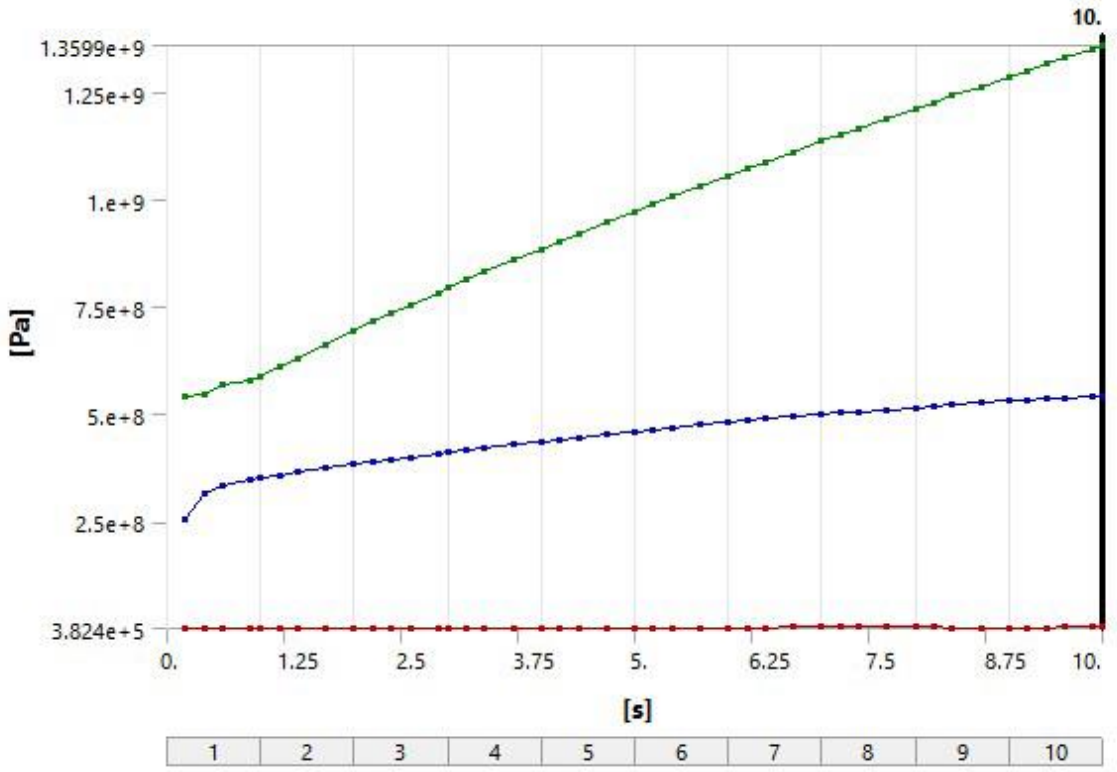

Figure 7.94 Equivalent (Von Mises) Stress Profiles: Tetrahedral 50%

7.6.4 Strain energy

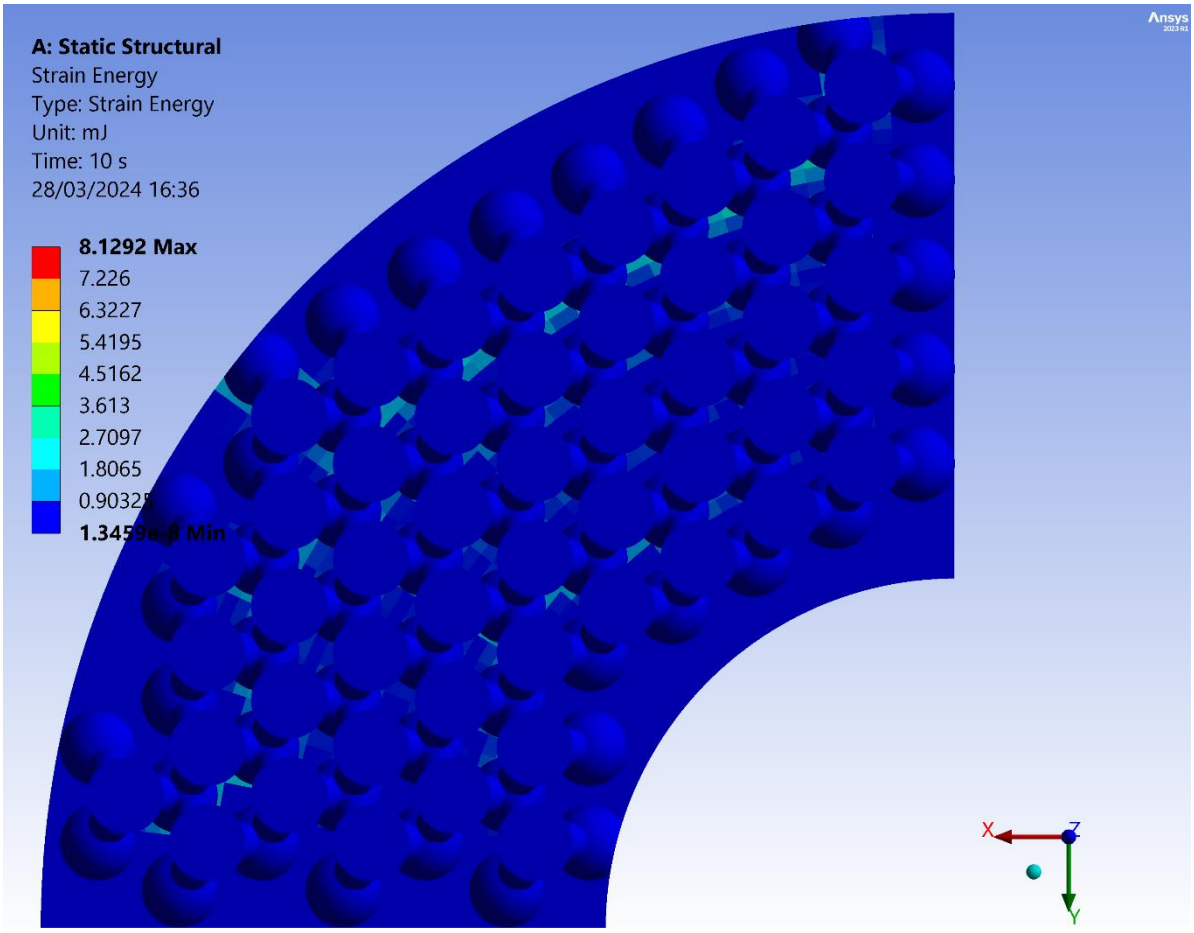

Figure 7.95 Strain Energy contour map: Tetrahedral 50% – top view

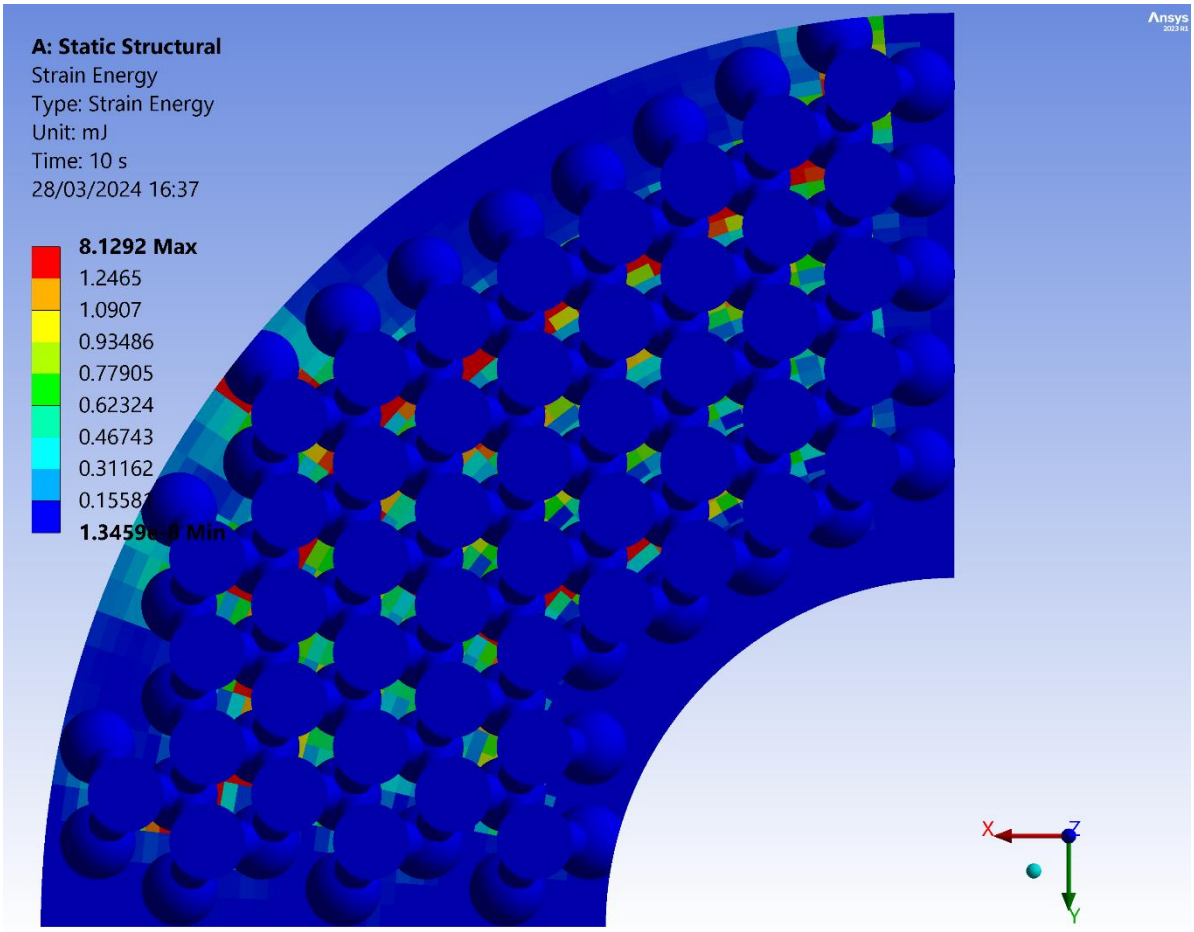

Figure 7.96 Strain Energy filtered contour map: Tetrahedral 50% – top view

Figure 7.95 depicts areas of heightened strain energy up to 2mJ. Moving forward to a filtered view of the strain map, in *Figure 7.96*, a symmetrical distribution of strain energy across the area is evident, with noticeably higher concentrations in the outer nodes. Notably, these concentrations go up to 1.3mJ, being significantly higher than the rest of the models. While these values are not exceptionally high, they underscore the significance of the differences between patterns.

Within *Table 7.9*, a comprehensive array of data unveils the minimum, maximum, and total strain energy values documented throughout the designated timeframe. This dataset acts as a reservoir of knowledge, offering valuable glimpses into the intricacies of structural behavior and the evolving nature of deformation responses. By meticulously analyzing this table, we can zero in on the total strain energy associated with the initial displacement, thereby deepening our comprehension of structural dynamics and response mechanisms over time. Notably, upon careful review, we note that the maximum and total strain energy readings reach 8.13mJ

and 100.42J respectively, offering valuable insights into the magnitude of structural deformation under various conditions.

Graphs are showcased in *Figure 7.33.*

Table 7.28 Strain Energy Data – Tetrahedral 50%

t(s)	Min Strain Energy (J)	Max Strain Energy (J)	Total Strain Energy (J)
0.2	1.3195e-013	7.186e-005	0.61578
0.4	1.0344e-013	1.5522e-004	2.0347
0.6	1.1111e-012	3.2161e-004	3.5641
0.9	2.0437e-012	5.7029e-004	5.9308
1.	9.1701e-013	6.541e-004	6.7341
1.2	1.5026e-012	8.2144e-004	8.3604
1.4	3.1014e-012	9.8938e-004	10.012
1.7	5.5984e-012	1.2423e-003	12.534
2.	6.2079e-012	1.4972e-003	15.109
2.2	6.3809e-012	1.6686e-003	16.855
2.4	6.0585e-012	1.8407e-003	18.624
2.6	5.6876e-012	2.0135e-003	20.415
2.9	5.0603e-012	2.2734e-003	23.143
3.	4.8494e-012	2.3607e-003	24.063
3.2	4.4194e-012	2.5358e-003	25.92
3.4	4.0078e-012	2.7109e-003	27.799
3.7	3.6392e-012	2.9744e-003	30.657
4.	3.7289e-012	3.239e-003	33.562
4.2	4.154e-012	3.4163e-003	35.524
4.4	4.9455e-012	3.5937e-003	37.507
4.7	5.4082e-012	3.8596e-003	40.52
5	6.0839e-012	4.1255e-003	43.577
5.2	6.5544e-012	4.3029e-003	45.64
5.4	7.7105e-012	4.4796e-003	47.722
5.7	1.066e-011	4.7434e-003	50.881
6.	1.5496e-011	5.0057e-003	54.083
6.2	2.0219e-011	5.18e-003	56.241
6.4	1.9438e-011	5.3528e-003	58.416
6.7	1.7852e-011	5.609e-003	61.714
7.	1.5514e-011	5.8616e-003	65.052
7.2	1.4041e-011	6.0282e-003	67.299

7.4	1.256e-011	6.1925e-003	69.563
7.7	1.0703e-011	6.4344e-003	72.99
8.	1.0252e-011	6.6712e-003	76.455
8.2	1.3529e-011	6.8269e-003	78.784
8.4	1.1092e-011	6.9805e-003	81.129
8.7	3.7581e-012	7.206e-003	84.676
9.	6.8205e-012	7.427e-003	88.256
9.2	8.2539e-012	7.5722e-003	90.661
9.4	1.7374e-011	7.7152e-003	93.08
9.6	1.6636e-011	7.8558e-003	95.513
9.9	1.4307e-011	8.0612e-003	99.187
10.	1.3459e-011	8.1292e-003	100.42

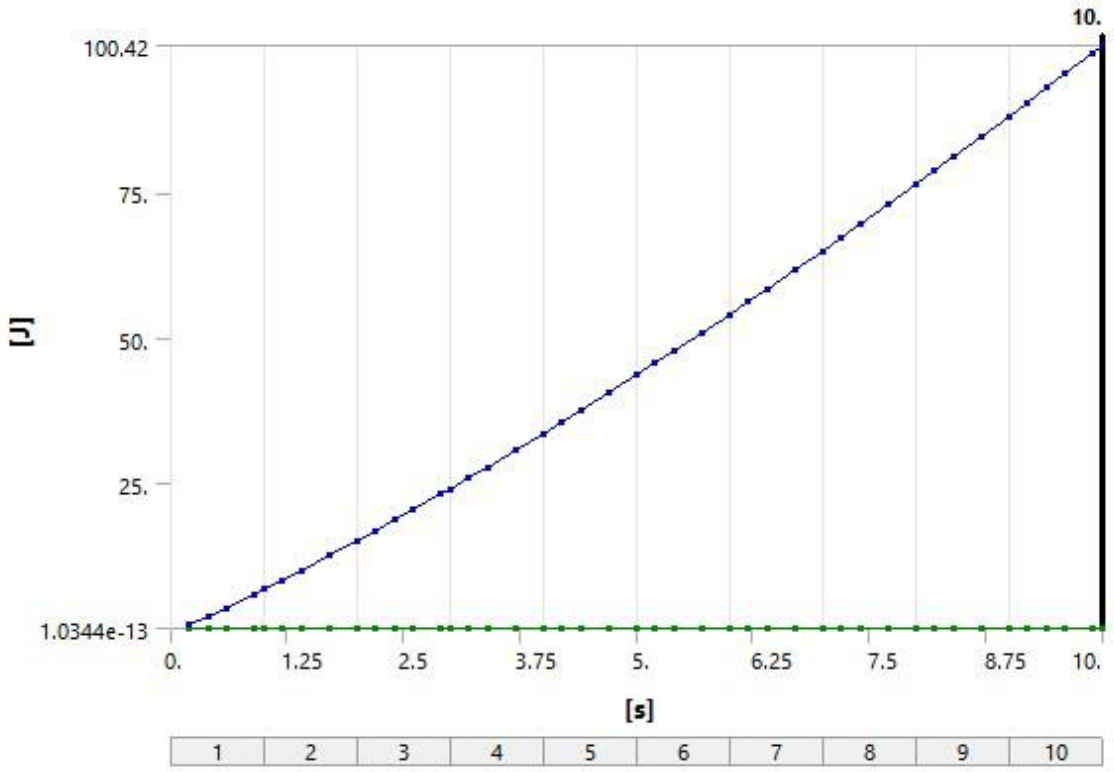

Figure 7.97 Strain Energy Profiles: Tetrahedral 50%

7.6.5 Force reaction

Table 7.29 portrays the application of force (F) over a duration of time (t), where negative values denote compressive force. Over the course of time, there's a progressive escalation in the magnitude of compressive force equaling up to 246690N, indicative of sustained pressure exertion. This implies an ongoing deformation or compression within the material or structure under examination. The consistent trajectory underscores the stability and uniformity of the applied force throughout the designated time frame. Further investigation could delve into associating these force magnitudes with particular mechanical reactions or structural responses. Correspondingly, *Figure 7.18* visually depicts the force reaction trend across time.

Table 7.29 Force reaction – Tetrahedral 50%

t(s)	F(N)
0.2	-1.2098e+005
0.4	-1.4987e+005
0.6	-1.5534e+005
0.9	-1.6001e+005
1.	-1.6137e+005
1.2	-1.6395e+005
1.4	-1.6638e+005
1.7	-1.6996e+005
2.	-1.7347e+005
2.2	-1.7577e+005
2.4	-1.7801e+005
2.6	-1.8025e+005
2.9	-1.8356e+005
3.	-1.8465e+005
3.2	-1.8683e+005
3.4	-1.8896e+005
3.7	-1.9213e+005
4.	-1.9526e+005
4.2	-1.9732e+005
4.4	-1.9935e+005
4.7	-2.0237e+005
5	-2.0534e+005
5.2	-2.073e+005
5.4	-2.0922e+005
5.7	-2.1208e+005
6.	-2.1489e+005
6.2	-2.1675e+005

6.4	-2.1856e+005
6.7	-2.2125e+005
7.	-2.2389e+005
7.2	-2.2561e+005
7.4	-2.2731e+005
7.7	-2.2979e+005
8.	-2.3222e+005
8.2	-2.338e+005
8.4	-2.3535e+005
8.7	-2.3762e+005
9.	-2.3982e+005
9.2	-2.4124e+005
9.4	-2.4266e+005
9.6	-2.4403e+005
9.9	-2.4604e+005
10.	-2.4669e+005

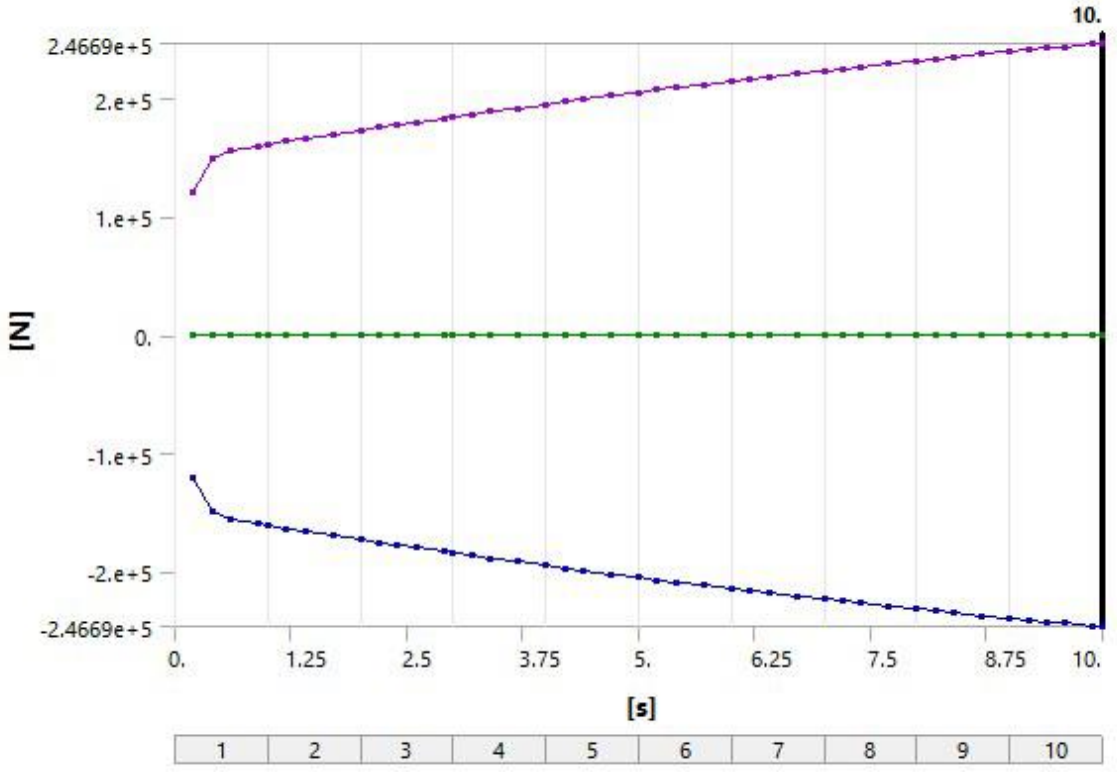

Figure 7.98 Force Reaction Profiles: Tetrahedral 50%

8. Discussion

8.1 Comparative Analysis

8.1.1 Maximum and Average Deformation

In comparing the various lattice models based on their maximum and average deformation values, we can discern nuanced differences in their structural responses *(Table 8.1).*

For the BCC 12% and BCC 50% models, both configurations exhibit similar maximum deformations, with values of 0.515 mm and 0.511 mm respectively. However, the BCC 50% model shows slightly higher average deformation at 0.262 mm compared to 0.254 mm for the BCC 12% model. This suggests that despite comparable maximum deformations, the BCC 50% lattice experiences slightly greater overall deformation on average.

Moving to the I-type configurations, both I-type 12% and I-type 30% models demonstrate maximum deformations of 0.508 mm, with average deformations of 0.253 mm and 0.25 mm respectively. Close similarities in both maximum and average deformations between the two configurations can be observed, indicating consistent structural responses despite differences in density.

Transitioning to the tetrahedral configurations, both tetrahedral 12% and tetrahedral 50% models exhibit identical maximum and average deformations of 0.503 mm and 0.231 mm, and 0.249 mm respectively. This uniformity suggests that the tetrahedral lattice structures, regardless of density, display consistent deformation characteristics under applied loads.

In summary, while each lattice configuration demonstrates unique deformation patterns, the comparison of maximum and average deformation values provides valuable insights into their structural behavior. These findings contribute to a deeper understanding of how different lattice designs respond to external forces and can inform the optimization of lattice structures for various engineering applications.

Table 8.1 Deformation comparison

Model	Maximum Deformation (mm)	Average Deformation (mm)
BCC 12%	0,515	0,254
BCC 50%	0,511	0,262
I-type 12%	0,508	0,253
I-type 30%	0,508	0,250
Tetra 12%	0,503	0,231
Tetra 50%	0,503	0,249

8.1.2 Maximum and Average Elastic Strain

Starting with the BCC lattice patterns, both 12% and 50% configurations exhibit notable differences in maximum and average elastic strain. The BCC 50% configuration shows higher values for both maximum and average elastic strain compared to the BCC 12% configuration, indicating a more pronounced deformation. Specifically, the BCC 50% lattice demonstrates a maximum elastic strain of 0.007 mm/mm and an average elastic strain of 0.003 mm/mm, while the BCC 12% lattice has a maximum elastic strain of 0.005 mm/mm and an average elastic strain of 0.002 mm/mm.

Moving on to the I-type lattice patterns, both 12% and 30% configurations exhibit higher maximum and average elastic strain values compared to the BCC configurations. The I-type lattice patterns show maximum elastic strain values of 0.011mm/mm and 0.010mm/mm for the 12% and 30% configurations, respectively, with average elastic strain values of 0.003mm/mm for both densities. These lower elastic strain values suggest less deformation and strain in the I-type lattice patterns compared to the BCC patterns. Additionally, Tetrahedral 50% exhibits similar stress concentration levels to BCC 50%.

Overall, the comparison of maximum and average elastic strain values across different lattice configurations provides valuable insights into their structural behavior, highlighting variations in deformation and strain levels based on the lattice pattern and density.

Table 8.2 Elastic strain comparison

Model	Maximum Elastic Strain (mm/mm)	Average Elastic Strain (mm/mm)
BCC 12%	0,005	0,002
BCC 50%	0,007	0,003
I-type 12%	0,011	0,003
I-type 30%	0,010	0,002
Tetra 12%	0,160	0,025
Tetra 50%	0,007	0,003

8.1.3 Maximum and Average Stress

For both BCC lattice patterns (12% and 50%), notable stress concentrations are observed, with higher stress levels recorded at incomplete nodes. The BCC 50% configuration exhibits significantly higher maximum and average stress values compared to BCC 12%, indicating a more pronounced structural response to applied loads.

Similarly, the I-type lattice configurations (12% and 30%) demonstrate substantial stress concentrations, particularly at incomplete nodes. However, the I-type 12% configuration exhibits higher maximum stress compared to I-type 30%, suggesting differences in structural stability and load-bearing capacity between the two densities.

The contrasting behavior between BCC and I-type lattices becomes apparent regarding density variations. In BCC structures, as density increases, there is a concurrent rise in both maximum and average stress levels, whereas in I-type configurations, an increase in density leads to a reduction in both maximum and average stresses.

In the tetrahedral lattice configurations, significant stress levels are observed, with both maximum and average stress values surpassing those of the BCC and I-type configurations. This indicates a potentially higher risk of structural failure in the tetrahedral lattice under similar loading conditions.

Overall, the comparison of stress values highlights the importance of selecting appropriate lattice configurations and densities to ensure structural integrity and performance in various applications. Additionally, it emphasizes the need for thorough analysis and optimization to mitigate potential failure risks and optimize the structural design for specific engineering requirements.

Table 8.3 Stress comparison

Model	Maximum stress (MPa)	Average stress (MPa)
bcc 12%	1054,4	306,7
bcc50%	1374,2	495,2
itype12%	2118,3	491,1
itype30%	1834,8	358,6
tetra50%	1359,9	543,3

8.1.4 Maximum and Total Strain Energy

When comparing various lattice configurations, an analysis of maximum and average strain energy provides valuable insights into their structural behavior. In the BCC 12% and BCC 50% configurations, significant differences in both maximum and average strain energy are evident. The BCC 12% model exhibits substantially higher maximum strain energy at 39.94 mJ compared to 10.235 mJ in the BCC 50% model. Similarly, the average strain energy is notably higher in the BCC 50% configuration at 82,484 mJ compared to 6,940.2 mJ in the BCC 12% configuration. These findings suggest that while both configurations experience strain concentration, the BCC 50% model undergoes more pronounced deformation overall.

The comparison of maximum and average strain energy across various lattice configurations unveils significant disparities in their structural behaviors and responses to applied loads. In both the BCC 12% and BCC 50% configurations, strain energy exhibits notable concentrations, with the BCC 50% model demonstrating a higher maximum strain energy of 10.235 mJ compared to the BCC 12% model's 0.4 mJ. However, the average strain energy is considerably higher in the BCC 50% configuration, reaching 82,484 mJ, compared to the BCC 12% configuration's 6,940.2 mJ, indicating a more widespread deformation across the lattice structure.

Conversely, the I-type lattice configurations (12% and 30%) showcase significantly lower maximum and average strain energy values compared to the BCC configurations. For the I-type 12% configuration, the maximum strain energy is 0.81 mJ, with an average of 15,654 mJ, while for the I-type 30% configuration, these values are slightly higher at 1.05 mJ and 28,698 mJ, respectively. These results suggest a more uniform distribution of strain energy across the lattice structure in the I-type configurations, indicating a more stable structural behavior with lower overall deformation.

In the Tetrahedral 50% configuration, the maximum and average strain energy values are moderate compared to the BCC and I-type configurations. With a maximum strain energy of 8.13 mJ and an average of 100,420 mJ, this configuration demonstrates a balanced structural stability and deformation under applied loads.

In summary, the analysis of maximum and average strain energy provides valuable insights into the structural behavior of different lattice configurations. While the BCC configurations exhibit higher levels of localized deformation, the I-type configurations display more uniform strain distribution, and the Tetrahedral 50% configuration demonstrates a moderate level of deformation across the lattice structure.

Table 8.4 Strain Energy Comparison

Model	Max Strain Energy (mJ)	Total Strain Energy (mJ)
bcc 12%	0.40	6940
Bcc 50%	10.23	82484
itype12%	0.81	15654
itype30%	1.05	28698
tetra50%	8.13	100420

8.1.5 Maximum Force Reaction

The comparison of maximum forces across various lattice configurations reveals significant differences in their structural behaviors and load-bearing capacities. In both the BCC 12% and BCC 50% configurations, the maximum forces recorded are 17,362 N and 191,610 N, respectively. This indicates a higher load-bearing capacity in the BCC 50% configuration compared to the BCC 12% configuration, attributed to the denser lattice structure.

Conversely, the I-type lattice configurations (12% and 30%) exhibit substantially higher maximum forces, with values of 37,034 N for I-type 12% and 77,375 N for I-type 30%. These configurations demonstrate a robust load-bearing capacity, likely due to their unique geometric arrangement and distribution of material.

In the Tetrahedral configurations, both Tetrahedral 12% and Tetrahedral 50% exhibit distinct maximum forces. Tetrahedral 12% records a remarkably high maximum force of 3,446,000 N, being also double the size of the other models, with 180^{o} range. On the other hand, Tetrahedral 50% demonstrates a maximum force of 246,690 N, still substantial in its own right and more than anything similar.

In summary, the analysis of maximum forces highlights the diverse load-bearing capabilities of different lattice configurations. While BCC configurations offer moderate load-bearing capacities, I-type configurations demonstrate robustness, and Tetrahedral configurations showcase exceptional load-bearing capabilities, especially Tetrahedral 12%. These findings underscore the importance of selecting an appropriate lattice configuration based on specific load requirements and structural performance criteria.

Table 8.5 Force Reaction comparison

Model	Maximum Force (N)
BCC 12%	17362
BCC 50%	191610
I-type 12%	37034
I-type 30%	77375
Tetra 50%	246690

8.2 Limitations

While the research endeavors to provide comprehensive insights into lattice clutch disk design, several limitations warrant acknowledgment, shaping the scope and depth of the study.

Firstly, the Cartesian unit cells utilized in the study present inherent limitations, primarily stemming from the presence of incomplete nodes and their associated stressful regions. These incomplete nodes can lead to stress concentrations, potentially affecting the structural integrity and performance of the lattice structures under varying loading conditions. Despite efforts to mitigate these effects through advanced computational techniques, such as finite element analysis (FEA), the influence of incomplete nodes remains a notable limitation in the study.

Additionally, the computational capacity available for conducting simulations represents a significant constraint. The complexity of lattice structures and the computational resources required for their analysis impose practical limitations, particularly for academic researchers or students with restricted access to high-performance computing facilities. While efforts were made to optimize simulation parameters and utilize efficient computational algorithms, the extent of analysis may have been constrained by computational resource limitations, potentially impacting the comprehensiveness of the study's findings.

Furthermore, the utilization of 90-degree models, chosen for computational efficiency, introduces limitations related to model representation and accuracy. While these simplified models expedite computational simulations, they may not fully capture the intricate geometric complexities and load distributions present in real-world clutch disk applications. Consequently, the accuracy and predictive capability of simulation results may be compromised, particularly in scenarios where non-linear or non-homogeneous material behaviors are prevalent.

Moreover, the study's reliance on certain assumptions in modeling, such as linear material behavior and isotropic properties, introduces potential sources of error and uncertainty. While these assumptions facilitate the simplification of complex phenomena for computational analysis, they may not accurately reflect the true mechanical behavior of lattice structures under dynamic loading conditions. As a result, the validity and reliability of simulation results may be subject to limitations associated with the accuracy of these underlying assumptions.

Furthermore, experimental validation of computational findings poses challenges due to limitations in access to experimental facilities and resources. The feasibility of conducting comprehensive validation experiments to corroborate simulation results may be constrained by factors such as budgetary constraints, equipment availability, and time limitations. Consequently, the validation of simulation results and the derivation of actionable insights from experimental data may be hindered, limiting the study's ability to provide robust conclusions.

Lastly, scaling up lattice structures from laboratory-scale prototypes to full-scale industrial applications presents significant challenges. While the study provides valuable insights into the mechanical behavior of lattice clutch disks at a small scale, the translation of these findings to real-world applications may encounter obstacles related to manufacturability, cost-effectiveness, and structural integrity. The scalability of lattice structures for industrial implementation remains an area of ongoing research and development, necessitating further investigation beyond the scope of this study.

In summary, while the research strives to advance understanding in the field of lattice clutch disk design, these acknowledged limitations underscore the need for cautious interpretation of results and highlight avenues for future research and refinement. Addressing these limitations through continued interdisciplinary collaboration and methodological innovation is essential to foster progress and enhance the applicability of lattice structures in automotive and mechanical engineering domains.

9. Conclusions

The comparative analysis of various lattice models offers valuable insights into their structural behaviors, delineating nuanced differences in their responses to applied loads. Across the spectrum of lattice configurations, distinctive patterns emerge, elucidating the intricate interplay between density, deformation, and stress distribution.

Beginning with the exploration of BCC lattice patterns, both the 12% and 50% configurations unveil intriguing dynamics. Despite exhibiting comparable maximum deformations, the BCC 50% lattice demonstrates marginally higher average deformation, indicating a subtle yet discernible variation in structural response. This disparity suggests that even within the same lattice type, subtle shifts in density can engender notable changes in deformation characteristics, underscoring the sensitivity of lattice structures to compositional alterations.

Transitioning to the realm of I-type configurations, a contrasting narrative unfolds. Here, the interplay between density and structural response manifests in a different manner. Unlike the BCC counterparts, the I-type lattice configurations showcase a more uniform distribution of elastic strain, irrespective of density variations. This uniformity implies a more consistent structural behavior across different density levels, hinting at inherent stability within the lattice framework.

Moreover, the exploration extends to Tetrahedral configurations, where intriguing parallels with BCC patterns surface. Notably, the Tetrahedral 50% configurations mirror the stress concentration levels observed in the BCC 50% lattice, hinting at underlying structural similarities between these distinct lattice types. This convergence underscores the multifaceted nature of lattice structures, where diverse configurations can exhibit analogous responses under specific loading conditions, thereby broadening our understanding of lattice mechanics.

Furthermore, delving into the realm of strain energy unveils a rich tapestry of structural dynamics. While BCC configurations showcase higher levels of localized deformation, the I-type counterparts offer a more uniform distribution of strain energy. This dichotomy highlights the nuanced interplay between lattice geometry, density, and strain energy distribution, underscoring the multifactorial nature of structural response in lattice materials.

In summary, the comparative analysis serves as a pivotal cornerstone in elucidating the intricate nuances of lattice structural behavior. By unraveling the complex interplay between density, deformation, stress distribution, and strain energy, this exploration provides invaluable insights into the optimization and design of lattice structures for diverse engineering applications.

10. Future Implications

In this chapter, the future implications and potential avenues for further exploration in the field of lattice clutch disk design are explored. Building upon the foundational analysis presented earlier, the focus broadens to consider broader perspectives, including comparisons with alternative materials, exploration of different lattice densities, and investigation into various geometric configurations. By delving into these future implications, the goal is to deepen the understanding of lattice structures and their application in clutch disk design, driving innovation and advancements in automotive and mechanical engineering.

One area of exploration involves comparing lattice structures with conventional materials such as AlSi10Mg, Manufacturing Steel, and Titanium. By examining the mechanical properties of these materials, such as strength and durability, insights are sought into how lattice structures stack up against traditional options, offering insights into potential alternatives for clutch disk applications.

Furthermore, a comprehensive study is conducted to explore the relationship between lattice density and mechanical properties. Through this exploration, understanding is sought regarding how varying densities impact factors such as deformation, stress distribution, and fatigue resistance, providing valuable insights into optimizing lattice design for specific performance requirements.

Additionally, a comparative analysis between cartesian and cylindrical lattice configurations is undertaken to determine their relative effectiveness under different operating conditions. By evaluating factors such as structural integrity, load-bearing capacity, and manufacturability, the optimal lattice geometry for clutch disk applications is identified.

In addition to the explored future implications, further research could investigate the development of fully parameterized mechanical properties for lattice clutch systems. This endeavor would involve an in-depth examination of how the mechanical characteristics of lattice clutches vary in response to changes in parameters such as the diameter of the struts or other geometric properties. By establishing comprehensive parameterization, researchers can better understand the nuanced relationships between lattice clutch design variables and mechanical performance, facilitating the optimization of lattice clutch structures for specific engineering requirements. This approach holds the potential to enhance the precision and efficiency of lattice clutch design processes, ultimately contributing to advancements in automotive and mechanical engineering domains.

Moreover, advanced Finite Element Analysis (FEA) techniques are leveraged to simulate torsional and shear loading conditions on lattice clutch disks. Through this analysis, understanding is sought regarding how different loading scenarios affect structural performance, deformation patterns, and stress distribution, providing a comprehensive understanding of the disk's behavior under varying operating conditions.

Expanding simulations to incorporate larger displacement scenarios allows observation of the disk's response under extreme loading conditions. By investigating how the lattice structure accommodates increased deformation, the impact on performance and durability is assessed, offering valuable insights for design optimization.

Furthermore, the feasibility of additively manufacturing lattice clutch disks and conducting comprehensive compression tests to evaluate their mechanical properties and structural integrity is explored. By assessing factors such as material homogeneity, load-bearing capacity, and failure modes, the suitability of lattice structures for real-world applications is validated.

Finally, rigorous fatigue testing is conducted on lattice clutch disks to assess their long-term durability and performance under cyclic loading conditions. By investigating factors such as fatigue life, crack propagation, and failure mechanisms, the reliability and longevity of lattice structures in clutch disk applications are ascertained. Through these comprehensive analyses and experiments, valuable insights are provided to guide future research endeavors in this exciting field.

By exploring these future implications, your thesis can contribute significantly to advancing the understanding and application of lattice structures in clutch disk design, paving the way for innovative solutions and enhanced performance in automotive and mechanical engineering domains.

11. List of Figures

12. List of Tables

13. References

1. Agwu, U. O., Wang, K., Singh, C., Leemhuis, C., Yamakawa, S., & Shimada, K. (2021). Assessing tetrahedral lattice parameters for engineering applications through finite element analysis. *3D Print Addit Manuf*, 8(4), 238-252. doi:10.1089/3dp.2020.0222
2. Al-Ketan, O., Rowshan, R., & Abu Al-Rub, R. K. (2018). Topology-mechanical property relationship of 3D printed strut, skeletal, and sheet based periodic metallic cellular materials. *Additive Manufacturing*, 19, 167–183. doi:10.1016/j.addma.2017.12.006
3. Al-Saedi, D. S. J., Masood, S. H., Faizan-Ur-Rab, M., Alomarah, A., & Ponnusamy, P. (2018). Mechanical properties and energy absorption capability of functionally graded F2BCC lattice fabricated by SLM. *Materials & Design*, 144, 32–44. doi:10.1016/j.matdes.2018.01.059
4. Alsalla, H., Hao, L., & Smith, C. (2016). Fracture toughness and tensile strength of 316L stainless steel cellular lattice structures manufactured using the selective laser melting technique. *Materials Science and Engineering: A*, 669, 1-6. https://doi.org/10.1016/j.msea.2016.05.075
5. An, L., Guo, Z., Li, Z., et al. (2022). Tailoring thermal insulation architectures from additive manufacturing. *Nat Commun*, 13, 4309. https://doi.org/10.1038/s41467-022-32027-3
6. Berger, J., Wadley, H., & McMeeking, R. (2017). Mechanical metamaterials at the theoretical limit of isotropic elastic stiffness. *Nature*, 543, 533–537. https://org/10.1038/nature21075
7. Bonatti, C., & Mohr, D. (2018). Smooth-shell metamaterials of cubic symmetry: Anisotropic elasticity, yield strength and specific energy absorption. *Acta Materialia*. doi:10.1016/j.actamat.2018.10.034
8. Bonatti, C., & Mohr, D. (2017). Large deformation response of additively-manufactured FCC metamaterials: From octet truss lattices towards continuous shell mesostructures. *International Journal of Plasticity*, 92, 122-147. https://doi.org/10.1016/j.ijplas.2017.02.003
9. Cao, X., Duan, S., Liang, J., Wen, W., & Fang, D. (2018). Mechanical properties of an improved 3D-printed rhombic dodecahedron stainless steel lattice structure of variable cross section. *International Journal of Mechanical Sciences*, 145, 53-63. https://doi.org/10.1016/j.ijmecsci.2018.07.006
10. Chen, Z., Xie, Y. M., Wu, X., Wang, Z., Li, Q., & Zhou, S. (2019). On hybrid cellular materials based on triply periodic minimal surfaces with extreme mechanical properties. *Materials & Design*, 183, 108109. https://doi.org/10.1016/j.matdes.2019.108109
11. P. Coelho, H. Rodrigues, Hierarchical topology optimization addressing material design constraints and application to sandwich-type structures, Structural and Multidisciplinary Optimization 52(1) (2015) 91-104
12. Das, S., Bourell, D. L., & Babu, S. S. (2016). Metallic materials for 3D printing. *MRS Bulletin*, 41(10), 729–741. doi:10.1557/mrs.2016.217
13. Fernandes, M. C., Aizenberg, J., Weaver, J. C., et al. (2021). Mechanically robust lattices inspired by deep-sea glass sponges. *Nat. Mater.*, 20, 237–241. https://doi.org/10.1038/s41563-020-0798-1
14. Feng, J., Liu, B., Lin, Z., & Fu, J. (2021). Isotropic octet-truss lattice structure design and anisotropy control strategies for implant application. *Materials & Design*, 203, 109595. https://doi.org/10.1016/j.matdes.2021.109595

15. Frazier, W. E. (2014). Metal Additive Manufacturing: A Review. *J. of Materi Eng and Perform*, 23, 1917–1928. https://doi.org/10.1007/s11665-014-0958-z
16. Guo, X., Li, X., Wang, E., Fuh, J. Y. H., Lu, W. F., & Zhai, W. (2023). Bioinspired hierarchical diamond triply periodic minimal surface lattices with high energy absorption and damage tolerance. *Additive Manufacturing*, 76, 103792. https://doi.org/10.1016/j.addma.2023.103792
17. Guo, X., Ding, J., Li, X., Qu, S., Song, X., Fuh, J. Y. H., Lu, W. F., & Zhai, W. (2022). Enhancement in the mechanical behaviour of a Schwarz Primitive periodic minimal surface lattice structure design. *International Journal of Mechanical Sciences*, 216, 106977. https://doi.org/10.1016/j.ijmecsci.2021.106977
18. Hassanin, H., Modica, F., El-Sayed, M. A., Liu, J., & Essa, K. (2016). Manufacturing of Ti-6Al-4V Micro-Implantable Parts Using Hybrid Selective Laser Melting and Micro-Electrical Discharge Machining. *Advanced Engineering Materials*, 18(9), 1544–1549. doi:10.1002/adem.201600172
19. Han, L., & Che, S. (2018). An Overview of Materials with Triply Periodic Minimal Surfaces and Related Geometry: From Biological Structures to Self-Assembled Systems. *Advanced Materials*, 30(17), 1705708. doi:10.1002/adma.201705708
20. Jeon, S.-Y., Shen, B., Traugutt, N. A., Zhu, Z., Fang, L., Yakacki, C. M., Nguyen, T. D., & Kang, S. H. (2022). Synergistic Energy Absorption Mechanisms of Architected Liquid Crystal Elastomers. *Adv. Mater.*, 34, 2200272. https://doi.org/10.1002/adma.202200272
21. Kolken, H. M. A., Callens, S. J. P., Leeflang, M. A., Mirzaali, M. J., & Zadpoor, A. A. (2022). Merging strut-based and minimal surface meta-biomaterials: Decoupling surface area from mechanical properties. *Additive Manufacturing*, 52, 102684. https://doi.org/10.1016/j.addma.2022.102684
22. Kong, D., Dong, C., Wei, S., Ni, X., Zhang, L., Li, R., & Li, X. (2021). About metastable cellular structure in additively manufactured austenitic stainless steels. *Additive Manufacturing*, 38, 101804. doi:10.1016/j.addma.2020.101804
23. Kooistra, G. (2004). Compressive behavior of age hardenable tetrahedral lattice truss structures made from aluminium. *Acta Materialia*, 52(14), 4229–4237. doi:10.1016/j.actamat.2004.05.039
24. Kundu, R. D., & Zhang, X. S. (2023). Additive manufacturing of stiff and strong structures by leveraging printing-induced strength anisotropy in topology optimization. *Additive Manufacturing*, 75, 103730. https://doi.org/10.1016/j.addma.2023.103730
25. Kuziak, R., Kawalla, R., & Waengler, S. (2008). Advanced high strength steels for automotive industry. *Archives of Civil and Mechanical Engineering*, 8(2), 103–117. doi:10.1016/s1644-9665(12)60197-6
26. Lewandowski, J. J., & Seifi, M. (2016). Metal Additive Manufacturing: A Review of Mechanical Properties. *Annual Review of Materials Research*, 46(1), 151-186.
27. Li, T., Jarrar, F., Abu Al-Rub, R., & Cantwell, W. (2021). Additive manufactured semi-plate lattice materials with high stiffness, strength and toughness. *International Journal of Solids and Structures*, 230-231, 111153. doi:10.1016/j.ijsolstr.2021.111153
28. Li, X., Chua, J. W., Yu, X., Li, Z., Zhao, M., Wang, Z., & Zhai, W. (Year). 3D-Printed Lattice Structures for Sound Absorption: Current Progress, Mechanisms and Models, Structural-Property.

29. Li, X., Yu, X., Chua, J. W., Lee, H. P., Ding, J., & Zhai, W. (2021). Microlattice Metamaterials with Simultaneous Superior Acoustic and Mechanical Energy Absorption. *Small*, 17(24), 2100336. doi:10.1002/smll.202100336
30. Li, X., Zhao, M., Yu, X., Chua, J. W., Yang, Y., Lim, K. M., & Zhai, W. (2023). Multifunctional and customizable lattice structures for simultaneous sound insulation and structural applications. *Materials & Design*, 234, 112354. https://doi.org/10.1016/j.matdes.2023.112354
31. Li, X., Tan, Y. H., Willy, H. J., Wang, P., Lu, W., Cagirici, M., Ong, C. Y. A., Herng, T. S., Wei, J., & Ding, J. (2019). Heterogeneously tempered martensitic high strength steel by selective laser melting and its micro-lattice: Processing, microstructure, superior performance and mechanisms. *Materials & Design*, 178, 107881. https://doi.org/10.1016/j.matdes.2019.107881
32. Maskery, N. Aboulkhair, A. Aremu, C. Tuck, I. Ashcroft, R.D. Wildman, R.J. Hague, A mechanical property evaluation of graded density Al-Si10-Mg lattice structures manufactured by selective laser melting, Materials Science and Engineering: A 670 (2016) 264-274
33. Ma, Q., Zhang, L., Ding, J., Qu, S., Fu, J., Fu, M. W., Song, X., & Wang, M. Y. (2023). Analytical design of stretching-dominated truss lattices with tailored elasticity from transversely isotropic base materials. *Materials & Design*, 230, 111995. https://doi.org/10.1016/j.matdes.2023.111995
34. Meza, L. R., Zelhofer, A. J., Clarke, N., Mateos, A. J., Kochmann, D. M., & Greer, J. R. (2015). Resilient 3D hierarchical architected metamaterials. *Proceedings of the National Academy of Sciences*, 112(37), 11502–11507. doi:10.1073/pnas.1509120112
35. Niendorf, T., Leuders, S., Riemer, A., Richard, H. A., Tr¨oster, T., & Schwarze, D. (2013). Highly anisotropic steel processed by selective laser melting. *Metall. Mater. Trans. B*, 44(4), 794–796.
36. Osakada, K., & Shiomi, M. (2006). Flexible manufacturing of metallic products by selective laser melting of powder. *International Journal of Machine Tools and Manufacture*, 46(11), 1188–1193. doi:10.1016/j.ijmachtools.2006.01
37. Pham, M. S., Liu, C., Todd, I., & et al. (2019). Damage-tolerant architected materials inspired by crystal microstructure. *Nature*, 565, 305–311. https://doi.org/10.1038/s41586-018-0850-3
38. Soyarslan, C., Blümer, V., Bargmann, S., & et al. (Year). Tunable auxeticity and elastomechanical symmetry in a class of very low density core-shell cubic crystals. *Acta Materialia*, (Volume).
39. Shamsujjoha, M., Agnew, S. R., Fitz-Gerald, J. M., Moore, W. R., & Newman, T. A. (2018). High Strength and Ductility of Additively Manufactured 316L Stainless Steel Explained. *Metallurgical and Materials Transactions A*, 49(7), 3011–3027. doi:10.1007/s11661-018-4607-2
40. Sugimura, Y. (2004). Mechanical response of single-layer tetrahedral trusses under shear loading. *Mechanics of Materials*, 36(8), 715–721. doi:10.1016/j.mechmat.2003.05.002
41. Sun, Z. J., Tan, X. P., Tor, S. B., & Chua, C. K. (2018). Simultaneously enhanced strength and ductility for 3D-printed stainless steel 316L by selective laser melting. *NPG Asia Mater.*, 10(4), 127–136.
42. Su, R., Chen, J., Zhang, X., Wang, W., Li, Y., He, R., & Fang, D. (Year). 3D-Printed Micro/Nano-Scaled Mechanical Metamaterials: Fundamentals, Technologies, Progress, Applications, and Challenges. *Small*, 19, 2206391. https://doi.org/10.1002/smll.202206391

43. Tancogne-Dejean, T., & Mohr, D. (2018). Elastically-isotropic truss lattice materials of reduced plastic anisotropy. *International Journal of Solids and Structures*, 138, 24-39. https://doi.org/10.1016/j.ijsolstr.2017.12.025
44. Tancogne-Dejean, T., Diamantopoulou, M., Gorji, M. B., Bonatti, C., & Mohr, D. (2018). Adv. Mater. 2018, 30, 1803334. https://doi.org/10.1002/adma.201803334
45. Wu, J., Wang, W., & Gao, X. (2019). Design and Optimization of Conforming Lattice Structures. IEEE Transactions on Visualization and Computer Graphics. Advance online publication. https://doi.org/10.1109/tvcg.2019.2938946
46. Yan, C., Hao, L., Hussein, A., & Raymont, D. (2012). Evaluations of cellular lattice structures manufactured using selective laser melting. International Journal of Machine Tools and Manufacture, 62, 32–38. https://doi.org/10.1016/j.ijmachtools.2012.06
47. Yan, C., Hao, L., Hussein, A., & Raymont, D. (2012). Evaluations of cellular lattice structures manufactured using selective laser melting. International Journal of Machine Tools and Manufacture, 62, 32–38. https://doi.org/10.1016/j.ijmachtools.2012.06.00
48. Yadroitsev, I., & Smurov, I. (2010). Selective laser melting technology: From the single laser melted track stability to 3D parts of complex shape. Physics Procedia, 5, 551–560. https://doi.org/10.1016/j.phpro.2010.08.083
49. Tong Yu, Xinwei Li, Miao Zhao, Xiao Guo, Junhao Ding, Shuo Qu, Thomas Wei Jie Kwok, Tao Li, Xu Song, Beng Wah Chua. (2023). Truss and plate hybrid lattice structures: Simulation and experimental investigations of isotropy, large-strain deformation, and mechanisms. Materials Today Communications, 35, 106344. https://doi.org/10.1016/j.mtcomm.2023.106344
50. Zhang, L., Ma, Q., Ding, J., Qu, S., Fu, J., Fu, M. W., Song, X., & Wang, M. Y. (2022). Design of elastically isotropic shell lattices from anisotropic constitutive materials for additive manufacturing. Additive Manufacturing, 59(Part B), 103185. https://doi.org/10.1016/j.addma.2022.103185
51. Wang, D., Liu, Y., Yang, Y. Q., & Xiao, D. M. (2016). Theoretical and experimental study on surface roughness of 316L stainless steel metal parts obtained through selective laser melting. Rapid Prototyp. J., 22(4), 706–716.
52. Wang, Y.M., Voisin, T., McKeown, J.T., Ye, J., Calta, N.P., Li, Z., Zeng, Z., Zhang, Y., Chen, W., Roehling, T.T., Ott, R.T., Santala, M.K., Depond, P.J., Matthews, M.J., Hamza, A. V., & Zhu, T. (2018). Additively manufactured hierarchical stainless steels with high strength and ductility. Nat. Mater., 17(1), 63–71.
53. White, B. C., Garland, A., Alberdi, R., & Boyce, B. L. (2021). Interpenetrating lattices with enhanced mechanical functionality. Additive Manufacturing, 38, 101741. doi:10.1016/j.addma.2020.101741
54. Xinxin Wang, Zhendong Li, Xinwei Li, Kai Wei, Zhonggang Wang. (2023). Customizable plateau in face-centered cubic hierarchical lattices achieved by self-similar embedded design. Materials & Design, 233, 112186. https://doi.org/10.1016/j.matdes.2023.112186
55. Yu, X., Wang, F., Luo, Z., Kang, Z., & Wang, Y. (2023). Design of hierarchical microstructures with isotropic elastic stiffness. Materials & Design, 229, 111895. https://doi.org/10.1016/j.matdes.2023.111895
56. Zhang, X., Wang, Y., Ding, B., & Li, X. (2020). Design, Fabrication, and Mechanics of 3D Micro-/Nanolattices. Small, 16, 1902842. https://doi.org/10.1002/smll.201902842

57. Zhang, Z., Song, B., Yao, Y., Zhang, L., Wang, X., Fan, J., & Shi, Y. (2022). Bioinspired, Simulation-Guided Design of Polyhedron Metamaterial for Simultaneously Efficient Heat Dissipation and Energy Absorption. Adv. Mater. Technol., 7, 2200076. https://doi.org/10.1002/admt.202200076
58. Zhang, Z., Zhang, L., Song, B., Yao, Y., Shi, Y., & Wang, X. (2022). Bamboo-inspired, simulation-guided design and 3D printing of light-weight and high-strength mechanical metamaterials. Applied Materials Today, 26, 101268. https://doi.org/10.1016/j.apmt.2021.101268
59. Zhang, L., Feih, S., Daynes, S., Chang, S., Wang, M. Y., Wei, J., & Lu, W. F. (2018). Energy absorption characteristics of metallic triply periodic minimal surface sheet structures under compressive loading. Additive Manufacturing. doi:10.1016/j.addma.2018.08.007
60. Zhang, L., Feih, S., Daynes, S., Chang, S., Wang, M.Y., Wei, J., & Lu, W.F. (2018). Energy absorption characteristics of metallic triply periodic minimal surface sheet structures under compressive loading. Addit. Manuf., 23, 505–515.
61. Zhang, G., Ma, L., Wang, B., & Wu, L. (2012). Mechanical behaviour of CFRP sandwich structures with tetrahedral lattice truss cores. Composites Part B: Engineering, 43(2), 471–476. doi:10.1016/j.compositesb.2011.11.017
62. Zhao, M., Li, X., Zhang, D. Z., & Zhai, W. (2023). Geometry effect on mechanical properties and elastic isotropy optimization of bamboo-inspired lattice structures. Additive Manufacturing, 64, 103438. https://doi.org/10.1016/j.addma.2023.103438
63. Zhao, M., Li, X., Zhang, D. Z., & Zhai, W. (2023). Design, mechanical properties and optimization of lattice structures with hollow prismatic struts. International Journal of Mechanical Sciences, 238, 107842. https://doi.org/10.1016/j.ijmecsci.2022.107842
64. Miao Zhao, Xinwei Li, David Z. Zhang, Wei Zhai. (2023). TPMS-based interpenetrating lattice structures: Design, mechanical properties and multiscale optimization. International Journal of Mechanical Sciences, 244, 108092. https://doi.org/10.1016/j.ijmecsci.2022.108092
65. Zhong, T., He, K., Li, H., & Yang, L. (2019). Mechanical properties of lightweight 316L stainless steel lattice structures fabricated by selective laser melting. Materials & Design, 181, 108076. https://doi.org/10.1016/j.matdes.2019.108076
66. Odell, D., Wright, P. K., Montero, M., Roundy, S., & Ahn, S. (2002). Anisotropic Material Properties of Fused Deposition Modeling ABS. *Rapid Prototyp. J.*, 8, 248−257.
67. Ma, Q., Zhang, L., Ding, J., Qu, S., Fu, J., Fu, M. W., Song, X., & Wang, M. Y. (2023). Analytical design of stretching-dominated truss lattices with tailored elasticity from transversely isotropic base materials. *Materials & Design*, 230, 111995. https://doi.org/10.1016/j.matdes.2023.111995
68. Boyer, R. R. (1996). An overview on the use of titanium in the aerospace industry. *Materials Science and Engineering: A*, 213(1-2), 103–114. doi:10.1016/0921-5093(96)10233-1

69. Zhang, P., Liu, J., & To, A. C. (2017). Role of anisotropic properties on topology optimization of additive manufactured load bearing structures. *Scripta Materialia*, 135, 148–152. doi:10.1016/j.scriptamat.2016.10

70. Maskery, I., Aremu, A. O., Simonelli, M., Tuck, C., Wildman, R. D., Ashcroft, I. A., & Hague, R. J. M. (2015). Mechanical Properties of Ti-6Al-4V Selectively Laser Melted Parts with Body-Centred-Cubic Lattices of Varying cell size. *Experimental Mechanics*, 55(7), 1261–1272. doi:10.1007/s11340-015-0021-5

71. Wang, X., Xu, S., Zhou, S., Xu, W., Leary, M., Choong, P., Qian, M., Brandt, M., & Xie, Y. M. (2016). Topological design and additive manufacturing of porous metals for bone scaffolds and orthopaedic implants: A review. *Biomaterials, 83*, 127-141. https://doi.org/10.1016/j.biomaterials.2016.01.012

72. Karamoozian, A., Jiang, H., Tan, C. A., Wang, L., & Wang, Y. (2020). *An Integrated Approach for Instability Analysis of Lattice Brake System Using Contact Pressure Sensitivity. IEEE Access, 8, 19948–19969.* doi:10.1109/access.2020.2964337